Copper-Catalysed Autocatalytic Reactions

Elias A. J. Post

A thesis submitted for the degree of

Doctor of Philosophy

of the

University of Oxford



Worcester College

Trinity Term 2020

Declaration

This thesis describes work conducted under the supervision of Professor Stephen Fletcher in the Chemistry Research Laboratory, Oxford, between October 2016 and June 2020. The thesis is entirely my own work except where otherwise indicated and acknowledged. It has not been submitted for any other degree at this university or at any other institution.

Elias A. J. Post

Acknowledgements

Firstly, I would like to thank Steve for welcoming me into the Fletcher group and for steering me away from total synthesis towards autocatalysis. I have truly enjoyed working in this exciting and thought-provoking area of research. You have always been very supportive and have given me the freedom to explore various project ideas, and for that I am grateful.

Special thanks to Andrew. Your guidance during my first year was valuable and much appreciated. I am sure that without your help my research would not have been as fruitful.

The Fletcher group was a fun and supportive environment to work in. Thank you to Reece, Thomas, Wieland, Rob, Elena, Chus, Alex, Nisha, Lucy and all other members for the great times we had together playing board games, singing karaoke, travelling or just chatting in the pub. I am grateful to all the proofreaders (Sarah, Ton, Michael, among others) that helped improve this manuscript.

Thanks to Dhanya Babu, Dr. Dipak Samanta and Prof. Nathalie Katsonis for welcoming me into their lab and helping with the supramolecular characterisation of my protocells.

I am indebted to my parents Jack and Charlotte and my brother Manuel who have always challenged me intellectually and shaped me into the person I am today. I appreciate that you are always there for me and support me in whatever choice I make.

I was very lucky to meet my partner Heather here in Oxford. You are always by my side and have helped me in ways that no one else ever could.

Finally, I thank the ERC and EPSRC for funding my research.

Abstract

The work contained within this thesis describes the development and study of self-reproducing systems, created from simple chemical building blocks, that exhibit emergent, life-like properties. Several different autocatalytic systems that are driven by copper-catalysed azide-alkyne cycloaddition (CuAAC) reactions are reported.

Chapter 1 introduces the fundamental concepts relevant to the bottom-up construction of minimal living systems and highlights relevant synthetic advances in the field of systems chemistry.

The following two chapters describe an autocatalytic system where surfactant formation from phase-separated components is linked to a CuAAC reaction. In Chapter 2, the influence of product seed on the rate of the reaction and the impact of surfactant tail length on the kinetics of the reaction is investigated. Chapter 3 expands upon this system by exploiting the link between the secondary catalyst and the autocatalytic cycle to drive new reaction outcomes. A mechanistic model is formulated that rationalises the kinetic profiles based on the phase behaviour of the coupling partners and the catalyst.

Chapter 4 presents an out-of-equilibrium self-reproducing protocell system that models biological cells more faithfully. Selection and inhibition processes are observed between competing replicators and orthogonal downstream chemical reactivity is incorporated.

Chapter 5 describes the ongoing development of an asymmetric autocatalytic CuAAC reaction through formation of enantioenriched polytriazole ligands *via* dynamic kinetic resolution of allylic azides. An initial finding shows that this new class of chiral ligand induces chirality in asymmetric CuAAC reactions.

Finally, Chapter 6 offers concluding remarks and details future work that may improve upon the reported systems.

Abbreviations

Ac	acetyl
app	apparent
aq	aqueous
Ar	aryl
ATP	adenosine triphosphate
Bn	benzyl
br	broad
Bu	butyl or *n*-butyl
c	concentration
CAC	critical aggregation concentration
$CHCl_3$	chloroform
CH_2Cl_2	dichloromethane
CMC	critical micelle concentration
COSY	correlation spectroscopy
CSTR	continuous stirred-tank reactor
CuAAC	copper-catalysed azide-alkyne cycloaddition
CVC	critical vesicle concentration
d	doublet
d	deuterated
D	configuration relative to dextrorotatory glyceraldehyde
DKR	dynamic kinetic resolution
DLS	dynamic light scattering
DMAP	4-dimethylaminopyridine
DME	1,2-dimethoxyethane
DMF	dimethylformamide
DMSO	dimethyl sulfoxide
DOSY	diffusion-ordered spectroscopy
E	entgegen
ee	enantiomeric excess
eq. or equiv.	equivalents
ESI	electrospray ionisation
Et	Ethyl
Et_2O	diethyl ether
EtOAc	ethyl acetate
EtOH	ethanol
g	grams
GARD	graded autocatalysis replication domain
GTP	guanosine triphosphate
GUV	giant unilaminar vesicles
h	hours
hept	heptet
HPLC	high performance liquid chromatography
HRMS	high resolution mass spectrometry
HSQC	heteronuclear single quantum correlation spectroscopy
Hz	hertz
i	*ipso* or *iso*
IR	infrared

iSCAT	interferometric scattering microscopy
J	joules
J	coupling constant (Hz)
L	litre
L	configuration relative to levorotatory glyceraldehyde
LRMS	low resolution mass spectrometry
M	molar concentration
m	metre
m	multiplet (NMR)
m	*meta*
Me	methyl
MeOH	methanol
min	minute
mol	mole
Ms	methanesulfonyl
m/z	mass to charge ratio
Nu	nucleophile
ND	not determined
NMR	nuclear magnetic resonance
o	*ortho*
OPD	*o*-phenylenediamine
p	*para*
P	pentet
PCR	polymerase chain reaction
Ph	phenyl
pH	decimal logarithm of the reciprocal of the hydrogen ion activity
PhMe	toluene
pKa	decimal logarithm of the acid dissociation constant
ppm	parts per million
Pr	propyl
PYBOX	pyridine-2,6-bis(oxazoline)
q	quartet
quat	quaternary
R	chemical moiety
R	rectus
RNA	Ribonucleic acid
rpm	revolutions per minute
S	sinister
SFC	supercritical fluid chromatography
sp	orbital hybridisation: 1:1 p:s character
sp^2	orbital hybridisation: 2:1 p:s character
t	triplet
t	*tert,* tertiary
TBS	*tert*-butyldimethylsilyl
TBTA	tris(benzyltriazolylmethyl)amine
TEM	transmission electron microscopy
TFA	trifluoroacetic acid
THF	tetrahydrofuran
THPTA	tris(3-hydroxypropyltriazolylmethyl)amine

TLC	thin layer chromatography
TMS	tetramethylsilane
t_R	retention time
UPLC	ultra high performance chromatography
UV	ultraviolet
v	volume
δ	chemical shift
λ	wavelength
ν_{max}	maximum absorbance
°C	degree Celsius

Contents

Chapter 1 General Introduction 1

1.1 What is life? 2

1.2 Autocatalysis 4

1.3 Protocells: growth, division and self-reproduction 11

1.4 Out-of-equilibrium aggregation and self-reproduction 17

1.5 The origin of biological homochirality 22

1.6 Project aim: self-reproducing protocells coupled to a secondary catalyst 24

1.7 References 26

Chapter 2 Self-reproducing micelles coupled to a secondary catalyst 33

2.1 Introduction 34

2.2 CuAAC based physical autocatalysis 35

2.3 Mechanistic study 43

2.4 Conclusions 49

2.5 Experimental 51

2.6 References 74

Chapter 3 Controlling the Kinetics of Self-Reproducing Micelles by Catalyst Compartmentalization in a Biphasic System 77

3.1 Introduction 78

3.2 Controlling catalyst compartmentalization by tuning ligand polarity 80

3.3 Inverting the polarity of the system 86

3.4 Deuterium exchange experiments 90

3.5 Mechanistic rationalisation 92

3.6 Conclusions 100

3.7 Experimental 102

3.8 References 120

Chapter 4 Out-of-Equilibrium Self-Reproducing Protocells: Competition, Inhibition and Secondary Metabolism 125

4.1 Introduction 126

4.2 Results and discussion 128

4.3 Out-of-equilibrium self-reproduction 134

4.4 Reaction conditions select the winner of competition experiments 137

4.5 Mechanisms of selection and inhibition 141

4.6 Metabolism through orthogonal reactivity 146

4.7 Conclusions 149

4.8 Experimental 151

4.9 References 216

Chapter 5 Asymmetric Autocatalytic Copper-Catalysed Alkyne-Azide Cycloadditions 219

5.1 Introduction 220

5.2 Asymmetric CuAAC 221

5.3 Project aim 228

5.4 System design 230

5.5 Testing conditions for asymmetric CuAAC *via* DKR 231

5.6 Asymmetric synthesis of chiral tris-triazole ligands 233

5.7 Asymmetric synthesis of chiral bis-triazole ligands 236

5.8 Conclusions 242

5.9 Experimental 243

5.10 References 258

Chapter 6 Conclusions and Future Work 261

6.1 Physical autocatalysis driven by a copper catalyst 262

6.2 Asymmetric autocatalytic CuAAC 267

6.3 Concluding remarks 272

6.4 References 274

Chapter 1 General Introduction

1.1 What is life?

This fundamental question, memorably posed by Erwin Schrödinger, has enthralled scientists and philosophers throughout the ages.[1,2] Yet, despite the vast wealth of knowledge that has been amassed in the physical sciences over the past centuries, it remains unanswered.[3] Disciplines such as genomics and metabolomics have given us a thorough, detailed understanding of the complex network of molecules and processes that together constitute a living organism.[4] However, there still exists no falsifiable theory and no experimental observation of how life can emerge from non-living matter.

At the root of this lies the fact that there is no generally accepted definition of "life".[5] How is one to investigate and replicate a phenomenon that evades definition? The various definitions of life that have been proposed differ widely; however, they broadly share certain commonalities. Three overarching criteria appear to be fundamental to life: metabolism, hereditary information and compartmentalisation.[5,6] Metabolism enables a living system to harvest energy and building blocks from the environment to maintain homeostasis, to grow and to reproduce, keeping the system away from thermodynamic equilibrium. Hereditary information ensures that an organism can evolve and adapt to its environment over time. While compartmentalisation generates a protective boundary wherein hereditary information can be stored and metabolic processes can take place. The commonly used definition coined by NASA, which states that life is a "self-sustaining chemical system capable of Darwinian evolution",[7] incorporates these three concepts succinctly.

To gain greater insight into what constitutes a living system, scientists have made attempts at creating a minimal living cell in the lab. There are two fundamental ways to tackle this monumental task: a top-down and a bottom-up approach.[8] The top-down

approach, generally taken by synthetic biologists, involves stripping down an existing cell to its minimal components by reducing and simplifying the genome.[9] In reducing the complexity towards a minimal cell, the essential properties required for cellular life may become clear. The bottom-up approach, taken by chemists in field of systems chemistry,[10–12] starts out with simple synthetic building blocks and uses these to construct artificial cells that exhibit lifelike properties. These investigations further our understanding of living systems but also of abiogenesis, the process of the origin of life where life arose from non-living matter on early Earth. Systems chemistry investigates how supramolecular interactions between molecules can lead to the emergence of new properties through non-biological physical and chemical processes.[13] Some of the systems studied within this discipline exhibit properties that can be broadly divided among the three criteria for life: metabolism, hereditary information and compartmentalisation. There are few examples where two of these properties have successfully been combined within one chemical system and there is no case where all three are incorporated. This accomplishment would herald a great advancement in the field and bring us a step closer to synthesising something truly living in a laboratory.[10]

The literature surveyed in this chapter, and the results described throughout this thesis, focus on bottom-up approaches to creating minimal living systems. This chapter will explain the fundamental concepts relevant to synthesising systems with emergent, life-like properties and highlight important advances in the field of systems chemistry that are relevant to the research reported in the following chapters.

1.2 Autocatalysis

A fundamental trait of all living organisms is their ability to self-reproduce: through creating more of "itself", by generating offspring, the population of a species can survive and propagate.[14] Self-reproduction enables Darwinian evolution[15] as it is during the copying of hereditary information for offspring that errors occur which lead to variations in phenotype, these changes can be selected for by fitness through natural selection. The methods currently used by organisms for self-reproduction involve highly evolved biological machinery. However, in a bottom-up approach to creating life this machinery is not available, so this trait must be incorporated in a different manner. This is accomplished through methods of molecular self-reproduction, where one molecule can generate more of itself. This process is known as autocatalysis: a reaction where the product acts as a catalyst for its own formation.[16,17]

An autocatalytic reaction has two unique traits that differentiate it from a typical chemical reaction (Figure 1.1). Firstly, the reaction profile is exponential at early reaction times since the rate is proportional to the product concentration. Consequently, a sigmoidal curve is often observed for the reaction profile of autocatalytic reactions. At the start of the reaction, during the lag period, the rate is low which is followed by an exponential increase in product concentration as more catalyst is continuously generated until the reaction slows down due to a depletion of starting materials or product inhibition. Secondly, the addition of product at start of the reaction has a positive correlation with the initial rate of the reaction resulting in elimination or shortening of the lag period and a faster initial rate of reaction. Sigmoidal kinetics are not sufficient evidence to conclude autocatalysis: slow activation of a catalyst complex could give a lag period or inefficient autocatalysis could give a normal rate profile.[18]

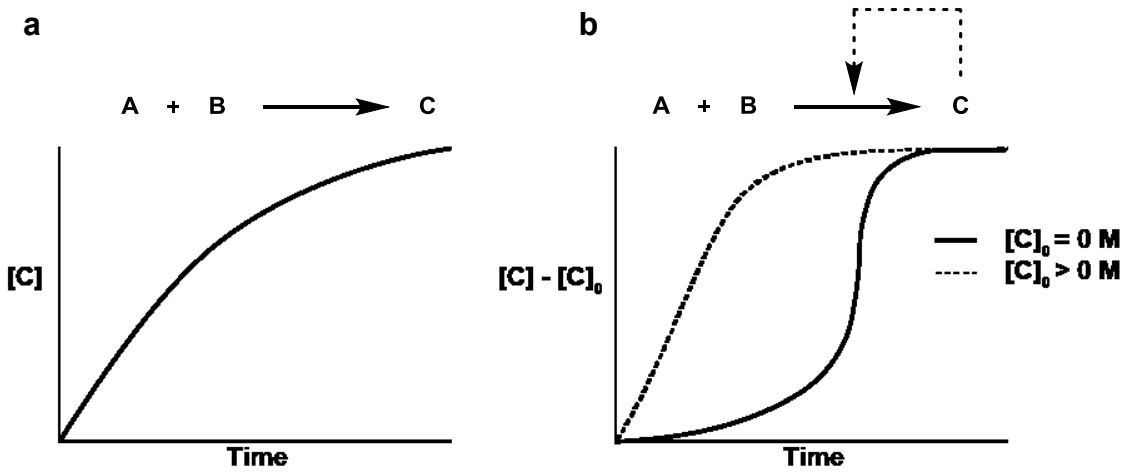


Figure 1.1 a. Reaction profile of a standard bimolecular reaction. **b.** Reaction profile of an autocatalytic reaction, where product **C** is a catalyst for its own formation. Formation of **C** is exponential: a slower lag period is followed by an acceleration in the rate of the reaction affording a sigmoidal rate profile. Seeding with product **C** at the start of the reaction eliminates the lag period and increases the initial reaction rate.

Systems that show autocatalytic behaviour can be broadly divided into three categories based on the mechanism that is operating: network, template or physical autocatalysis (Figure 1.2). During network autocatalysis, the final product is consumed as starting material in a series of reactions to eventually generate more equivalents of product than initially consumed (Figure 1.2a). One of the oldest and best-known examples of this concept is the formose reaction where glycolaldehyde undergoes two consecutive aldol reactions with formaldehyde followed by a retro-aldol reaction to yield two equivalents of glycolaldehyde.[19] Glycolaldehyde can keep reacting with formaldehyde to eventually form a complex mixture of pentoses and hexoses and has therefore been considered as potential prebiotic source of sugars.[20] A more recent example utilised a reaction network with cysteamine, where a positive feedback loop through thiol-thioester exchange followed by native chemical ligation and thiol-disulfide exchange led to a multiplication factor of two for cysteamine within one reaction cycle (Figure 1.3).[21] A great achievement as mimicking a metabolic cycle with prebiotically relevant small molecules was considered implausible.[22] The authors were able to generate oscillations within the total thiol concentration by linking this auto-amplification network to both a trigger and an

inhibition reaction, showcasing the complexity of kinetic behaviour that can be achieved by utilising autocatalysis. Such feedback mechanisms are prevalent in nature where they enable homeostasis and provide fine-tuned control over the concentration of compounds within metabolic networks.

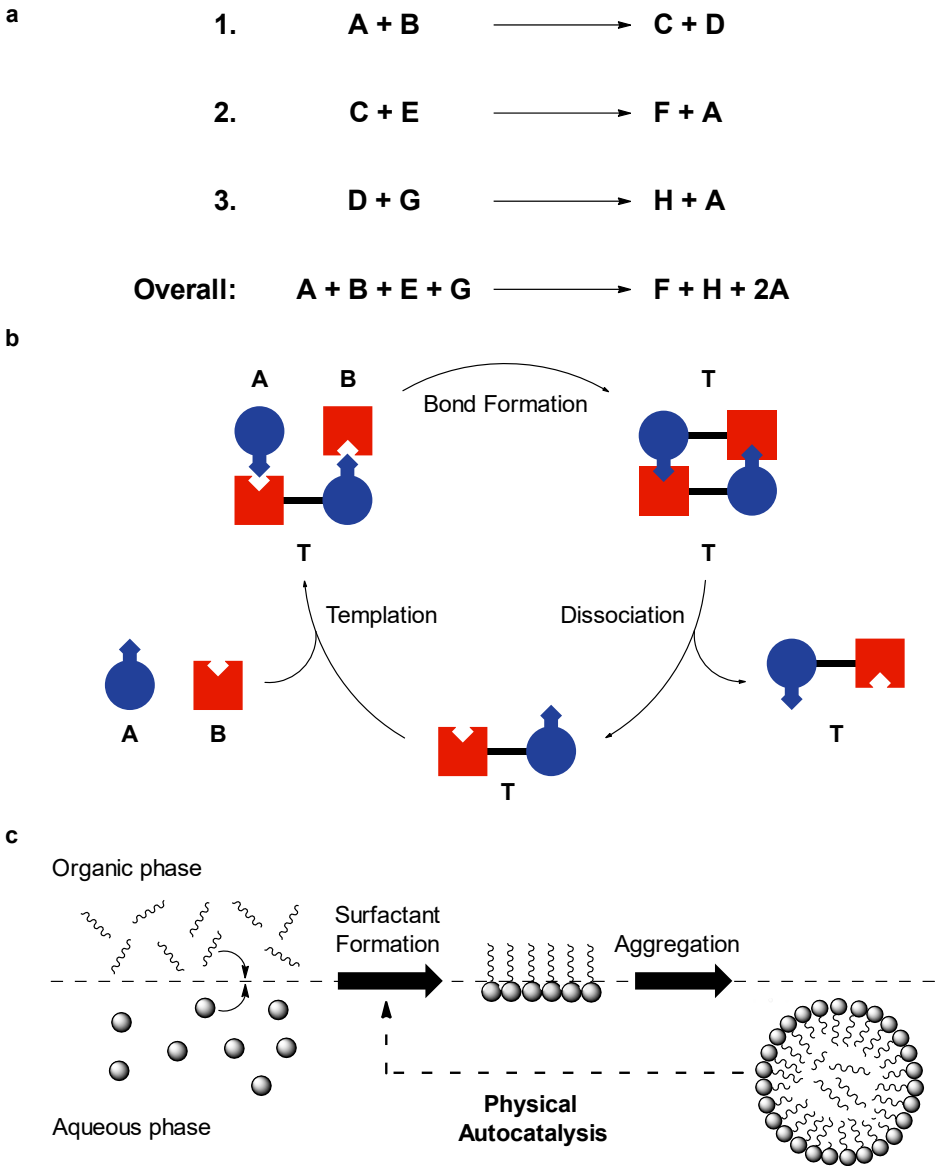


Figure 1.2 Schematic representation of three different categories of autocatalysis. a. Network autocatalysis: Final product reacts as starting material in a series of reactions to eventually generate more equivalents of product than initially consumed. **b.** Template replication: Starting materials bind to recognition sites on template molecule to form an additional template product. **c.** Physical autocatalysis: Multiple product molecules form catalytically active supramolecular aggregates that accelerate additional product formation.

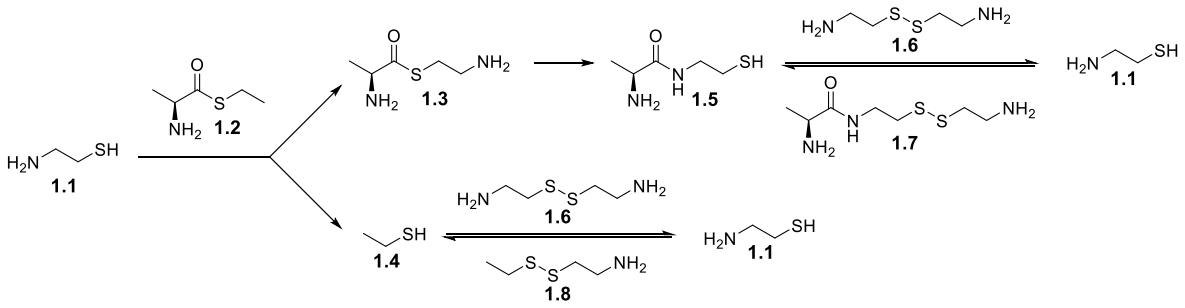


Figure 1.3 Experimental example of network autocatalysis where cysteamine is generated with a multiplication factor of two within one reaction cycle.[21] Cysteamine **1.1** performs thiol-thioester exchange with thioester **1.2** to form **1.3** and ethanethiol **1.4**. Amide **1.5** is obtained through native chemical ligation and subsequent thiol-disulfide exchange with disulfide **1.6** generates the first equivalent of cysteamine **1.1** plus **1.7**. Meanwhile, **1.4** undergoes thiol-disulfide with **1.6** to generate a second equivalent of cystamine **1.1** and **1.8**.

The second category of autocatalysis is template replication. Here starting materials reversibly bind to functional groups on the product molecule which act as recognition sites (Figure 1.2b).[14,17,23] Templation increases the effective concentration between precursors, thereby accelerating bond formation to yield an additional template product. After the complex dissociates, the newly formed and the original template both start to catalyse their own formation closing the autocatalytic cycle. A common issue with template replication is inefficient autocatalysis due to product inhibition caused by a low disassociation constant of product dimer preventing further turnover in the catalytic cycle. Low disassociation constants were a long-standing hurdle that had to be overcome to achieve exponential replication.[24]

Template replication is an obvious candidate for the replication of hereditary information in artificial systems, as biological informational polymers already utilise templating for their reproduction in combination with enzymes. The first experimental example of non-enzymatic template replication was a nucleotide based system developed by von Kiedrowski.[25] Condensation between two trinucleotide subunits was accelerated through templating with the complementary hexamer product. Nucleotide based self-replication was developed further into an elaborate system where a biologically-derived ribozyme autocatalytically self-assembles from four separate fragments (Figure 1.4).[26] Ribozymes

are unusual RNA molecules that catalyse biochemical reactions in addition to carrying genetic information and are considered potential candidates for the first replicators in the RNA world hypothesis.[27,28]

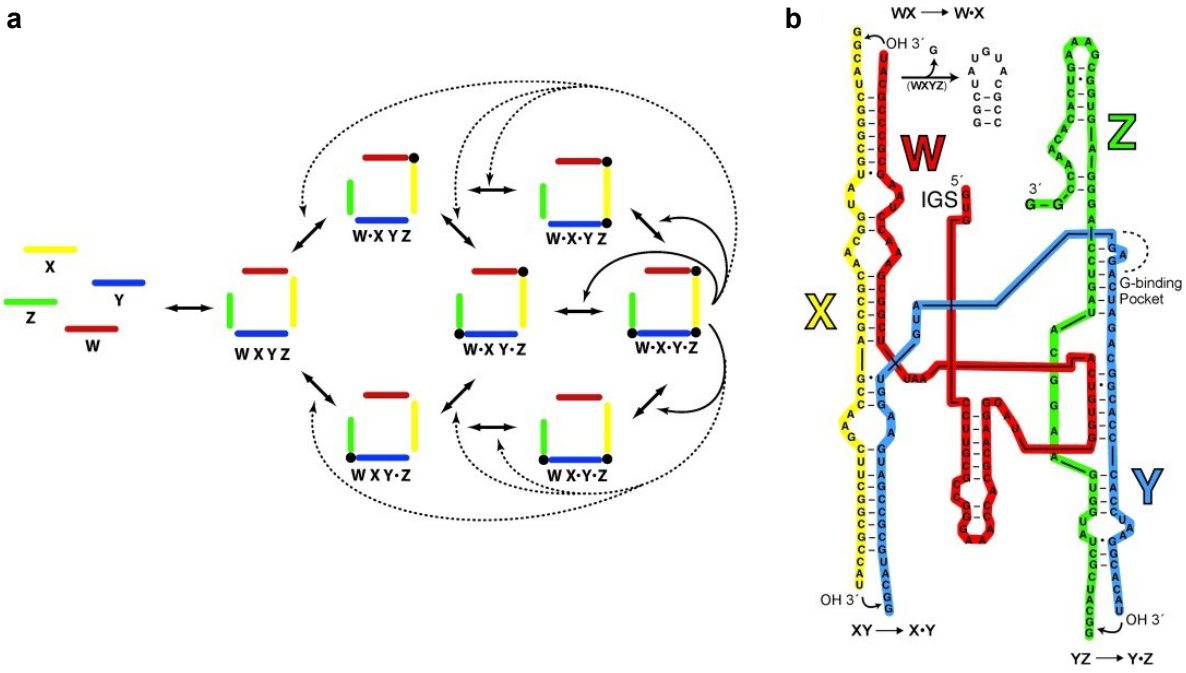


Figure 1.4 Experimental realisation of template replication. **a.** Autocatalytic formation of a fully covalent ribozyme **W·X·Y·Z** from four fragments through a series of intermediates. The ribozyme accelerates its own formation and the production of any intermediates. **b.** Proposed secondary structure of non-covalent **W X Y Z** intermediate with the sites of phosphodiester bond formation. Adapted with permission from reference.[26]

The third category, physical autocatalysis, relies on multiple product molecules forming catalytically active supramolecular aggregates such as micelles or vesicles (Figure 1.2c).[16] Physical autocatalysis is generally driven through *in situ* amphiphile formation from phase-separated reagents in biphasic systems, although other types of mechanisms are possible such as fibre formation.[29] Once a critical concentration of surfactant is reached, aggregates form that facilitate phase-transfer of precursors into the opposing phase and therefore catalyse their own formation. It is worthy of note that the term aggregation and aggregate is used interchangeably with self-assembly and assembly in this thesis. This is contrary to common usage in the biophysics community were

aggregation refers to an irreversible, uncontrolled assembly process commonly associated with loss of function, whereas self-assembly is considered a reversible, dynamic process.

Since the product aggregates formed during physical autocatalysis have an undefined size and shape, product formed during the reaction is not necessarily an exact replica of the catalyst. Due to this distinction, physical autocatalysis is sometimes referred to as self-*reproduction* contrary to processes in the former two categories which undergo self-*replication*. This type of autocatalyst is not "selfish" due to their supramolecular nature: they can catalyse other orthogonal reactions. Physical autocatalysis is one of the main areas of research within the Fletcher group and is most relevant to the work reported throughout this thesis.

First examples of physical autocatalysis were reported by Luisi and colleagues. He described his early work on self-reproduction of vesicles and micelles as autopoiesis: "an autopoietic unit is a system that is capable of self-sustaining owing to an inner network of reactions that re-generate all the system's components".[30] However, this terminology is controversial and not generally accepted in the community[31] and we have therefore adopted the term physical autocatalysis to describe these systems.

The early systems developed by Luisi involved aggregation of octanoate surfactants into normal[32,33] and reverse[34,35] micelles depending on the reaction conditions. Micelles of octanoate were generated either through aqueous hydrolysis of hydrophobic precursors or by oxidation of octanol. Since this pioneering work by Luisi, few other reactions have been developed that exhibited physical autocatalytic behaviour.[16] Virtually all systems are driven by hydrolysis to smaller fragments with the exception of *N*-oxidation of an amine[36] and reversible imine condensation.[37,38]

Initial investigations by Dr Andrew Bissette in the Fletcher group made clear that the field of physical autocatalysis was lacking reactions that increased molecular complexity. He argued that synthetic reactions, where a more complex product is obtained from simple starting materials, are more relevant to prebiotic synthesis than bond-cleaving or oxidation reactions.[39] The lipid world[40] hypothesis postulates that heterogeneous assemblies of simple, reproducing amphiphiles could form rudimentary systems with life-like properties and experience basic form of Darwinian natural selection in the absence of genetic and metabolic systems.[41,42] This would require a diverse population of unique self-reproducing lipids which can only obtained from a small range of precursors through combinatorial bond-forming processes, whereas the variety of lipids that can be generated from bond-cleaving processes is inherently limited.

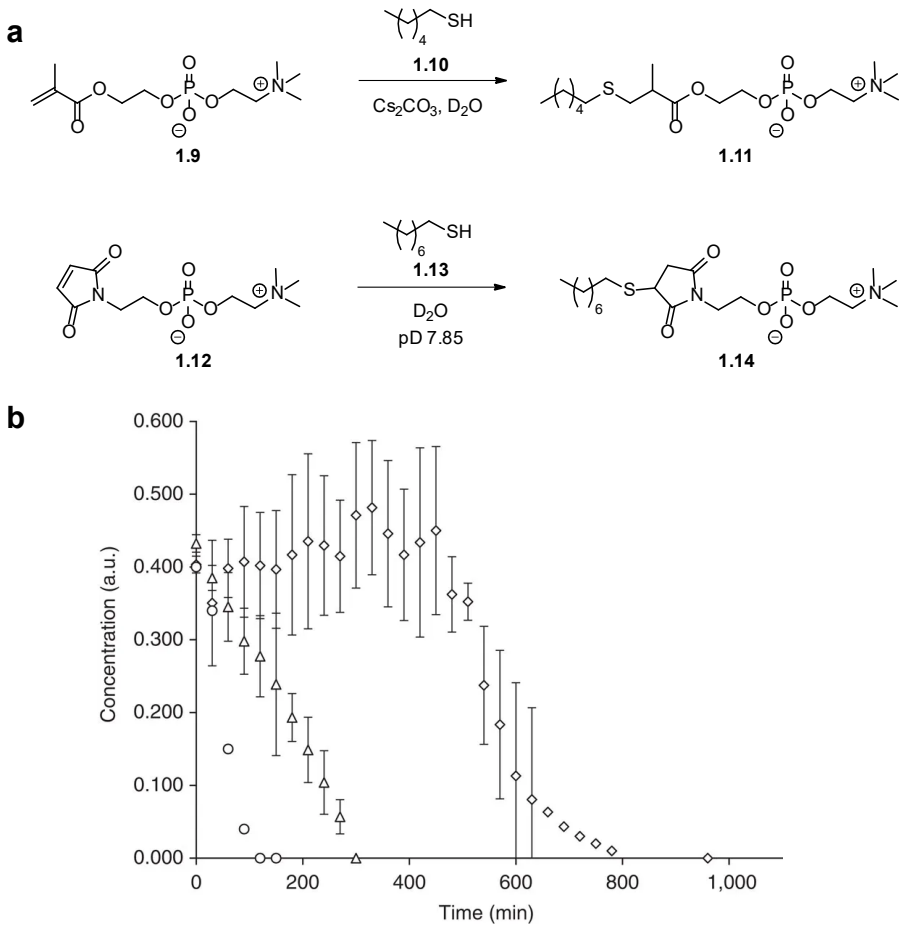


Figure 1.5 Systems based on physical autocatalysis developed in the Fletcher group driven by a thiol-ene coupling reaction. **a.** In the first-generation systems, phase-separated hydrophobic thiol **1.10** reacts with a hydrophilic phosphocholine-based Michael acceptor **1.9** to form phospholipids **1.11** that aggregate into

micelles and accelerates further surfactant formation. The second-generation system incorporates a maleimide in phosphocholine **1.12** which reacts with thiol **1.13** under milder conditions to form surfactant **1.14 b.** Kinetic profile of consumption of starting material **1.12** in the second-generation system. Unseeded reaction (diamonds) experiences a lag period followed by a rate acceleration. Upon seeding with product **1.14** (20 mM, triangles) the lag period was eliminated and when increasing the amount of seed (70 mM, circles) the reaction was accelerated further. Adapted with permission from reference.[39]

Work in the Fletcher group has therefore focused on the development of systems where physical autocatalysis is driven by bond-forming reactions. Initially, two systems based on a 1,4-conjugate addition of thiols to α,β-unsaturated carbonyls were developed (Figure 1.5).[39] Phase-separated hydrophobic thiol reacts with a hydrophilic phosphocholine-based Michael acceptor to form phospholipids that aggregate into micelles. The first system only functioned under harsh conditions at high pH and was limited due to hydrolysis of the starting material. A second-generation system incorporated a more reactive maleimide functional group which undergoes the thiol-ene reaction at milder conditions. The kinetic profile displayed a characteristic sigmoidal curve and the lag period was eliminated through seeding with product at the start of the reaction. Mechanistic studies of this system using DOSY NMR showed that hydrophobic thiol was solubilised by the micelles into the aqueous phase and stayed strongly associated with the aggregates throughout the reaction.

The autocatalytic mechanism of this thiol-ene reaction was investigated further by performing interferometric scattering microscopy (iSCAT) measurements on an analogous system.[43] This technique enabled the real-time visualisation of *in situ* single aggregate formation at the nanometre scale, illuminating the diversity and complexity in the dynamics of physical autocatalysts at this submicroscopic level.

1.3 Protocells: growth, division and self-reproduction

In the search for the minimal criteria for life and in attempts at modelling behaviour of biological systems, bottom-up synthetic approaches focus mainly on the generation of

vesicles.[44,45] As opposed to the micellar aggregates described in previous examples, vesicles are considered better models of artificial cells and prebiotically relevant protocells.[46] They exhibit physical properties in which micelles are lacking when attempting to create lifelike systems. Firstly, the bilayer structure of vesicles is more defined, static and robust than that of micelles which are dynamic and continuously exchange components with their environment.[44,47] This enables study an individual vesicle over time which techniques such as confocal microscopy. In addition to hydrophobic substrates, vesicles can encapsulate polar compounds into their aqueous interior, creating an environment different from the exterior.[48] Living cells utilise concentrations gradients between the interior and exterior to drive many processes such as the storage of chemical energy by ATP synthase.[49] Finally, the structure and composition of vesicles is more similar to biological cells relative to micelles.

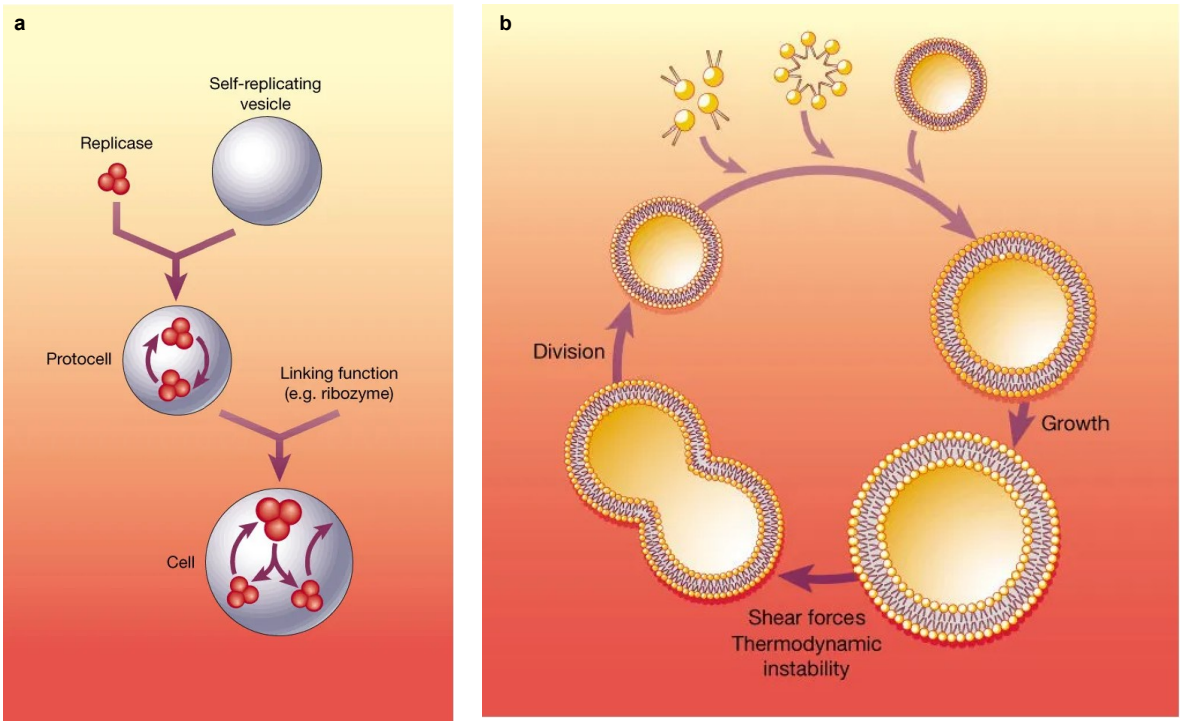


Figure 1.6 a. Schematic presentation of core-and-shell reproduction, where replication of the compartment and of encapsulated hereditary information are linked together. **b.** Multiplication of protocells through growth and division. Formation of lipids or addition of sacrificial micelles and vesicles can facilitate membrane growth. Thermodynamic instability or shearing forces can induce division processes where a protocell divides into two daughter cells. Adapted with permission from reference.[50]

A protocell model has been proposed that merges two fundamentally different reproducing systems, namely the informational genome and the compartment which encapsulates it.[50] The process of coupling vesicle self-reproduction to the replication of informational molecules within its compartment is known as core-and-shell reproduction (Figure 1.6a). Szostak and Luisi held the view that such a system might be subject to variation and selection, and thus be capable of a rudimentary form of Darwinian evolution. For example, a core-and-shell replicator that contains a mutated ribozyme which synthesises phospholipids at a faster rate could impart a higher survival rate over competitor replicators with a less efficient ribozyme. Systems exhibiting core-and-shell reproduction come close to what is considered living and their creation has therefore been a long-standing research goal.

Methods of membrane formation and division and their underlying mechanisms have been studied to create sophisticated self-reproducing lipid compartments (Figure 1.6b). Vesicles do not necessarily become thermodynamically unstable upon reaching a particular size: external forces are usually required to induce division. This is contrary to micelles which are inherently restricted in size due to their hydrophobic interior. Membranes can grow gradually through slow incorporation of individual molecules or micelles into pre-existing vesicles. The growth and division of protocell membranes through addition of oleate micelles has been experimentally verified.[51] Furthermore, pre-existing fatty acid or phospholipid vesicle mixtures appear to accelerate micelle-to-vesicle transformations in an autocatalytic manner.[52,53] Encapsulated clay montmorillonite, known to catalyse RNA polymerisation, also catalysed micelle-to-vesicle conversions.[54]

Vesicle growth can occur in stepwise fashion through the fusion of two vesicles. Protocells with encapsulated RNA grow in size at the expense of isotonic vesicles due to

osmotic forces.[55] This implies that RNA replicating within protocells could impart a growth advantage by generating osmotic pressure. This effect was exploited to enable homeostasis within these primitive cells by modulating ribozyme activity.[56] At high concentration activity is inhibited due to reversible binding with short oligonucleotides, however as the vesicles grow internal dilution induces ribozyme activation. This led to homeostatic behaviour where ribozyme activity is constant per unit volume during protocell growth. In a different system, a dipeptide generated by an encapsulated catalyst imparted an enhanced affinity for fatty acids after it bound to vesicle membranes thus promoting vesicle growth at the cost of catalyst-free vesicles.[57] These examples are the beginnings of a core-and-shell reproduction systems where internal processes are linked to growth of compartments, however in these cases no replication or reproduction occurs and they can therefore not be classified as core-and-shell reproduction.

The *in situ* synthesis of membrane forming compounds has been achieved through both enzyme catalysis[58] and physical autocatalysis[59,60]. Physical self-reproduction of vesicles was combined with enzymatic RNA synthesis through encapsulation of polynucleotide phosphorylase, however these two processes operated independently.[61] A self-reproducing vesicle system based on a copper-catalysed azide-alkyne cycloaddition (CuAAC) was developed by Devaraj and colleagues which displayed sigmoidal kinetics due to an autoinductive cycle (Figure 1.7).[62]

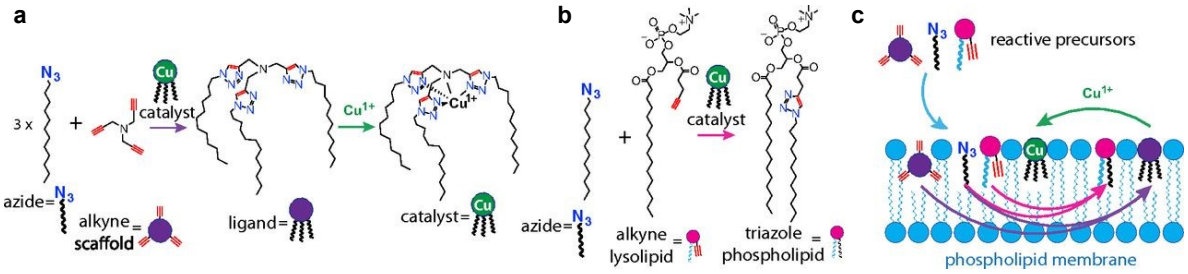


Figure 1.7 Self-reproduction of copper ligand linked to generation of additional phospholipid. **a.** CuAAC reaction drives additional ligand production. **b.** Copper-ligand complex facilitates triazole phospholipid production from an alkyne lysolipid precursor. **c.** Vesicle membrane growth and division is driven linking a self-reproducing catalyst complex to phospholipid production. Adapted with permission from reference.[62]

This reaction is considered autoinductive as the product is a ligand that increases catalytic efficiency contrary to autocatalysis where the product itself is the catalyst.[18] The maximum rate acceleration by product during autoinduction is therefore inherently limited to catalyst loading. The triazole product generated in the reported system accelerated the CuAAC reaction once bound to excess free copper. Simultaneously, the conversion of alkyne lysolipid into membrane forming triazole phospholipid was catalysed driving overall membrane growth, coupling compartment growth to an internal self-reproducing reaction.

Sugawara and colleagues developed several systems of self-reproducing giant vesicles by generating amphiphiles through either formation or hydrolysis of imine bonds.[38,63,64] The physical location of the reaction in these systems could be precisely controlled with organic acid-catalysts due to the pH-sensitive nature of the imine bond. The mechanism of self-reproduction was robust enough to facilitate DNA synthesis within the vesicle interior through polymerase chain reaction (PCR). This enabled formation of an advanced protocell system that comes close to true core-and-shell reproduction (Figure 1.8).[65]

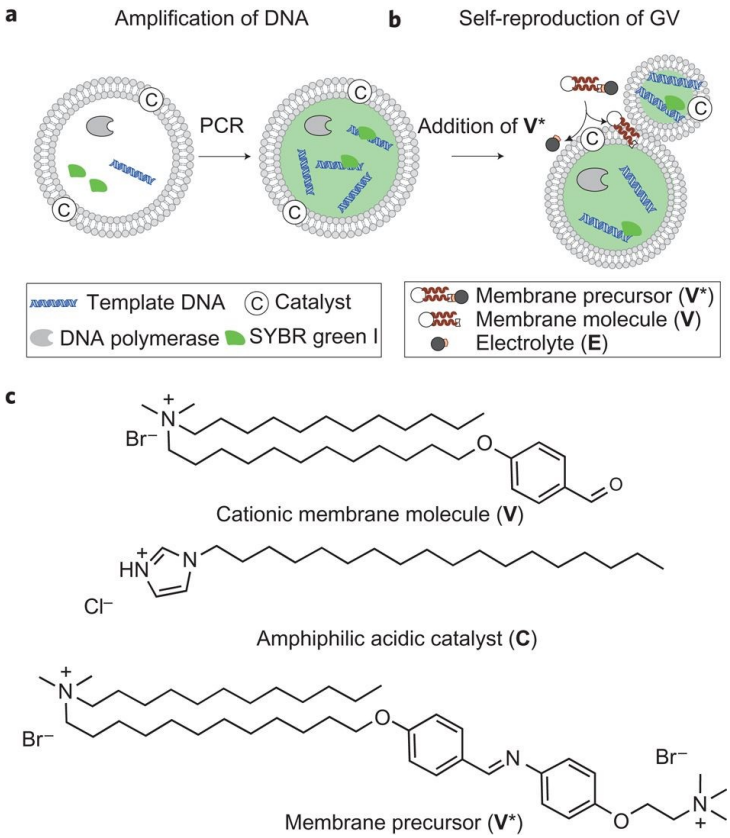


Figure 1.8 Example of core-and-shell reproduction: Self-reproduction of protocells is linked to the amplification of DNA with aqueous interior. **a.** DNA is amplified by thermal cycling of PCR reagents within the vesicle. **b.** Self-reproduction of the giant vesicles occurs through hydrolysis of precursor **V*** by catalyst **C** to form amphiphile **V** by in the bilayer. **c.** Molecular structures of cationic membrane molecule (**V**), amphiphilic acidic catalyst (**C**) and membrane precursor (**V***). Adapted with permission from reference.[65]

DNA amplification within the giant vesicles was achieved by thermal cycling of PCR reagents. Meanwhile, an amphiphilic acidic catalyst (**C**) embedded in the vesicle bilayer catalyses the hydrolysis of a membrane precursor ($\mathbf{V}^*$) to a cationic membrane molecule (**V**). Crucially, binding of amplified DNA to membrane destabilised the vesicles, accelerating division processes whereby DNA partitions into daughter vesicles. Furthermore, DNA accelerated hydrolysis of $\mathbf{V}^*$ to **V** led to faster overall membrane growth and division, firmly establishing a link between membrane reproduction and genetic replication. This impressive feat is a vital step towards core-and-shell reproduction and the creation of a living system. However, since several components such as the acid catalyst, and PCR substrates and catalyst do not replicate, this system would eventually stop functioning after a certain amount of replication cycles due to "death by

dilution"[66]. An unlimited replication should be feasible for true core-and-shell reproduction to allow for open ended evolution.

1.4 Out-of-equilibrium aggregation and self-reproduction

An awareness has grown within the scientific community that aggregation and self-reproduction processes operating under thermodynamic control do not accurately mimic natural self-assembly processes occurring in nature.[67,68] Biological structures are thermodynamically unstable and are maintained in out-of-equilibrium steady states through continuous consumption of energy and matter from the environment. This allows for precise spatial and temporal control over formation of transient biomolecular assemblies such as microtubules. Man-made dissipative supramolecular materials have similarly shown unique properties such as autonomous self-healing[69], exquisite spatiotemporal control[70] and adaptation to changes in the environment[71]. Contrary to standard synthetic systems, these properties are controlled by a combination of reaction rates and fuel levels, and not by thermodynamic equilibrium compositions. To achieve open-ended evolution in a chemical system a continuous increase in order, complexity and function needs to be possible. This can only be achieved if the system operates away from thermodynamic equilibrium, where a chemical fuel pays entropic costs.[72,73]

In order to move a chemical system to an out-of-equilibrium regime, a chemical species must be generated transiently. This is achieved by linking a reaction that generates the compound while consuming a fuel to a second reaction that continuously decomposes that same compound. Since the transiently formed molecule is no longer the thermodynamic product it is destroyed when thermodynamic equilibrium is reached. Hence, the species must be continuously regenerated to maintain a stable population, resulting in a system that is held out-of-equilibrium.

One of the first implementations of this concept was achieved by Luisi where he used out-of-equilibrium self-reproduction to model homeostasis.[74] Hydrolysis of oleic anhydride in the presence of $OsO_4/K_3[Fe(CN)_6]$, led to transient formation of vesicles that subsequently degrade after oxidation of the oleate double bond. Careful balancing of addition rates of both oleic anhydride and oxidant resulted in either degradation, growth or an out-of-equilibrium steady state of the vesicle population. Unique to this system is that phase-separation prevents degradation of hydrophobic starting materials by the oxidant.

A more refined system of out-of-equilibrium self-assembling vesicles was developed by Prins and colleagues (Figure 1.9).[75] Aggregation into vesicles by surfactant building blocks was induced through coordination to adenosine triphosphate (ATP) which acts as the chemical fuel. Enzymatic hydrolysis of ATP by potato apyrase induced degradation of the supramolecular structure back to micellar aggregates and thus enabled transient formation of vesicles. While ATP was present to maintain the out-of-equilibrium aggregated state, the vesicle could function as a nanoreactor and sustain an orthogonal chemical reaction.

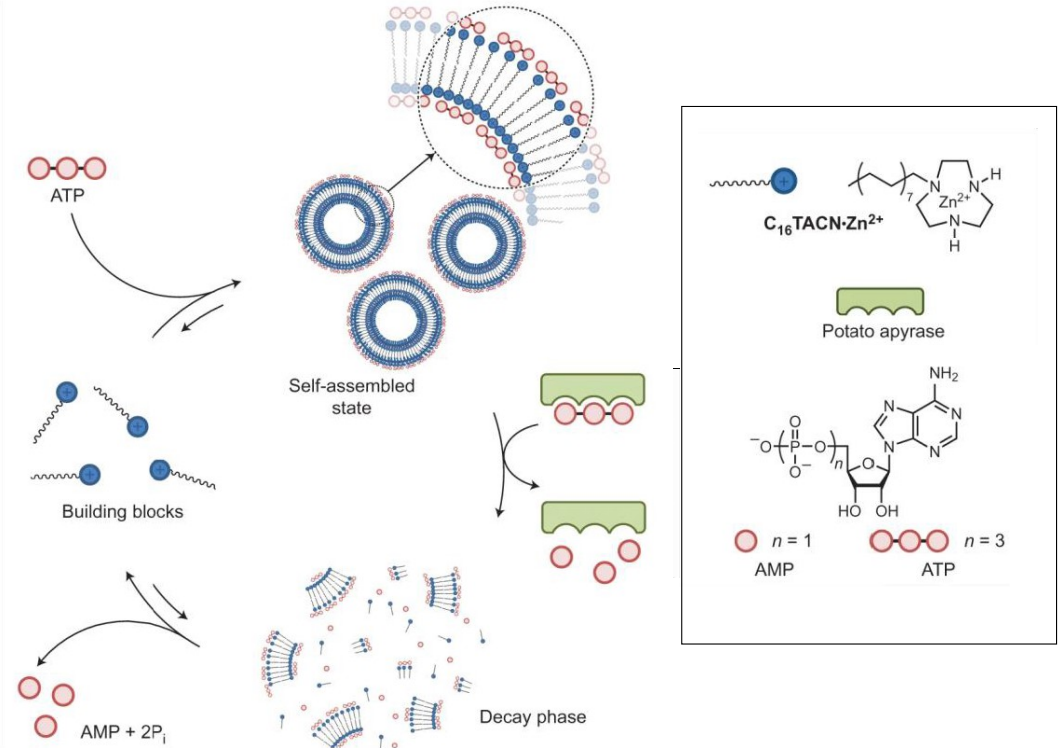


Figure 1.9 A system of dissipative self-assembling vesicles. ATP induces aggregation of surfactant building blocks into supramolecular vesicular structures through non-covalent interactions. Potato apyrase hydrolyses ATP to AMP which causes degradation of vesicle structures. As long as sufficient ATP is present the out-of-equilibrium self-assembled state can be maintained. Adapted with permission from reference.[75]

In nature dissipative assemblies tend to be catalytically active and degrade the fuel responsible for inducing assembly themselves such as hydrolysis of GTP by microtubules.[76,77] To mimic this process more accurately, a second generation system was developed by the same group where substrate-induced self-assembling vesicles acted as cooperative catalysts for degradation of the same substrate.[78]

Boekhoven and co-workers designed a system where vesicles were formed by dissipative self-assembly driven by hydrolysis of a fuel.[79] Reaction with carbodiimide resulted in anhydride formation in the surfactant which induced vesicle assembly. However, passive hydrolysis of the anhydride by the aqueous environment led to subsequent disassembly, enabling transient vesicle formation and continuous membrane remodelling.

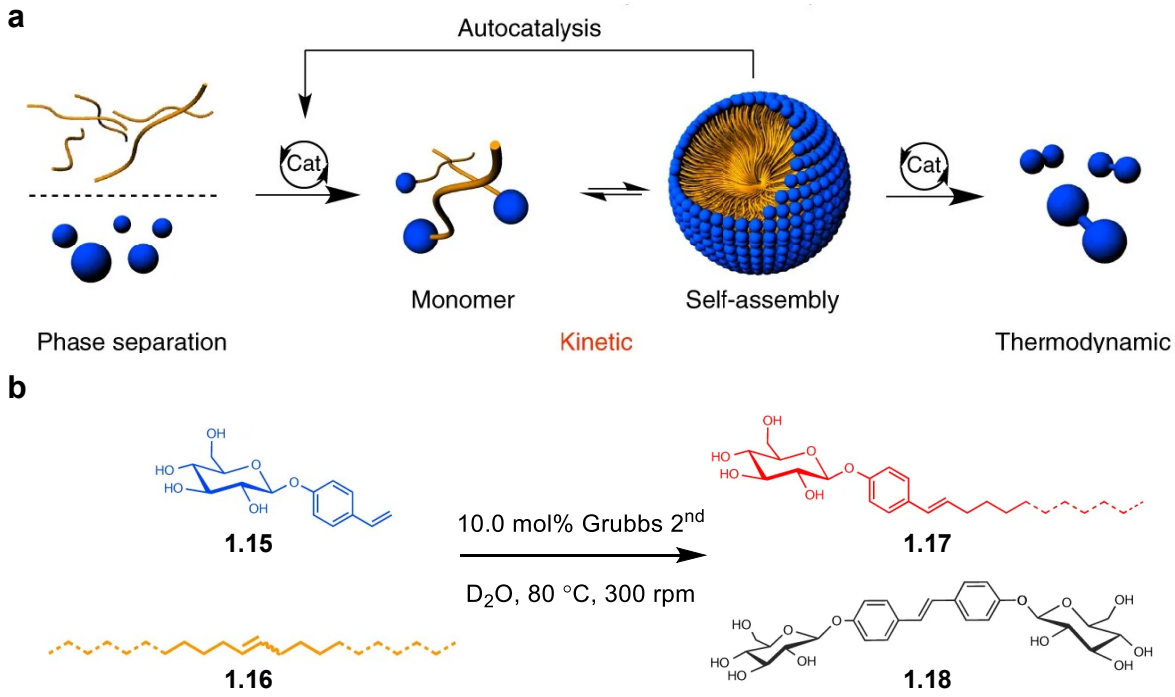


Figure 1.10 A transient physical autocatalyst based on alkene metathesis. **a.** Cross metathesis between phase-separated reagents generates surfactant monomers as the kinetic product. After aggregation into micelles, autocatalysis through phase-transfer occurs. Monomers are degraded into a thermodynamic wasteproduct. **b.** Cross metathesis between glucosylated styrene **1.15** and aliphatic alkene **1.16** catalysed by Grubbs 2nd-generation generates surfactant **1.17** and stilbene **1.18**. Adapted with permission from reference.[80]

The first transient physical autocatalyst developed in the Fletcher group was based on alkene metathesis (Figure 1.10).[80] Glucosylated styrene **1.15** was dissolved in the aqueous phase, whereas aliphatic internal alkene **1.16** constituted the hydrophobic organic phase. Grubb's 2nd-generation catalyst facilitated cross metathesis reaction between the two substrates to form surfactant product **1.17**. However, under biphasic conditions the surfactant is thermodynamically unstable and undergoes second metathesis reaction with **1.15** to form the more stable stilbene double bond as thermodynamic product **1.18**. The transient nature of this autocatalyst was further exploited by performing the reaction in a continuously stirred tank reactor (CSTR) which maintained an out-of-equilibrium steady-state through continuous supply of starting materials.[81] This enabled selection processes from a pool of self-assembling replicators, where phase separation and autocatalytic kinetics were vital for selection to occur.

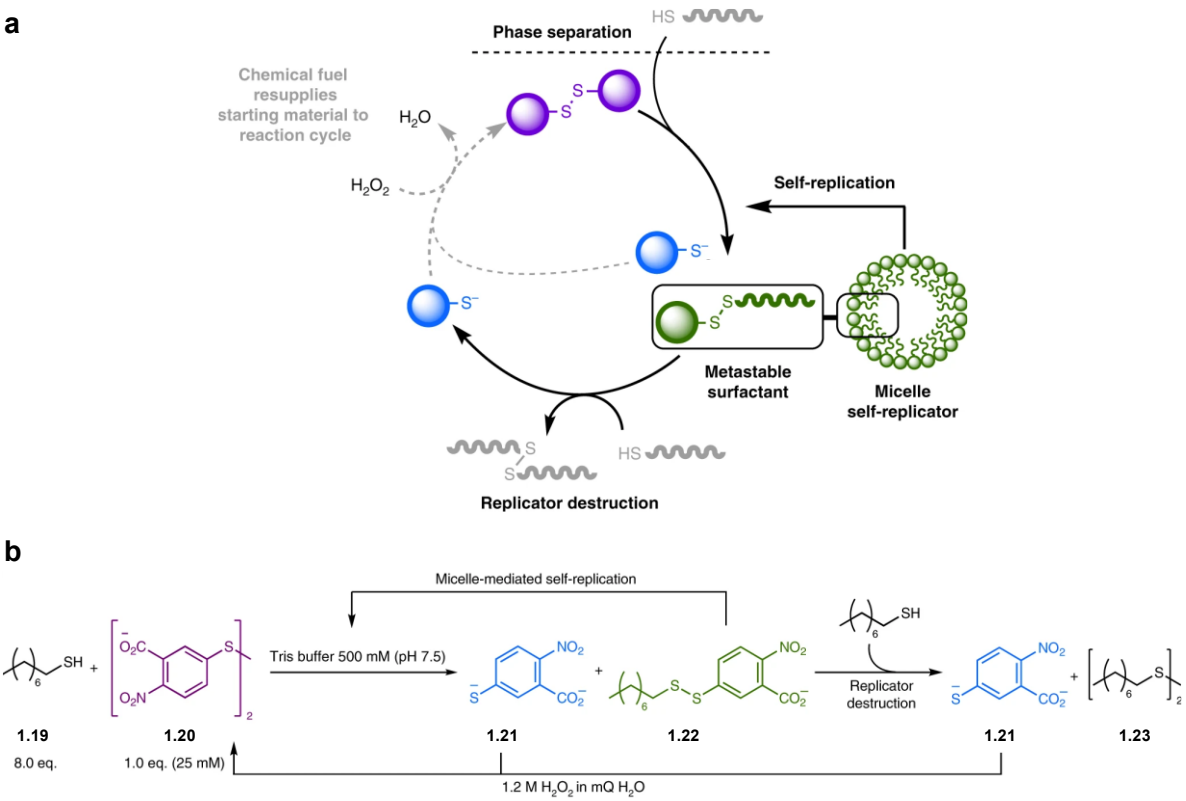


Figure 1.11 Out-of-equilibrium self-reproduction through continuous regeneration of starting material. **a.** Hydrophobic thiol in the organic phase attacks a hydrophilic aromatic disulfide to form a metastable surfactant that aggregates into micelles and accelerates its own formation. Attack by a second equivalent of thiol destroys the replicator to form an aliphatic disulfide. Aromatic thiolate can be oxidised to regenerate aromatic disulfide starting material, closing the reaction cycle. **b.** Aliphatic thiol **1.19** reacts with aromatic disulfde **1.20** to form thiolate **1.21** and surfactant **1.22**. A second attack by **1.19** degrades product **1.22** to yield aliphatic disulfide **1.23** and a second equivalent of **1.23**. Adapted with permission from reference.[82]

A second transient replicator system reported by the Fletcher group was based on thiol-disulfide exchange and featured a fully closed reaction cycle (Figure 1.11).[82] Surfactant **1.22** formed after addition of hydrophobic octanethiol **1.19** to hydrophilic Ellman's reagent **1.20**, an aromatic disulfide, while generating aromatic thiolate **1.21** as a side product. A second attack by excess aliphatic thiol destroys **1.22** to yield a thermodynamically more stable aliphatic disulfide **1.23** plus a second equivalent of **1.21**. Unique to this system was the ability to regenerate disulfide **1.20** through selective oxidation of wasteproduct **1.21** by hydrogen peroxide closing the reaction cycle. Out-of-equilibrium steady-states could be maintained as long as oxidant was present as a chemical fuel, contrary to the previous system where continous addition of starting material was required.

1.5 The origin of biological homochirality

Biological homochirality is a universal hallmark of life that has not yet been addressed in this chapter. Many of life's building blocks exist almost exclusively as single enantiomers such as L-amino acids and D-sugars. This property is considered vital for effective molecular recognition and replication processes and thus must have played an important part in the origin of life.[83] However, it is not clear whether homochirality is a prerequisite for abiogenesis or whether living systems can exist in a racemic, scalemic or achiral states and subquently inherently drive themselves towards a homochiral state.[84–88]

The mechanism through which homochirality arose from a racemic prebiotic world remains an even bigger mystery. It must have involved a chiral symmetry breaking event, where a chiral imbalance between two enantiomers is created.[83,89] This small enantiomeric excess (ee) is subsequently amplified asymmetrically by some chemical or physical process to a homochiral state. Various sources for initial symmetric breaking have been proposed from the parity violating weak force[90] to circularly polarised light[91] to simple stochastic fluctuations[92]. Proposed mechanisms through which this imbalance might be amplified to obtain an ever increasing enantiomeric excess are based on phase behaviour models[93–96] and more relevant to this thesis, absolute asymmetric autocatalysis.[89]

Absolute asymmetric autocatalysis is based on a theoretical model proposed by Frank, where a chiral molecule acts as a catalyst for its own formation and simultaneously inhibits catalytic activity of the opposite enantiomer (Figure 1.12).[97] *Mutual antagonism* between enantiomer L and D causes deactivation of both molecules when they interact, reducing their capacity to self-replicate. This inhibition is essential for amplification of

ee and allows a small imbalance in L:D ratio to grow with each subsequent replication cycle.

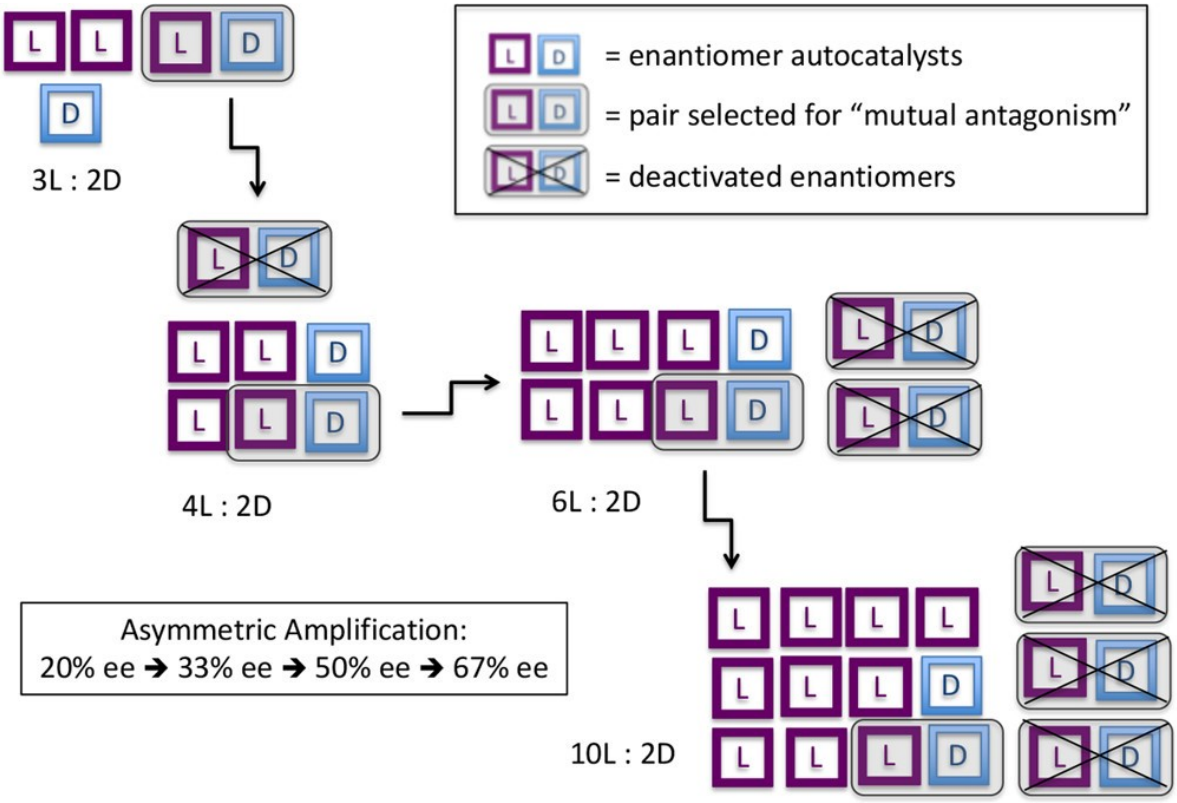


Figure 1.12 Frank's model for asymmetric amplification of chirality. Enantiomers are autocatalytic and self-replicate but through mutual antagonism a pair of enantiomers becomes inactive. Each replication cycle, the ee is amplified asymmetrically. Adapted with permission from reference.[98] Copyright 2020 American Chemical Society.

A ground-breaking report by Soai and coworkers is only instance where Frank's model has been experimentally validated.[99] The Soai reaction consists of autocatalytic alkylation of pyrimidyl aldehyde **1.24** by diisopropyl zinc **1.26**, where catalytic amounts of alcohol product **1.25** accelerate the reaction (Figure 1.13). Furthermore, if seeding occurs with low enantiomeric excess the final product composition yields a high enantiomeric excess. External chiral initiators such as low ee amino acids produced from circularly polarized light[100], inorganic chiral quartz crystals[101] and even compounds with carbon ($^{12}C/^{13}C$) isotope chirality[102] have shown to control the handedness of the product and resulted in amplifications to high ee. Only very minimal imbalances are required to bias the chirality of this reaction.

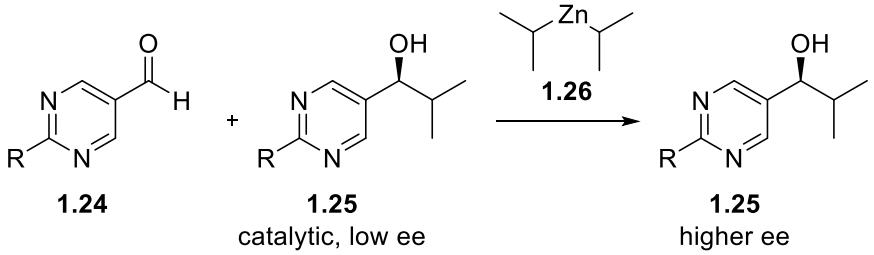


Figure 1.13 Reaction scheme of the Soai reaction.[99] Pyrimidyl aldehyde **1.24** is alkylated by diisopropyl zinc **1.26**. Catalytic amounts of enantiomerically enriched alcohol product **1.25** accelerate and amplify the ee of the reaction.

The mechanism by which mutual antagonism manifests in the Soai reaction and the type of catalyst aggregate that is responsible for the nonlinear effects have been the focus of many mechanistic investigations. A dimeric catalyst model was initially proposed[103–106] but after the discovery of an inverse dependence of the reaction rate on temperature and elucidation of X-ray crystal structures of the enantiopure and racemic alkoxides, a tetrameric alkoxide aggregate is now considered more likely.[107–110] Recently a combined structural, mechanistic and computational study yielded a plausible model of how this tetramer complex unifies the phenomena of autocatalysis, enantioselective catalysis and nonlinear effects required for amplification of chirality in the Soai reaction.[111]

1.6 Project aim: self-reproducing protocells coupled to a secondary catalyst

Various synthetic approaches at creating chemical systems that mimic emergent properties characteristic to life have been covered throughout this introductory chapter. The overarching goal of this research has been to further our understanding of the rules that govern and the forces that drive the creation of life. What criteria need to be fulfilled to create something that is truly defined as living and how do we achieve this as synthetic chemists? This must involve the unification metabolism, hereditary information and

compartmentalisation into a functioning, dynamic whole that can reproduce while being maintained in an out-of-equilibrium state through the continuous consumption of energy.

This thesis outlines an approach towards this goal by starting out with self-reproducing lipid aggregates coupled to a secondary catalyst. Starting with a platform of self-reproducing compartments allows for subsequent incorporation of metabolic or genetic features. However, first a robust system is required that is resilient to environmental changes and is compatible orthogonal types of chemistry. Furthermore, a thorough understanding of the mechanism of self-reproduction is needed to eventually develop more complex systems. While precise control over the kinetics of self-reproduction would allow multiple chemical processes to be combined and finetuned within one system.

Resilience, mechanistic understanding and control over kinetics might be obtained within a self-reproducing system by linking physical autocatalysis to a secondary catalyst. This introduces additional variables that can be tuned such as catalyst loading but more importantly the physical location of the reaction within the biphasic system can be controlled through coordination with different ligands. Design and development of a system where physical autocatalysis by micelles is linked to a copper-catalysed azide-alkyne cycloaddition (CuAAC) is reported in Chapter 2. An in-depth study into the mechanism of this reaction, while controlling the kinetics by catalyst compartmentalisation using hydrophobic and hydrophilic ligands, is covered in Chapter 3. A transition to self-reproducing vesicles as a protocell model is described in Chapter 4, which incorporates several emergent, lifelike properties such as out-of-equilibrium self-reproduction, competition and inhibition processes, and secondary metabolism. Chapter 5 discusses the development of an asymmetric autocatalytic CuAAC reaction by employing racemizing allylic azides to from chiral triazole-based copper ligands. Lastly,

Chapter 6 covers further experimental approaches that improve upon the reported systems and offers concluding remarks.

1.7 References

1 E. Schrödinger, *What is life? The physical aspects of the living cell.*, Cambridge University Press, 1944.

2 A. Pross, *What is Life? How chemistry becomes biology*, Oxford University Press, 2012.

3 P. Schwille, How Simple Could Life Be?, *Angew. Chemie Int. Ed.*, 2017, **56**, 10998–11002.

4 N. C. Duarte, S. A. Becker, N. Jamshidi, I. Thiele, M. L. Mo, T. D. Vo, R. Srivas and B. O. Palsson, Global reconstruction of the human metabolic network based on genomic and bibliomic data, *Proc. Natl. Acad. Sci.*, 2007, **104**, 1777–1782.

5 E. N. Trifonov, Vocabulary of Definitions of Life Suggests a Definition, *J. Biomol. Struct. Dyn.*, 2011, **29**, 259–266.

6 K. Ruiz-Mirazo, C. Briones and A. de la Escosura, Prebiotic Systems Chemistry: New Perspectives for the Origins of Life, *Chem. Rev.*, 2014, **114**, 285–366.

7 M. Vitas and A. Dobovišek, Towards a General Definition of Life, *Orig. Life Evol. Biosph.*, 2019, **49**, 77–88.

8 C. Xu, S. Hu and X. Chen, Artificial cells: from basic science to applications, *Mater. Today*, 2016, **19**, 516–532.

9 C. A. Hutchison, R.-Y. Chuang, V. N. Noskov, N. Assad-Garcia, T. J. Deerinck, M. H. Ellisman, J. Gill, K. Kannan, B. J. Karas, L. Ma, J. F. Pelletier, Z.-Q. Qi, R. A. Richter, E. A. Strychalski, L. Sun, Y. Suzuki, B. Tsvetanova, K. S. Wise, H. O. Smith, J. I. Glass, C. Merryman, D. G. Gibson and J. C. Venter, Design and synthesis of a minimal bacterial genome, *Science*, 2016, **351**, aad6253–aad6253.

10 D. Kroiss, G. Ashkenasy, A. B. Braunschweig, T. Tuttle and R. V. Ulijn, Catalyst: Can Systems Chemistry Unravel the Mysteries of the Chemical Origins of Life?, *Chem*, 2019, **5**, 1917–1920.

11 G. von Kiedrowski, S. Otto and P. Herdewijn, Welcome Home, Systems Chemists!, *J. Syst. Chem.*, 2010, **1**, 1.

12 B. Grzybowski, S. Otto and D. Philp, Systems chemistry: a web themed issue, *Chem. Commun.*, 2014, **50**, 14924–14925.

13 P. Walde, H. Umakoshi, P. Stano and F. Mavelli, Emergent properties arising from the assembly of amphiphiles. Artificial vesicle membranes as reaction promoters and regulators, *Chem. Commun.*, 2014, **50**, 10177–10197.

14 K. Le Vay, L. I. Weise, K. Libicher, J. Mascarenhas and H. Mutschler, Templated Self-Replication in Biomimetic Systems, *Adv. Biosyst.*, 2019, **3**, 1800313.

15 C. Darwin, *On the origin of species by means of natural selection, or preservation*

of favoured races in the struggle for life., J. Murray, London, 1859.

16 A. J. Bissette and S. P. Fletcher, Mechanisms of autocatalysis, *Angew. Chemie - Int. Ed.*, 2013, **52**, 12800–12826.

17 G. Clixby and L. Twyman, Self-replicating systems, *Org. Biomol. Chem.*, 2016, **14**, 4170–4184.

18 D. G. Blackmond, An Examination of the Role of Autocatalytic Cycles in the Chemistry of Proposed Primordial Reactions, *Angew. Chemie Int. Ed.*, 2009, **48**, 386–390.

19 A. Butlerow, Formation synthétique d'une substance sucrée, *Comptes rendus l'Académie des Sci.*, 1861, **53**, 145–147.

20 D. Kopetzki and M. Antonietti, Hydrothermal formose reaction, *New J. Chem.*, 2011, **35**, 1787.

21 S. N. Semenov, L. J. Kraft, A. Ainla, M. Zhao, M. Baghbanzadeh, V. E. Campbell, K. Kang, J. M. Fox and G. M. Whitesides, Autocatalytic, bistable, oscillatory networks of biologically relevant organic reactions, *Nature*, 2016, **537**, 656–660.

22 L. E. Orgel, The Implausibility of Metabolic Cycles on the Prebiotic Earth, *PLoS Biol.*, 2008, **6**, e18.

23 A. Robertson, A. J. Sinclair and D. Philp, Minimal self-replicating systems, *Chem. Soc. Rev.*, 2000, **29**, 141–152.

24 S. Yao, I. Ghosh, R. Zutshi and J. Chmielewski, Selective amplification by auto- and cross-catalysis in a replicating peptide system, *Nature*, 1998, **396**, 447–450.

25 G. von Kiedrowski, A Self-Replicating Hexadeoxynucleotide, *Angew. Chemie Int. Ed. English*, 1986, **25**, 932–935.

26 E. J. Hayden, G. von Kiedrowski and N. Lehman, Systems Chemistry on Ribozyme Self-Construction: Evidence for Anabolic Autocatalysis in a Recombination Network, *Angew. Chemie Int. Ed.*, 2008, **47**, 8424–8428.

27 W. Gilbert, Origin of life: The RNA world, *Nature*, 1986, **319**, 618–618.

28 J. W. Szostak, The eightfold path to non-enzymatic RNA replication, *J. Syst. Chem.*, 2012, **3**, 2.

29 J. W. Sadownik, E. Mattia, P. Nowak and S. Otto, Diversification of self-replicating molecules, *Nat. Chem.*, 2016, **8**, 264–269.

30 P. L. Luisi, Autopoiesis: a review and a reappraisal., *Naturwissenschaften*, 2003, **90**, 49–59.

31 P. Razeto-Barry, Autopoiesis 40 years Later. A Review and a Reformulation, *Orig. Life Evol. Biosph.*, 2012, **42**, 543–567.

32 P. A. Bachmann, P. Walde, P. L. Luisi and J. Lang, Self-replicating micelles: aqueous micelles and enzymatically driven reactions in reverse micelles, *J. Am. Chem. Soc.*, 1991, **113**, 8204–8209.

33 P. A. Bachmann, P. L. Luisi and J. Lang, Autocatalytic self-replicating micelles as models for prebiotic structures, *Nature*, 1992, **357**, 57–59.

34 P. A. Bachmann, P. Walde, P. L. Luisi and J. Lang, Self-replicating reverse micelles and chemical autopoiesis, *J. Am. Chem. Soc.*, 1990, **112**, 8200–8201.

35 P. A. Bachmann, P. L. Luisi and J. Lang, Self-replicating Reverse Micelles, *Chim. Int. J. Chem.*, 1991, **45**, 266–268.

36 P. R. Kust and J. F. Rathman, Synthesis of Surfactants by Micellar Autocatalysis: N,N-Dimethyldodecylamine N-Oxide, *Langmuir*, 1995, **11**, 3007–3012.

37 R. Nguyen, L. Allouche, E. Buhler and N. Giuseppone, Dynamic Combinatorial Evolution within Self-Replicating Supramolecular Assemblies, *Angew. Chemie Int. Ed.*, 2009, **48**, 1093–1096.

38 K. Takakura, T. Toyota and T. Sugawara, A novel system of self-reproducing giant vesicles, *J. Am. Chem. Soc.*, 2003, **125**, 8134–8140.

39 A. J. Bissette, B. Odell and S. P. Fletcher, Physical autocatalysis driven by a bond-forming thiol-ene reaction., *Nat. Commun.*, 2014, **5**, 4607.

40 D. Segré, D. Ben-Eli, D. W. Deamer and D. Lancet, The Lipid World, *Orig. Life Evol. Biosph.*, 2001, **31**, 119–145.

41 A. Kahana, P. Schmitt-Kopplin and D. Lancet, Enceladus: First Observed Primordial Soup Could Arbitrate Origin-of-Life Debate, *Astrobiology*, 2019, **19**, 1–16.

42 D. Lancet, R. Zidovetzki and O. Markovitch, Systems protobiology: origin of life in lipid catalytic networks, *J. R. Soc. Interface*, 2018, **15**, 20180159.

43 J. Ortega-Arroyo, A. J. Bissette, P. Kukura and S. P. Fletcher, Visualization of the spontaneous emergence of a complex, dynamic, and autocatalytic system, *Proc. Natl. Acad. Sci.*, 2016, **113**, 11122–11126.

44 J. C. Blain and J. W. Szostak, Progress Toward Synthetic Cells, *Annu. Rev. Biochem.*, 2014, **83**, 615–640.

45 B. C. Buddingh' and J. C. M. van Hest, Artificial Cells: Synthetic Compartments with Life-like Functionality and Adaptivity, *Acc. Chem. Res.*, 2017, **50**, 769–777.

46 E. Rideau, R. Dimova, P. Schwille, F. R. Wurm and K. Landfester, Liposomes and polymersomes: a comparative review towards cell mimicking, *Chem. Soc. Rev.*, 2018, **47**, 8572–8610.

47 R. M. Garavito and S. Ferguson-Miller, Detergents as Tools in Membrane Biochemistry, *J. Biol. Chem.*, 2001, **276**, 32403–32406.

48 I. A. Chen and P. Walde, From Self-Assembled Vesicles to Protocells, *Cold Spring Harb. Perspect. Biol.*, 2010, **2**, a002170.

49 H. Lodish, A. Berk, P. Matsudaira, C. A. Kaiser, M. Krieger, M. P. Scott, L. Zipursky and J. Darnell, *Molecular Cell Biology*, W. H. Freeman, New York, 2000.

50 J. W. Szostak, D. P. Bartel and P. L. Luisi, Synthesizing life, *Nature*, 2001, **409**, 387–390.

51 T. F. Zhu and J. W. Szostak, Coupled Growth and Division of Model Protocell Membranes, *J. Am. Chem. Soc.*, 2009, **131**, 5705–5713.

52 E. Blöchliger, M. Blocher, P. Walde and P. L. Luisi, Matrix Effect in the Size Distribution of Fatty Acid Vesicles, *J. Phys. Chem. B*, 1998, **102**, 10383–10390.

53 S. Lonchin, P. L. Luisi, P. Walde and B. H. Robinson, A Matrix Effect in Mixed Phospholipid/Fatty Acid Vesicle Formation, *J. Phys. Chem. B*, 1999, **103**, 10910–10916.

54 M. M. Hanczyc, Experimental Models of Primitive Cellular Compartments: Encapsulation, Growth, and Division, *Science*, 2003, **302**, 618–622.

55 I. A. Chen, R. W. Roberts and J. W. Szostak, The Emergence of Competition Between Model Protocells, *Science*, 2004, **305**, 1474–1476.

56 A. E. Engelhart, K. P. Adamala and J. W. Szostak, A simple physical mechanism enables homeostasis in primitive cells, *Nat. Chem.*, 2016, **8**, 448–453.

57 K. Adamala and J. W. Szostak, Competition between model protocells driven by an encapsulated catalyst, *Nat. Chem.*, 2013, **5**, 495–501.

58 P. K. Schmidli, P. Schurtenberger and P. L. Luisi, Liposome-mediated enzymatic synthesis of phosphatidylcholine as an approach to self-replicating liposomes, *J. Am. Chem. Soc.*, 1991, **113**, 8127–8130.

59 P. Walde, R. Wick, M. Fresta, A. Mangone and P. L. Luisi, Autopoietic Self-Reproduction of Fatty Acid Vesicles, *J. Am. Chem. Soc.*, 1994, **116**, 11649–11654.

60 A. Veronese and P. L. Luisi, An Autocatalytic Reaction Leading to Spontaneously Assembled Phosphatidyl Nucleoside Giant Vesicles, *J. Am. Chem. Soc.*, 1998, **120**, 2662–2663.

61 P. Walde, P. A. Monnard, M. Wessicken, A. Goto and P. L. Luisi, Oparin's Reactions Revisited: Enzymatic Synthesis of Poly (adenylic acid) in Micelles and Self-Reproducing Vesicles, *J. Am. Chem. Soc.*, 1994, **116**, 7541–7547.

62 M. D. Hardy, J. Yang, J. Selimkhanov, C. M. Cole, L. S. Tsimring and N. K. Devaraj, Self-reproducing catalyst drives repeated phospholipid synthesis and membrane growth, *Proc. Natl. Acad. Sci.*, 2015, **112**, 8187–8192.

63 H. Takahashi, Y. Kageyama, K. Kurihara, K. Takakura, S. Murata and T. Sugawara, Autocatalytic membrane-amplification on a pre-existing vesicular surface, *Chem. Commun.*, 2010, **46**, 8791.

64 K. Kurihara, K. Takakura, K. Suzuki, T. Toyota and T. Sugawara, Cell-sorting of robust self-reproducing giant vesicles tolerant to a highly ionic medium, *Soft Matter*, 2010, **6**, 1888.

65 K. Kurihara, M. Tamura, K. Shohda, T. Toyota, K. Suzuki and T. Sugawara, Self-reproduction of supramolecular giant vesicles combined with the amplification of encapsulated DNA, *Nat. Chem.*, 2011, **3**, 775–781.

66 P. L. Luisi, *The Emergence of Life: From Chemical Origins to Synthetic Biology*, Cambridge University Press, 2006.

67 S. A. P. van Rossum, M. Tena-Solsona, J. H. van Esch, R. Eelkema and J. Boekhoven, Dissipative out-of-equilibrium assembly of man-made supramolecular materials, *Chem. Soc. Rev.*, 2017, **46**, 5519–5535.

68 B. Rieß, R. K. Grötsch and J. Boekhoven, The Design of Dissipative Molecular Assemblies Driven by Chemical Reaction Cycles, *Chem*, 2020, **6**, 552–578.

69 J. Boekhoven, W. E. Hendriksen, G. J. M. Koper, R. Eelkema and J. H. van Esch, Transient assembly of active materials fueled by a chemical reaction, *Science*, 2015, **349**, 1075–1079.

70 P. K. Kundu, D. Samanta, R. Leizrowice, B. Margulis, H. Zhao, M. Börner, T. Udayabhaskararao, D. Manna and R. Klajn, Light-controlled self-assembly of non-photoresponsive nanoparticles, *Nat. Chem.*, 2015, **7**, 646–652.

71 J. J. D. de Jong, P. R. Hania, A. Pug?lys, L. N. Lucas, M. de Loos, R. M. Kellogg, B. L. Feringa, K. Duppen and J. H. van Esch, Light-Driven Dynamic Pattern Formation, *Angew. Chemie Int. Ed.*, 2005, **44**, 2373–2376.

72 K. Ruiz-Mirazo, J. Peretó and A. Moreno, A Universal Definition of Life: Autonomy and Open-Ended Evolution, *Orig. Life Evol. Biosph.*, 2004, **34**, 323–346.

73 R. Pascal, A. Pross and J. D. Sutherland, Towards an evolutionary theory of the origin of life based on kinetics and thermodynamics, *Open Biol.*, 2013, **3**, 130156.

74 H. H. Zepik, E. Blöchliger and P. L. Luisi, A Chemical Model of Homeostasis, *Angew. Chemie Int. Ed.*, 2001, **40**, 199–202.

75 S. Maiti, I. Fortunati, C. Ferrante, P. Scrimin and L. J. Prins, Dissipative self-assembly of vesicular nanoreactors, *Nat. Chem.*, 2016, **8**, 725–731.

76 G. Ragazzon and L. J. Prins, Energy consumption in chemical fuel-driven self-assembly, *Nat. Nanotechnol.*, , DOI:10.1038/s41565-018-0250-8.

77 R. C. Weisenberg, W. J. Deery and P. J. Dickinson, Tubulin-nucleotide interactions during the polymerization and depolymerization of microtubules, *Biochemistry*, 1976, **15**, 4248–4254.

78 P. Solís Muñana, G. Ragazzon, J. Dupont, C. Z. J. Ren, L. J. Prins and J. L. Y. Chen, Substrate-Induced Self-Assembly of Cooperative Catalysts, *Angew. Chemie - Int. Ed.*, 2018, **57**, 16469–16474.

79 C. Wanzke, A. Jussupow, F. Kohler, H. Dietz, V. R. I. Kaila and J. Boekhoven, Dynamic Vesicles Formed By Dissipative Self-Assembly, *ChemSystemsChem*, 2020, **2**, 1–7.

80 I. Colomer, S. M. Morrow and S. P. Fletcher, A transient self-assembling self-replicator, *Nat. Commun.*, 2018, **9**, 2239.

81 I. Colomer, A. Borissov and S. P. Fletcher, Selection from a pool of self-assembling lipid replicators, *Nat. Commun.*, 2020, **11**, 176.

82 S. M. Morrow, I. Colomer and S. P. Fletcher, A chemically fuelled self-replicator, *Nat. Commun.*, 2019, **10**, 1011.

83 D. G. Blackmond, The Origin of Biological Homochirality, *Cold Spring Harb. Perspect. Biol.*, 2010, **2**, a002147–a002147.

84 J. S. Siegel, Homochiral imperative of molecular evolution, *Chirality*, 1998, **10**, 24–27.

85 J. L. Bada, Origins of homochirality, *Nature*, 1995, **374**, 594–595.

86 J. T. Sczepanski and G. F. Joyce, A cross-chiral RNA polymerase ribozyme, *Nature*, 2014, **515**, 440–442.

87 F. Jafarpour, T. Biancalani and N. Goldenfeld, Noise-induced symmetry breaking far from equilibrium and the emergence of biological homochirality, *Phys. Rev. E*, 2017, **95**, 032407.

88 J. D. Carroll, A new definition of life, *Chirality*, 2009, **21**, 354–358.

89 B. L. Feringa and R. A. van Delden, Absolute Asymmetric Synthesis: The Origin, Control, and Amplification of Chirality, *Angew. Chemie Int. Ed.*, 1999, **38**, 3418–3438.

90 W. J. Meiring, Nuclear β-decay and the origin of biomolecular chirality, *Nature*, 1987, **329**, 712–714.

91 J. Shao and P. Hänggi, Control of molecular chirality, *J. Chem. Phys.*, 1997, **107**, 9935–9941.

92 D. K. Kondepudi and K. Asakura, Chiral Autocatalysis, Spontaneous Symmetry Breaking, and Stochastic Behavior, *Acc. Chem. Res.*, 2001, **34**, 946–954.

93 D. K. Kondepudi, R. J. Kaufman and N. Singh, Chiral Symmetry Breaking in Sodium Chlorate Crystallizaton, *Science*, 1990, **250**, 975–976.

94 C. Viedma, Chiral Symmetry Breaking and Complete Chiral Purity by Thermodynamic-Kinetic Feedback Near Equilibrium: Implications for the Origin of Biochirality, *Astrobiology*, 2007, **7**, 312–319.

95 M. Klussmann, A. J. P. White, A. Armstrong and D. G. Blackmond, Rationalization and Prediction of Solution Enantiomeric Excess in Ternary Phase Systems, *Angew. Chemie Int. Ed.*, 2006, **45**, 7985–7989.

96 S. P. Fletcher, R. B. C. Jagt and B. L. Feringa, An astrophysically-relevant mechanism for amino acid enantiomer enrichment, *Chem. Commun.*, 2007, 2578.

97 F. C. Frank, On spontaneous asymmetric synthesis, *Biochim. Biophys. Acta*, 1953, **11**, 459–463.

98 D. G. Blackmond, Autocatalytic Models for the Origin of Biological Homochirality, *Chem. Rev.*, 2020, **120**, 4831–4847.

99 K. Soai, T. Shibata, H. Morioka and K. Choji, Asymmetric autocatalysis and amplification of enantiomeric excess of a chiral molecule, *Nature*, 1995, **378**, 767–768.

100 T. Shibata, J. Yamamoto, N. Matsumoto, S. Yonekubo, S. Osanai and K. Soai, Amplification of a Slight Enantiomeric Imbalance in Molecules Based on Asymmetric Autocatalysis: The First Correlation between High Enantiomeric Enrichment in a Chiral Molecule and Circularly Polarized Light, *J. Am. Chem. Soc.*, 1998, **120**, 12157–12158.

101 K. Soai, S. Osanai, K. Kadowaki, S. Yonekubo, T. Shibata and I. Sato, d - and l - Quartz-Promoted Highly Enantioselective Synthesis of a Chiral Organic Compound, *J. Am. Chem. Soc.*, 1999, **121**, 11235–11236.

102 T. Kawasaki, Y. Matsumura, T. Tsutsumi, K. Suzuki, M. Ito and K. Soai, Asymmetric Autocatalysis Triggered by Carbon Isotope (13C/12C) Chirality, *Science*, 2009, **324**, 492–495.

103 D. G. Blackmond, C. R. McMillan, S. Ramdeehul, A. Schorm and J. M. Brown, Origins of Asymmetric Amplification in Autocatalytic Alkylzinc Additions, *J. Am. Chem. Soc.*, 2001, **123**, 10103–10104.

104 F. G. Buono and D. G. Blackmond, Kinetic Evidence for a Tetrameric Transition State in the Asymmetric Autocatalytic Alkylation of Pyrimidyl Aldehydes †, *J. Am. Chem. Soc.*, 2003, **125**, 8978–8979.

105 D. G. Blackmond, Mechanistic study of the Soai autocatalytic reaction informed by kinetic analysis, *Tetrahedron: Asymmetry*, 2006, **17**, 584–589.

106 I. D. Gridnev, J. M. Serafimov and J. M. Brown, Solution structure and reagent binding of the zinc alkoxide catalyst in the Soai asymmetric autocatalytic reaction, *Angew. Chemie - Int. Ed.*, 2004, **43**, 4884–4887.

107 J. Klankermayer, I. D. Gridnev and J. M. Brown, Role of the isopropyl group in asymmetric autocatalytic zinc alkylations, *Chem. Commun.*, 2007, 3151.

108 M. Quaranta, T. Gehring, B. Odell, J. M. Brown and D. G. Blackmond, Unusual Inverse Temperature Dependence on Reaction Rate in the Asymmetric Autocatalytic Alkylation of Pyrimidyl Aldehydes, *J. Am. Chem. Soc.*, 2010, **132**, 15104–15107.

109 I. D. Gridnev and A. K. Vorobiev, Quantification of Sophisticated Equilibria in the Reaction Pool and Amplifying Catalytic Cycle of the Soai Reaction, *ACS Catal.*, 2012, **2**, 2137–2149.

110 A. Matsumoto, T. Abe, A. Hara, T. Tobita, T. Sasagawa, T. Kawasaki and K. Soai, Crystal Structure of the Isopropylzinc Alkoxide of Pyrimidyl Alkanol: Mechanistic Insights for Asymmetric Autocatalysis with Amplification of Enantiomeric Excess, *Angew. Chemie Int. Ed.*, 2015, **54**, 15218–15221.

111 S. V. Athavale, A. Simon, K. N. Houk and S. E. Denmark, Demystifying the asymmetry-amplifying, autocatalytic behaviour of the Soai reaction through structural, mechanistic and computational studies, *Nat. Chem.*, 2020, **12**, 412–423.

Chapter 2 Self-reproducing micelles coupled to a secondary catalyst

The results of this chapter have been published in *Chemical Communications*.[1] All experiments were designed and performed by Elias Post under the supervision of Dr. Andrew Bissette and Prof. Stephen Fletcher.

2.1 Introduction

The work reported in this chapter expands upon the initial system developed in the Fletcher group based on physical autocatalysis driven by a bond-forming thiol-ene reaction.[2] The aim of this project was to find a bond-forming reaction suitable for physical autocatalysis that is dependent on a secondary catalyst contrary to the uncatalyzed thiol-ene reaction. Previously reported physical autocatalytic reactions relied on a select group of reactions[3–6] with few examples where surfactant self-reproduction was coupled to a secondary catalytic cycle.[7] Linking self-reproduction to a secondary catalyst might lead to different kinetic and physical behaviour than autocatalysis driven by spontaneous reactions. The properties of this novel type of autocatalytic system may be controlled in news ways that would not otherwise be feasible.

As described in Section 1.2, physical autocatalysis relies on the formation of surfactants at the interface of a biphasic system, by reaction between hydrophobic tails and hydrophilic headgroups to form amphiphile products (Figure 2.1a, step 1). Surfactants form supramolecular aggregates such as micelles and vesicles once a critical concentration is reached (step 2). These aggregates facilitate mixing of reaction components by encapsulating hydrophobic components and transporting them to the opposing phase. This accelerates further surfactant formation closing the autocatalytic cycle, enabling self-reproduction of micelles.

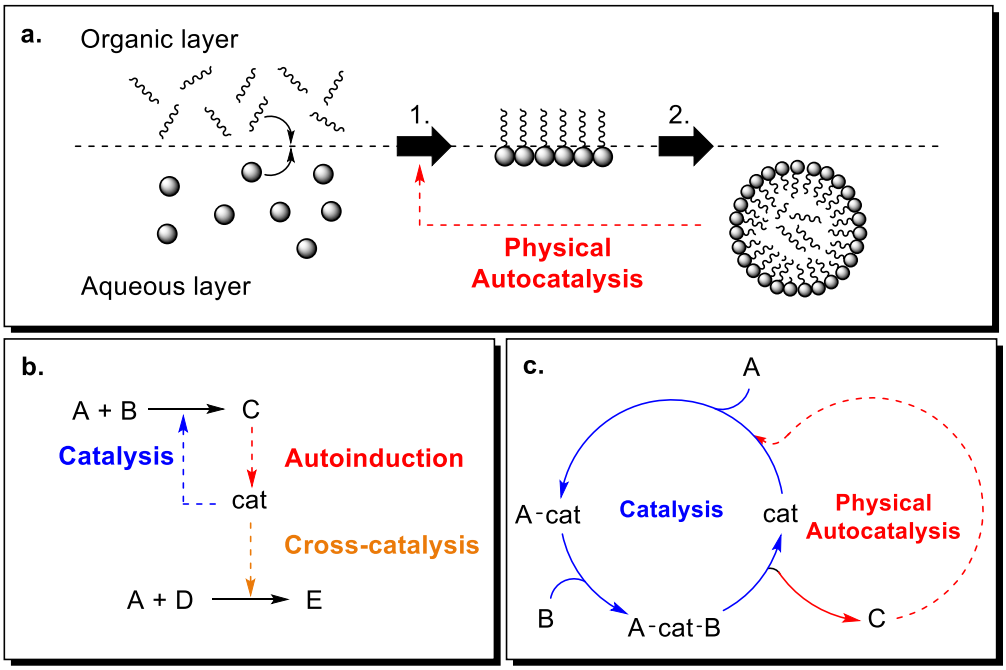


Figure 2.1 a. Overview of the mechanism of physical autocatalysis. **b**. An autoinductive reaction where a ligand is formed that enhances catalytic activity and has a cross-catalytic relationship with a lipid forming reaction (Devaraj, 2015). **c**. This work: product micelles accelerate formation of a catalytic intermediate.

2.2 CuAAC based physical autocatalysis

Copper-catalysed 1,3-dipolar cycloaddition of azides and terminal alkynes (CuAAC) was considered a promising candidate for coupling physical autocatalysis to a secondary catalyst due to the robust and reliable nature of this "click" reaction. It is tolerant to aqueous conditions and compatible with a broad range of functional groups, while the copper catalyst can be stabilized by various modular ligands.[8] This offers opportunities to tune properties of the catalyst complex opening up a way to control the kinetics of the reaction. The products are irreversibly formed and are exclusively stable 1,4-substituted triazoles. Furthermore, the system promises to be highly modular in nature, the polar headgroup or hydrophobic tails might readily be varied without disturbing the underlying mechanism of the autocatalytic reaction.

Devaraj and co-workers have previously applied CuAAC conditions in a system where membrane bound copper (cat) catalyses formation of its own ligand (C) and a membrane forming lipid (E) (Figure 2.1b).[9] As mentioned in Section 1.3, this is an *autoinductive*

mechanism with respect to the copper catalyst: product C is catalytically inactive however upon binding to free catalyst the reaction rate increases, accelerating its own formation.[10] The system reported in this chapter differs from the autoinductive system by generating micelle forming surfactants *via* a CuAAC reaction that once aggregated become catalytically active and allow phase separated reagents to react, linking physical autocatalysis to a secondary catalytic cycle (Figure 2.1c).

2.2.1 System design and characterisation

Reactions between phase-separated hydrophilic maltose azide **2.1** and hydrophobic aliphatic terminal alkynes **2.2a-d** to yield surfactants **2.3a-d**, were selected for study (Figure 2.2). Sugar-based surfactants were employed due to the facile nature by which highly polar, water soluble maltose azide can be synthesised on gram scale using protecting group chemistry (Section 2.5.2).[11] In addition, linear terminal alkynes of various chain length are commercially available, allowing for screening of a wide range of surfactants. Furthermore, previous literature reports of analogous compounds indicated that sugar-derived, triazole-containing amphiphiles aggregated into micelles in aqueous environments at practical concentrations,[12,13] a prerequisite for physical autocatalysis.

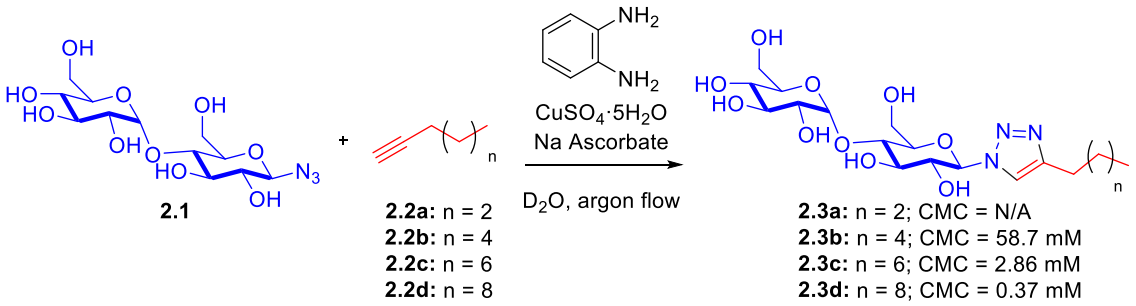


Figure 2.2 System where physical autocatalysis is linked to a secondary catalytic cycle through CuAAC between phase-separated reagents. Maltose azide **2.1** is coupled to alkynes **2.2a-d** of various chain lengths via a CuAAC reaction to form surfactants **2.3a-d** in deuterated water under an inert atmosphere.

A series of surfactant products were synthesized (Section 2.5.2), varying in the length of the hydrophobic tail from 4 (**2.3a**) up to 10 carbons (**2.3d**). Fluorimetry measurements of

surfactant products indicated critical micelle concentrations (CMC) in the millimolar range (Section 2.5.3), whereas Dynamic Light Scattering (DLS) measurements demonstrated aggregation into nanometre-size micelles (Section 2.5.4). A trend was observed where surfactants with shorter chain lengths have a higher critical micelle concentration (CMC). No aggregation was observed for compound **2.3a**, therefore reactions involving alkyne **2.2a** can be considered control reactions where no physical autocatalysis takes place.

2.2.2 Kinetic study

Initial attempts at performing the CuAAC reaction under conventional aqueous conditions, namely in situ reduction of $CuSO_4$ with sodium ascorbate, gave low conversion and irreproducible results. This was likely due to catalyst deactivation by oxidation of Cu(I) to Cu(II). Addition of *o*-phenylenediamine (OPD) as a ligand provided reproducible kinetic behaviour by stabilising copper towards oxidation.[14] However, the solution had to be thoroughly degassed with argon before addition of sodium ascorbate and a continuous flow of argon had to be maintained throughout the reaction to prevent oxidation.

The kinetics of reaction between azide **2.1** and alkyne **2.2c** to form surfactant **2.3c** under biphasic conditions were studied by continuous sampling of aliquots that were measured by ^{1}H NMR spectroscopy. This revealed formation of **2.3c** after an initial lag period of 30 minutes followed by acceleration in product formation (Figure 2.3, red squares). When the reaction was seeded at $t = 0$ with product **2.3c** at a concentration well above the CMC (2.28 mM), the lag was period removed and product formation was significantly accelerated (black circles). As discussed in Chapter 1, these observations are indicative of an autocatalytic mechanism.[10]

Consistent with previous studies, the reaction was extremely sensitive to physical parameters. Duration of the lag period and overall reaction time were affected by minor variations in stirring rate and concentration but also by size of stirrer bar and location of the flask above the stirrer plate.[2] Even when every possible variable was kept constant, there is significant variability between independent repeats. Performing reactions in triplicate and plotting the average with standard deviation as error bars, revealed that overall trends in this system are reproducible.

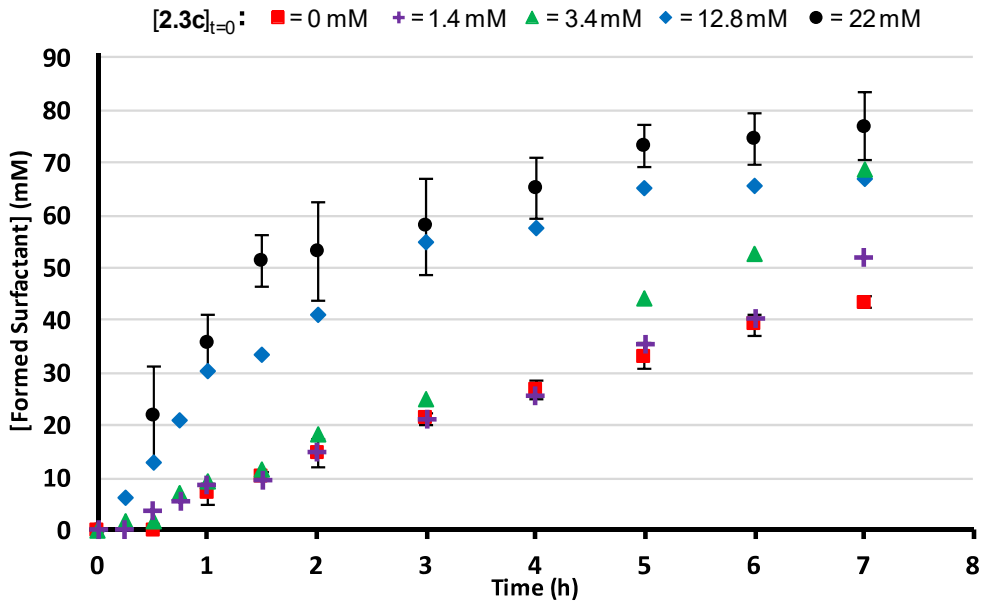


Figure 2.3 Kinetic study of phase-separated CuAAC with azide **2.1** and alkyne **2.2c** as coupling partners and *O*-phenylenediamine as a ligand showing formation of surfactant **2.3c**. The reaction is monitored by consumption of **2.1** and formation of **2.3c** by ^{1}H NMR spectroscopy. Points are the mean of three independent experiments and the error bars are the standard deviation (n=3). *Unseeded reaction* (red squares): **2.1** (150 mg, 91 mM) and **2.2c** (150 uL, 0.83 mmol, 2 eqv) are stirred at 200 rpm with $CuSO_4 \cdot 5H_2O$ (6 mg, 5.3 mM), *O*-phenylenediamine (6.6 mg, 13.6 mM) and sodium ascorbate (16.2 mg, 18.2 mM) in D_2O (4.5 mL). A lag period of half an hour followed by a faster reaction period is observed. *Seeded reactions*: when the reaction is seeded with surfactant **2.3c** (22 mM for black circles, 12.8 mM for blue diamonds, 3.4 mM for green triangles and 1.4 mM for purple pluses) at t = 0 above the CMC (2.28 mM) the lag period is eliminated and the reaction proceeds at a faster rate. Higher concentrations of seeding lead to a more pronounced increase in the rate of product formation.

The influence of product seeding on the overall rate of the reaction was investigated in more depth through additional seeding experiments at increasing concentrations. Seeding at concentrations slightly above and below the CMC (Figure 2.3, 1.4 mM for purple crosses and 3.4 mM for green triangles) leads to accelerations in rate only at later time

points. Whereas an immediate significant rate increase occurs when seeded at a concentration further above the CMC (12.8 mM for blue diamonds). However, the autocatalytic effect starts to saturate at higher concentrations of **2.3c** (22 mM, black circles) with comparatively no significant further increase in rate.

Interestingly, the unseeded reaction never reaches the high rates of product formation observed for the heavily seeded reactions, even when comparing timepoints where the total concentration of autocatalytic species **2.3c** is identical in both systems. This difference might be caused by reduced concentrations of starting material for the unseeded reaction, which have been depleted by the time comparable concentrations of product are generated.

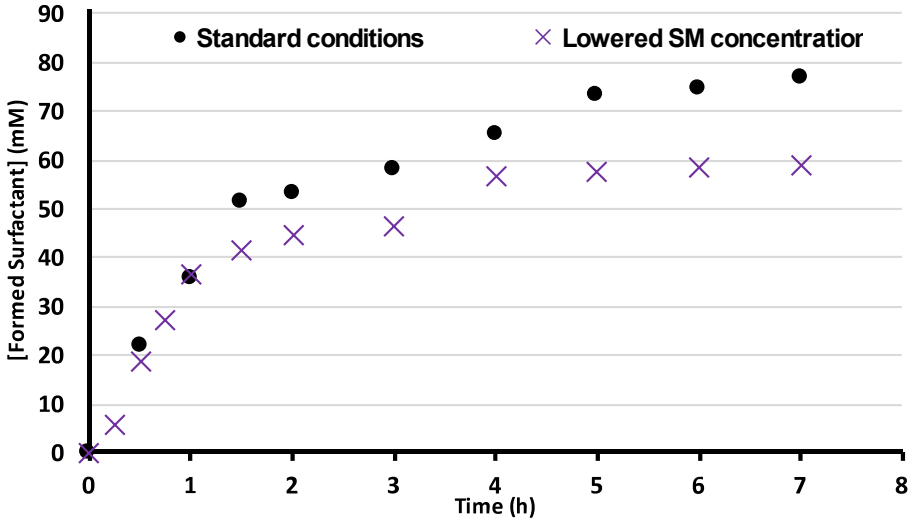


Figure 2.4 Kinetic profile for formation of **2.3c** from **2.1** and **2.2c** when seeded with 22 mM of **2.3c** under normal conditions (black circles) or with lowered concentration of starting materials (purple crosses). The concentration of starting materials is lowered by 22 mM by adding **2.1** (113 mg, 0.309 mmol) and **2.2c** (129 mg, 0.717 mmol) instead of the standard conditions (n = 1).

To test this hypothesis, a seeded reaction (22 mM) was repeated but the concentrations of **2.1** and **2.2c** were lowered by 22 mM (Figure 2.4, purple crosses). This appeared to have a minimal influence on the overall reaction kinetics, showing with a similar rate of initial product formation as original reaction (black circles). Overall, it appears that the

autocatalytic efficiency of product **2.3c** that is manually added differs from **2.3c** generated *in situ*. It is currently unclear what causes with variation, it could possibly be due to variations in the supramolecular composition of **2.3c** which subsequently influences catalytic efficiency.

2.2.3 Varying surfactant chain length

The system of CuAAC-based physical autocatalysis was probed further by studying structure-reactivity relationships. A range of analogous surfactants (**2.3a-d**) were generated by varying the chain length of alkyne coupling partner (**2.2a-d**) (Figure 2.2 and 2.5).

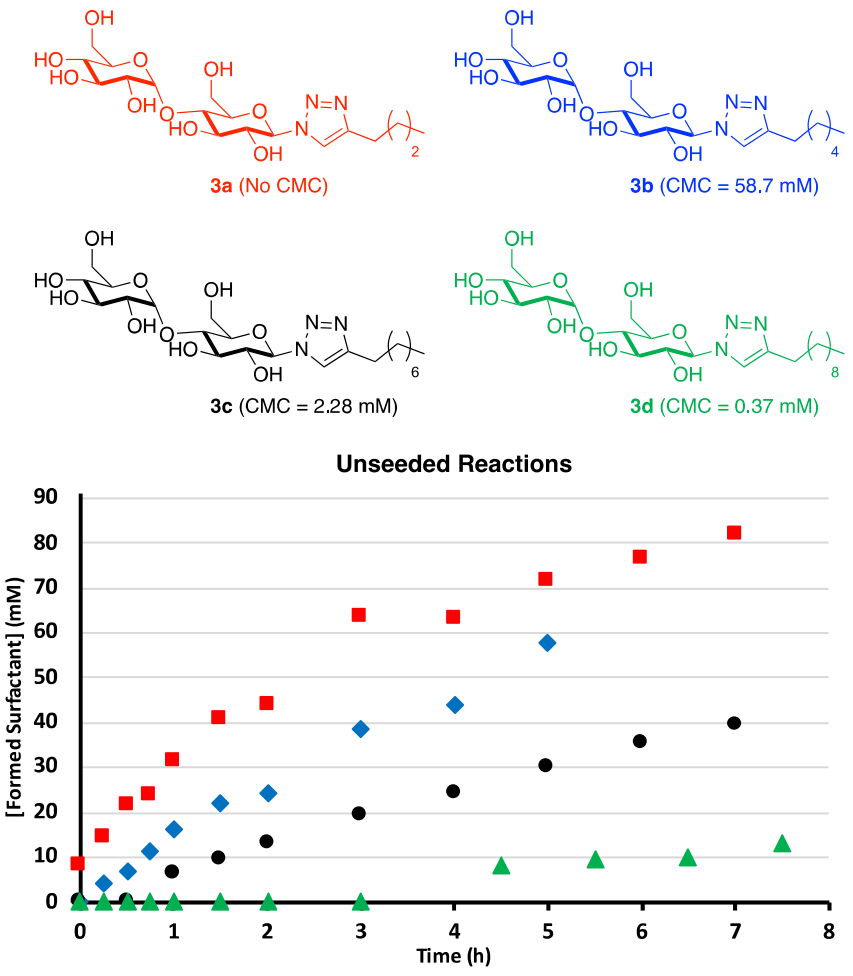


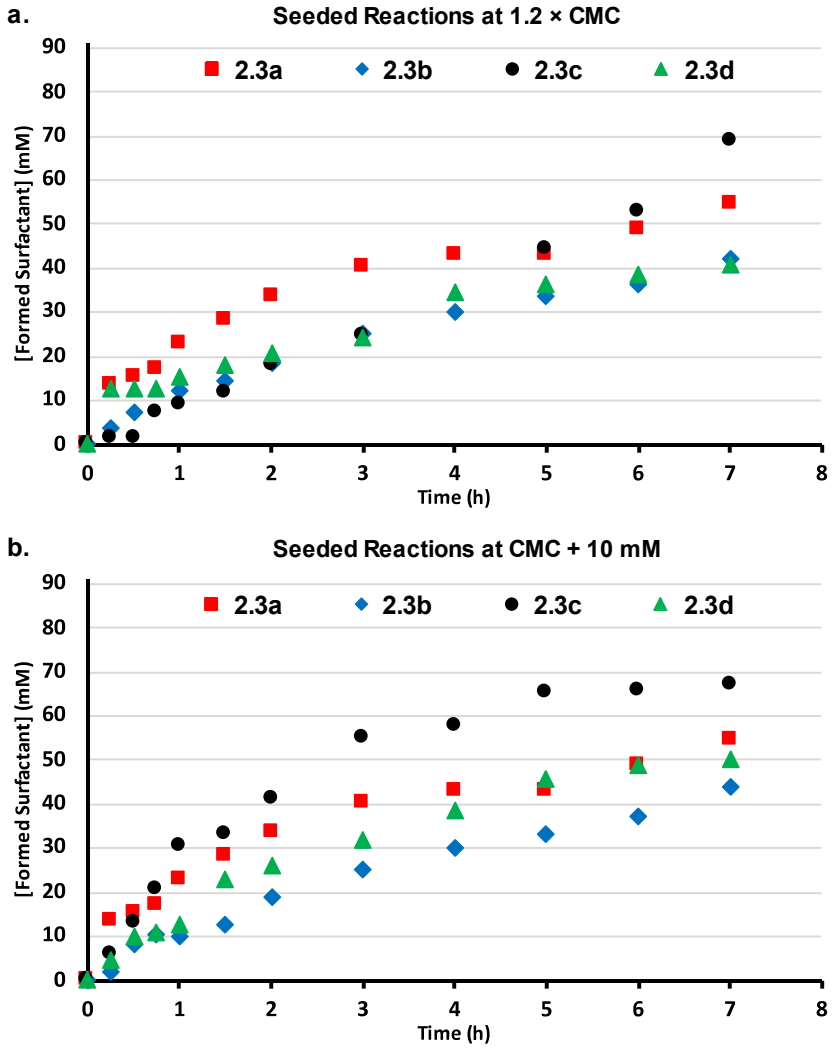
Figure 2.5 Kinetic profile for unseeded reactions using **2.1** and different chain length alkynes **2.2a-d** as coupling partners. A clear trend between the chain length and reaction rates is observed; **2.2a** (red squares), **2.2b** (blue diamonds), **2.2c** (black circles) and **2.2d** (green triangles) (n = 1).

When the kinetics of this group of autocatalysis was studied, a negative correlation between chain length and reaction rate became apparent: surfactants with longer hydrophobic chains had longer lag periods and lower rates of product formation (Figure 2.5). Initially, we expected longer chain amphiphiles to be catalytically active at lower concentrations and have shorter lag periods since fluorimetry measurements (Section 2.5.3) indicated lower CMCs. However, longer alkynes have a markedly decreased solubility in the aqueous layer (0.36 mg/mL for **2.2a** while it is 0.024 mg/mL for **2.2b**)[15]. Overall, the solubility of the alkyne in the aqueous layer appears to have a more significant impact on reaction rate than the CMC value, with lower solubilities leading to longer lag periods and slower product formation.

The variation of CMC values across the range of studied surfactants meant that seeding experiments could not be compared in a useful way at a single absolute concentration for all systems. Instead, two different systematic approaches to seeding were applied that accounted for the varying CMC value. In one case the reactions were seeded relative to the CMC at 1.2 times the value (Figure 2.6a), whereas in the other case reactions were seeded at an absolute value of 10 mM above the CMC (Figure 2.6b). As surfactant **2.3a** does not aggregate and does not have a CMC, an arbitrary amount of 80 mM was added as seed.

These seeding approaches resulted in a significantly higher concentration of seed for **2.3a** and **2.3b** compared to **2.3c** and **2.3d**. Seeding at these >50 mM concentrations resulted in reaction inhibition for **2.3a** and **2.3b** as they formed at slower rates under seeded conditions. The initial rate of product formation was extracted for both reactions and was plotted as a ratio of seeded over unseeded rate. A value lower than one was obtained for both these surfactants indicating that seeding with product results in inhibition of product formation (Table in Figure 2.6a and b).

Meanwhile, formation of longer chain surfactants **2.3c** and **2.3d** did not experience inhibition but were accelerated under seeded conditions. Lag periods were removed when seeded at 1.2 × CMC with a minimal rate increase (a rate ratio of 1.26 for **2.3c** and 3.86 for **2.3d**), whereas a more significant acceleration was observed for CMC + 10 mM conditions (a rate ratio of 3.06 for **2.3c** and 4.62 for **2.3d**). Overall, longer tailed surfactants benefit more from seeding with product than their shorter tailed counterparts.



	$\frac{V_{seeded}}{V_{unseeded}}$
2.3a	$\frac{16.2\ mMh^{-1}}{23.6\ mMh^{-1}} = 0.686$
2.3b	$\frac{9.11\ mMh^{-1}}{12.5\ mMh^{-1}} = 0.729$
2.3c	$\frac{8.41\ mMh^{-1}}{6.69\ mMh^{-1}} = 1.26$
2.3d	$\frac{10.2\ mMh^{-1}}{2.64\ mMh^{-1}} = 3.86$

	$\frac{V_{seeded}}{V_{unseeded}}$
2.3a	$\frac{16.2\ mMh^{-1}}{23.6\ mMh^{-1}} = 0.686$
2.3b	$\frac{8.97\ mMh^{-1}}{12.5\ mMh^{-1}} = 0.718$
2.3c	$\frac{20.5\ mMh^{-1}}{6.69\ mMh^{-1}} = 3.06$
2.3d	$\frac{12.2\ mMh^{-1}}{2.64\ mMh^{-1}} = 4.62$

Figure 2.6 a. Kinetic profile for seeded reactions at 1.2 times the CMC; seeded with 80 mM of **2.3a** (red squares), 70.4 mM of **2.3b** (blue diamonds), 3.40 mM of **2.3c** (black circles) and 0.44 mM of **2.3d** (green triangles) (n = 1). **b**. Kinetic profile for seeded reactions at the CMC plus 10 mM; seeded with 80.0 mM of **3a** (red squares), 68.7 mM of **2.3b** (blue diamonds), 12.8 mM of **2.3c** (black circles) and 10.4 mM of **2.3d** (green triangles) (n = 1). The table next to each graph reports on the ratio of the rate of product formation between the seeded and unseeded reaction during the first three hours after the lag period for each of the four surfactants. A ratio below one indicates inhibition, whereas a ratio above one represents an acceleration.

2.3 Mechanistic study

2.3.1 Investigating the inhibition mechanism

In order to better understand the kinetic behaviour observed in our system, the mechanism by which seeding inhibits formation of **2.3a** and **2.3b** was investigated. Triazoles are known to coordinate to copper and have been incorporated into copper ligands.[16] It was hypothesised that at higher concentrations triazole containing surfactants could start to strongly bind to copper and inhibit turnover of the reaction.

If this hypothesis is correct and inhibition only occurs at higher concentrations, lower concentrations of product seed should still accelerate the reaction. This was tested by repeating the seeding experiment for **2.3b** at a lower concentration (36 mM) below the CMC (Figure 2.7, blue diamonds). No inhibition occurred and a rate acceleration was observed when the CMC (58.7 mM) was reached after 20 mM of additional product had formed at t = 1 h.

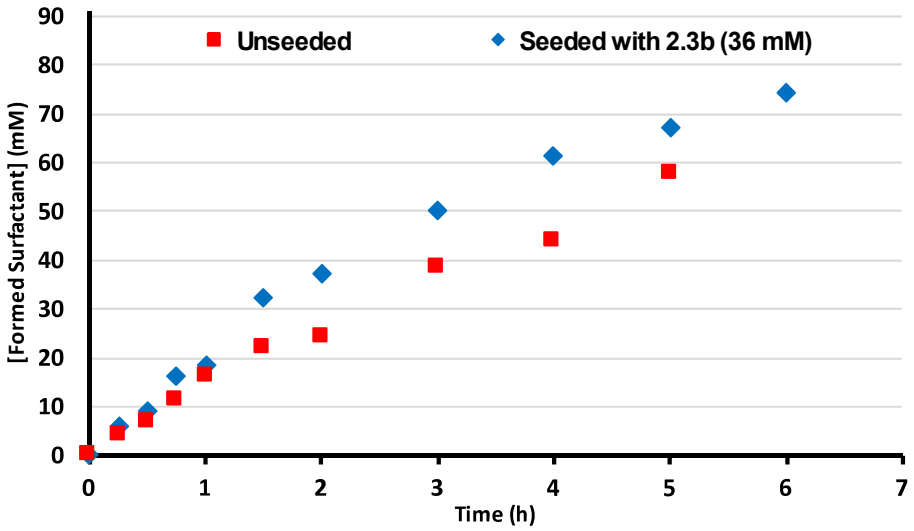


Figure 2.7 Kinetic profiles for reactions between **2.1** and **2.2b** to form **2.3b** showing a rate acceleration when seeded below the CMC. Red squares are the unseeded conditions while blue diamonds correspond to the experiment seeded with 36 mM of **2.3b** (n = 1).

Seeding a reaction between **2.1** and **2.2a** with a lower concentration of **2.3a** (50 mM) still led to inhibition albeit to a lower degree (Figure 2.8b; red squares). Additionally, maltose triazole **2.3e** was synthesized from propargyl alcohol and **2.1** (Figure 2.8a and Section 2.5.2). This compound is not a surfactant due to its polarity and does not aggregate in solution. Addition of **2.3e** (80 mM) to a reaction between **2.1** and **2.2a** still resulted in inhibition (blue triangles), indicating that the inhibition mechanism does not require supramolecular aggregation. Overall, water-soluble compounds bearing a maltose triazole motif appear to inhibit CuAAC when present at high concentrations in an aqueous environment.

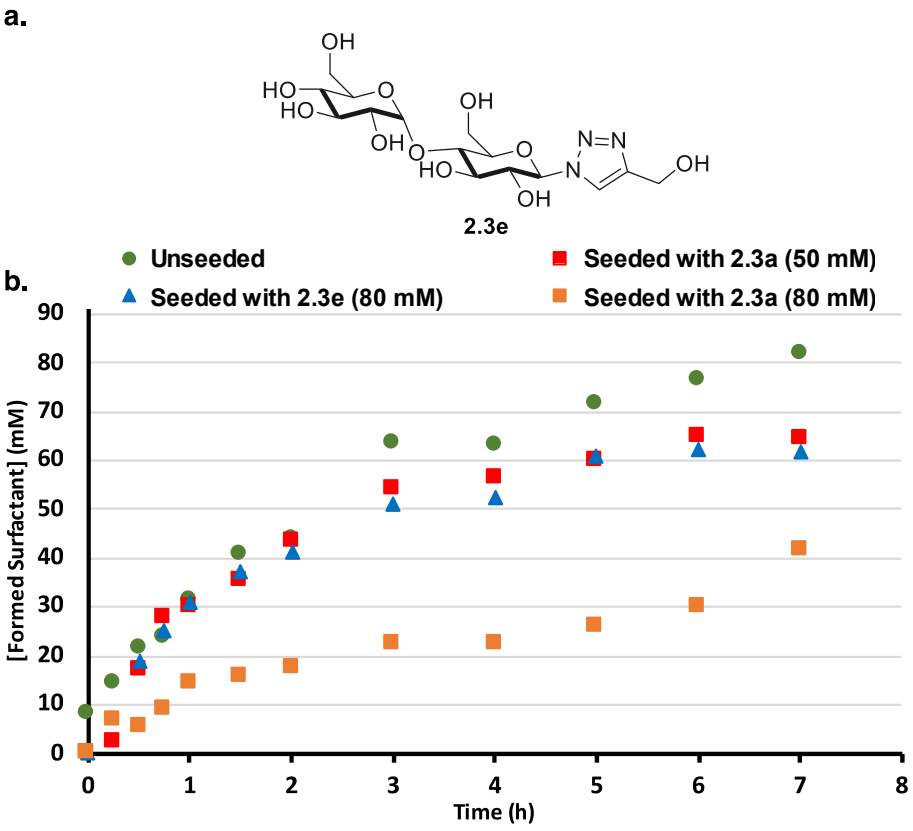


Figure 2.8 a. Structure of polar maltose triazole **2.3e** which is not a surfactant. **b.** Kinetic profiles for reactions between **2.1** and **2.2a** to form **2.3a** showing inhibition when seeding with higher concentrations. Green circles represent the unseeded reaction. Red squares are when seeded with 50 mM of **2.3a**. Blue triangles are when seeded with 80 mM of **2.3e**. Orange squares are when seeded with 80 mM of **2.3a**. (n = 1) Seeding with a non-surfactant such as **2.3e** still appears to lead to inhibition indicating that the maltose-triazole moiety might be inhibitively binding to the copper catalyst at higher concentrations.

2.3.2 Phase behaviour of reaction components

We investigated the phase behaviour of the reaction components to gain insight into the mechanism of physical autocatalysis using diffusion ordered spectroscopy (DOSY). The phase behaviour of reagents and their association with the micelle can be studied by measuring their diffusion constant. A molecule that diffuses at a similar rate to the micellar aggregate is associated to and likely encapsulated by the surfactant product.

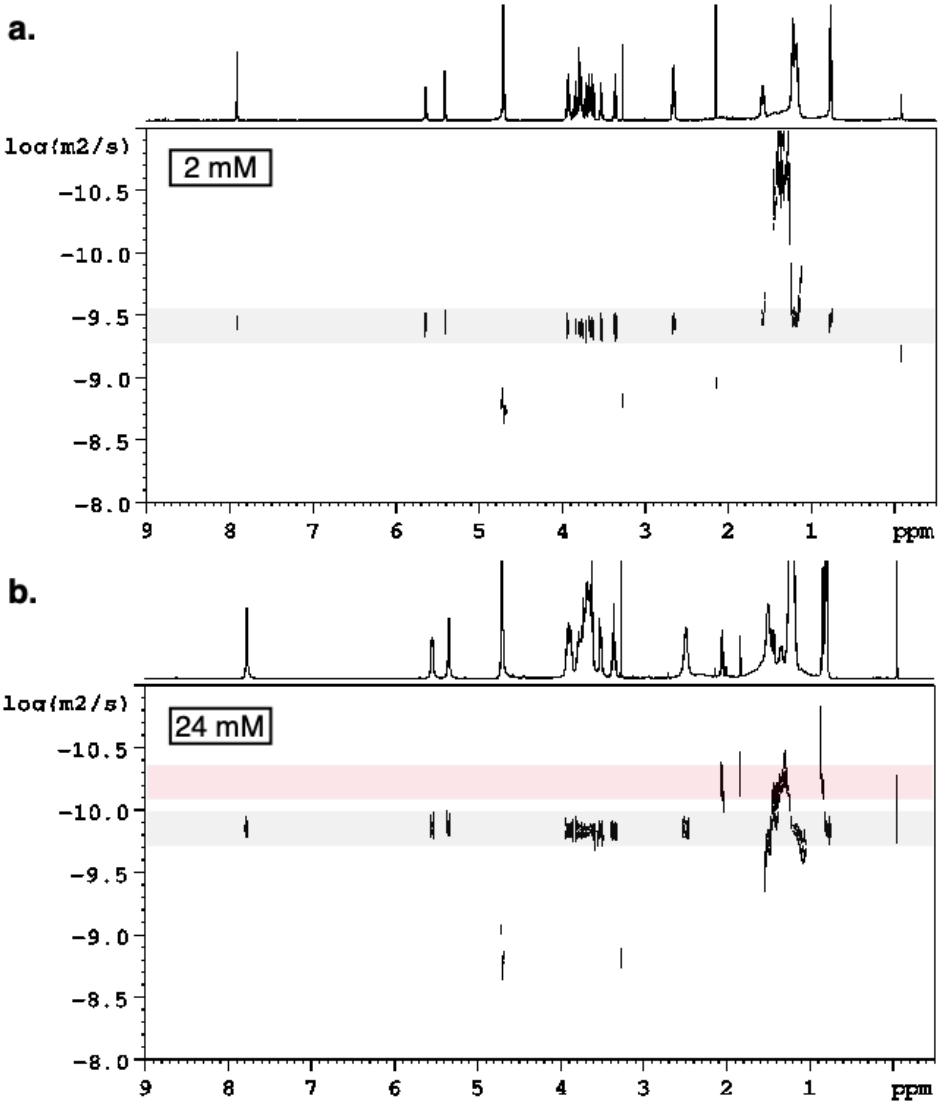


Figure 2.9 2D-DOSY spectra of surfactant **2.3c** (n = 6) at a concentration of 2 mM (**a**) below and 24 mM (**b**) above the CMC (3 mM) in the presence of alkyne **2.2c**. The x-axis represents the chemical shift in ppm while the y-axis represents the diffusion rate in log(m^2/s). The diffusion rate for surfactant **2.3c** is highlighted in grey and while the rate for **2.2c** is highlighted in red. At a concentration below the CMC the surfactant diffuses at a fast rate and **2.2c** is not solubilised. However, at a higher concentration above the CMC when micelles are present the surfactant diffuses at a slower rate and **2.2c** appears to be highly associated with the micelles by diffusing at an even slower rate.

DOSY measurements showed a decrease in the diffusion constant for surfactant **2.3c** when the concentration was raised above the CMC, indicating slower diffusion due to aggregation into micelles (Table 2.1, Entry A and B). Alkyne **2.2c** is insoluble at concentrations of **2.3c** below the CMC but becomes solubilized and fully associated with the micelle above the CMC (Figure 2.9 and Table 2.1, Entry C and D). The water-soluble ligand diffuses at a slower rate in the presence of copper possibly indicating coordination but is unaffected by the presence of **2.3c** (Entry E-H). Meanwhile, azide **2.1** is fully water soluble and does not detectably associate with **2.3c** at any surfactant concentration (Entry I-K).

Entry	Species present	*D* (2.3c)	*D* (2.2c)	*D* (OPD)	*D* (2.1)	*D* (TMS)
A	**2.3c** (2 mM)	3.6	-	-	-	8.2
B	**2.3c** (22 mM)	1.3	-	-	-	1.2
C	**2.3c** (2 mM) **2.2c** (saturated)	3.8	ND	-	-	4.1
D	**2.3c** (22 mM) **2.2c** (saturated)	1.3	0.58	-	-	1.1
E	OPD (saturated)	-	-	9.1	-	7.0
F	$[Cu(OPD)_2]^+$ (6.8 mM)	-	-	5.8	-	13
G	**2.3c** (2 mM) $[Cu(OPD)_2]^+$ (6.8 mM)	3.7	-	5.7	-	8.0
H	**2.3c** (22 mM) $[Cu(OPD)_2]^+$ (6.8 mM)	1.3	-	5.7	-	1.6
I	**2.1** (91 mM)	-	-	-	4.3	-
J	**2.3c** (2 mM) **2.1** (91 mM)	3.6	-	-	4.4	7.6
K	**2.3c** (22 mM) **2.1** (91 mM)	1.2	-	-	4.9	1.2

Table 2.1 Diffusion coefficients extracted from DOSY experiments. The diffusion coefficients were recorded for all reaction components present in the system during the synthesis of **2.3c** in water. *D* values reported in 10^{-10} m^2s^{-1}. A decrease in the diffusion coefficient in the presence of surfactant **2.3c** above the

CMC indicates a strong association with the micelle. ND indicates that the diffusion coefficient could not be extracted because of the limited solubility of the compound in water. The Morris' correlation[17] for small molecules predicts a MW of 516 g/mol for entry **A** and a MW of 339.5 g/mol for entry **I**. These predicted values are in close agreement with the actual molecular weights considering the model used for the predictions.

The kinetics of the CuAAC reaction were measured in a 1:1 water/*tert*-butanol mixture to test whether the autocatalytic kinetics could be fully attributed to phase separation and aggregation. This solvent system facilitates phase mixing and resulted in full elimination of the lag period and fast reaction with complete conversion in 1.5 hours (Figure 2.10). Surprisingly, a residual sigmoidal rate profile was present even though **2.2c** was completely dissolved under these conditions. Closer inspection showed that upon addition of copper and ligand to the reaction, minimal phase separation occurred resulting in some inhomogeneity. Repeating the reaction under seeded conditions removed the sigmoidal profile but the total reaction time remained the same at 1.5 hours. Overall, these results are consistent with the hypothesis that phase separation is responsible for the lag period and autocatalytic kinetics.

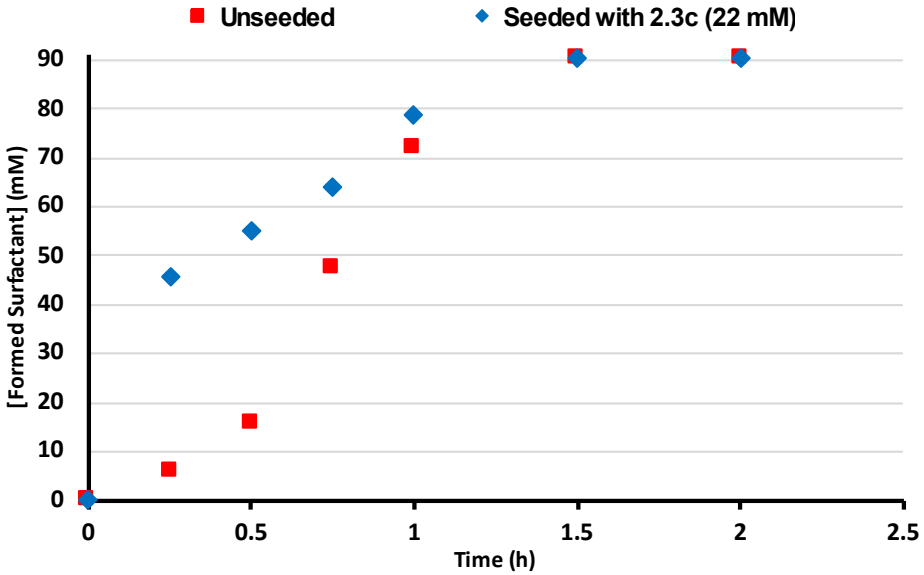


Figure 2.10 Reaction kinetics for CuAAC between **2.1** and **2.2c** to form **2.3c** in *t*BuOH/D_2O (1:1). Complete conversion in 1.5 hours and no lag period is observed. The unseeded reaction (red squares) still appears to have a sigmoidal rate profile. Seeding the reaction (blue diamonds) with 22 mM of product **2.3c** removes the sigmoidal shape but the total reaction time remains the same. (n = 1)

2.3.3 Proposed Mechanism

Previous investigations and kinetic modelling of the mechanism of physical autocatalysis yielded two competing mechanistic models. Luisi and coworkers proposed that rate accelerations in biphasic micellar systems are predominantly due to micellar catalysis.[4,18] Meanwhile, Buhse and coworkers found through modelling that physical autocatalytic processes mainly occur through a mechanism of phase transfer catalysis.[19,20] Both models agree that surfactants facilitate transfer of hydrophobic components to the opposing phase but differ on where the subsequent reaction takes place: According to Luisi *et al.* the reaction occurs within the micelle interior, whereas Buhse *et al.* propose dissociation of a precursor-surfactant complex before the reaction takes place in the bulk aqueous phase.

It is important to note that the previous models were based on systems that relied on passive hydrolysis of hydrophobic anhydrides by a basic aqueous medium, whereas in the system reported here bond formation is driven by copper to generate maltose based triazole surfactants. For all surfactants analysed, the product concentration needed to exceed the CMC before rate accelerations were observed. Micellar aggregation therefore is a prerequisite for autocatalysis to occur. However, from these experiments one cannot conclude whether micellar catalysis or phase transfer catalysis or both mechanisms are operating. DOSY measurements showed a strong alkyne–micelle association which is consistent with micellar catalysis. However, the location where the subsequent CuAAC reaction takes place is not clearly defined. The alkyne might diffuse from the hydrophobic interior of the micelle into the water phase before reacting, which would mean a phase transfer mechanism is operating. On the other hand, hydrophilic azide and the copper-ligand complex need to diffuse into the micelles for micellar catalysis to occur, which was not observed by DOSY.

Based on the available data a mechanistic hypothesis was formulated (Figure 2.11). First, the organic alkyne needs to coordinate to the aqueous copper catalyst which initially only occurs at the interface and is therefore likely the rate limiting step (step 1). After complexation between copper and alkyne, aqueous azide reacts with the newly formed catalyst complex in the aqueous phase (step 2). However, the complex will be more polar since it consists of a hydrophobic alkyne and a hydrophilic ligand, so this step should proceed at a faster rate. After triazole formation, the copper-ligand complex demetallates and re-enters the catalytic cycle, whereas surfactant product starts to form micelles once the CMC is reached. Micelles drastically accelerate the first step by solubilizing alkyne into the aqueous phase, facilitating interaction with the copper-complex and closing the autocatalytic cycle (step 3).

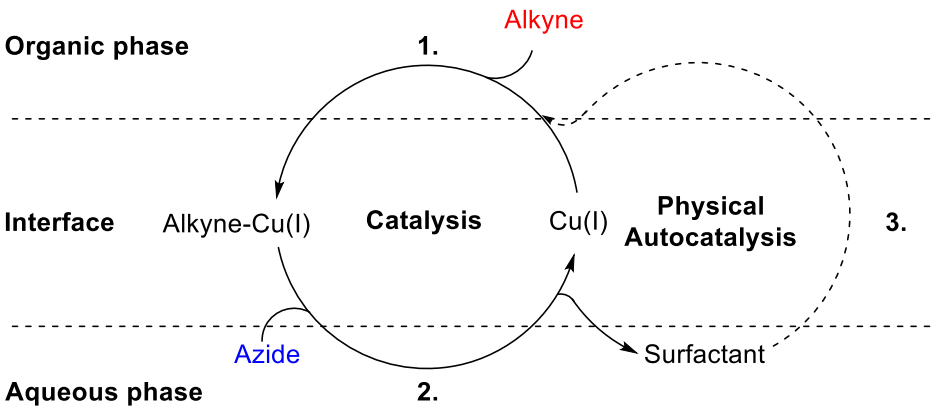


Figure 2.11 Current mechanistic model of the reported system where a catalytic cycle operates in tandem with a physical autocatalytic cycle.

2.4 Conclusions

A new autocatalytic reaction was developed based on surfactant formation from phase-separated components driven by CuAAC. Study of seeding experiments at varying concentrations, surfactant analogues varying in tail-length, and diffusion rates of reaction components has shown that physical autocatalysis was successfully linked to a secondary cycle with unique kinetic and supramolecular behaviour.

The system has the potential to be modular and allow for variations in polar head group and hydrophobic tail without disrupting the underlying autocatalytic mechanism. Copper-catalysed physical autocatalysis opens new opportunities to control the kinetics and phase behaviour of the overall system. The properties of ligands might easily be varied and used as a handle to finetune compartmentalisation of the secondary catalyst by supramolecular assemblies of autocatalytic surfactants.

Chapter 3 describes a further study of this system, where simple, rational variations in catalyst structure are employed as a method to control the kinetics of the reaction. Combined with structure-reactivity studies, a deeper mechanistic understanding is obtained of reactions where physical autocatalysis is linked to a secondary catalyst.

2.5 Experimental

2.5.1 General Information

Materials and reaction setup: All chemicals were purchased from Sigma Aldrich or Fluorochem Scientific and used without further purification. Dry $CHCl_3$, THF, CH_2Cl_2, Et_2O, toluene, benzene, hexane, pentane, DMF, and acetonitrile were collected fresh from an mBraun SPS-5 solvent purification system having been passed through anhydrous alumina columns. All other solvents were used as purchased from Sigma-Aldrich, Honeywell, or Fisher Scientific. Procedures using oxygen- and/or moisture-sensitive materials were performed with anhydrous solvents under an atmosphere of anhydrous argon in flame-dried flasks, using standard Schlenk techniques. Cooling of reaction mixtures to 0 °C was achieved using an ice-water bath. Cooling to –10 °C was achieved using a salt-ice bath. Cooling to –78 °C was achieved using a dry ice-acetone bath.

Chromatography: Analytical TLC was performed on precoated aluminum-backed plates (Silica Gel 60 F254; Merck), and visualised using aqueous ceric ammonium molybdate (CAM), aqueous basic potassium permanganate, or ninhydrin stains. Flash column chromatography was carried out using Merck Geduran® Si 60 (40-63 μm) silica gel. Compound was loaded on to the columns with Chemtube Hydromatrix from Agilent Technologies. Pressure was applied at the column head via a flow of nitrogen with the solvent system used in parentheses.

Nuclear magnetic resonance spectroscopy: All Nuclear magnetic resonance spectroscopy (NMR) spectra were recorded at ambient probe temperature. ^{1}H NMR spectra were recorded using Bruker AVIII HD 400 (400/101 MHz) and AVIII HD 500 (500/126 MHz) spectrometers. Chemical shifts (δ) are reported as parts per million (ppm) and coupling constants (J) are given in hertz (Hz). Chemical shifts are referenced to the residual solvent

peak: $CDCl_3$ (δ 7.26), CD_3OD (δ 3.31), acetone-d_6 (δ 2.05), D_2O (δ 4.79) or DMSO-d_6 (δ 2.50). Resonances are described as s (singlet), d (doublet), t (triplet), q (quartet) and m (multiplet). Assignments of ^1H resonances were determined on the basis of unambiguous chemical shifts, coupling patterns, by analysis of 2D NMR experiments (COSY and HSQC) and/or by analogy to fully interpreted spectra of closely structurally related compounds. ^{13}C NMR spectra (^1H decoupled) were recorded using Bruker AVIII HD 400 (101 MHz) and AVIII HD 500 (126 MHz) spectrometers, referenced to the solvents $CDCl_3$ (δ 77.2), CD_3OD (δ 49.2), acetone-d_6 (δ 29.8) or DMSO-d_6 (δ 39.5).

Diffusion ordered spectroscopy: Diffusion ordered spectroscopy (DOSY) NMR measurements were performed using a Bruker AVIII HD 500 equipped with a TFI probehead at 298 K using the 2D sequence for diffusion measurement using double stimulated echo for convection compensation and longitudinal eddy current delay, using bipolar gradient pulses for diffusion, and using three spoil gradients (Bruker terminology: dstebpgp35) pulse sequence. The samples were thoroughly mixed using a Vortex Genie 2 mixer (Scientific Industries), and were then clarified using a hand centrifuge (Hettich, model 1011) and then measured. Samples containing saturated alkyne consequently had a small layer of neat alkyne above the D_2O layer; sufficient D_2O was used to ensure that the alkyne layer was not detectible by the NMR probe. Experiments were performed in two stages: initially 1D-edited DOSY experiments were used to optimize the diffusion period to Δ=100 ms. The 2D dstebpgp35 sequence was then used, based on the optimized Δ from the previous procedure and with δ=4 ms, with gradient amplitude ranging from 2 to 85% with 16 points in between. Data were analysed using the T_1T_2 module in TOPSPIN 3.2 and plots were generated using the eddosy module.

Mass spectrometry: High-resolution mass spectra (EI and ESI) were recorded using a Bruker MicroTOF spectrometer by the internal service at the University of Oxford. Low-resolution mass spectra were recorded using a Walters LCT premier XE.

Infrared spectroscopy: Infrared measurements (thin film) were carried out using a Bruker Tensor 27 FTIR with internal calibration in the range 4000-600 cm^{-1}.

Optical rotations:Optical rotations were recorded using a Perkin-Elmer 241 polarimeter at 25 °C in a 10 cm cell in the stated solvent. $[\alpha]_D$ values are given in 10^{-1} $deg \cdot cm^2 \cdot g^{-1}$, with concentration c given as g/100 mL.

Fluorimetry: Fluorimetry was performed using Edinburgh Instruments Spectrofluorometer FS5 model with Fluoracle software. The slit width for both excitation and emission was set at 1 nm.

Dynamic Light Scattering: Dynamic Light Scattering (DLS) measurements were recorded using a Malvern Zetasizer Nano ZS DLS instrument and analysed with Zetasizer software. All samples were prepared in ultrapure Milli-Q water and filtered through 0.2 μm PTFE filters before measuring.

2.5.2 Experimental Procedures and Characterisation of Compounds

General procedure 1: Synthesis of protected surfactant products via CuAAC reaction

Conditions adapted from Shao *et al*.[21] To a stirred suspension of CuI (0.020 eq) in degassed CH_2Cl_2 (160 mM) was added protected maltose azide 1a (1.0 eq), DIPEA (0.040 eq), AcOH (0.040 eq) and alkyne (1.4 eq). The resultant solution was stirred for 18 h. The reaction mixture was concentrated *in vacuo*, and the crude was purified with flash column chromatography. The column was eluted with EtOAc:hexane (1:1) to yield the product.

General procedure 2: Acetyl deprotection

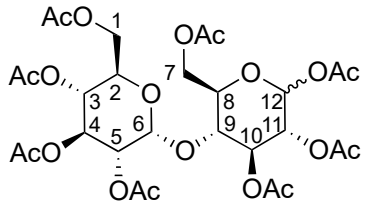
Synthesis according to Mahon *et al*.[13] To a stirred suspension of protected sugar (150 mM) in MeOH was added sodium methoxide (0.10 eq). Upon dissolution of the solid and concurrent disappearance of protected sugar (TLC control) the solution was neutralised using Amberlyst 15 resin (H^+ form). The resin was filtered off and washed with MeOH and the filtrate was concentrated *in vacuo*. The residue was dried under high vacuum to give a deprotected sugar as a tacky, hygroscopic white foam.

General procedure 3: Setup of kinetic experiments

Maltose azide **2.1b** (150 mg, 0.408 mmol, 1.00 eq, 1.5 mL of 100 mg/mL standard solution in D_2O), $CuSO_4 \cdot 5H_2O$ (6.0 mg, 0.024 mmol, 0.06 eq, 1 mL of 6 mg/mL standard solution in D_2O) (and deprotected surfactant in the reported concentrations for the seeded reactions) were added to D_2O (2.0 mL) to give a total volume of 4.5 mL in a round bottom flask (25 mL) with a stirrer bar of a similar size for each experiment. The flask was capped with a septum and the solution was degassed by bubbling argon through it for 30 minutes. *O*-phenylenediamine (6.6 mg, 0.061 mmol, 0.15 eq), alkyne (2.0 eq) and sodium

ascorbate (16.2 mg, 0.0820 mmol, 0.200 eq) were added. The reaction mixture was stirred at 200 rpm under a continuous flow of argon. Samples for analysis during the kinetic experiments were prepared at regular intervals by diluting 0.1 mL of the reaction mixture in 0.4 mL of D_2O and immediately taking a ^1H NMR measurement.

α/β-D-maltose octaacetate



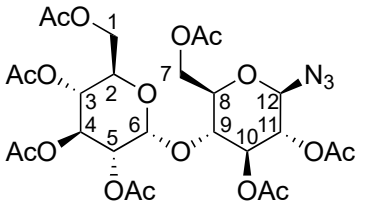
Chemical Formula: $C_{28}H_{38}O_{19}$
Molecular Weight: 678.59

Synthesised according to Harvey *et al.*[11] NaOAc (5.00 g, 61.0 mmol, 1.10 eq) was added to a stirred suspension of D-maltose (10.0 g, 29.2 mmol, 1.00 eq) in Ac_2O (50 mL) at 140 °C. The reaction was stirred until deemed complete by disappearance of maltose (TLC control, 2:1 petroleum ether/EtOAc) (approx. 1 h). The reaction mixture was diluted with CH_2Cl_2 (50 mL). The organic mixture was washed with saturated aqueous $NaHCO_3$ (3 × 100 mL), dried (Na_2SO_4) and concentrated *in vacuo* to yield the peracetylated D-maltose (23.0 g, quantitative yield, α:β ~ 1:4.55) as an amorphous white solid.

^{1}H NMR (400 MHz, $CDCl_3$) δ 5.74 (d, *J* = 8.1 Hz, 1H, C<u>H</u>-6), 5.40 (d, *J* = 4.1 Hz, 1H, C<u>H</u>-12), 5.35 (dd, *J* = 10.6, 9.5 Hz, 1H, C<u>H</u>-4), 5.29 (t, *J* = 9.0 Hz, 1H, C<u>H</u>-10), 5.05 (dd, *J* = 10.2, 9.5 Hz, 1H, C<u>H</u>-3), 4.97 (dd, *J* = 9.2, 8.2 Hz, 1H, C<u>H</u>-5), 4.85 (dd, *J* = 10.5, 4.0 Hz, 1H, C<u>H</u>-11), 4.45 (dd, *J* = 12.3, 2.5 Hz, 1H, C<u>H$_a$H$_b$</u>-7), 4.30 – 4.17 (m, 2H, CH$_a$<u>H$_b$</u>-7 and C<u>H$_a$H$_b$</u>-1), 4.07 – 3.99 (m, 2H, CH$_a$<u>H$_b$</u>-1 and C<u>H</u>-9), 3.97 – 3.92 (m, 1H, C<u>H</u>-2), 3.83 (ddd, *J* = 9.7, 4.5, 2.6 Hz, 1H, 10.1, 3.1 Hz, 1H, C<u>H</u>-8), 2.22 (s, 6H, C<u>H$_3$</u>CO), 2.13 (s, 3H, C<u>H$_3$</u>CO), 2.09 (s, 6H, C<u>H$_3$</u>CO), 2.04 (s, 3H, C<u>H$_3$</u>CO), 2.02 (s, 3H, C<u>H$_3$</u>CO), 2.01 (s, 3H, C<u>H$_3$</u>CO), 2.01 (s, 3H, C<u>H$_3$</u>CO), 2.00 (s, 3H, C<u>H$_3$</u>CO); **^{13}C{^{1}H} NMR** (101 MHz, $CDCl_3$)

δ 170.7, 170.6, 170.6, 170.1, 170.1, 170.0, 169.5, 169.0, 95.9, 88.9, 72.4, 72.3, 70.20, 70.15, 69.8, 69.3, 68.7, 68.0, 62.5, 61.4, 21.1, 21.0, 20.9, 20.8, 20.73 (2C), 20.71, 20.6; **HRMS** (ESI) *m/z* calcd for $C_{28}H_{38}O_{19}Na$ $[M+Na]^+$: 701.1900, found: 701.1896. Data reported here is for the β-anomer and is consistent with reported literature values.[13]

Hepta-O-acetyl-1-deoxy-1-azido-β-D-maltopyranose (2.4)



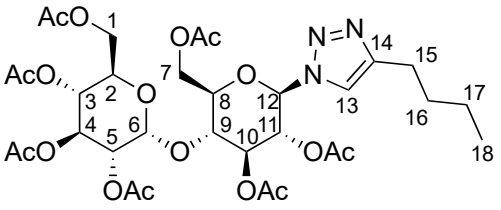
Chemical Formula: $C_{26}H_{35}N_3O_{17}$
Molecular Weight: 661.57

Synthesised according to Mahon *et al*.[13] The crude maltose octaacetate (40.8 g, 60.1 mmol, 1.00 eq) was dissolved in CH_2Cl_2 (80 mL). HBr (80 mL, 33% solution in AcOH, 7.7 eq) was added slowly at 0 °C and the reaction stirred at rt until complete (TLC control, 3:1 petroleum ether/EtOAc, approx. 3 h). The reaction mixture was diluted with CH_2Cl_2 (100 mL) and H_2O (100 mL). The layers were separated, and the organic layer was washed with saturated aqueous $NaHCO_3$ (3 × 200 mL) and then brine (1 × 200 mL). The organic layer was dried (Na_2SO_4) and concentrated *in vacuo* to give a syrupy yellow oil (43.7 g). The crude bromide was dissolved in $CHCl_3$ (90 mL) and saturated aqueous $NaHCO_3$ (90 mL) was added. Tetrabutylammonium iodide (20.0 g, 54.1 mmol, 0.900 eq) was added, followed by NaN_3 (slow addition, 5 min, 18.00 g, 213.8 mmol, 4.600 eq) and the reaction was stirred at rt for 18 h. The layers were partitioned, and the organic layer washed with H_2O (100 mL), saturated aqueous $NaHCO_3$ (100 mL) and brine (100 mL). The organic layer was dried ($MgSO_4$) and concentrated *in vacuo* to give a brown solid. The crude product was recrystallised from a minimum of hot MeOH to give hepta-O-

acetyl-1-deoxy-1-azido-β-D-maltopyranose **2.4** (26.0 g, 39.3 mmol, 65% over two steps) as a white crystalline solid.

^{1}H NMR (400 MHz, $CDCl_3$) δ 5.40 (d, *J* = 4.0 Hz, 1H, C<u>H</u>-6), 5.34 (dd, *J* = 10.6, 9.5 Hz, 1H, C<u>H</u>-4), 5.25 (t, *J* = 8.9 Hz, 1H, C<u>H</u>-10), 5.04 (dd, *J* = 10.3, 9.5 Hz, 1H, C<u>H</u>-3), 4.84 (dd, *J* = 10.6, 4.0 Hz, 1H, C<u>H</u>-5), 4.77 (t, = 8.9 Hz, 1H, C<u>H</u>-11), 4.70 (d, *J* = 8.7 Hz, 1H, C<u>H</u>-12), 4.50 (dd, *J* = 12.2, 2.6 Hz, 1H, C<u>H$_a$</u>H$_b$-7), 4.23 (ddd, *J* = 12.3, 4.2, 2.0 Hz, 2H, CH$_a$<u>H$_b$</u>-7 and C<u>H$_a$</u>H$_b$-1), 4.04 (dd, *J* = 12.5, 2.3 Hz, 1H, CH$_a$<u>H$_b$</u>-1), 4.01 (dd, *J* = 9.8, 8.7 Hz, 1H, C<u>H</u>-9), 3.98 – 3.89 (m, 1H, C<u>H</u>-2), 3.77 (ddd, *J* = 9.8, 4.5, 2.6 Hz, 1H, C<u>H</u>-8), 2.15 (s, 3H, C<u>H$_3$</u>CO), 2.09 (s, 3H, C<u>H$_3$</u>CO), 2.04 (s, 3H, C<u>H$_3$</u>CO), 2.03 (s, 3H, C<u>H$_3$</u>CO), 2.02 (s, 3H, C<u>H$_3$</u>CO), 2.00 (s, 3H), 1.99 (s, 3H, C<u>H$_3$</u>CO); **^{13}C{^{1}H} NMR** (101 MHz, $CDCl_3$) δ 170.7, 170.6, 170.2, 170.1, 169.64, 169.56, 95.8, 87.6, 75.2, 74.4, 72.5, 71.6, 70.1, 69.4, 68.8, 68.1, 62.7, 61.6, 51.0, 21.0, 20.90, 20.8, 20.72, 20.69 (3C); **HRMS** (ESI) *m/z* calcd for $C_{26}H_{35}O_{17}N_3Na$ $[M+Na]^+$: 684.1859, found: 684.1855. Consistent with reported literature values.[13]

1-(Hepta-O-acetyl-1-deoxy-β-D-maltopyranosyl)-4-butyl triazole (2.5a)

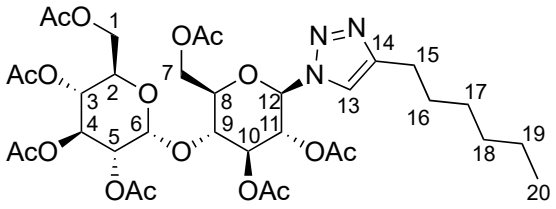


Chemical Formula: $C_{32}H_{45}N_3O_{17}$
Molecular Weight: 743.72

Synthesised according to general procedure 1 using maltose azide **2.4** (1.00 g, 1.51 mmol, 1.00 eq), CuI (6.0 mg, 0.032 mmol, 0.021 eq), DIPEA (10 μL, 0.060 mmol, 0.040 eq), AcOH (3.5 μL, 0.060 mmol, 0.040 eq) and 1-hexyne (173 μL, 1.51 mmol, 1.00 eq). Flash column chromatography (50% EtOAc in hexane) provided 1-(hepta-O-acetyl-1-deoxy-β-D-maltopyranosyl)-4-butyl triazole **2.5a** (986 mg, 1.33 mmol, 88%) as a white foam.

^{1}H NMR (400 MHz, $CDCl_3$) δ 7.42 (d, *J* = 0.8 Hz, 1H, C<u>H</u>-13), 5.86 (d, *J* = 9.3 Hz, 1H, C<u>H</u>-12), 5.50 – 5.40 (m, 2H, C<u>H</u>-6 and C<u>H</u>-10), 5.43 – 5.28 (m, 2H, C<u>H</u>-4 and C<u>H</u>-11), 5.08 (t, *J* = 9.9 Hz, 1H, C<u>H</u>-3), 4.88 (dd, *J* = 10.6, 4.0 Hz, 1H, C<u>H</u>-5), 4.48 (dd, *J* = 12.4, 2.4 Hz, 1H, C<u>H</u>$_a$H$_b$-7), 4.27 (dd, *J* = 4.3, 3.0 Hz, 1H, C<u>H</u>$_a$H$_b$-1), 4.24 (t, *J* = 3.7 Hz, 1H, CH$_a$<u>H</u>$_b$-7), 4.17 – 4.11 (m, 1H, C<u>H</u>-9), 4.07 (dd, *J* = 12.6, 2.4 Hz, 1H, CH$_a$<u>H</u>$_b$-1), 4.00 – 3.94 (m, 2H, C<u>H</u>-2 and C<u>H</u>-8), 2.74 – 2.68 (m, 2H, C<u>H</u>$_2$-15), 2.13 (s, 3H, C<u>H</u>$_3$CO), 2.11 (s, 3H, C<u>H</u>$_3$CO), 2.07 (s, 3H, C<u>H</u>$_3$CO), 2.04 (s, 3H, C<u>H</u>$_3$CO), 2.03 (s, 3H, C<u>H</u>$_3$CO), 2.01 (s, 3H, C<u>H</u>$_3$CO), 1.64 (p, *J* = 7.6 Hz, 2H, C<u>H</u>$_2$-16), 1.39 – 1.32 (m, 2H, C<u>H</u>$_2$-17), 0.92 (t, *J* = 7.3 Hz, 3H, C<u>H</u>$_2$-18); **^{13}C{^{1}H} NMR** (101 MHz, $CDCl_3$) δ 170.7, 170.6, 170.4, 170.0 (2C), 169.5, 169.4, 149.2, 118.8, 96.0, 85.2, 75.4 (2C), 72.6, 71.0, 70.1, 69.3, 68.8, 68.0, 62.6, 61.5, 31.3, 25.4, 22.3, 20.9, 20.9, 20.8, 20.7 (3C), 20.3, 13.9; **HRMS** (ESI) *m/z* calcd for $C_{32}H_{45}O_{17}N_3Na$ $[M+Na]^+$: 766.2641, found: 766.2632; **IR** (ATR) ν (cm^{-1}) thin film, CH_2Cl_2: 2959 (w), 1748 (s), 1434 (w), 1369 (m), 1225 (s), 1036 (s), 899 (w); **[α]^{25}$_D$** = +72.8 (c = 0.63, CH_2Cl_2).

1-(Hepta-O-acetyl-1-deoxy-β-D-maltopyranosyl)-4-hexyl triazole (2.5b)

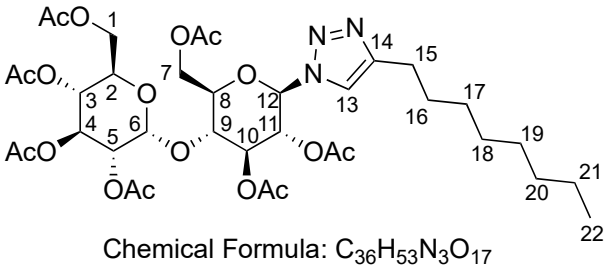


Chemical Formula: $C_{34}H_{49}N_3O_{17}$
Molecular Weight: 771.77

Synthesised according to general procedure 1 using maltose azide **2.4** (1.00 g, 1.51 mmol, 1.00 eq), CuI (6.0 mg, 0.032 mmol, 0.021 eq), DIPEA (10 µL, 0.060 mmol, 0.040 eq), AcOH (3.5 µL, 0.060 mmol, 0.040 eq) and 1-octyne (230 µL, 1.60 mmol, 1.06 eq). Flash column chromatography (50% EtOAc in hexane) provided 1-(hepta-O-acetyl-1-deoxy-β-D-maltopyranosyl)-4-hexyl triazole **2.5b** (782 mg, 1.05 mmol, 67%) as a white foam.

^{1}H NMR (400 MHz, $CDCl_3$) δ 7.42 (s, 1H, C<u>H</u>-13), 5.85 (d, *J* = 9.3 Hz, 1H, C<u>H</u>-12), 5.48 – 5.42 (m, 2H, C<u>H</u>-6 and C<u>H</u>-10), 5.42 – 5.30 (m, 2H, C<u>H</u>-4 and C<u>H</u>-11), 5.07 (t, *J* = 9.9 Hz, 1H, C<u>H</u>-3), 4.88 (dd, *J* = 10.6, 4.0 Hz, 1H, C<u>H</u>-5), 4.48 (dd, *J* = 12.4, 2.4 Hz, 1H, C<u>H</u>$_a$H$_b$-7), 4.27 (t, *J* = 4.0 Hz, 1H, C<u>H</u>$_a$H$_b$-1), 4.24 (t, *J* = 4.0 Hz, 1H, CH$_a$<u>H</u>$_b$-7), 4.14 (dd, *J* = 9.8, 8.7 Hz, 1H, C<u>H</u>-9), 4.07 (dd, *J* = 12.4, 2.3 Hz, 1H, CH$_a$<u>H</u>$_b$-1), 4.01 – 3.93 (m, 2H, C<u>H</u>-2 and C<u>H</u>-8), 2.70 (dd, *J* = 8.6, 6.7 Hz, 2H, C<u>H</u>$_2$-15), 2.13 (s, 3H, C<u>H</u>$_3$CO), 2.11 (s, 3H, C<u>H</u>$_3$CO), 2.07 (s, 3H, C<u>H</u>$_3$CO), 2.03 (s, 3H, C<u>H</u>$_3$CO), 2.03 (s, 3H, C<u>H</u>$_3$CO), 2.01 (s, 3H, C<u>H</u>$_3$CO), 1.65 (p, *J* = 7.4 Hz, 2H, C<u>H</u>$_2$-16), 1.29 (m, 6H, (C<u>H</u>$_2$)$_3$-17,18,19), 0.90 – 0.85 (m, 3H, C<u>H</u>$_2$-20); **^{13}C{^{1}H} NMR** (101 MHz, $CDCl_3$) δ 170.7, 170.6, 170.4, 170.0 (2C), 169.5, 169.3, 149.2, 118.8, 96.0, 85.2, 75.39, 75.36, 72.6, 71.0, 70.1, 69.3, 68.9, 68.0, 62.7, 61.6, 31.6, 29.2, 28.9, 25.7, 22.6, 20.9, 20.9, 20.8, 20.7 (2C), 20.3, 14.1; **HRMS** (ESI) *m/z* calcd for $C_{34}H_{49}O_{17}N_3Na$ $[M+Na]^+$: 794.2954, found: 794.2945. Consistent with data in the literature.[22]

1-(Hepta-O-acetyl-1-deoxy-β-D-maltopyranosyl)-4-octyl triazole (2.5c)

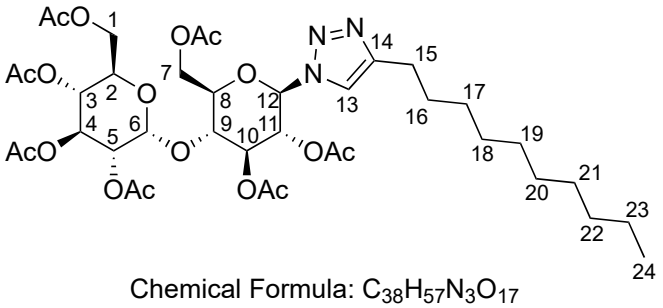


Chemical Formula: $C_{36}H_{53}N_3O_{17}$
Molecular Weight: 799.82

Synthesised according to general procedure 1 using maltose azide **2.4** (1.00 g, 1.51 mmol, 1.00 eq), CuI (6.0 mg, 0.032 mmol, 0.021 eq), DIPEA (10 µL, 0.060 mmol, 0.040 eq), AcOH (3.5 µL, 0.060 mmol, 0.040 eq) and 1-decyne (290 µL, 1.60 mmol, 1.06 eq). Flash column chromatography (50% EtOAc in hexane) provided 1-(hepta-O-acetyl-1-deoxy-β-D-maltopyranosyl)-4-octyl triazole **2.5c** (1.20 g, 1.50 mmol, quantitative yield) as a white foam.

^{1}H NMR (400 MHz, $CDCl_3$) δ 7.42 (s, 1H, C<u>H</u>-13), 5.86 (d, *J* = 9.3 Hz, 1H, C<u>H</u>-12), 5.48 – 5.42 (m, 2H, C<u>H</u>-6 and C<u>H</u>-10), 5.35 (m, 2H, C<u>H</u>-4 and C<u>H</u>-11), 5.08 (t, *J* = 9.8 Hz, 1H, C<u>H</u>-3), 4.88 (dd, *J* = 10.5, 4.0 Hz, 1H, C<u>H</u>-5), 4.48 (dd, *J* = 12.4, 2.4 Hz, 1H, C<u>H</u>$_a$H$_b$-7), 4.27 (t, *J* = 3.9 Hz, 1H, C<u>H</u>$_a$H$_b$-1), 4.24 (t, *J* = 4.0 Hz, 1H, CH$_a$H$_b$-7), 4.12 (dd, *J* = 9.8, 8.7 Hz, 1H, C<u>H</u>-9), 4.05 (dd, *J* = 12.5, 2.3 Hz, 1H, CH$_a$<u>H</u>$_b$-1), 3.97 (m, 2H, C<u>H</u>-2 and C<u>H</u>-8), 2.74 – 2.67 (m, 2H, C<u>H</u>$_2$-15), 2.13 (s, 3H, C<u>H</u>$_3$CO), 2.11 (s, 3H, C<u>H</u>$_3$CO), 2.07 (s, 3H, C<u>H</u>$_3$CO), 2.03 (s, 3H, C<u>H</u>$_3$CO), 2.03 (s, 3H, C<u>H</u>$_3$CO), 2.01 (s, 3H, C<u>H</u>$_3$CO), 1.84 (s, 3H, C<u>H</u>$_3$CO), 1.65 (m, 2H, C<u>H</u>$_2$-16), 1.36 – 1.21 (m, 10H, (C<u>H</u>$_2$)$_5$-17,18,19,20,21), 0.91 – 0.85 (m, 3H, C<u>H</u>$_2$-22); **^{13}C{^{1}H} NMR** (101 MHz, $CDCl_3$) δ 170.7, 170.6, 170.4, 170.0 (2C), 169.5, 169.3, 149.2, 118.8, 96.0, 85.2, 75.38, 75.35, 72.6, 71.0, 70.1, 69.3, 68.9, 68.0,. 62.7, 61.6, 31.9, 29.4, 29.3, 29.2 (2C), 25.7, 22.7, 20.9, 20.9, 20.8, 20.7, 20.3, 14.2; **HRMS** (ESI) *m/z* calcd for $C_{36}H_{54}O_{17}N_3$ $[M+H]^+$: 800.3448, found: 800.3441. Consistent with data in the literature.[22]

1-(Hepta-O-acetyl-1-deoxy-β-D-maltopyranosyl)-4-decyl triazole (2.5d)



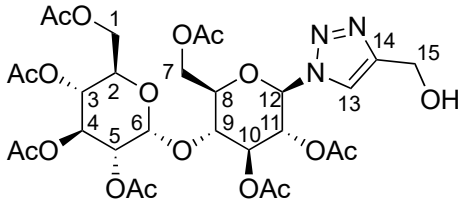
Chemical Formula: $C_{38}H_{57}N_3O_{17}$
Molecular Weight: 827.88

Synthesised according to general procedure 1 using maltose azide **2.4** (1.00 g, 1.51 mmol, 1.00 eq), CuI (6.0 mg, 0.032 mmol, 0.021 eq), DIPEA (10 μL, 0.060 mmol, 0.040 eq), AcOH (3.5 μL, 0.060 mmol, 0.040 eq) and 1-dodecyne (340 μL, 1.60 mmol, 1.06 eq). Flash column chromatography (50% EtOAc in hexane) provided 1-(hepta-O-acetyl-1-

deoxy-β-D-maltopyranosyl)-4-decyl triazole **2.5d** (1.01 g, 1.22 mmol, 81%) as a white foam.

^{1}H NMR (400 MHz, $CDCl_3$) δ 7.39 (s, 1H, C<u>H</u>-13), 5.83 (d, *J* = 9.3 Hz, 1H, C<u>H</u>-12), 5.45 – 5.40 (m, 2H, C<u>H</u>-6 and C<u>H</u>-10), 5.39 – 5.26 (m, 2H, C<u>H</u>-4 and C<u>H</u>-11), 5.04 (t, *J* = 9.9 Hz, 1H, C<u>H</u>-3), 4.85 (dd, *J* = 10.5, 4.0 Hz, 1H, C<u>H</u>-5), 4.45 (dd, *J* = 12.4, 2.4 Hz, 1H, C<u>H</u>$_a$H$_b$-7), 4.24 (t, *J* = 4.1 Hz, 1H, C<u>H</u>$_a$H$_b$-1), 4.21 (t, *J* = 4.1 Hz, 1H, CH$_a$<u>H</u>$_b$-7), 4.11 (dd, *J* = 9.8, 8.6 Hz, 1H, C<u>H</u>-9), 4.05 (dd, *J* = 12.5, 2.4 Hz, 1H, CH$_a$<u>H</u>$_b$-1), 3.95 (ddd, *J* = 10.0, 4.6, 2.5 Hz, 2H, C<u>H</u>-2 and C<u>H</u>-8), 2.66 (dd, *J* = 8.6, 6.7 Hz, 2H, C<u>H</u>$_2$-15), 2.10 (s, 3H, C<u>H</u>$_3$CO), 2.08 (s, 3H, C<u>H</u>$_3$CO), 2.04 (s, 3H, C<u>H</u>$_3$CO), 2.00 (s, 3H, C<u>H</u>$_3$CO), 2.00 (s, 3H, C<u>H</u>$_3$CO), 1.98 (s, 3H, C<u>H</u>$_3$CO), 1.81 (s, 3H, C<u>H</u>$_3$CO), 1.62 (p, *J* = 7.7 Hz, 2H, C<u>H</u>$_2$-16), 1.25 (m, 14H, (C<u>H</u>$_2$)$_7$-17-23), 0.84 (t, *J* = 6.7 Hz, 3H, C<u>H</u>$_2$-24); **^{13}C{^{1}H} NMR** (101 MHz, $CDCl_3$) δ 170.7, 170.6, 170.4, 169.98, 169.95, 169.5, 169.3, 149.2, 118.8, 96.0, 85.2, 75.4, 72.6, 71.0, 70.1, 69.3, 68.8, 68.0, 62.7, 61.6, 32.0, 29.7, 29.6, 29.42, 29.38, 29.2 (2C), 25.7, 22.8, 20.90, 20.85, 20.8, 20.7 (2C), 20.2, 14.2; **HRMS** (ESI) *m/z* calcd for $C_{38}H_{57}O_{17}N_3Na$ $[M+Na]^+$: 850.3580, found: 850.3563. Consistent with data in the literature.[22]

1-(Hepta-O-acetyl-1-deoxy-β-D-maltopyranosyl)-4-hydroxymethyl triazole (2.5e)



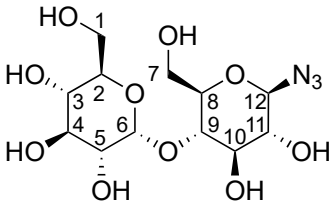
Chemical Formula: $C_{29}H_{39}N_3O_{18}$
Molecular Weight: 717.6340

Synthesised according to general procedure 1 using maltose azide **2.4** (1.00 g, 1.51 mmol, 1.00 eq), CuI (6.0 mg, 0.032 mmol, 0.021 eq), DIPEA (10 µL, 0.060 mmol, 0.040 eq), AcOH (3.5 µL, 0.060 mmol, 0.040 eq) and propargyl alcohol (96 µL, 1.7 mmol, 1.23 eq).

Flash column chromatography (50% EtOAc in hexane) provided 1-(hepta-O-acetyl-1-deoxy-β-D-maltopyranosyl)-4-hydroxymethyl triazole **2.5e** (755 mg, 1.05 mmol, 70%) as a white foam.

^{1}H NMR (400 MHz, $CDCl_3$) δ 7.70 (s, 1H, C<u>H</u>-13), 5.89 (d, *J* = 9.3 Hz, 1H, C<u>H</u>-12), 5.50 – 5.44 (m, 2H, C<u>H</u>-6 and C<u>H</u>-10), 5.41 – 5.31 (m, 2H, C<u>H</u>-4 and C<u>H</u>-11), 5.07 (t, *J* = 9.9 Hz, 1H, C<u>H</u>-3), 4.88 (dd, *J* = 10.5, 4.0 Hz, 1H, C<u>H</u>-5), 4.80 (d, *J* = 5.7 Hz, 2H, C<u>H</u>$_2$OH-15), 4.49 (dd, *J* = 12.5, 2.4 Hz, 1H, C<u>H</u>$_a$H$_b$-7), 4.28 – 4.22 (m, 2H, C<u>H</u>$_a$H$_b$-1 and CH$_a$<u>H</u>$_b$-7), 4.14 (m, 1H, C<u>H</u>-9), 4.07 (dd, *J* = 12.4, 2.3 Hz, 1H, CH$_a$<u>H</u>$_b$-1), 3.98 (m, 2H, C<u>H</u>-2 and C<u>H</u>-8), 2.19 (t, *J* = 6.1 Hz, 1H, CH$_2$O<u>H</u>-15), 2.13 (s, 3H, C<u>H</u>$_3$CO), 2.11 (s, 3H, C<u>H</u>$_3$CO), 2.06 (s, 3H, C<u>H</u>$_3$CO), 2.03 (s, 6H, C<u>H</u>$_3$CO and C<u>H</u>$_3$CO), 2.01 (s, 3H, C<u>H</u>$_3$CO), 1.86 (s, 3H, C<u>H</u>$_3$CO); **^{13}C{^{1}H} NMR** (101 MHz, $CDCl_3$) δ 170.7, 170.6, 170.5, 170.1 (2C), 169.6, 169.4, 120.2, 96.0, 85.4, 75.5, 75.3, 72.5, 71.1, 70.2, 69.4, 68.9, 68.1, 62.6, 61.6, 56.8, 21.0, 20.9, 20.8, 20.7 (3C), 20.4; **HRMS** (ESI) *m/z* calcd for $C_{29}H_{39}O_{18}N_3Na$ $[M+Na]^+$: 740.2121, found: 740.2111.

1-Deoxy-1-azido-β-D-maltopyranose (2.1)

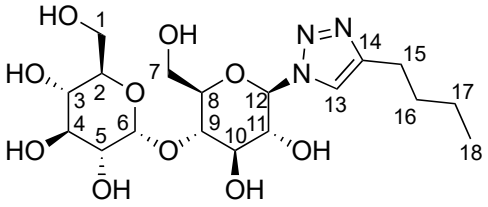


Chemical Formula: $C_{12}H_{21}N_3O_{10}$
Molecular Weight: 367.31

Synthesised according to general procedure 2 using protected maltose azide **2.4** (2.00 g, 3.02 mmol, 1.00 eq) and NaOMe (20 mg, 0.37 mmol, 0.12 eq). After concentration *in vacuo* 1-deoxy-1-azido-β-D-maltopyranose **2.1** (1.13 g, quantitative yield) was obtained as a hygroscopic, off-white foam.

^{1}H NMR (400 MHz, D_2O) δ 5.37 (d, *J* = 3.9 Hz, 1H, C<u>H</u>-6), 4.71 (d, *J* = 8.8 Hz, 1H, C<u>H</u>-12), 3.92 – 3.87 (m, 1H, C<u>H</u>-11), 3.81 (dd, *J* = 12.1, 2.1 Hz, 1H, C<u>H$_a$H$_b$</u>-7), 3.75 (ddd, *J* = 12.9, 4.3, 2.3 Hz, 2H, C<u>H$_a$H$_b$</u>-1 and CH$_a$<u>H$_b$</u>-7), 3.71 – 3.61 (m, 6H, CH$_a$<u>H$_b$</u>-1 and C<u>H</u>-2 and C<u>H</u>-4 and C<u>H</u>-8 and C<u>H</u>-9 and C<u>H</u>-10), 3.53 (dd, *J* = 9.9, 3.9 Hz, 1H, C<u>H</u>-5), 3.37 (t, *J* = 9.4 Hz, 1H, C<u>H</u>-3), 3.25 (t, *J* = 9.1 Hz, 1H C<u>H</u>-11); **^{13}C{^{1}H} NMR** (101 MHz, D_2O) δ 99.5, 89.9, 76.4, 76.1, 76.0, 72.7, 72.6 (2C), 71.6, 69.2, 60.42, 60.37; **HRMS** (ESI) *m/z* calcd for $C_{12}H_{20}O_{10}N_3$ [M-H]$^-$: 366.1154, found: 366.1153. Consistent with reported literature values.[22]

1-(1-Deoxy-β-D-maltopyranosyl)-4-butyl triazole (2.3a)



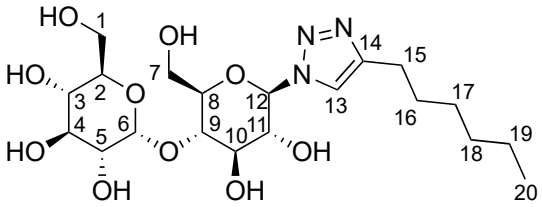
Chemical Formula: $C_{18}H_{31}N_3O_{10}$
Molecular Weight: 449.46

Synthesised according to general procedure 2 using protected surfactant **2.5a** (986 mg, 1.33 mmol, 1.00 eq) and NaOMe (40 mg, 0.74 mmol, 0.56 eq). After concentration *in vacuo* surfactant 1-(1-deoxy-β-D-maltopyranosyl)-4-butyl triazole **2.3a** (422 mg, 0.939 mmol, 71%) was obtained as a hygroscopic, off-white foam.

^{1}H NMR (400 MHz, D_2O) δ 7.89 (s, 1H, C<u>H</u>-13), 5.62 – 5.58 (m, 1H, C<u>H</u>-12), 5.36 (d, *J* = 3.9 Hz, 1H, C<u>H</u>-6), 3.90 – 3.85 (m, 2H, C<u>H</u>-11 and C<u>H</u>-4), 3.79 (d, *J* = 11.6 Hz, 1H, C<u>H$_a$H$_b$</u>-7), 3.78 – 3.70 (m, 5H, CH$_a$<u>H$_b$</u>-7 and C<u>H$_a$H$_b$</u>-1 and CH$_a$<u>H$_b$</u>-1 and C<u>H</u>-2 and C<u>H</u>-10), 3.69 – 3.56 (m, 3H, C<u>H</u>4 and C<u>H</u>-8 and C<u>H</u>-9), 3.48 (dd, *J* = 9.9, 3.9 Hz, 1H, C<u>H</u>-5), 3.31 (t, *J* = 9.4 Hz, 1H, C<u>H</u>-3), 2.62 (t, *J* = 7.4 Hz, 2H, C<u>H</u>-15), 1.51 (p, *J* = 7.5 Hz, 2H, C<u>H$_2$</u>-16), 1.25 – 1.13 (m, 2H, C<u>H$_2$</u>-17), 0.77 (t, *J* = 7.4 Hz, 3H, C<u>H$_3$</u>-18); **^{13}C{^{1}H} NMR** (101 MHz, D_2O) δ 148.9, 122.2, 99.5, 87.1, 77.4, 76.3, 75.6, 72.74, 72.68, 72.0, 71.6,

69.2, 60.4, 60.3, 30.5, 24.0, 21.3, 12.9; **HRMS** (ESI) *m/z* calcd for $C_{18}H_{31}O_{10}N_3Na$ $[M+Na]^+$: 472.1902, found: 472.1900; **IR** (ATR) ν (cm^{-1}) thin film, MeOH: 3350 (s), 2931 (m), 2360 (w), 1653 (w), 1457 (m), 1041 (s); $\mathbf{[\alpha]^{25}_D}$ = +73.6 (c = 1.00, MeOH).

1-(1-Deoxy-β-D-maltopyranosyl)-4-hexyl triazole (2.3b)

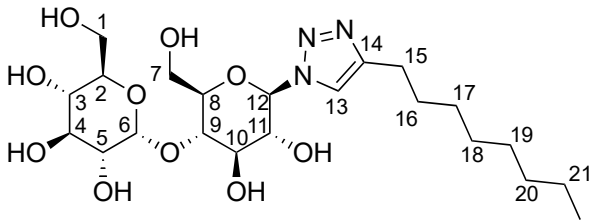


Chemical Formula: $C_{20}H_{35}N_3O_{10}$
Molecular Weight: 477.51

Synthesised according to general procedure 2 using protected surfactant **2.5b** (782 mg, 1.01 mmol, 1.00 eq) and NaOMe (20 mg, 0.37 mmol, 0.37 eq). After concentration *in vacuo* 1-(1-deoxy-β-D-maltopyranosyl)-4-hexyl triazole **2.3b** (405 mg, 0.848 mmol, 84%) was obtained as a hygroscopic, off-white foam.

^{1}H NMR (400 MHz, D_2O) δ 7.85 (s, 1H, C<u>H</u>-13), 5.60 – 5.55 (m, 1H, C<u>H</u>-12), 5.34 (d, *J* = 3.9 Hz, 1H, C<u>H</u>-6), 3.92 – 3.54 (m, 10H, C<u>H</u>-11, C<u>H</u>-10, C<u>H</u>$_2$-1, C<u>H</u>$_2$-7, C<u>H</u>$_2$-3, C<u>H</u>-4, C<u>H</u>-8, C<u>H</u>-9), 3.47 (dd, *J* = 9.9, 3.8 Hz, 1H, C<u>H</u>-5), 3.31 (t, *J* = 9.3 Hz, 1H, C<u>H</u>-2), 2.55 (t, *J* = 7.5 Hz, 2H, C<u>H</u>$_2$-15), 1.49 (t, *J* = 7.2 Hz, 2H, C<u>H</u>$_2$-16), 1.46 –1.25 (m, 6H, (C<u>H</u>$_2$)$_3$-17,18,19), 0.71 (d, *J* = 6.5 Hz, 3H, C<u>H</u>$_3$-20); **^{13}C{^{1}H} NMR** (101 MHz, D_2O) δ 122.1, 99.6, 87.2, 77.4, 76.4, 75.8, 72.8, 72.7, 72.1, 71.6, 69.2, 60.4, 60.3, 30.9, 28.4, 28.0, 24.5, 22.0, 13.4; **HRMS** (ESI) *m/z* calcd for $C_{20}H_{36}O_{10}N_3$ $[M+H]^+$: 478.2395, found: 478.2392. Consistent with data in the literature.[22]

1-(1-Deoxy-β-D-maltopyranosyl)-4-octyl triazole (2.3c)

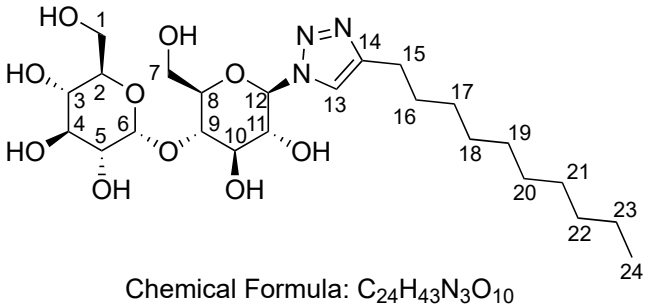


Chemical Formula: $C_{22}H_{39}N_3O_{10}$
Molecular Weight: 505.57

Synthesised according to general procedure 2 using protected surfactant **2.5c** (2.15 g, 2.79 mmol, 1.00 eq) and NaOMe (40 mg, 0.74 mmol, 0.27 eq). After concentration *in vacuo* 1-(1-deoxy-β-D-maltopyranosyl)-4-octyl triazole **2.3c** (1.30 g, 2.58 mmol, 92%) was obtained as a hygroscopic, off white foam.

^{1}H NMR (400 MHz, D_2O) δ 7.85 (s, 1H, C<u>H</u>-13), 5.50 (d, *J* = 7.7 Hz, 1H, C<u>H</u>-12), 5.33 – 5.27 (m, 1H, C<u>H</u>-6), 3.90 – 3.68 (m, 4H, C<u>H</u>-11 and C<u>H</u>-10 and $CH_a\underline{H}_b$-7 and $C\underline{H}_aH_b$-1), 3.68 – 3.48 (m, 6H, $CH_a\underline{H}_b$-7 and $CH_a\underline{H}_b$-1 and C<u>H</u>-3 and C<u>H</u>-4 and C<u>H</u>-8 and C<u>H</u>-9), 3.47 – 3.38 (m, 1H, C<u>H</u>-5), 3.34 – 3.27 (m, 1H, C<u>H</u>-2,), 2.42 (m, 2H, $C\underline{H}_2$-15), 1.43 (m, 2H, $C\underline{H}_2$-16), 1.13 (m, 10H, $(C\underline{H}_2)_5$-17,18,19,20,21), 0.72 (t, *J* = 6.0 Hz, 3H, $C\underline{H}_3$-22); **^{13}C{^{1}H} NMR** (101 MHz, D_2O) δ 147.8, 125.7, 99.9, 87.3, 77.4, 76.4 (2C), 72.8 (2C), 72.1, 72.0, 69.1, 62.4, 60.4, 31.8, 29.2 (3C), 28.8, 25.0, 22.5, 13.7; **HRMS** (ESI) *m/z* calcd for $C_{22}H_{39}O_{10}N_3Na$ $[M+Na]^+$: 528.2528, found: 528.2525. Consistent with reported literature values.[22]

1-(1-Deoxy-β-D-maltopyranosyl)-4-decyl triazole (2.3d)

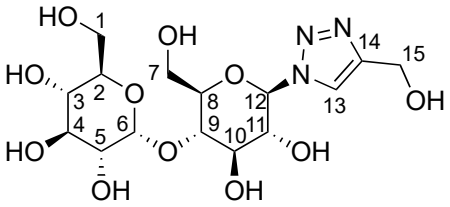


Chemical Formula: $C_{24}H_{43}N_3O_{10}$
Molecular Weight: 533.62

Synthesised according to general procedure 2 using protected surfactant **2.5d** (1.09 g, 1.32 mmol, 1.00 eq) and NaOMe (40 mg, 0.74 mmol, 0.56 eq). After concentration *in vacuo* 1-(1-deoxy-β-D-maltopyranosyl)-4-decyl triazole **2.3d** (643 mg, 1.20 mmol, 92%) was obtained as a hygroscopic, off white foam.

^{1}H NMR (400 MHz, MeOD) δ 7.94 (s, 1H, C<u>H</u>-13), 5.56 (d, *J* = 9.1 Hz, 1H, C<u>H</u>-12), 5.20 (d, *J* = 3.8 Hz, 1H, C<u>H</u>-6), 3.91 (t, *J* = 9.1 Hz, 1H, C<u>H</u>-11), 3.83 – 3.77 (m, 4H, C<u>H</u>$_a$H$_b$-1 and C<u>H$_2$</u>-7 and C<u>H</u>-11), 3.75 – 3.68 (m, 1H, CH$_a$<u>H$_b$</u>-1), 3.68 – 3.62 (m, 3H, C<u>H</u>-3 and C<u>H</u>-4 and C<u>H</u>-8), 3.62 – 3.57 (m, 1H, C<u>H</u>-9), 3.44 (dd, *J* = 9.7, 3.7 Hz, 1H, C<u>H</u>-5), 3.27 (t, *J* = 9.3 Hz, 1H, C<u>H</u>-2), 2.67 (t, *J* = 7.6 Hz, 2H, C<u>H$_2$</u>-15), 1.68 – 1.58 (m, 2H, C<u>H$_2$</u>-16), 1.36 – 1.19 (m, 14,H, (C<u>H$_2$</u>)$_7$-17-23), 0.88 – 0.83 (m, 3H, C<u>H$_3$</u>-24); **^{13}C{^{1}H} NMR** (101 MHz, MeOD) δ 122.52, 102.90, 89.34, 80.25, 79.54, 78.23, 75.04, 74.85, 74.15, 73.54, 71.45, 62.70, 61.81, 33.05, 30.73, 30.68, 30.49 (2C), 30.45, 30.26, 26.26, 23.72, 14.44; **HRMS** (ESI) *m/z* calcd for $C_{24}H_{43}O_{10}N_3Na$ $[M+Na]^+$: 556.2841, found: 556.2841. Consistent with data in the literature.[22]

1-(1-Deoxy-β-D-maltopyranosyl)-4-hydroxymethyl triazole (2.3e)



Chemical Formula: $C_{15}H_{25}N_3O_{11}$
Molecular Weight: 423.3750

Synthesised according to general procedure 2 using protected surfactant **2.5e** (755 mg, 1.05 mmol, 1.00 eq) and NaOMe (20 mg, 0.37 mmol, 0.35 eq). After concentration *in vacuo* 1-(1-deoxy-β-D-maltopyranosyl)-4-hydroxymethyl triazole **2.3e** (338 mg, 0.798 mmol, 76%) was obtained as a hygroscopic, off white foam.

^{1}H NMR (400 MHz, MeOD) δ 8.13 (s, 1H, C<u>H</u>-13), 5.61 (d, *J* = 9.1 Hz, 1H, C<u>H</u>-12), 5.22 (d, *J* = 3.8 Hz, 1H, C<u>H</u>-6), 4.68 (bs, 2H, C<u>H</u>$_2$OH-15), 3.92 (t, *J* = 9.1 Hz, 1H, C<u>H</u>-11), 3.89 – 3.78 (m, 4H, C<u>H</u>$_a$H$_b$-1 and C<u>H</u>$_2$-7 and C<u>H</u>-11), 3.74 (t, *J* = 9.0 Hz, 1H, CH$_a$<u>H</u>$_b$-1), 3.70 – 3.65 (m, 2H, C<u>H</u>-3 and C<u>H</u>-8), 3.65 – 3.57 (m, 2H, C<u>H</u>-4 and C<u>H</u>-9), 3.45 (dd, *J* = 9.7, 3.8 Hz, 1H, C<u>H</u>-5), 3.26 – 3.23 (m, 1H, CH$_2$O<u>H</u>-15); **^{13}C{^{1}H} NMR** (101 MHz, MeOD) δ 147.58, 122.05, 101.55, 88.10, 78.87, 78.23, 76.81, 73.67, 73.49, 72.78, 72.23, 70.08, 61.33, 60.43, 54.95; **HRMS** (ESI) *m/z* calcd for $C_{15}H_{25}O_{11}N_3Na$ $[M+Na]^+$: 446.1381, found: 446.1379.

2.5.3 Fluorimetry Data

The critical micelle concentrations of the surfactants was determined with a fluorimetric procedure reported by London *et al*.[23] The fluorescent molecule 1,6-diphenyl-1,3,5-hexatriene (DPH) emits a large increase in fluorescence when present in an apolar environment such as the micellar interior when a surfactant exceeds the critical micelle concentration. This property was used to determine the unknown CMC of various surfactant compounds. Fluorescence measurements were made with an Edinburgh Instruments Spectrofluorometer FS5 model. Instrument control and data processing were performed using Fluoracle software. The excitation wavelength was 358 nm and the emission wavelength was 430 nm. The excitation and emission slits were set at bandwidths of 1 nm. In all experiments, 1 cm path length quartz cuvettes were used. The protocol for CMC determination was as follows: 3 μL of 5 mM DPH dissolved in THF was added to various amounts of surfactant dissolved in a total volume of 3 ml of aqueous solution. The intercept of two trendlines, through the data points before and after the spike in fluorescence, was taken as the CMC.

Note: No increase in fluorescence was observed for surfactant **3a** indicating that a 4-carbon aliphatic tail is likely too short to induce aggregation.

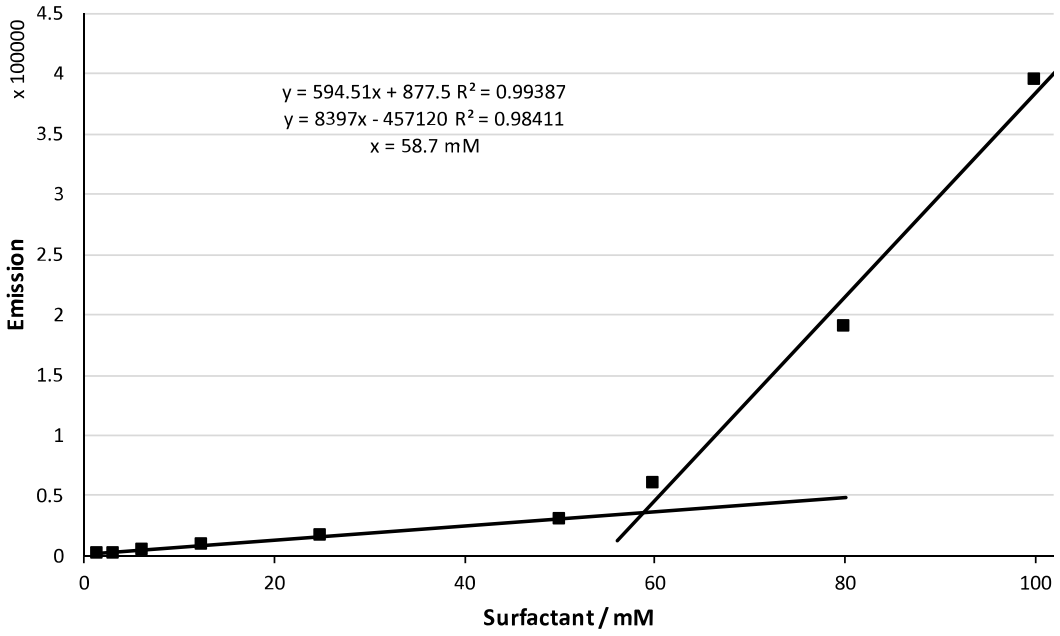


Figure 2.12 CMC of 58.7 mM was extracted from a plot of fluorescence measurements at various concentrations for surfactant **2.3b.**

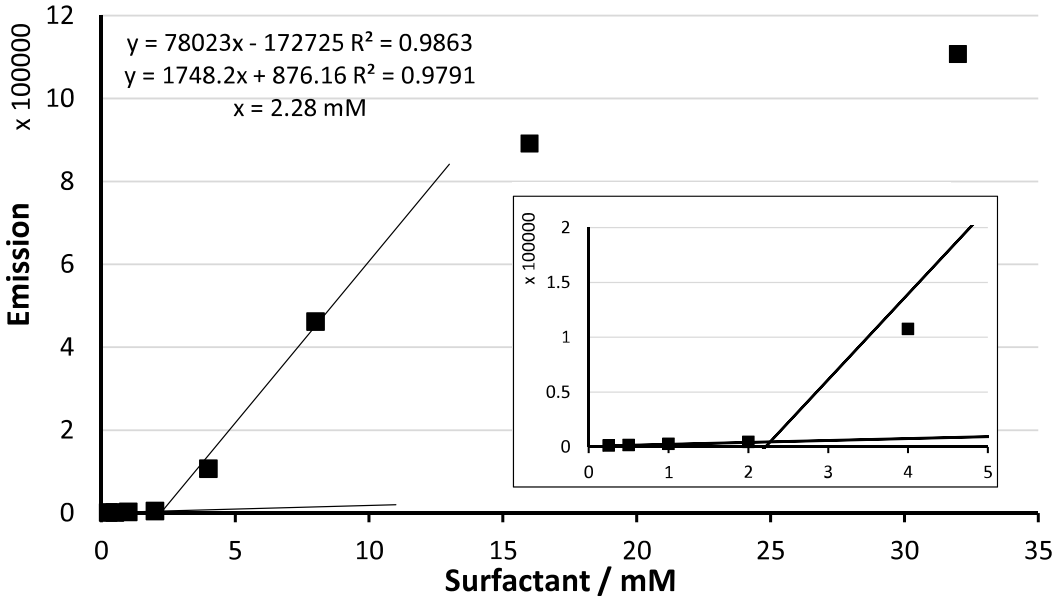


Figure 2.13 CMC of 2.28 mM was extracted from a plot of fluorescence measurements at various concentrations for surfactant **2.3c.**

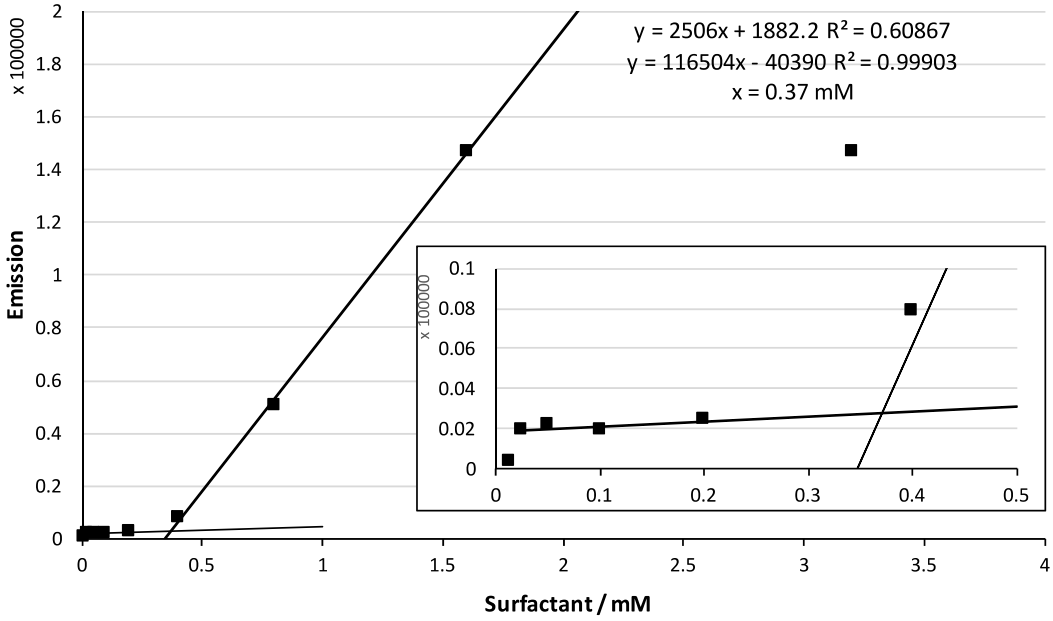


Figure 2.14 CMC of 0.37 mM was extracted from a plot of fluorescence measurements at various concentrations for surfactant **2.3d.**

2.5.4 DLS data

Samples were prepared by dissolving an amount of surfactant in 1 mL of ultrapure Milli-Q water at a concentration above the CMC. This solution was filtered through a 0.2 µm PTFE filter right before performing a DLS measurement.

Note: DLS results for surfactant **2.3a** showed no aggregation around 10 nm only around 100 nm which can likely be attributed to noise. This agrees with the fluorimetry data and indicates that a 4-carbon aliphatic tail is too short to induce aggregation.

Sample Name:	EPoctyne52mM 1		
SOP Name:	Standard method.sop		
File Name:	Hexyne+Dodecyne surfactants 08-02-2...	**Dispersant Name:**	Water
Record Number:	11	**Dispersant RI:**	1.330
Material RI:	1.45	**Viscosity (cP):**	0.8872
Material Absorbtion:	0.001	**Measurement Date and Time:**	08 February 2017 10:39 am

Temperature (°C):	25.0	**Duration Used (s):**	70
Count Rate (kcps):	246.6	**Measurement Position (mm):**	3.00
Cell Description:	Disposable micro cuvette (40µl)	**Attenuator:**	9

			Size (d.nm):	**% Intensity:**	**St Dev (d.nm):**
Z-Average (d.nm):	6.744	**Peak 1:**	7.168	93.4	2.824
PdI:	0.238	**Peak 2:**	3533	6.6	1226
Intercept:	0.758	**Peak 3:**	0.000	0.0	0.000
Result quality :	Good				

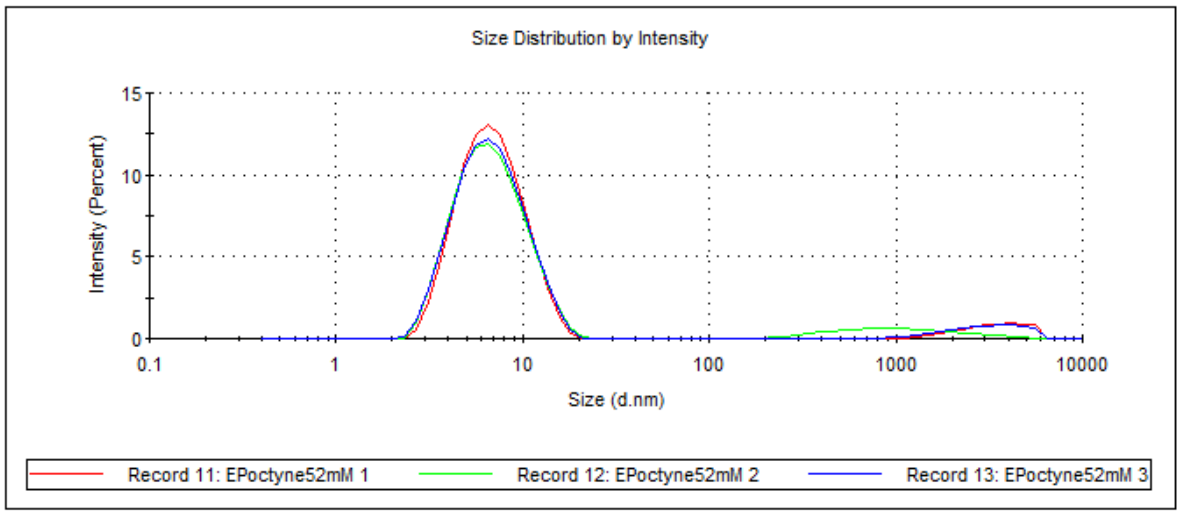


Figure 2.15 The size distribution by intensity of a DLS measurement of surfactant **2.3b** at 52 mM indicates micelle aggregates with a size of around 7 nm.

Sample Name:	EP_decyne_24mM 1		
SOP Name:	mansettings.nano		
File Name:	Sarah.dts	**Dispersant Name:**	Water
Record Number:	61	**Dispersant RI:**	1.330
Material RI:	1.59	**Viscosity (cP):**	0.8872
Material Absorbtion:	0.010	**Measurement Date and Time:**	19 December 2016 1:45 pm

Temperature (°C):	25.0	**Duration Used (s):**	60
Count Rate (kcps):	377.7	**Measurement Position (mm):**	3.00
Cell Description:	Disposable micro cuvette (40µl)	**Attenuator:**	11

			Size (d.nm):	**% Intensity:**	**St Dev (d.nm):**
Z-Average (d.nm):	6.983	**Peak 1:**	7.541	90.5	3.117
PdI:	0.260	**Peak 2:**	1543	9.5	960.0
Intercept:	0.730	**Peak 3:**	0.000	0.0	0.000

Result quality : Good

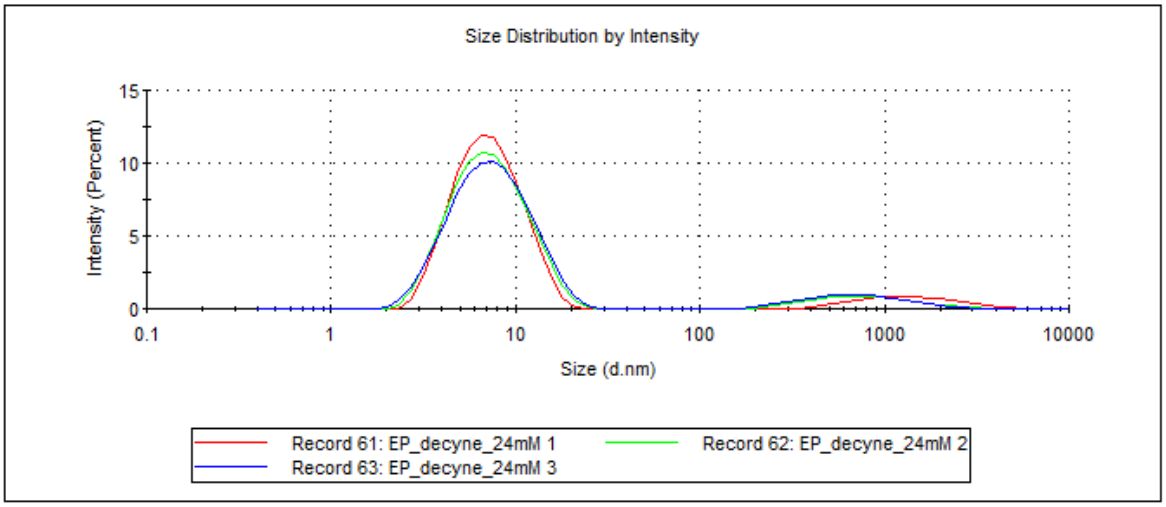


Figure 2.16 The size distribution by intensity of a DLS measurement of surfactant **2.3c** at 24 mM indicates micelle aggregates with a size of around 7.5 nm.

Sample Name:	EPdodecyne5mMGeldiluted 1		
SOP Name:	Standard method.sop		
File Name:	Hexyne+Dodecyne surfactants 08-02-2...	**Dispersant Name:**	Water
Record Number:	20	**Dispersant RI:**	1.330
Material RI:	1.45	**Viscosity (cP):**	0.8872
Material Absorbtion:	0.001	**Measurement Date and Time:**	08 February 2017 11:14 am

Temperature (°C):	25.1	**Duration Used (s):**	80
Count Rate (kcps):	114.3	**Measurement Position (mm):**	3.00
Cell Description:	Disposable micro cuvette (40µl)	**Attenuator:**	11

			Size (d.nm):	**% Intensity:**	**St Dev (d.nm):**
Z-Average (d.nm):	11.67	**Peak 1:**	14.59	100.0	7.195
PdI:	0.193	**Peak 2:**	0.000	0.0	0.000
Intercept:	0.731	**Peak 3:**	0.000	0.0	0.000

Result quality : Good

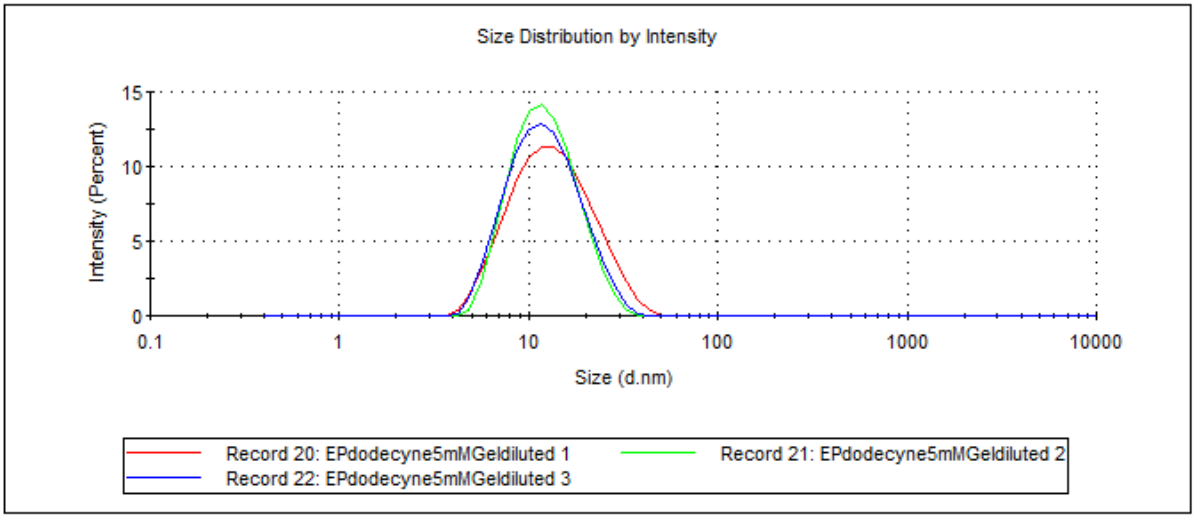


Figure 2.17 The size distribution by intensity of a DLS measurement of surfactant **2.3d** at 5 mM indicates micelle aggregates with a size range distributed around 15 nm.

2.6 References

1 E. A. J. Post, A. J. Bissette and S. P. Fletcher, Self-reproducing micelles coupled to a secondary catalyst, *Chem. Commun.*, 2018, **54**, 8777–8780.

2 A. J. Bissette, B. Odell and S. P. Fletcher, Physical autocatalysis driven by a bond-forming thiol–ene reaction, *Nat. Commun.*, 2014, **5**, 4607.

3 A. J. Bissette and S. P. Fletcher, Mechanisms of autocatalysis, *Angew. Chemie - Int. Ed.*, 2013, **52**, 12800–12826.

4 P. A. Bachmann, P. L. Luisi and J. Lang, Autocatalytic self-replicating micelles as models for prebiotic structures, *Nature*, 1992, **357**, 57–59.

5 P. Stano and P. L. Luisi, Achievements and open questions in the self-reproduction of vesicles and synthetic minimal cells, *Chem. Commun.*, 2010, **46**, 3639–3653.

6 K. Ruiz-Mirazo, C. Briones and A. de la Escosura, Prebiotic Systems Chemistry: New Perspectives for the Origins of Life, *Chem. Rev.*, 2014, **114**, 285–366.

7 K. Takakura, T. Toyota and T. Sugawara, A novel system of self-reproducing giant vesicles, *J. Am. Chem. Soc.*, 2003, **125**, 8134–8140.

8 M. Meldal and C. W. Tornøe, Cu-Catalyzed Azide−Alkyne Cycloaddition, *Chem. Rev.*, 2008, **108**, 2952–3015.

9 M. D. Hardy, J. Yang, J. Selimkhanov, C. M. Cole, L. S. Tsimring and N. K. Devaraj, Self-reproducing catalyst drives repeated phospholipid synthesis and membrane growth, *Proc. Natl. Acad. Sci.*, 2015, **112**, 8187–8192.

10 D. G. Blackmond, An Examination of the Role of Autocatalytic Cycles in the Chemistry of Proposed Primordial Reactions, *Angew. Chemie Int. Ed.*, 2009, **48**, 386–390.

11 R. Batchelor, P. T. Northcote and J. E. Harvey, Stereochemical Control in Carbohydrate Chemistry, *J. Chem. Educ.*, 2008, **85**, 689–691.

12 V. Neto, R. Granet and P. Krausz, Novel class of non-ionic monocatenary and bolaform alkylglycoside surfactants. Synthesis by microwave-assisted glycosylation and olefin cross-metathesis or by 'click-chemistry': physicochemical studies, *Tetrahedron*, 2010, **66**, 4633–4646.

13 E. Mahon, T. Aastrup and M. Barboiu, Dynamic glycovesicle systems for amplified QCM detection of carbohydrate-lectin multivalent biorecognition, *Chem. Commun.*, 2010, **46**, 2441.

14 A. Baron, Y. Blériot, M. Sollogoub and B. Vauzeilles, Phenylenediamine catalysis of "click glycosylations" in water: practical and direct access to unprotected neoglycoconjugates, *Org. Biomol. Chem.*, 2008, **6**, 1898.

15 C. McAuliffe, Solubility in Water of Paraffin, Cycloparaffin, Olefin, Acetylene, Cycloolefin, and Aromatic Hydrocarbons [1], *J. Phys. Chem.*, 1966, **70**, 1267–1275.

16 T. R. Chan, R. Hilgraf, K. B. Sharpless and V. V Fokin, Polytriazoles as Copper(I)-Stabilizing Ligands in Catalysis, *Org. Lett.*, 2004, **6**, 2853–2855.

17 R. Evans, Z. Deng, A. K. Rogerson, A. S. McLachlan, J. J. Richards, M. Nilsson and G. A. Morris, Quantitative interpretation of diffusion-ordered NMR spectra: Can we rationalize small molecule diffusion coefficients?, *Angew. Chemie - Int. Ed.*, 2013, **52**, 3199–3202.

18 F. Mavelli and P. L. Luisi, Autopoietic Self-Reproducing Vesicles: A Simplified Kinetic Model, *J. Phys. Chem.*, 1996, **100**, 16600–16607.

19 T. Buhse, R. Nagarajan, D. Lavabre and J. C. Micheau, Phase-transfer model for the dynamics of '"micellar autocatalysis"', *J. Phys. Chem. A*, 1997, **101**, 3910–3917.

20 T. Buhse, D. Lavabre, R. Nagarajan and J. C. Micheau, Origin of autocatalysis in the biphasic alkaline hydrolysis of C-4 to C-8 ethyl alkanoates, *J. Phys. Chem. A*, 1998, **102**, 10552–10559.

21 C. Shao, X. Wang, Q. Zhang, S. Luo, J. Zhao and Y. Hu, Acid-base jointly promoted copper(I)-catalyzed azide-alkyne cycloaddition, *J. Org. Chem.*, 2011, **76**, 6832–6836.

22 A. J. Bissette, University of Oxford, 2015.

23 A. Chattopadhyay and E. London, Fluorimetric determination of critical micelle concentration avoiding interference from detergent charge, *Anal. Biochem.*, 1984, **139**, 408–412.

Chapter 3 Controlling the Kinetics of Self-Reproducing Micelles by Catalyst Compartmentalization in a Biphasic System

The results of this chapter have been published in *The Journal of Organic Chemistry*.[1] All experiments were designed and performed by Elias Post under the supervision of Prof. Stephen Fletcher.

3.1 Introduction

The autocatalytic system developed in Chapter 2 successfully linked physical autocatalysis to a secondary catalytic cycle. Some preliminary investigations into the mechanism of this reaction were performed but the secondary catalyst was not yet effectively utilised to drive new reaction outcomes. This chapter delves into how the polarity of the copper ligand can be used to control the spatial location of the catalyst which enables compartmentalisation of the reaction and ultimately influences the kinetics of the system.

Nano- or micro-scale environments such as micelles, vesicles, and emulsion droplets can be employed to perform compartmentalized reactions.[2] When these compartments are used as nanoreactors, the higher effective concentrations and phase separation of specific reagents can offer increased reaction rates and control in a heterogenous setting.[3] Living cells utilise compartmentalization to control complex multi-step reactions. NADPH metabolism relies on physical separation between chemical steps along the metabolic pathway[4], whereas reactions take place in three different intracellular compartments during gluconeogenesis.[5,6] Our understanding of biochemical processes may advance through the study of compartmentalized reactions and new ways to control chemical reactivity may emerge.[7–9]

Lipid aggregates are often used to model cellular membranes[10–12] and can undergo complex supramolecular transformations such as deformation and division.[13–16] Chemical self-reproduction of micelles and vesicles drives growth and division processes.[17–19] The system of self-reproducing giant vesicles developed by Sugawara and co-workers as described in Chapter 1 is one of the rare examples where self-reproduction is driven by a secondary catalyst.[20] In this case dehydrocondensation between a lipophilic aniline

precursor and amphiphilic aldehyde is catalysed by an amphiphilic acid catalyst. However, in their system compartmentalization of the secondary catalyst cannot be controlled which would be required to develop and study more sophisticated reaction networks.

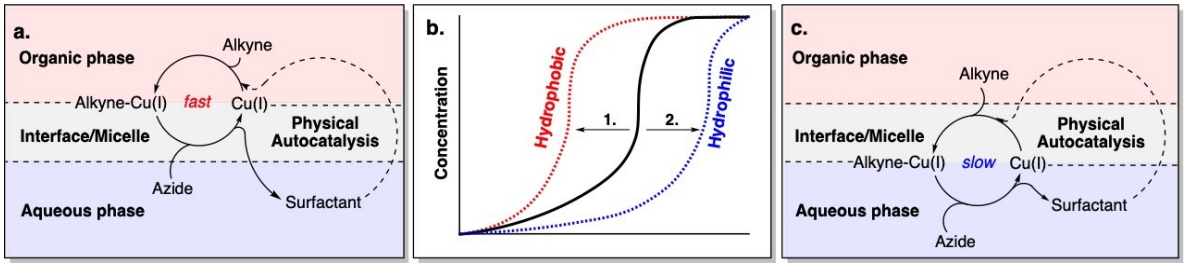


Figure 3.1 a. Hydrophobic Cu-ligand promotes retention of Cu-catalyst in the organic phase leading to faster turnover. **b.** Representation of how tuning the hydrophilicity of the catalyst alters reaction kinetics. (1) A hydrophobic ligand leads to a shorter lag period and higher rate while (2) a hydrophilic ligand retards the reaction. **c.** Hydrophilic Cu-ligand retains the Cu-catalyst in the aqueous phase and slows turnover.

Here we show how tuning the solubility properties of a Cu-catalyst controls the kinetic behaviour of self-reproducing lipid aggregates. Relative to the system reported in Chapter 2, the introduction of a hydrophobic ligand accelerates turnover of the catalytic cycle, whereas the hydrophilic variant slows the reaction down (Figure 3.1a-c). Additionally, different combinations of hydrophobic and hydrophilic alkyne/azide coupling partners are investigated, leading to a wide range of reactivity patterns. Phase behaviour of all reaction components and how compartmentalization influences the location of catalyst are considered to rationalize the different reaction outcomes. A mechanistic model is formulated to explain how these differing conditions lead to widely varying autocatalytic efficiencies. A novel system based on a phosphocholine polar headgroup is developed and studied to test how accurately the mechanistic model predicts autocatalytic efficiency.

3.2 Controlling catalyst compartmentalization by tuning ligand polarity

New ligands of varying hydrophobicity were synthesised to alter the solubility properties of the Cu-catalyst with the goal of controlling the spatial location of the reaction. Tristriazole ligands stabilize Cu(I) towards oxidation and disproportionation, and accelerate the rate of CuAAC relative to free copper.[21] Interestingly, this class of ligands was discovered when the kinetic study of CuAAC on polyvalent substrates indicated autocatalytic product formation[22], the mechanism which this occurs was recently elucidated.[23]

As previously discussed, Devaraj and co-workers exploited the autocatalytic nature of tristriazole compounds to drive membrane growth, and to generate self-assembling peptide nanomaterials.[24,25] Polytriazole ligands are effective in water since they bind weakly to copper, contrary to strongly coordinating ligands that inhibit reaction by blocking the azide from reaching the metal centre.[26] Additionally, these ligands prevent formation of unreactive polynuclear copper acetylides.[27–29] Solubility properties can easily be varied by altering the azide coupling partner during ligand synthesis, without affecting catalytic activity of the final ligand-copper complex.

The coupling conditions of the system investigated in this Chapter are identical to those reported in Chapter 2: maltose azide **3.1** reacts with hydrophobic aliphatic alkyne **3.2** via a CuAAC to form surfactant **3.3** (Figure 3.2a). The data of the unseeded reaction with ligand **A** is reproduced (Figure 3.2b; green circles) for comparison, whereas for the seeded reaction data for addition of 22 mM of **3.3** is reported (Figure 3.2c; green circles). Two known tristriazole ligands were selected for study: one strongly hydrophilic due to three

alcohol groups (ligand **B**, blue triangles) and one hydrophobic due to three benzyl moieties (ligand **C**, red diamonds) to compare with the previously investigated ligand **A**.

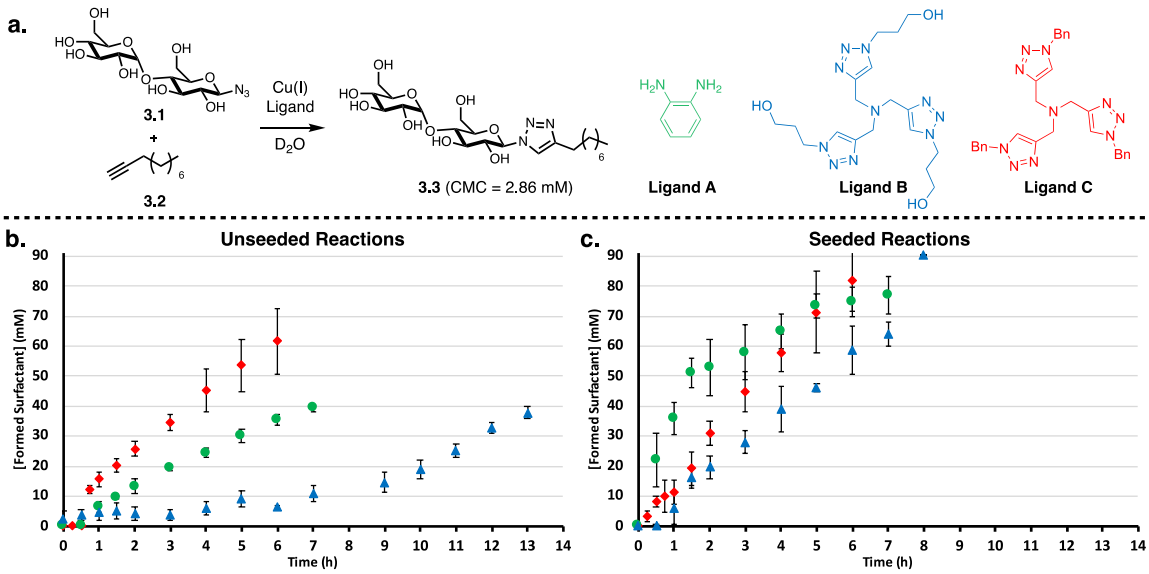


Figure 3.2 a. Maltose azide **3.1** is coupled to alkyne **3.2** via a CuAAC reaction to form surfactant **3.3** with ligands of varying structure. **b.** Kinetic results showing the influence of the ligands, **A** (green circles), **B** (blue triangles) and **C** (red diamonds), on the rate of conversion. Increased hydrophobicity of the ligand results in higher rates of product formation. **c.** Seeding the reaction with 22 mM of **3.3** eliminates the lag period and gives higher reaction rates for all ligands. The reaction is monitored by consumption of azide **3.1** and formation of surfactant **3.3** by ^{1}H NMR spectroscopy. Points are the mean of three independent experiments and the error bars are the standard deviation (n=3).

Under unseeded conditions, ligand **C** accelerates the reaction almost twofold relative to ligand **A** (Figure 3.2b; Section 3.7.5 for extracted reaction rates). Conversely, ligand **B** slows the reaction down with a longer lag period and gradual initial product formation. Seeding the reaction with 22 mM of product affects each ligand differently. Ligand **A** experiences the strongest, product-induced rate acceleration and has the highest initial rate of the three reactions (Figure 3.2c; Section 3.7.5 for extracted reaction rates). Ligand **B** experienced a ~2x rate increase compared to unseeded reaction. Surprisingly, this seeded reaction retained a 30 minute lag period without any gradual initial product formation. Meanwhile, hydrophobic ligand **C** does not benefit significantly from addition of product and experiences only a modest increase in rate over the unseeded reaction, even though the lag period is eliminated.

3.2.1 Influence of ligand B on the lag period

We investigated why the unseeded reaction with ligand **B** experienced gradual initial product formation (up to 10 mM) during the lag period. This was novel kinetic behaviour not previously observed in the Fletcher group. Normally product concentration stays near zero during the lag period before quickly increasing once the autocatalytic mechanism starts to operate.

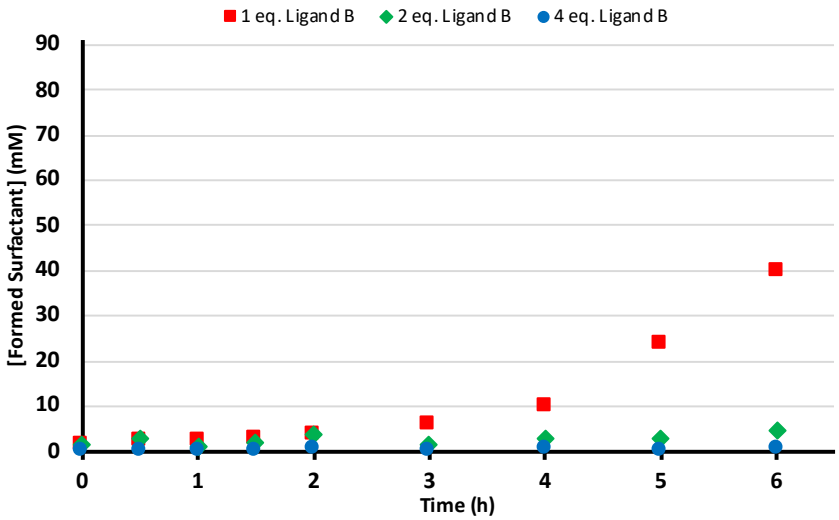


Figure 3.3 Control experiments investigating the influence of varying amounts ligand **B** on the lag period during CuAAC of maltose azide **3.1** with **3.2** (n=1). One equivalent of **B** (red squares) increases the rate relative to the original 2 equivalents (green diamonds). Increasing to four equivalents of ligand **B** (blue circles) results in no product formation during the first 6 hours. An increase in the amount of ligand added, slows down the reaction and increases the duration of the lag period.

The influence of ligand **B** on initial product formation was probed by varying the amount of **B** added (Figure 3.3). The length of the lag period and the overall reaction time correlated directly to the concentration of ligand. Lowering to one equivalent greatly accelerated the reaction, whereas increasing to four equivalents of ligand shut down the reaction with no product formation during the first six hours (after 5 days approximately 10% conversion was observed). This could be caused by inhibitive binding of ligand **B** to copper at higher concentrations slowing down turnover. Overall, gradual initial product

formation appears to be caused by an excess of ligand **B** which inhibits reaction at higher concentrations.

3.2.2 Control Experiments

Similar to the control experiment in Chapter 2, reaction with ligand **B** or **C** was repeated in a 1 : 1 water/*tert*-butanol mixture to facilitate phase mixing (Figure 3.4). This solvent system largely eliminates phase-behaviour in the system and allows for a direct comparison between the inherent reactivities of ligand **B** and **C**. Under these conditions lag periods were eliminated and reaction was accelerated to comparative rates for all three ligands, going to completion within 2 hours in all cases. Phase behaviour appears to be responsible for the lag period and slower kinetics observed, and the ligands have a similar reactivity in the absence of phase separation. Interestingly, when no ligand was added (yellow triangles) the reaction shut down in the first 15 minutes indicating catalyst deactivation occurs rapidly, likely due to oxidation of copper.[30]

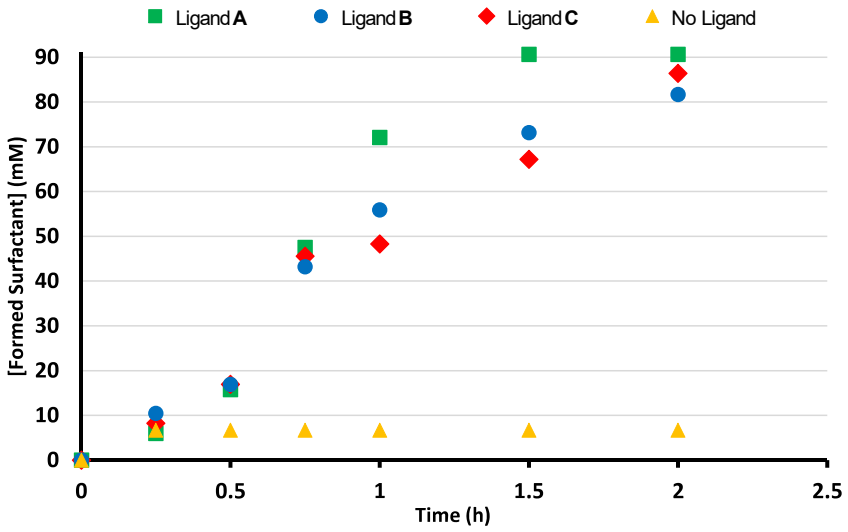


Figure 3.4 Reaction kinetics for CuAAC of three different ligands in tBuOH/D_2O (1:1) shows similar reaction rates for all ligands in a reaction between **3.1** and **3.2** to form **3.3**. Complete conversion in 2 hours and no lag period is observed for ligand **A** (green squares), ligand **B** (blue circles and ligand **C** (red diamonds). Catalyst deactivation occurs in the absence of ligand (yellow triangles). (n=1)

In Chapter 2, we reported that use of ligand **A** in combination with 1-dodecyne (**3.2b**) gave extremely slow reaction due to low solubility in water: a lag period of over 3 hours

and a total reaction time of multiple days were observed (Figure 3.5, blue circles). Repeating the same *unseeded* reaction with hydrophobic ligand **C** greatly accelerated formation of **3.3b** and fully eliminated the lag period (red squares). A different mechanism appears to operate when ligand **C** is present: the rate limiting step appears to have changed, where low solubility of **3.2b** no longer slows down the rate of reaction.

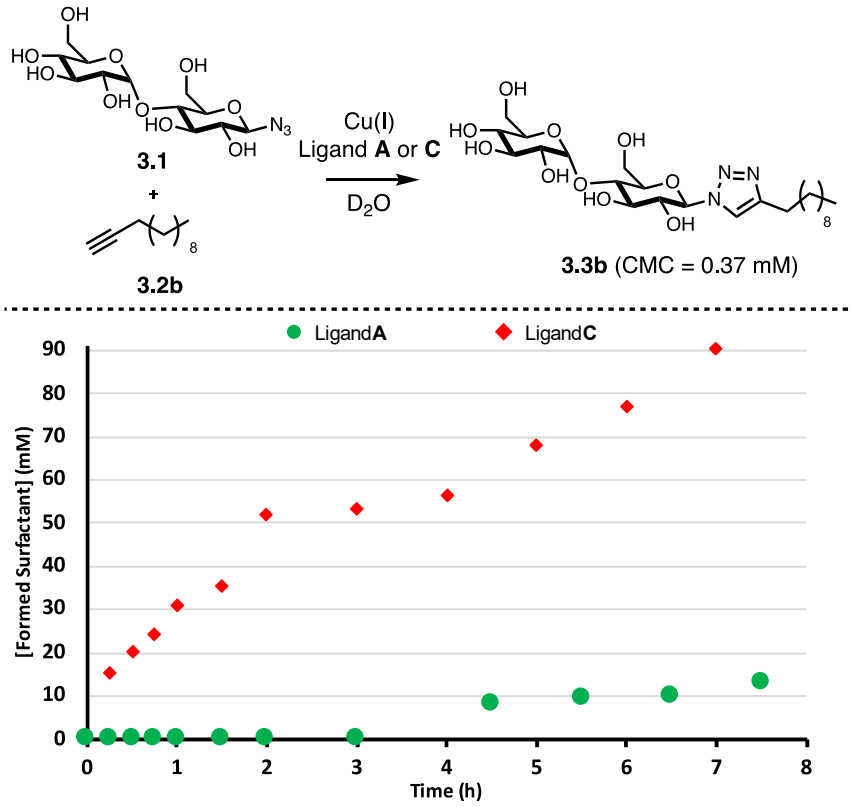


Figure 3.5 Reaction kinetics when coupling azide **3.1** to 1-dodecyne **3.2b** to form longer-chained surfactant **3.3b** under unseeded conditions with ligand **A** (green circles) and with ligand **C** (red diamonds).

3.2.3 DOSY study

Phase behaviour of the new ligands was probed with diffusion ordered spectroscopy (DOSY) and compared with the diffusion constants obtained in Chapter 2. Surfactant aggregated into micelles will have a lower diffusion coefficient (*D*) than free surfactant at concentrations below the CMC. Compounds encapsulated by the micelle will diffuse at a similar rate as the amphiphile. Tetramethylsilane (TMS) is added as a control

hydrophobic substrate to confirm the diffusion constant and formation of micellar aggregates by **3.3**.

Entry	Species present	*D* (3.3)	*D* (3.2)	*D* (ligand)	*D* (3.1)	*D* (TMS)
A	**3.3** (2 mM) = *	3.6	-	-	-	8.2
B	**3.3** (22 mM) = **	1.3	-	-	-	1.2
C	* + **3.2** (saturated)	3.8	ND	-	-	4.1
D	** + **3.2** (saturated)	1.3	0.58	-	-	1.1
E	**A** (saturated)	-	-	9.1	-	7.0
F	[Cu-**A**)] (6.8 mM)	-	-	5.8	-	13
G	* + [Cu-**A**)] (6.8 mM)	3.7	-	5.7	-	8.0
H	** + [Cu-**A**] (6.8 mM)	1.3	-	5.7	-	1.6
I	**B** (8.3 mM)	-	-	4.1	-	9.0
J	* + **B** (8.3 mM)	3.7	-	4.1	-	-
K	** + **B** (8.3 mM)	1.3	-	3.9	-	1.3
L	[Cu-**B**] (8.3 mM)	-	-	3.1	-	9.8
M	* + [Cu-**B**] (8.3 mM)	3.1	-	3.0	-	9.3
N	** + [Cu-**B**] (8.3 mM)	1.3	-	2.8	-	1.5
O	**3.2** (saturated) + [Cu-**B**] (8.3 mM)	-	19	2.3	-	-
P	* + **C** (saturated)	3.8	-	ND	-	8.6
Q	** + **C** (saturated)	1.3	-	1.0	-	1.5
R	** + [Cu-**C**] (saturated)	1.1	-	0.67	-	1.2
S	**3.1** (91 mM)	-	-	-	4.3	-
T	* + **3.1** (91 mM)	3.6	-	-	4.4	7.6
U	** + **3.1** (91 mM)	1.2	-	-	4.9	1.2

Table 3.1 Legend: * = **3.3** (2 mM) and ** = **3.3** (22 mM). Diffusion coefficients extracted from DOSY experiments. The diffusion coefficients were recorded for all reaction components at the concentrations present in the system during the synthesis of **3** in water. *D* values are reported in 10^{-10} m^2s^{-1}. A decrease in the diffusion coefficient in the presence of surfactant **3** above the CMC indicates a strong association with the micelle. ND indicates that the diffusion coefficient could not be extracted because of the limited solubility of the compound in water. The Morris' correlation[31] for small molecules predicts a MW of 516 g/mol for entry **A**, a MW of 379.3 g/mol for entry **L**, a MW of 339.5 g/mol for entry **S**. These predicted values are in close agreement with the actual molecular weights considering the model used for the predictions.

Our previous experiments had shown that surfactant **3.3** aggregates above the CMC (Table 3.1, entries **A**-**B)** and that alkyne **3.2** is fully associated at this concentration (entries **C**-**D**), whereas hydrophilic Cu-**A** and azide **3.1** did not associate with the micelles (entries **E**-**H** and **S**-**U**). Hydrophilic complex Cu-**B** diffuses slower than free ligand,

indicating coordination to copper (entries **I** and **L**), however both free and coordinated **B** shows no association with surfactant **3.3** (entries **J**-**K** and **M**-**N**). On the other hand, hydrophobic ligand **C** is insoluble in water and is solubilised with strong binding to micelles at concentrations above the CMC for both free **C** and the Cu-**C** complex (entries **P**-**R**).

The diffusion rates of the free small molecules, such as surfactant below CMC, azide, and free **B** are in agreement with their molecular weights according to Morris' correlation.[31] Using the Stokes-Einstein relationship we calculate a hydrodynamic radius of 1.9 nm for micelles of surfactant **3** at 22 mM, which is in agreement with the data obtained from DLS.[32]

3.3 Inverting the polarity of the system

The polarity of the coupling partners was inverted to study a broader substrate scope of physical autocatalysis driven by CuAAC and to investigate how the phase behaviour of azide and alkyne moieties affects the mechanism and kinetics of this autocatalytic reaction. The inversion of polarity of the reaction components was achieved by synthesising hydrophilic, maltose-based alkyne **3.4** and a hydrophobic alkyl azide **3.5** (Section 3.7.2) that upon undergoing CuAAC form surfactant product **3.6** (Figure 3.6a). DLS and fluorimetry measurements indicated that **3.6** aggregates into micelles of around 6 nm at 15 mM (Section 3.7.3 and 3.7.4).

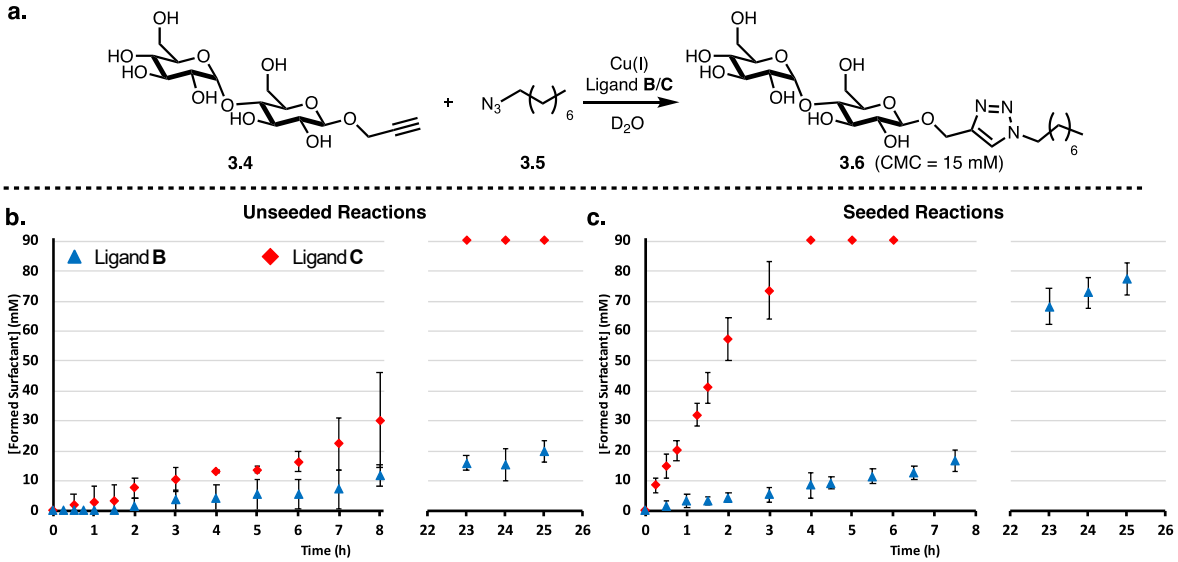


Figure 3.6 a. Reaction scheme for the 'inverted system' where hydrophilic alkyne **3.4** is coupled to hydrophobic azide **3.5** to give surfactant **3.6**. **b.** Kinetics of unseeded reaction in inverted system using ligands **B** (blue triangles) and **C** (red diamonds) with identical reaction conditions as the original system. **c.** Kinetics when the inverted system is seeded with **3.6** (30 mM). Points are the mean of three independent experiments and the error bars are the standard deviation (n=3).

The kinetics of this 'inverse' reaction was studied with ligand **B** and **C**. The inversion of polarity for the coupling partners slowed down the reaction significantly with long lag periods for both ligands relative to the original system (Figure 3.6b). However, the trend of **C** leading to faster reaction rates than **B** remains (Section 3.7.5 for extracted rates). Surprisingly, reaction with **C** greatly benefited from seeding with product contrary to the original system which experienced minimal acceleration: the lag period was eliminated, and the extremely fast reaction was complete in 4 hours (Figure 3.6c). Meanwhile, the seeded reaction with **B** experienced a minimal increase in rate with a similar lag period still present. The reaction did not reach full conversion after 24 hours, an autocatalytic system that has such low responsivity to seeding has not previously been observed in the Fletcher group.

When the inverted system was studied under homogeneous conditions in a 1 : 1 water/*tert*-butanol mixture complete conversion occurred in 30 minutes for both ligands (Figure 3.7). Interestingly, this is a faster reaction time than for the original system under

homogeneous conditions which required 2 hours to reach full conversion, while under biphasic conditions the inverted system is significantly slower.

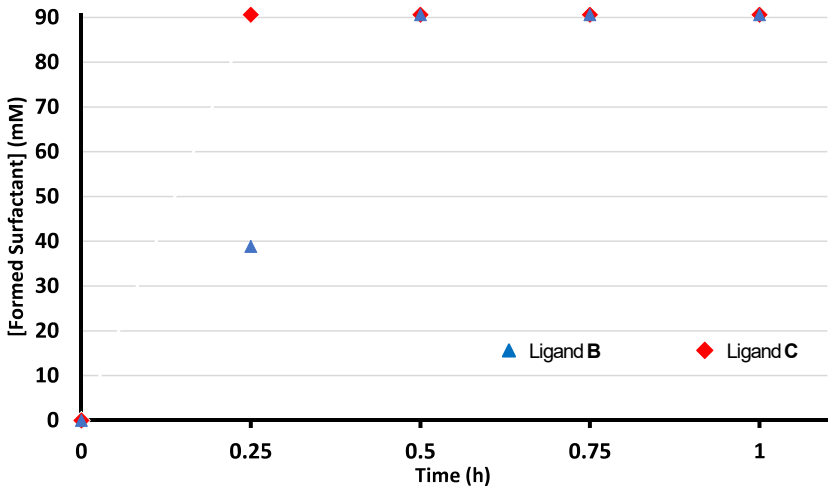


Figure 3.7 Reaction kinetics for CuAAC between **3.4** and **3.5** to form **3.6** with ligand **B** (blue triangles) and ligand **C** (red diamonds) in tBuOH/D_2O (1:1). Complete conversion in 30 minutes and no lag period is observed for both ligands. (n=1)

3.3.1 DOSY analysis of the inverted system

The phase behaviour of the reaction components in the inverse system was probed with DOSY experiments. Similar behaviour as in the original system was observed in that only hydrophobic components associate with the micelle, whereas hydrophilic compounds remain in the bulk aqueous phase (Table 3.2). Surfactant **3.6** diffuses at a slower rate above the CMC indicating aggregation into micelles (Table 3.2, entries **A**-**B**). Hydrophobic azide **3.5** is insoluble in water but becomes fully associated with micelles of **3.6** above the CMC (entries **C**-**D**), increasing concentration of **3.6** further to 60 mM led to even stronger association with **3.5** (entry **E**).

Water-soluble Cu-**B** diffuses slower than the respective free ligand (entries **F**+**H**) and is not encapsulated by micelles in either case (entries **G**+**I**), whereas hydrophobic Cu-**C** does dissolve in water below the CMC and binds strongly to **3.6** upon micelle formation

(entries **J**-**L**). Alkyne **3.4** is fully soluble and never associates with **3.6** (entries **M**-**O**). The diffusion coefficient of surfactant **3.6** in entry **H** appears to be an outlier with a value of 2.3 10^{-10} m^2s^{-1} and not the standard 3.3 10^{-10} m^2s^{-1}. However, TMS doesn't diffuse at a slower rate under these conditions indicating that no aggregation and encapsulation is taking place. The lower *D*-value could indicate association of **3.6** with Cu-**B** complex.

Entry	Species present	*D* (3.6)	*D* (3.5)	*D* (ligand)	*D* (3.4)	*D* (TMS)
A	**3.6** (3 mM) = *	3.4	-	-	-	7.2
B	**3.6** (30 mM) = **	2.1	-	-	-	1.9
C	* + **3.5** (saturated)	3.3	ND	-	-	7.0
D	** + **3.5** (saturated)	1.9	1.9	-	-	1.7
E	**3.6** (60 mM) + **3.5** saturated)	1.4	0.82	-	-	-
F	* + **B** (8.3 mM)	3.3	-	3.7	-	7.2
G	** + **B** (8.3 mM)	2.2	-	3.5	-	2.1
H	* + [Cu-**B**] (8.3 mM)	2.3	-	2.5	-	7.8
I	** + [Cu-**B**] (8.3 mM)	2.2	-	2.6	-	2.1
J	* + [Cu-**C**] (saturated)	3.3	-	ND	-	7.1
K	** + **C** (saturated)	2.2	-	1.5	-	2.1
L	** + [Cu-**C**] (saturated)	1.4	-	1.0	-	2.0
M	**3.4** (91 mM)	-	-	-	3.8	-
N	* + **3.4** (91 mM)	3.2	-	-	3.8	5.0
O	** + **3.4** (91 mM)	1.9	-	-	3.7	1.9
P	**3.4** (91 mM) + [Cu-**B**] (8.3 mM)	-	-	2.2	3.6	-
Q	** + **3.4** (91 mM) [Cu-**B**] (8.3 mM)	1.7	-	2.4	3.0	-

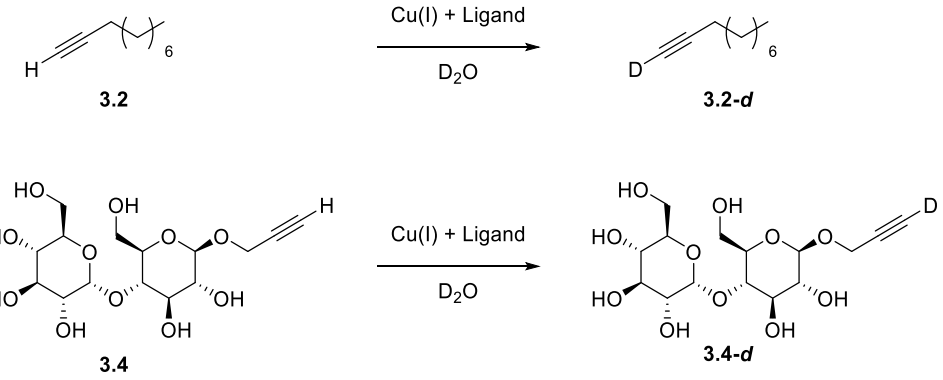
Table 3.2 Legend: * = **3.6** (3 mM) and ** = **3.6** (30 mM). Diffusion coefficients extracted from DOSY experiments. The diffusion coefficients were recorded for all reaction components at the concentrations present in the system during the synthesis of **3.6** in water. *D* values reported in 10^{-10} m^2s^{-1}.

The inverted system enabled additional DOSY experiments impossible with the original system. Initial coordination of alkyne **3.4** to Cu-**B** could be probed since both are water soluble (entries **P**-**Q**). The slightly lowered *D*-values for both compounds in entry **P** might indicate partial association. Entry **Q** shows a significantly slower diffusion rate for alkyne **3.4** when both Cu-**B** complex and surfactant **3.6** are present. This could indicate interaction between surfactant and alkyne when copper is present. However, overlap

between NMR resonances of **3.4** and **3.6** leads to some uncertainty and possibly unreliable diffusion coefficients for this measurement.

3.4 Deuterium exchange experiments

Resonance by the triazole proton of the CuAAC product is often not observed during ^{1}H NMR analysis when the reaction is performed in deuterated water. This is caused by a proton-deuterium exchange event either during demetallation of copper from the triazole or after reversible coordination of alkyne starting material to copper. The rate of deuterium exchange catalysed by copper for alkynes **3.2** and **3.4** to yield **3.2**-*d* and **3.4**-*d* in D_2O can be measured by following the decrease in integral of the alkyne proton relative to the rest of the substrate's protons over time (Scheme 3.1 and Table 3.3). This gives insight into how readily alkynes **3.2** and **3.4** coordinate to Cu-**L** and subsequently interact with deuterated water. Probing this behaviour gives insight into how the first step of the CuAAC mechanism, where alkyne coordinates to copper, is affected by changes in hydrophobicity of the ligand and the presence of product to accelerate the reaction.



Scheme 3.1 Deuterium exchange of alkyne **3.2** and **3.4** to **3.2**-*d* and **3.4**-*d* respectively is catalysed by copper and is followed by ^{1}H NMR analysis over time. The rate of exchange gives insight into the influence of seeding and ligand hydrophilicity on the rate for the first step of the CuAAC mechanism.

A control experiment showed no deuterium exchange for hydrophobic alkyne **3.2** in the absence of copper (Table 3.3, entry 1). H- to D-exchange was slow for **3.2** with both Cu-**B** and Cu-**C** complex resulting in 58% and 32% conversion respectively after one day

(entries 2 and 3). Faster exchange by Cu-**B** might enabled by the hydrophilicity of the complex which facilitates interaction with deuterated water. Seeding the exchange experiments with **3.3** led to full conversion to **3.2**-*d* within 5 hours for *both* ligands (entry 4 and 5). Therefore, phase transfer by micelles appears to speed up deuterium exchange for the hydrophobic alkyne **3.2**.

Entry[a]	Alkyne	Ligand[b]	Seed (mM)[c]	Conv. (%)[d]	Time
1	**3.2**	N/A[e]	0	0	24 h
2	**3.2**	**B**	0	58	24 h
3	**3.2**	**C**	0	32	24 h
4	**3.2**	**B**	22	100	5 h
5	**3.2**	**C**	22	100	5 h
6	**3.4**	N/A	0	0	24 h
7	**3.4**	**B**	0	100	<1 min
8	**3.4**	**C**	0	100	3 h
9	**3.4**	**C**	30	100	2.5 h

Table 3.3 Conversion and reaction time for the deuterium exchange reactions with alkyne **3.2** and **3.4**. [a]Standard reaction conditions were applied in D_2O in the absence of azide to prevent turnover. [b]Different rates of deuterium exchange were observed when ligand **B** or **C** was applied. [c]Seeding the system with **3.3** (for **3.2**) or **3.6** (for **3.4**) increased the rate of D-exchange in all cases. [d]Reactions monitored and conversion determined by following change in relative integral of triazole proton by ^{1}H NMR spectroscopy. [e]Control reaction in the absence of copper.

A control experiment with hydrophilic alkyne **3.4** similarly resulted in no deuterium exchange in the absence of copper (entry 6). Exchange was extremely quick for the combination of **3.4** with ligand **B**, we observed full conversion under one minute at the first data point (entry 7). Hydrophobic **C** was slower and achieved full exchange to **3.4**-*d* after three hours (entry 8). Hydrophilic Cu-**B** complex and **3.4** combined in the aqueous phase to give much faster deuterium exchange than when the alkyne is phase-separated with Cu-**C**. Surprisingly, Cu-**C** mediated exchange of **3.4** to **3.4**-*d* was not significantly accelerated when seeded with product **3.6** (entry 9). CuAAC reaction of the inverted system does not appear to benefit from solubilisation of Cu-**C** complex by micelles and likely is accelerated by phase-transfer of hydrophobic azide **3.5** to the aqueous phase instead during the second step of the mechanism.

Overall, the deuterium exchange does not occur without copper, whereas phase separation heavily influences interaction between Cu-**L**-complex and alkyne, and consequently the rate of exchange. Addition of surfactant product speeds up deuterium exchange for alkyne **3.2**, meanwhile hydrophilic **3.4** experiences minimal benefits from seeding. These results indicate that the first step in the CuAAC mechanism might be accelerated by product formation for alkyne **3.2**, while this step is unaffected for alkyne **3.4** in the inverted system.

3.5 Mechanistic rationalisation

The kinetic data gathered from the original and inverted system in combination with DOSY measurements and deuterium exchange experiments allowed us to develop a mechanistic model that accounts for the kinetic behaviour observed during physical autocatalysis driven by CuAAC. The mechanism operating in this type of system is reminiscent of phase transfer catalysis, where a catalyst enables two compounds to react, even though they separated between two immiscible phases, by transferring a substrate to the opposing phase. Phase-transfer catalysis is a well developed field but mechanisms for these reaction types are still not fully understood due to the complex nature of monitoring biphasic systems and the various variables that need to be controlled.[33–35] As mentioned in Chapter 2, the mechanism of micellar autocatalysis based on hydrolysis has previously been investigated[36–38], however these models never accounted for the presence of a secondary catalyst such as reported here.

3.5.1 Mechanistic model of the original system

A model that rationalizes the influence of the hydrophilicity of the copper ligand on the kinetics of the original system is displayed in Figure 3.8. The system consists of three phases: an organic phase (neat alkyne), a bulk aqueous phase, and an interfacial phase

where interaction between phase-separated compounds occurs. Micelles can be viewed as an extension of this interface as it increases the surface area where separated reagents can interact. The mechanism of the standard CuAAC reaction is complicated and has been revised multiple times.[39–46] Our model focuses on two key steps in this mechanism where interaction between phase-separated substrates occurs, namely the coordination of alkyne to copper and subsequent interaction of azide with this complex. Other important steps in the CuAAC mechanism, such as formation of the copper-ligand complex and demetallation of the triazole, are expected to occur rapidly relative to the phase separated steps and are therefore not incorporated into our model nor is the mono or dinuclear nature of the catalyst complex.

The relative rates of the first step involving coordination of alkyne to copper can be extracted from the deuterium exchange experiments and from this the relative rate of the second step can be inferred. The phase behaviour of complexes and intermediates described in this model is presumed to be analogous to that of the individual reaction components analysed by DOSY NMR.

Rate enhancements through phase transfer catalysis by the micelle are expected to vary depending on the concentration of *hydrophilic* reagent in the aqueous phase, as substrates solubilised in the micelle must subsequently interact with these aqueous compounds. Steps involving high concentrations of hydrophilic reagent are effectively promoted by micelles, whereas steps with low concentrations lead to less efficient phase transfer catalysis and are therefore weakly promoted by product (weakly autocatalytic). Colocalization, solubilization of two hydrophobic reagents within the micelle raises the local concentration drastically and will lead to a strongly promoted step, heavily affected by product formation. It is important to note that the catalytic activity of copper remains constant in all the systems. Whenever a step is described as faster, promoted or more

efficient, this is the result of change in rate of mass transport through the system not a change in catalytic activity by copper.

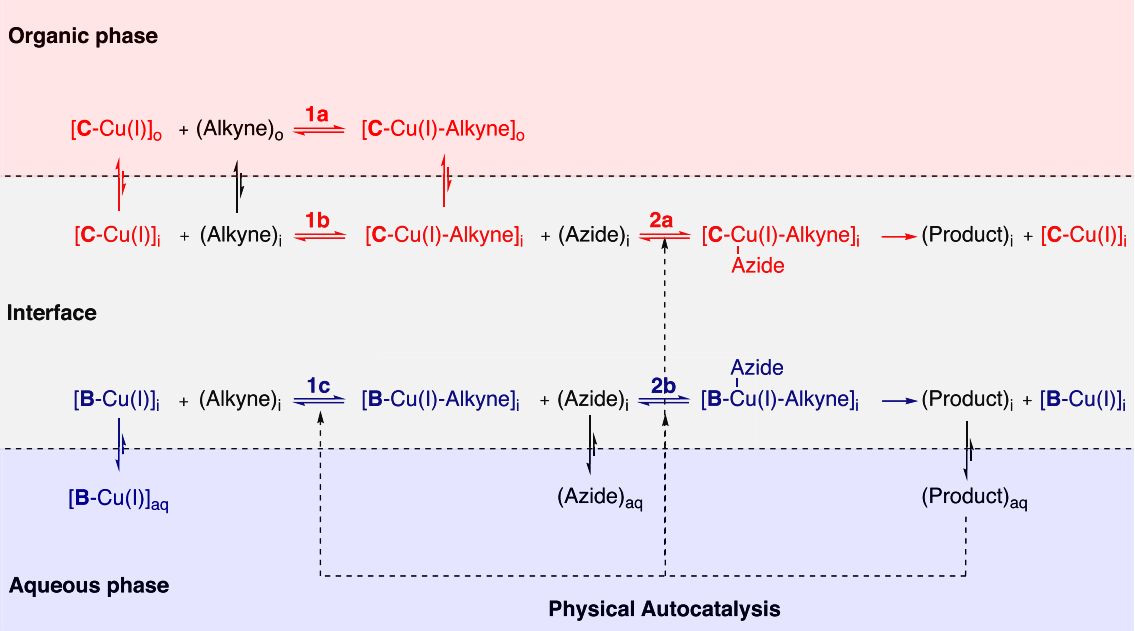


Figure 3.8 Proposed mechanistic model for physical autocatalysis in a biphasic system driven by CuAAC with hydrophobic alkyne and hydrophilic azide as coupling partners. Red represents processes catalysed by hydrophobic Cu-**C** complex, and blue by hydrophilic Cu-**B** complex.

*Step 1) Hydrophobic alkyne and Cu-**L** interact.* [**C**-Cu(I)]-complex and alkyne are both hydrophobic and solubilised in the organic phase resulting in quick complexation (Figure 3.8, step 1a and 1b). The rate of this step will not be affected by product formation. The hydrophilic [**B**-Cu(I)]-complex is fully dissolved in the aqueous phase and interacts with the alkyne at the interface only (step 1c). This slow step can be accelerated by autocatalysis but will be limited by low Cu-**B** complex concentration leading to weak promotion of this step.

*Step 2) Aqueous azide coordinates to Cu-**L**-alkyne complex.* Since hydrophilic azide is fully solubilised in water, this step will occur at the interface for both ligand **B** and **C** (Figure 3.8, step 2a and 2b) and is promoted by the presence of product. The amphiphilic Cu-**B**-alkyne complex is assumed to be restricted to the interface with ligand **B** unable to completely solubilize the complex into the aqueous phase (slow H-to-D exchange is

observed here, Table 3.3, entry 2). For step 2 both ligands will thus benefit similarly form product formation (Table 3.3, entry 4 and 5). Any surfactant **3** formed will start to accumulate at the interface, while Cu-**L** complex re-enters the catalytic cycle. When concentration of **3** surpasses the CMC, any additional product formed will aggregate into micelles and catalyse all biphasic steps.

This model accounts for the differences in kinetic behaviour between **B** and **C** (Figure 3.2). A significant lag-period (up to about 7 hours) is observed for **B** due to the slow, biphasic step 1c. Meanwhile, step 1a/b is fast as it is a single-phase reaction resulting in a short lag period for **C**. Step 2 presumably has significant biphasic character in either case and proceeds at a similar rate for both ligands.

Additionally, the differences between seeded and non-seeded reactions can be rationalised with the model. Ligand **B** greatly benefits from seeding with product leading to an elimination of the lag period and a doubling in maximum rate, likely by facilitating the interaction of hydrophilic catalyst and hydrophobic azide in step 1. Ligand **C** does not benefit from product addition with no significant difference in maximum rate between seeded and non-seeded reactions (Section 3.7.5 for extracted rates). Overall, ligand polarity effectively controls the rate of step 1: leading to a rapid rate for ligand **C**, whereas for ligand **B** step 1 becomes rate-limiting.

3.5.2 Mechanistic model of the inverted system

A new model was developed of the inverse system which accounts for phase-behaviour of the inverted coupling partners and rationalises the changes kinetic behaviour (Figure 3.9).

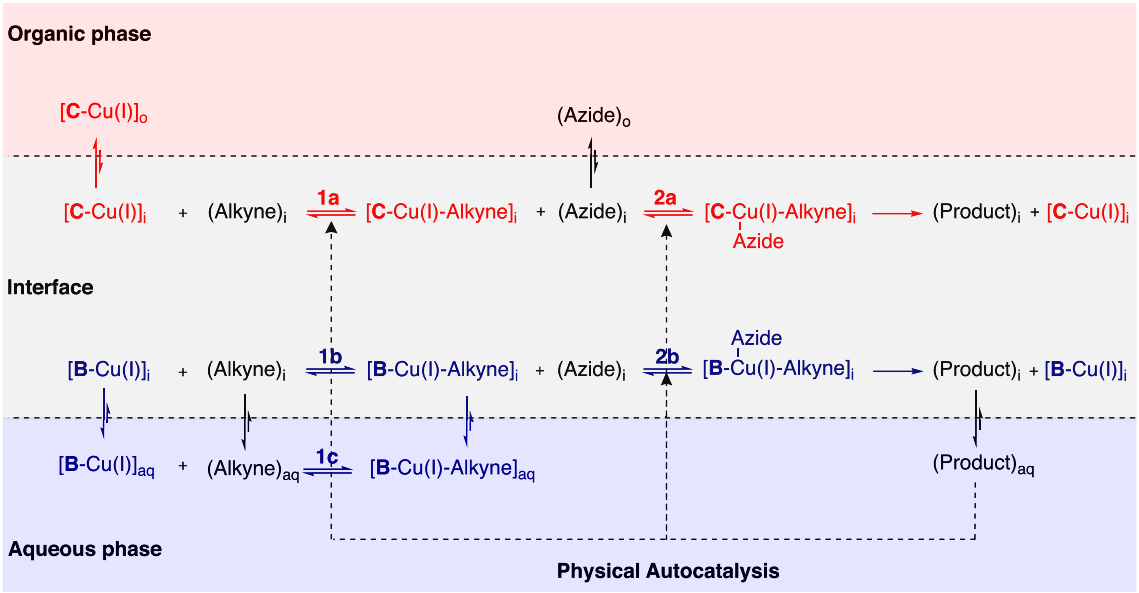


Figure 3.9 Proposed mechanistic model for physical autocatalysis in a biphasic system driven by CuAAC with hydrophilic alkyne and hydrophobic azide as coupling partners. Red represents processes catalysed by hydrophobic Cu-**C**, and blue by hydrophilic Cu-**B**.

*Step 1) Aqueous alkyne and Cu-**L** interact.* Hydrophobic [**C**-Cu(I)]-complex initially interacts slowly with aqueous alkyne at the interface (Figure 3.9, step 1a) and this process is only weakly promoted once micelles of **3.6** form. While this copper complex readily associates with the micelle (Table 3.2, entries J and L), alkyne **3.4** does not interact with the aggregate (Table 3.2, entries M-O). Additionally for ligand **C**, H- to D-exchange experiments indicated that micelles do not significantly affect the rate at which the complex and **3.4** encounter each other (Table 3.3, entries 8 and 9). Meanwhile, for ligand **B** step 1c is extremely fast as alkyne and [**B**-Cu(I)]-complex are both soluble in water (Table 3.3, entry 7).

*Step 2) Hydrophobic azide coordinates to Cu-**L**-alkyne complex.* Cu-**C**-alkyne is likely to be hydrophobic enough to colocalize with azide **3.5** inside the micelle which will strongly promote step 2a upon formation of micelles. Conversely, step 2b is likely to be weakly promoted: the organic azide needs to interact with Cu-**B**-alkyne, a complex consisting of two hydrophilic components which would not be expected to be encapsulated within micelles. Micellar phase transfer will increase the concentration of azide in the aqueous

phase but subsequent interaction with this highly polar complex will not be facile. Additionally, Cu-**B**-alkyne will be present at very low concentrations. Following this, product **3.6** will accumulate at the interface and once the CMC is reached, micelles will accelerate any biphasic steps.

The kinetics of this inverted system are slower relative to the original system, reactions with both ligands have pronounced lag periods and longer reaction times (Figure 3.6, b). Phase mixing experiments in a water/*tert*-butanol solvent system indicate that these slower rates are not due to substrate reactivity (Figure 3.4 and 3.7). In this system step 2 appears to be rate limiting as deuterium exchange experiments indicate faster rates overall for step 1 relative to the original system (Table 3.3). During step 2 the Cu-**L**-alkyne complex must interact with the hydrophobic substrate at the interface, this complex will only be present at concentrations equal or lower than the catalyst loading. This low complex concentration combined with the biphasic nature of step 2 could cause the slower kinetics observed in the absence of micelles.

Under seeded conditions the opposite kinetic behaviour was observed compared to the original system: reaction with ligand **C** experienced a significant acceleration, whereas reaction with ligand **B** was minimally impacted by the addition of product (Figure 3.6c). Micelles could co-localise Cu-**C**-alkyne complex and **3.5** generating a higher local concentration and greatly enhancing the rate of step 2. Whereas, the strongly hydrophilic Cu-**B**-alkyne complex does not readily associate with micelles, minimally benefiting step 2. Overall step 2 is rate limiting in this system and can be strongly promoted by addition of product **3**.**6** in combination with ligand **C** but not with ligand **B**.

3.5.3 Summary of the complete phase-transfer model

In total four different systems were investigated in this chapter, the original and inverted coupling partners in combination with ligand **B** or **C**. The relative rates of steps 1 and 2 and the degree to which product formation promotes each step have been summarized in Figure 3.10. Furthermore, the coupling partner/ligand combinations that will show the most significant autocatalytic effect are indicated. When reagents are in the same phase a step is fast, while phase-separated steps are slow. Phase-separated steps can be accelerated by micelle formation but if aqueous substrate is present at low concentrations the step will only be weakly promoted. The conditions in system 2 and 3 result in the most pronounced autocatalytic effect because the rate limiting steps (step 1 and 2 respectively) in these two systems are more effectively promoted by product.

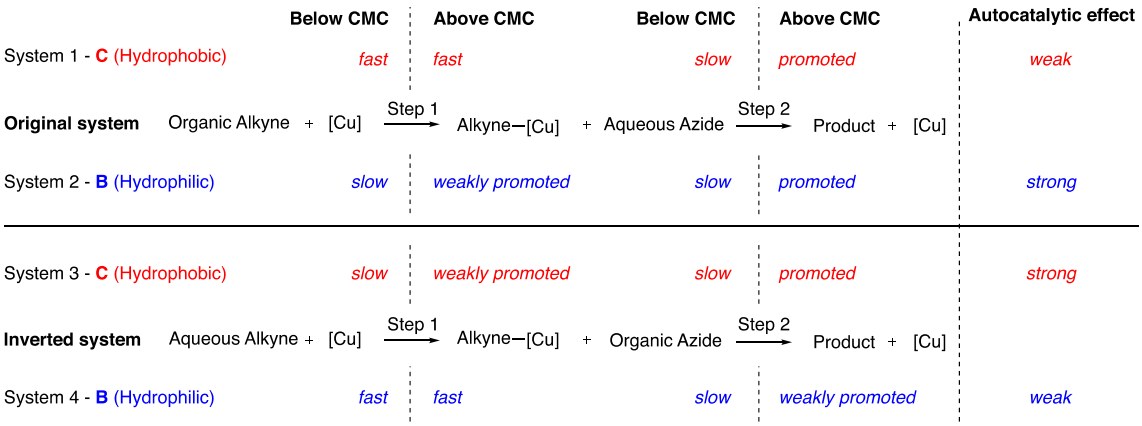


Figure 3.10 Summary of phase-transfer models used to rationalise the kinetics of Cu-catalysed self-reproducing micelles for differing ligands and coupling partner combinations. How pronounced the autocatalytic effect is that a system will experience upon addition or formation of product is indicated.

3.5.4 Testing the generality of the model

In Chapter 2 during development of this autocatalytic system CuAAC was selected as the ideal coupling reaction because of the presumption that coupling partners could readily be varied without disrupting the underlying autocatalytic mechanism. We have shown

that polarity of the functional groups can be inverted while retaining autocatalysis but changes to the type of polarity of headgroup have not yet been tested.

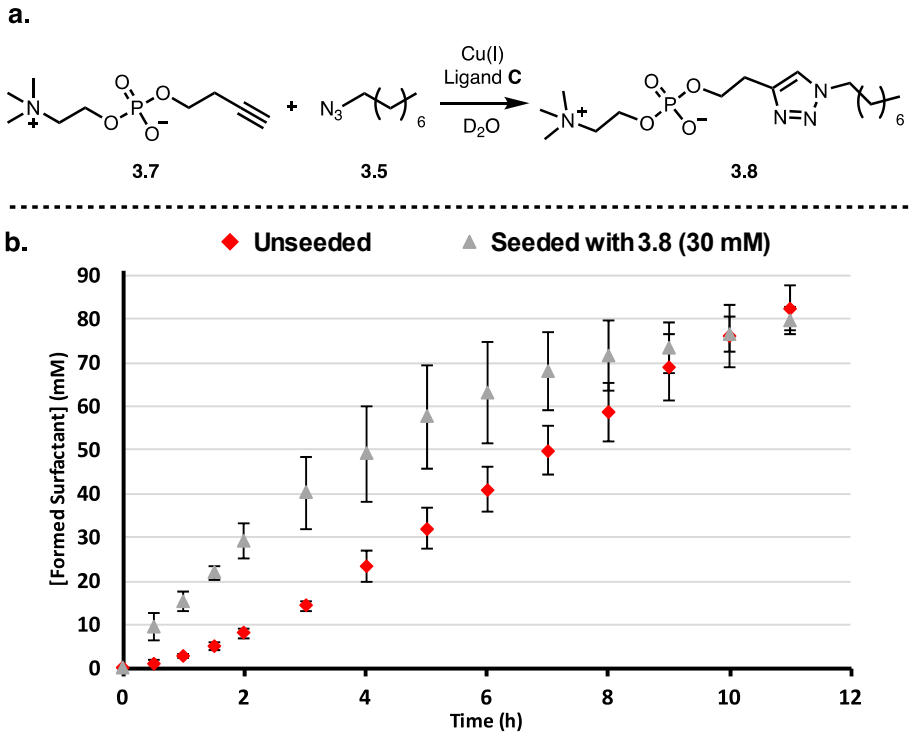


Figure 3.11 a. Coupling reaction of phosphocholine **3.7** with azide **3.5** to form phospholipid **3.8** driven by CuAAC with hydrophobic ligand **C** under biphasic conditions. **b.** Kinetics of the reaction: the unseeded reaction (red diamonds) exhibits a short lag period followed by an increased rate of product formation. Seeding the system with product **3.8** (30 mM, grey triangles) eliminates the lag period, and increases the rate of reaction. Points are the mean of three independent experiments and the error bars are the standard deviation.

An autocatalytic system with a novel polar headgroup was developed (Section 3.7.2) based on alkyne **3.7** which contains a zwitterionic phosphocholine moiety. Compound **3.7** is coupled to azide **3.5** in combination with hydrophobic ligand **C** to afford phospholipid **3.8** (Figure 3.11, a), utilising the reaction conditions that correlate to system 3 in Figure 3.10. This system allowed us to test the generality of CuAAC based physical autocatalysis and to gauge the accuracy of the phase-transfer model. Reaction with polar alkyne **3.7** is still expected to experience autocatalysis as the phase-transfer model indicates that phase-separation is the only prerequisite for product induced rate accelerations. The autocatalytic mechanism should be unaffected by the nature of the

polarity of the headgroup: zwitterionic, anionic and cationic polar headgroups should be tolerated.

Kinetic analysis of this system showed behaviour characteristic of autocatalysis (Figure 3.11, b**)**.[47] The unseeded reaction exhibited a lag period followed by a pronounced rate acceleration (red diamonds), whereas seeding the reaction eliminated the lag period and gave a faster initial rate (grey triangles). These results indicate that CuAAC based physical autocatalysis is general and different polar headgroups are tolerated without disrupting the autocatalytic mechanism. Furthermore, the phase-transfer model was able to predict autocatalytic efficiency accurately.

3.6 Conclusions

The results reported in this chapter have shown how linking a secondary catalyst to an autocatalytic cycle can be exploited to drive new reaction outcomes. Rational variations in ligand structure change the hydrophilicity of the copper complex which provides a handle to tune the kinetics of the system by virtue of phase behaviour. The hydrophilicity of the ligand controls the physical location of the active catalyst complex and provides a way to change the rate limiting step of the reaction. CuAAC-based physical autocatalysis has proven to be a general reaction that tolerates both inversion of the polarity of the coupling partners and a different type of polarity for the headgroup. The differences, in kinetic results and autocatalytic efficiencies between the systems studied, are not due to inherent substrate reactivity but can be rationalized in terms of the phase behaviour of the reaction components. Through mechanistic investigations a model was formulated that considers how phase separation influences the relative rates of each step in the mechanism through efficiency of mass transport. Furthermore, the degree to which these steps benefit

from product formation was taken into account. The model rationalises which set of reaction conditions will experience the most pronounced autocatalytic effect.

Chapter 4 showcases how the robust nature of physical autocatalysis linked to CuAAC along with the mechanistic knowledge obtained in this chapter can be used to develop a more elaborate and complex self-reproducing system. A system of self-reproducing vesicles is generated and is exposed to extremely basic reaction conditions in the presence of a wide range of additional substrates without disrupting the underlying autocatalytic mechanism. This affords a system of self-reproducing protocells that exhibits several different emergent, life-like properties.

3.7 Experimental

3.7.1 General Information

The general information for the work reported in this chapter is as described in Section 2.5.1.

3.7.2 Experimental Procedures and Characterisation of Compounds

General procedure 1: Synthesis of protected surfactant products via CuAAC reaction

Procedure as described in section 2.5.2

General procedure 2: Acetyl deprotection

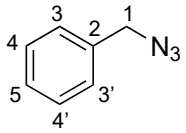
Procedure as described in section 2.5.2

General procedure 3: Setup of kinetic experiments

A solution of hydrophilic substrate (0.408 mmol, 1.00 eq, 1.50 mL of 272 mM standard solution in D_2O), $CuSO_4 \cdot 5H_2O$ (6.0 mg, 0.024 mmol, 0.060 eq, 1 mL of 6 mg/mL standard solution in D_2O) (and surfactant product in the reported concentrations for the seeded reactions) were added to D_2O (2 mL) to give a total volume of 4.5 mL in a round bottom flask (25 mL) with a stirrer bar of an identical size (4.5 mm diameter and 12 mm length) for each experiment. Subsequently ligand (0.12 eq), hydrophobic substrate (2.0 eq) were added and the flask was capped with a septum and the solution was degassed by bubbling argon through it for 30 minutes. Afterwards, sodium ascorbate (16.2 mg, 0.0820 mmol, 0.200 eq) was added to initiate the reaction. The reaction mixture was stirred at 200 rpm under a continuous flow of argon. Samples for analysis during the kinetic

experiments were prepared at regular intervals by diluting 0.1 mL of the reaction mixture in 0.4 mL of D_2O and immediately taking a ^1H NMR measurement.

Benzyl azide (3.9)

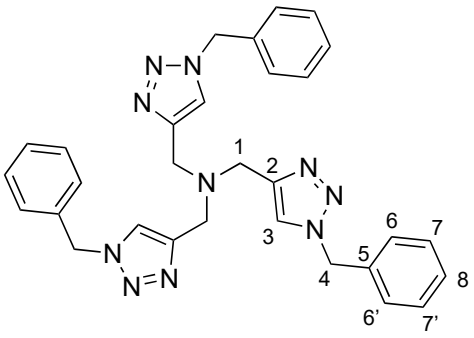


Chemical Formula: $C_7H_7N_3$
Molecular Weight: 133.15

Synthesised according to Healy *et al*.[48] Benzyl bromide (6.95 mL, 58.5 mmol, 1.00 eq) was added dropwise to a solution of sodium azide (7.60 g, 117 mmol, 2.00 eq) in (3:1 acetone/water, 100 mL) and the resulting mixture was stirred at room temperature for 1 h. The reaction was diluted with water (200 mL) and extracted with ethyl acetate (3 × 300 mL). The combined layers were washed with brine (2 × 200 mL), dried ($MgSO_4$) and concentrated *in vacuo* to give benzyl azide **3.9** as a crude colourless oil (7.32 g, 55.0 mmol, 94%). Due to instability **3.9** was immediately used in the next step.

^{1}H NMR (400 MHz, $CDCl_3$) δ 7.44 – 7.29 (m, 5H, C<u>H</u>-3 and C<u>H</u>-3' and C<u>H</u>-4 and C<u>H</u>-4' and C<u>H</u>-5), 4.35 (s, 2H, C<u>H</u>$_2$-1); **^{13}C{^{1}H} NMR** (101 MHz, $CDCl_3$) δ 128.9, 128.3, 128.2, 54.8. Consistent with reported literature values.[48]

Tris(benzyltriazolylmethyl)amine (TBTA, ligand C) (3.10)

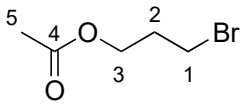


Chemical Formula: $C_{30}H_{30}N_{10}$
Molecular Weight: 530.64

Synthesised according to Zhu *et al*.[49] Benzyl azide **3.9** (6.87 mL, d = 1.066 g/mL, 55.0 mmol, 4.00 eq) was dissolved in *tert*-butyl alcohol (100 mL) in a 250 mL round-bottom flask equipped with a magnetic stir bar. Tripropargylamine (2.44 mL, d = 0.927 g/mL, 17.2 mmol, 1.00 eq) was subsequently added, and the flask was placed in a water bath at rt. $Cu(OAc)_2 \cdot H_2O$ (212 mg, 1.00 mmol, 0.0600 eq) was added in the solid form, and the reaction flask was left uncovered while being stirred for 5 min. The flask was then closed with a rubber septum equipped with an argon balloon. The reaction mixture was allowed to stir overnight, during which time a precipitate formed. The precipitate was purified by flash column chromatography (1-3% MeOH in DCM) to afford a pink solid. This was then dissolved in a minimum of hot MeCN and crystallization was induced through addition of Et_2O. The crystals were collected by filtration to provide TBTA **3.10** (7.78 g, 14.7 mmol, 85%) as a white crystalline solid.

^{1}H NMR (400 MHz, $CDCl_3$) δ 7.65 (s, 3H, C<u>H</u>-3), 7.38 – 7.30 (m, 9H, C<u>H</u>-6 and C<u>H</u>-6' and C<u>H</u>-8), 7.29 – 7.22 (m, 6H, C<u>H</u>-7 and C<u>H</u>-7'), 5.50 (s, 6H, C<u>H</u>$_2$-4), 3.70 (s, 6H, C<u>H</u>$_2$-1); **^{13}C{^{1}H} NMR** (101 MHz, $CDCl_3$) δ 134.7, 129.1, 128.7, 128.0, 54.2; **HRMS** (ESI) *m/z* calcd for $C_{30}H_{31}N_{10}$ $[M+H]^+$: 531.2728, found: 531.2725. Consistent with reported literature values.[49]

3-bromopropyl acetate (3.11)



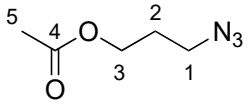
Chemical Formula: $C_5H_9BrO_2$
Molecular Weight: 181.03

Synthesised according to Hong *et al*.[50] A mixture of Ac_2O (2.24 mL, 21.6 mmol, 1.00 eq) and Et_3N (3.31 mL, 21.6 mmol, 1.00 eq) was added to 3-bromopropanol (1.88 mL, 21.6 mmol, 1.00 eq) dissolved in CH_2Cl_2 (30 mL) and stirred at room temperature for an hour. The reaction mixture was washed with saturated aqueous $NaHCO_3$ (2 × 40 mL) and brine

(2 x 40 mL). The organic layer was dried ($MgSO_4$) and concentrated *in vacuo* to afford 3-bromopropyl acetate **3.11** (3.50 g, 19.3 mmol, 90%) as colorless liquid.

^{1}H NMR (400 MHz, $CDCl_3$) δ 4.20 (t, *J* = 6.1 Hz, 2H, C$\underline{H}_2$-3), 3.47 (t, *J* = 6.5 Hz, 2H, C$\underline{H}_2$-1), 2.18 (p, *J* = 6.4 Hz, 2H, C$\underline{H}_2$-2), 2.06 (s, 3H, C$\underline{H}_3$-5); **^{13}C{^{1}H} NMR** (101 MHz, $CDCl_3$) δ 170.9, 62.2, 31.7, 29.4, 20.9. Consistent with reported literature values.[50]

3-Azidopropyl acetate (3.12)

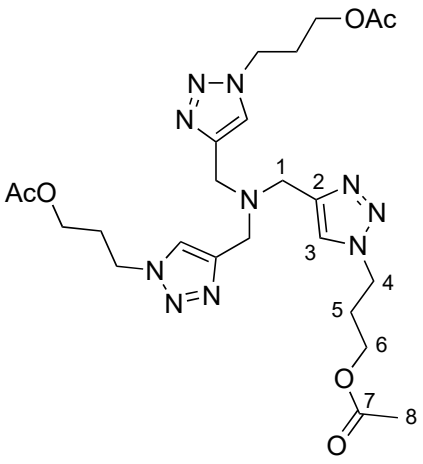


Chemical Formula: $C_5H_9N_3O_2$
Molecular Weight: 143.15

Synthesised according to Hong *et al*.[50] Water (100 mL) and NaN_3 (2.80 g, 43.0 mmol, 2.00 eq) were added to 3-bromopropyl acetate **3.11** (3.50 g, 19.3 mmol, 1.00 eq) and the resulting solution was stirred at 90 °C overnight. The mixture was extracted with dichloromethane (3 × 100 mL). The combined organic layers were dried ($MgSO_4$) and concentrated *in vacuo* to yield 3-azidopropyl acetate **3.12** as pale yellow oil (2.32 g, 15.2 mmol, 79%, some product was lost through evaporation and hydrolysis).

^{1}H NMR (400 MHz, $CDCl_3$) δ 4.15 (t, *J* = 6.2 Hz, 2H, C$\underline{H}_2$-3), 3.40 (t, *J* = 6.7 Hz, 2H, C$\underline{H}_2$-1), 2.06 (s, 3H, C$\underline{H}_3$-5), 1.91 (p, *J* = 6.5 Hz, 2H, C$\underline{H}_2$-2); **^{13}C{^{1}H} NMR** (101 MHz, $CDCl_3$) δ 171.0, 61.3, 48.2, 28.1, 20.9. Consistent with reported literature values.[50]

Tris(3-acetoxypropyltriazolylmethyl)amine (3.13)

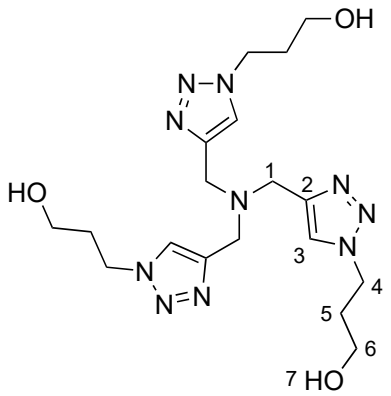


Chemical Formula: $C_{24}H_{36}N_{10}O_6$
Exact Mass: 560.28

Synthesised according to Hong *et al*.[50] 3-Azidopropyl acetate **3.11** (4.91 g, 34.2 mmol, 4.00 eq) was dissolved in *tert*-butyl alcohol (50 mL) in a 100 mL round-bottom flask equipped with a magnetic stir bar. Tripropargylamine (1.21 mL, 8.56 mmol, 1.00 eq) was subsequently added, and the flask was placed in a water bath at rt. $Cu(OAc)_2 \cdot H_2O$ (100 mg, 0.500 mmol, 0.0600 eq) was added in the solid form, and the reaction flask was left uncovered while being stirred for 5 min. The flask was then closed with a rubber septum equipped with an argon balloon. The reaction mixture was allowed to stir overnight, during which the solution gelated. Diethyl ether (100 mL) was added to the flask, and the stirring continued for another 10−20 min. The solvent was evaporated and flash column chromatography (1-3% MeOH in CH_2Cl_2) provided protected THPTA **3.13** (4.75 g, 8.48 mmol, 99% yield) as a white crystalline solid.

^{1}H NMR (400 MHz, $CDCl_3$) δ 7.81 (s, 3H, C<u>H</u>-3), 4.47 (t, *J* = 7.1 Hz, 6H, C<u>H</u>$_2$-4), 4.10 (t, *J* = 6.0 Hz, 6H, C<u>H</u>$_2$-6), 3.74 (s, 6H, C<u>H</u>$_2$-1), 2.32 – 2.23 (m, 6H, C<u>H</u>$_2$-5), 2.08 (s, 9H, C<u>H</u>$_3$-8); **^{13}C{^{1}H} NMR** (101 MHz, $CDCl_3$) δ 171.0, 143.9, 124.2, 61.0, 47.2, 47.0, 29.5, 21.0; **HRMS** (ESI) *m/z* calcd for $C_{24}H_{37}O_6N_{10}$ $[M+H]^+$: 561.2892, found: 561.2889. Consistent with reported literature values.[50]

Tris(3-hydroxypropyltriazolylmethyl)amine (THPTA, Ligand B) (3.14)

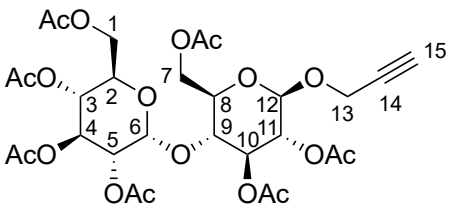


Chemical Formula: $C_{18}H_{30}N_{10}O_3$
Molecular Weight: 434.51

Synthesised according to Hong *et al*.[50] Tris(3-acetoxypropyltriazolylmethyl)amine **3.13** (4.75 g, 8.48 mmol, 1.00 eq) was treated with ammonia in MeOH (2 M, 160 mL) and the mixture was stirred at 40°C overnight. The solution was concentrated, and the residue dried under high vacuum. The resulting pale-yellow solid was dispersed in acetonitrile, sonicated to further break up the solid, filtered, washed with acetonitrile, and dried under vacuum to yield THPTA **3.14** (3.66 g, 84.2 mmol, quantitative yield) as a white solid.

^{1}H NMR (400 MHz, D_2O) δ 7.91 (s, 3H, C<u>H</u>-3), 4.48 (t, *J* = 7.0 Hz, 6H, C<u>H</u>$_2$-4), 3.80 (s, 6H, C<u>H</u>$_2$-1), 3.55 (t, *J* = 6.2 Hz, 6H, C<u>H</u>$_2$-6), 2.10 (p, *J* = 6.7 Hz, 6H, C<u>H</u>$_2$-5); **^{13}C{^{1}H} NMR** (101 MHz, D_2O) δ 143.9, 125.9, 58.8, 48.1, 47.8, 32.4; **HRMS** (ESI) *m/z* calcd for $C_{18}H_{31}O_3N_{10}$ $[M+H]^+$: 435.2575, found: 435.2573. Consistent with reported literature values.[50]

Propargyl hepta-O-acetyl-β-d-maltopyranoside (3.15)

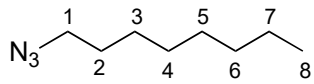


Chemical Formula: $C_{29}H_{38}O_{18}$
Molecular Weight: 674.61

A flame-dried 250 mL flask was charged with peracetylated maltose (19.0 g, 28.0 mmol, 1.00 eq) (Section 2.5.2) and 4 Å MS (5.00 g), capped with a rubber septum and filled with argon. To the flask, dry DCM (100 mL) and propargyl alcohol (3.26 mL, 56.0 mmol, 2.00 eq) were sequentially added via syringe. The reaction mixture was cooled to 0 °C with an ice bath and $BF_3 \cdot Et_2O$ (12.0 mL, 84.0 mmol, 3.00 eq) was slowly added dropwise. After stirring overnight, the reaction was quenched by slow addition of sat. aq. K_2CO_3 (100 mL). The organic layer was subsequently washed with H_2O (100 mL) and brine (100 mL), dried ($MgSO_4$), concentrated *in vacuo* and purified by flash column chromatography (30% EtOAc in hexane) to yield propargyl hepta-O-acetyl-β-d-maltopyranoside **3.15** (12.0 g, 17.8 mmol, 64%) as a brown foam. **3.15** was obtained exclusively as the β-anomer, residual starting material consisted of pure α-anomer.

^{1}H NMR (400 MHz, $CDCl_3$) δ 5.41 (d, *J* = 4.0 Hz, 1H, C<u>H</u>-6), 5.35 (dd, *J* = 10.6, 9.5 Hz, 1H, C<u>H</u>-4), 5.28 (t, *J* = 8.9 Hz, 1H, C<u>H</u>-10), 5.05 (dd, *J* = 10.3, 9.5 Hz, 1H, C<u>H</u>-3), 4.90 – 4.81 (m, 2H, C<u>H</u>-11 and C<u>H</u>-5), 4.80 (d, *J* = 7.8 Hz, 1H, C<u>H</u>-12), 4.50 (dd, *J* = 12.1, 2.7 Hz, 1H, C<u>H$_a$</u>H$_b$-7), 4.35 (d, *J* = 2.4 Hz, 2H, C<u>H$_2$</u>-13), 4.24 (ddd, *J* = 11.8, 7.4, 4.1 Hz, 2H, C<u>H$_a$</u>H$_b$-1 and CH$_a$<u>H$_b$</u>-7), 4.08 – 3.99 (m, 2H, CH$_a$<u>H$_b$</u>-1 and C<u>H</u>-9), 3.95 (ddd, *J* = 10.3, 3.9, 2.3 Hz, 1H, C<u>H</u>-2), 3.72 (ddd, *J* = 9.6, 4.3, 2.7 Hz, 1H, C<u>H</u>-8), 2.47 (t, *J* = 2.4 Hz, 1H, C<u>H</u>-15), 2.14 (s, 3H, C<u>H$_3$</u>CO), 2.10 (s, 3H, C<u>H$_3$</u>CO), 2.04 (s, 3H, C<u>H$_3$</u>CO), 2.04 (s, 3H, C<u>H$_3$</u>CO), 2.02 (s, 3H, C<u>H$_3$</u>CO), 2.01 (s, 3H, C<u>H$_3$</u>CO), 2.00 (s, 3H, C<u>H$_3$</u>CO); **^{13}C{^{1}H} NMR** (101 MHz, $CDCl_3$) δ 170.6, 170.6, 170.3, 170.1, 169.8, 169.5, 97.7, 95.6, 78.2, 75.7, 75.4, 72.6, 72.3, 71.9, 70.1, 69.4, 68.6, 68.1, 62.7, 61.6, 60.5, 56.0, 21.02, 20.95, 20.80, 20.79, 20.72, 20.70; **HRMS** (ESI) *m/z* calcd for $C_{29}H_{38}O_{18}Na$ $[M+Na]^+$: 697.1950, found: 697.1932; **IR** (ATR) ν (cm^{-1}) thin film, CH_2Cl_2: 3275 (w), 2960 (w), 1748 (s), 1434 (w), 1369 (m), 1229 (s), 1040 (s); **[α]**$^{25}_D$ = +40.8 (c = 1.00, CH_2Cl_2).

1-Azidooctane (3.5)

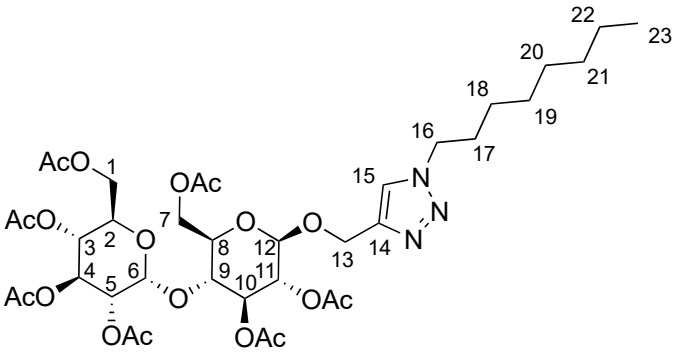


Chemical Formula: $C_8H_{17}N_3$
Molecular Weight: 155.25

Synthesised according to Murnane *et al*.[51] Bromo alkane (8.95 mL, 51.8 mmol, 1.00 eq) and sodium azide (10.0 g, 155 mmol, 3.00 eq) were added to a mixture of acetone:water (3:1, 80 mL). The solution was heated to 60 °C for 8 h. After completion of reaction, the solution was cooled to room temperature and excess solvent was removed under vacuum. The resulting aqueous solution was extracted with hexane (3 × 80 mL). The combined organic extracts were washed with brine, dried ($MgSO_4$) and excess solvent was removed *in vacuo* to obtain 1-azidooctane **3.5** (6.32 g, 40.7 mmol, 79%) as a transparent liquid.

^{1}H NMR (400 MHz, $CDCl_3$) δ 3.25 (t, *J* = 7.0 Hz, 2H, C<u>H</u>-1), 1.64 – 1.54 (m, 2H, C<u>H</u>-2), 1.42 – 1.19 (m, 10H, (C<u>H</u>$_2$)$_5$-3,4,5,6,7), 0.91 – 0.85 (m, 3H, C<u>H</u>$_3$-8); **^{13}C{^{1}H} NMR** (101 MHz, $CDCl_3$) δ 51.6, 31.9, 29.3, 29.2, 29.0, 26.8, 22.8, 14.2. Consistent with reported literature values.[51]

1-Octyl-4-(propargyl hepta-O-acetyl-β-d-maltopyranosidyl) triazole (3.16)



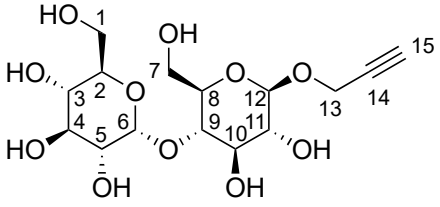
Chemical Formula: $C_{37}H_{55}N_3O_{18}$
Molecular Weight: 829.85

Synthesised according to general procedure 1 using maltose alkyne **3.15** (2.00 g, 2.96 mmol, 1.00 eq), CuI (28 mg, 0.15 mmol, 0.051 eq), DIPEA (60 µL, 0.36 mmol, 0.12 eq) AcOH (16 µL, 0.28 mmol, 0.90 eq) and 1-azidooctane (628 µL, 3.56 mmol, 1.20 eq).

Flash column chromatography (30% EtOAc in hexane) provided 1-octyl-4-(propargyl hepta-O-acetyl-β-d-maltopyranosidyl) triazole **3.16** (2.02 g, 2.44 mmol, 82%) as a white foam.

^{1}H NMR (400 MHz, $CDCl_3$) δ 7.50 (s, 1H, C<u>H</u>-15), 5.41 (d, *J* = 4.0 Hz, 1H, C<u>H</u>-6), 5.40 – 5.30 (m, 1H, C<u>H</u>-4), 5.24 (t, *J* = 9.1 Hz, 1H, C<u>H</u>10), 5.05 (t, *J* = 9.9 Hz, 1H, C<u>H</u>-3), 4.94 – 4.78 (m, 4H, C<u>H</u>-10 and C<u>H</u>-5 and C<u>H_2</u>-16), 4.68 (d, *J* = 7.9 Hz, 1H, C<u>H</u>-12), 4.52 (dd, *J* = 12.2, 2.7 Hz, 1H, C<u>H_a</u>H_b-7), 4.34 (t, *J* = 7.3 Hz, 2H, C<u>H_2</u>-13), 4.24 (ddd, *J* = 12.1, 10.0, 4.1 Hz, 2H, C<u>H_a</u>H_b-1 and CH_a<u>H_b</u>-7), 4.07 – 3.98 (m, 2H, CH_a<u>H_b</u>-1 and C<u>H</u>-9), 3.96 (ddd, *J* = 10.2, 3.8, 2.4 Hz, 1H, C<u>H</u>-2), 3.71 (ddd, *J* = 9.6, 4.3, 2.6 Hz, 1H, C<u>H</u>-8), 2.15 (s, 3H, C<u>H_3</u>CO), 2.10 (s, 3H, C<u>H_3</u>CO), 2.04 (s, 3H, C<u>H_3</u>CO), 2.03 (s, 3H, C<u>H_3</u>CO), 2.00 (s, 3H, C<u>H_3</u>CO), 1.99 (s, 3H, C<u>H_3</u>CO), 1.97 (s, 3H, C<u>H_3</u>CO), 1.90 (q, *J* = 7.2 Hz, 2H, C<u>H_2</u>-17), 1.35 – 1.21 (m, 10H, (C<u>H_2</u>)$_5$-18-22), 0.90 – 0.85 (m, 3H, C<u>H_3</u>-23); **^{13}C{^{1}H} NMR** (101 MHz, $CDCl_3$) δ 170.7, 170.6, 170.3, 170.1, 169.8, 169.6, 122.7, 99.5, 95.6, 75.4, 72.7, 72.4, 72.2, 70.1, 69.4, 68.6, 68.1, 63.1, 62.8, 61.6, 50.5, 31.8, 30.4, 29.2, 29.1, 26.6, 22.7, 21.0, 20.83, 20.78, 20.74, 20.73, 20.71, 14.2; **HRMS** (ESI) *m/z* calcd for $C_{37}H_{56}O_{18}N_3$ $[M+H]^+$: 830.3553, found: 830.3549; **IR** (ATR) ν (cm^{-1}) thin film, CH_2Cl_2: 2960 (w), 2858 (w), 1751 (s), 1436 (w), 1369 (m), 1230 (s), 1043 (s); **[α]**$^{25}_D$ = +28.7 (c = 0.50, CH_2Cl_2).

Propargyl-β-d-maltopyranoside (3.4)

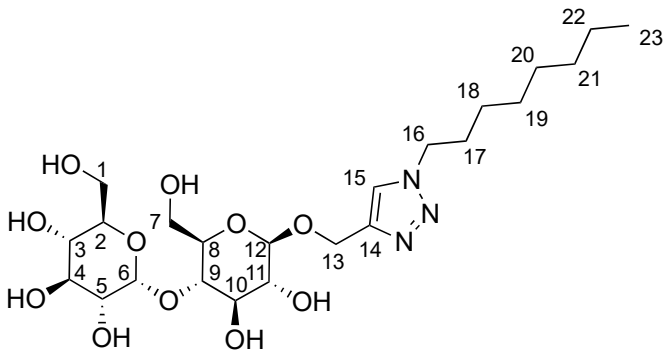


Chemical Formula: $C_{15}H_{24}O_{11}$
Molecular Weight: 380.35

Synthesised according to general procedure 2 using protected maltose alkyne **3.15** (1.46 g, 2.16 mmol, 1.00 eq) and NaOMe (50 mg, 0.93 mmol, 0.43 eq). After concentration *in vacuo* propargyl-β-d-maltopyranoside **4** (809 mg, 2.13 mmol, 98%) was obtained as a hygroscopic, off white foam.

^{1}H NMR (400 MHz, CD_3OD) δ 5.13 (d, *J* = 3.8 Hz, 1H, C<u>H</u>-6), 4.44 (d, *J* = 7.8 Hz, 1H, C<u>H</u>-12), 4.38 (dd, *J* = 4.1, 2.5 Hz, 2H, C<u>H$_2$</u>-13), 3.86 (dd, *J* = 12.2, 2.1 Hz, 1H, C<u>H$_a$</u>H$_b$-7), 3.81 – 3.74 (m, 2H, C<u>H$_a$</u>H$_b$-1 and CH$_a$<u>H$_b$</u>-7), 3.67 – 3.62 (m, 2H, CH$_a$<u>H$_b$</u>-1 and C<u>H</u>-3), 3.61 (d, *J* = 5.8 Hz, 1H, C<u>H</u>-10), 3.59 – 3.54 (m, 1H, C<u>H</u>-4), 3.50 (t, *J* = 9.2 Hz, 1H, C<u>H</u>-9), 3.40 (dd, *J* = 9.7, 3.8 Hz, 1H, C<u>H</u>-5), 3.34 (ddd, *J* = 9.7, 4.8, 2.2 Hz, 1H, C<u>H</u>-8), 3.22 (ddd, *J* = 9.3, 8.4, 5.0 Hz, 2H, C<u>H</u>-2 and C<u>H</u>-11), 2.84 (t, *J* = 2.4 Hz, 1H); **^{13}C{^{1}H} NMR** (101 MHz, CD_3OD) δ 102.9, 102.0, 81.2, 80.0, 77.72, 76.68, 76.3, 75.0, 74.8, 74.4, 74.1, 71.5, 62.7, 62.1, 56.6; **HRMS** (ESI) *m/z* calcd for $C_{15}H_{24}O_{11}Na$ $[M+Na]^+$: 403.1211, found: 403.1211; **IR** (ATR) ν (cm^{-1}) thin film, MeOH: 3355 (s), 2924 (w), 1362 (w), 1146 (m), 1073 (s), 1029 (s), 640 (m); **[α]**$^{25}_D$ = +29.9 (c = 1.00, MeOH).

1-Octyl-4-(propargyl-β-d-maltopyranosidyl) triazole (3.6)



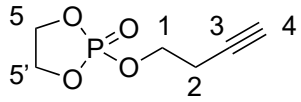
Chemical Formula: $C_{23}H_{41}N_3O_{11}$
Molecular Weight: 535.59

Synthesised according to general procedure 2 using protected surfactant **3.16** (2.00 g, 2.42 mmol, 1.00 eq) and NaOMe (50 mg, 0.93 mmol, 0.38 eq). After concentration 1-octyl-4-

(propargyl-β-d-maltopyranosidyl) triazole **3.6** (790 mg, 1.48 mmol, 61%) was obtained as a hygroscopic, off white foam.

^{1}H NMR (400 MHz, CD_3OD) δ 8.07 (s, 1H, C<u>H</u>-15), 5.12 (d, *J* = 3.8 Hz, 1H, C<u>H</u>-6), 4.94 (d, *J* = 12.6 Hz, 1H, C<u>H$_a$</u>H$_b$-13), 4.77 (d, *J* = 12.6 Hz, 1H, CH$_a$<u>H$_b$</u>-13), 4.31 (4.34 – 4.29 (m, 3H, C<u>H</u>-12 and C<u>H$_2$</u>-16), 3.88 (dd, *J* = 12.2, 2.1 Hz, 1H, C<u>H$_a$</u>H$_b$-7), 3.84 – 3.73 (m, 2H, C<u>H$_a$</u>H$_b$-1 and CH$_a$<u>H$_b$</u>-7), 3.64 (ddd, *J* = 8.6, 5.8, 1.6 Hz, 2H, CH$_a$<u>H$_b$</u>-1 and C<u>H</u>-3), 3.60 – 3.52 (m, 2H, C<u>H</u>-10 and C<u>H</u>-4), 3.51 – 3.47 (m, 1H, C<u>H</u>-9), 3.43 – 3.35 (m, 2H, C<u>H</u>-5 and C<u>H</u>-8), 3.25 – 3.21 (m, 2H, C<u>H</u>-2 and C<u>H</u>-11), 1.88 (p, *J* = 6.8 Hz, 2H, C<u>H$_2$</u>-17), 1.36 – 1.20 (m, 10H, (C<u>H$_2$</u>)$_5$-18-22), 0.89 – 0.83 (m, 3H, C<u>H$_3$</u>-23); **^{13}C{^{1}H} NMR** (101 MHz, CD_3OD) δ 145.2, 125.7, 103.6, 102.9, 81.3, 77.7, 76.7, 75.0, 74.8, 74.6, 74.1, 71.4, 62.7, 62.2, 51.8, 32.9, 31.2, 30.2, 30.0, 27.4, 23.7, 14.4; **HRMS** (ESI) *m/z* calcd for $C_{23}H_{41}O_{11}N_3Na$ $[M+Na]^+$: 558.2633, found: 558.2630; **IR** (ATR) ν (cm^{-1}) thin film, MeOH: 3362 (s), 2926 (s), 2857 (m), 1647 (w), 1458 (w), 1148 (m), 1106 (s), 1074 (s); **[α]**$^{25}_D$ = +41.0 (c = 1.00, MeOH).

2-(But-3-yn-1-yloxy)-1,3,2-dioxaphospholane 2-oxide (3.17)



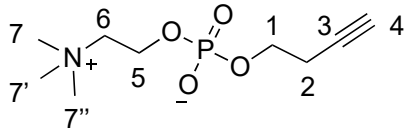
Chemical Formula: $C_6H_9O_4P$
Molecular Weight: 176.1078

Synthesised according to adapted procedure from Hu *et al*.[52] To a solution of 3-butyn-1-ol (1.06 mL, 14.0 mmol, 1.00 eq) in anhydrous THF (20 mL) was added triethylamine (2.15 mL, 15.4 mmol, 1.10 eq) at 0 °C under argon atmosphere. After slow addition of 2-chloro-2-oxo-1,3,2-dioxaphospholane (1.29 mL, 14.0 mmol, 1.00 eq), the mixture was warmed to room temperature and stirred for 2 hours. The white suspension was filtered over a sintered funnel, and the filtrate was concentrated by rotary evaporation and dried

in vacuo to give phospholane **3.17** (2.30 g, 13.1 mmol, 93%) as a yellow oil. This was used without further purification due to decomposition of **3.17** on silica.

^{1}H NMR (400 MHz, $CDCl_3$) δ 4.50 – 4.32 (m, 4H, C$\underline{H}_2$-5 and C$\underline{H}_2$-5'), 4.24 (dt, J = 9.5, 6.8 Hz, 2H, C$\underline{H}_2$-1), 2.62 (td, J = 6.8, 2.7 Hz, 2H, C$\underline{H}_2$-2), 2.04 (t, J = 2.7 Hz, 1H, C$\underline{H}$-4); **^{13}C{^{1}H} NMR** (101 MHz, $CDCl_3$) δ 79.2, 70.6, 66.4 (d, J_{CP} = 5.7 Hz), 66.2 (d, J_{CP} = 3.1 Hz, 2C), 20.9 (d, J_{CP} = 6.6 Hz); **^{31}P NMR** (162 MHz, $CDCl_3$) δ 17.4. Consistent with reported literature values.[53]

But-3-yn-1-yl (2-(trimethylammonio)ethyl) phosphate (3.7)



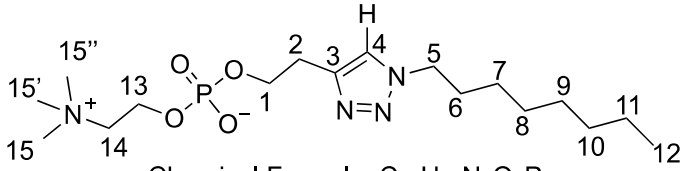
Chemical Formula: $C_9H_{18}NO_4P$
Molecular Weight: 235.2198

Synthesized according to adapted procedure from Liu *et al*.[54] Crude phospholane **3.17** (2.30 g, 13.1 mmol, 1.00 eq) was dissolved in dry MeCN (20 mL) in a 100 mL flame dried flask under argon. After trimethylamine (21 mL, 21 mmol, 1.6 eq, 1 M in THF) was added, the flask was closed and heated to 70 °C for 48 h. The crude mixture was concentrated *in vacuo* and purified by flash column chromatography (10% H_2O and 40% MeOH in CH_2Cl_2) to yield phosphocholine **3.7** (2.42 g, 10.3 mmol, 79%) as a transparent oil that crystallizes in the freezer.

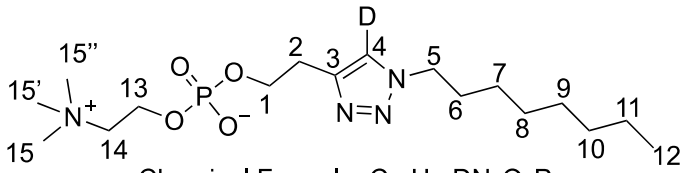
^{1}H NMR (400 MHz, CD_3OD) δ 4.29 (tq, J = 6.9, 2.7 Hz, 2H, C$\underline{H}_2$-5), 3.96 (q, J = 7.0 Hz, 2H, C$\underline{H}_2$-1), 3.67 – 3.62 (m, 2H, C$\underline{H}_2$-6), 3.23 (s, 9H, C$\underline{H}_3$-7 and C$\underline{H}_3$-7' and C$\underline{H}_3$-7''), 2.53 (td, J = 6.8, 2.7 Hz, 2H, C$\underline{H}_2$-2), 2.30 (t, J = 2.6 Hz, 1H, C$\underline{H}_2$-4); **^{13}C{^{1}H} NMR** (101 MHz, CD_3OD) δ 81.8, 71.0, 67.5 – 67.3 (m, J_{CN^+} and J_{CP}), 65.0 (d, J_{CP} = 5.6 Hz), 60.4 (d, J_{CN^+} = 4.9 Hz), 54.8 – 54.6 (m, 3C, J_{CN^+}), 49.8, 30.7, 24.2, 21.6 (d, J_{CP} = 7.9 Hz); **^{31}P NMR** (162 MHz, CD_3OD) δ -0.55; **HRMS** (ESI) *m/z* calcd for $C_9H_{19}NO_4P$ $[M+H]^+$:

236.1046, found: 236.1045; **IR** (ATR) ν (cm^{-1}) thin film, MeOH: 3273 (broad m), 2361 (w), 1654 (w), 1479 (w) 1229 (m), 1083 (s), 1051 (s), 970 (w), 926 (w).

2-(1-Octyl-1*H*-1,2,3-triazol-4-yl)ethyl (2-(trimethylammonio)ethyl) phosphate (3.8)



Chemical Formula: $C_{17}H_{35}N_4O_4P$
Molecular Weight: 390.4648



Chemical Formula: $C_{17}H_{34}DN_4O_4P$
Molecular Weight: 391.4709

A solution of phosphocholine **3.7** (192 mg, 0.816 mmol, 1 eq, 2 mL of 96 mg/mL standard solution in D_2O), $CuSO_4 \cdot 5H_2O$ (6.0 mg, 0.024 mmol, 0.030 eq, 1.0 mL of 6.0 mg/mL standard solution in D_2O) were added to *t*-BuOH (2 mL). The flask was capped with a septum and the solution was degassed by bubbling argon through it for 30 minutes. Subsequently ligand **B** (25.5 mg, 0.600 eq), azide **3.5** (288 µL, 1.63 mmol, 2.00 eq) and sodium ascorbate (16.2 mg, 0.0820 mmol, 0.100 eq) were added. The crude mixture was concentrated *in vacuo* and purified by flash column chromatography (10% H_2O and 40% MeOH in CH_2Cl_2) to yield phosphocholine **3.8** (263 mg, 0.672 mmol, 82%) as a colorless wax. Partial deuteration of the triazole occurred because the reaction was performed in the presence of deuterated water.

^{1}H NMR (400 MHz, CD_3OD) δ 7.88 (s, 1H, C<u>H</u>-4), 4.36 (t, J = 7.2 Hz, 2H, C<u>H</u>$_2$-5), 4.26 – 4.17 (m, 2H, C<u>H</u>$_2$-13), 4.13 (q, J = 6.4 Hz, 2H, C<u>H</u>$_2$-1), 3.65 – 3.59 (m, 2H, C<u>H</u>$_2$-14), 3.22 (s, 9H, C<u>H</u>$_3$-15 and C<u>H</u>$_3$-15' and C<u>H</u>$_3$-15''), 3.04 (t, J = 6.3 Hz, 2H, C<u>H</u>$_2$-2), 1.89 (p, J = 7.1 Hz, 2H, C<u>H</u>$_2$-6), 1.41 – 1.21 (m, 10H, (C<u>H</u>$_2$)$_5$-7-11), 0.96 – 0.86 (m, 2H, C<u>H</u>$_3$-12); **^{13}C{^{1}H} NMR** (101 MHz, CD_3OD) δ 67.6 – 67.2 (m, J_{CN^+} and J_{CP}), 65.6 (d, J_{CP} = 5.2

Hz), 60.3 (d, J_{CN}^{+} = 4.5 Hz), 55.42 – 52.40 (m, 3C, J_{CN}^{+}), 51.3, 32.9, 31.3, 30.2, 30.1, 28.2 (d, J = 7.4 Hz), 27.5, 23.6, 14.4; **^{31}P NMR** (162 MHz, CD_3OD) δ -0.58; **HRMS** (ESI) *m/z* calcd for $C_{17}H_{34}DO_4N_4P$ $[M+H]^+$: 392.2532, found: 392.2534; **IR** (ATR) ν (cm^{-1}) thin film, MeOH: 3377 (broad s), 2926 (m), 2856, (w), 2359 (m), 2342 (w), 1655 (w), 1469 (w) 1227 (m), 1086 (s), 970 (w).

3.7.3 Fluorimetry Data

The critical micelle concentrations of surfactant **3.6** was determined as described in Section 2.5.3.

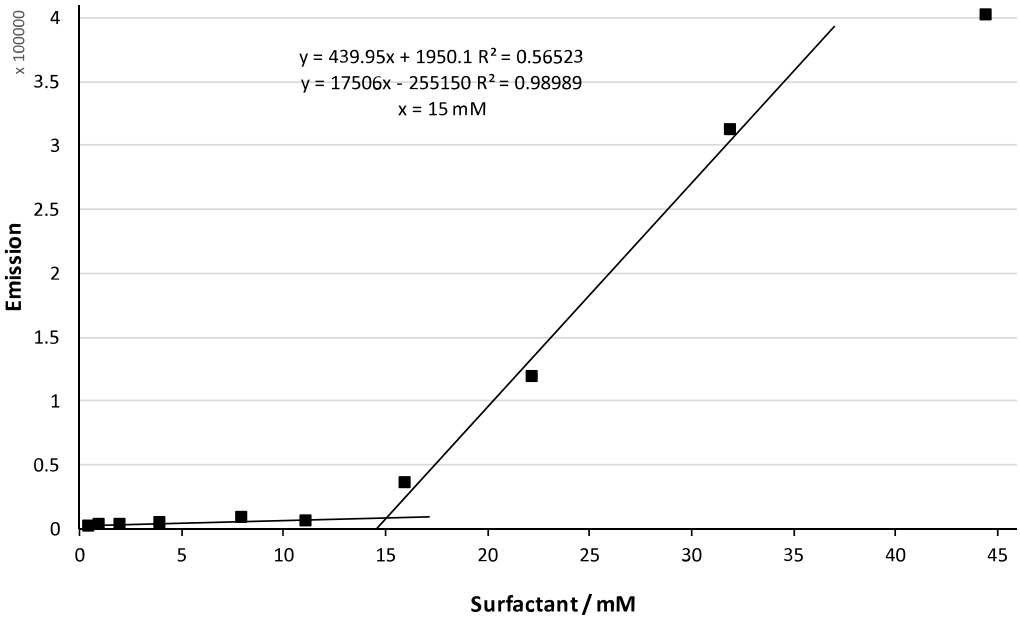


Figure 3.12 CMC of 15 mM was extracted from a plot of fluorescence measurements at various concentration for surfactant **3.6**.

3.7.4 DLS data

Measurements were performed as described in section 2.5.4.

Sample Name:	EP140flipfiltered 1		
SOP Name:	Water-25C.sop		
File Name:	210817.dts	**Dispersant Name:**	Water
Record Number:	4	**Dispersant RI:**	1.330
Material RI:	1.45	**Viscosity (cP):**	0.8872
Material Absorbtion:	0.001	**Measurement Date and Time:**	21 August 2017 2:04 pm

Temperature (°C):	25.0	**Duration Used (s):**	60
Count Rate (kcps):	330.6	**Measurement Position (mm):**	3.00
Cell Description:	Disposable micro cuvette (40µl)	**Attenuator:**	11

			Size (d.nm):	**% Intensity:**	**St Dev (d.nm):**
Z-Average (d.nm):	5.580	**Peak 1:**	5.938	91.0	2.604
PdI:	0.240	**Peak 2:**	845.9	9.0	609.8
Intercept:	0.730	**Peak 3:**	0.000	0.0	0.000

Result quality : Good

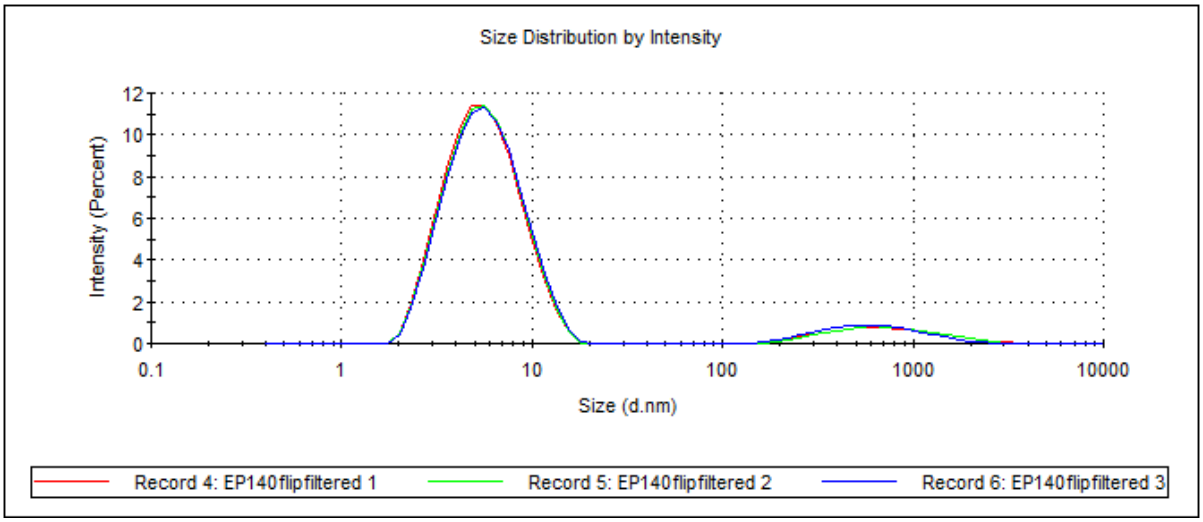
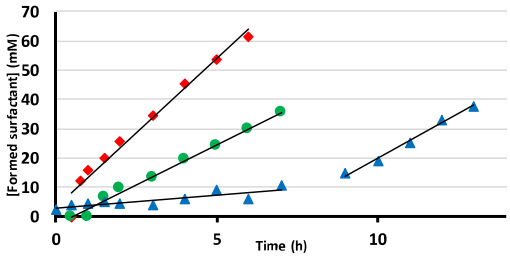


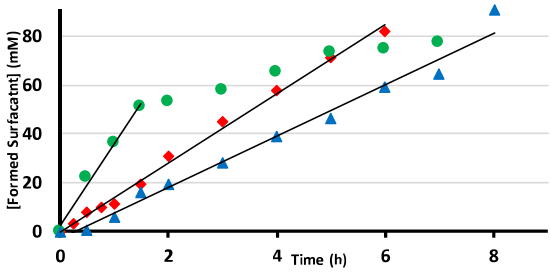
Figure 3.13 The size distribution by intensity of a DLS measurement of surfactant **3.6** at 30 mM indicates micelle aggregates with a size of around 6 nm.

3.7.5 Tables of extract reaction rates



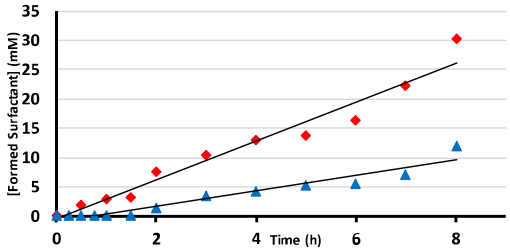
Ligand A	Ligand B_1	Ligand B_2	Ligand C
V_{max} = 5.86 ± 0.13 mM h^{-}	V_{lag} = 0.922 ± 0.06 mM h^{-}	V_{max} = 5.72 ± 0.34 mM h^{-}	V_{max} =10.2 ± 1.80 mM h^{-}
R^2 = 0.988	R^2 = 0.747	R^2 = 0.992	R^2 = 0.972

Table 3.4 Maximum rate of conversion with standard deviation over three independent repeats extracted from Figure 2, **B** with a trend line. Where B_1 is from data points during the lag period and B_2 is after the lag period.



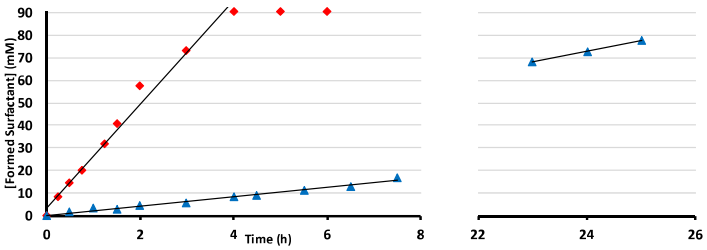
Ligand A	Ligand B	Ligand C
V_{max} = 33.5 ± 2.00 mM h^{-1}	V_{max} = 10.7 ± 0.01 mM h^{-1}	V_{max} = 14.1 ± 1.69 mM h^{-1}
R^2 = 0.989	R^2 = 0.997	R^2 = 0.996

Table 3.5 Maximum rate of conversion with standard deviation over three independent repeats extracted from Figure 2, **C** with a trendline.



Ligand B	Ligand C
V_{lag} = 1.46 ± 0.60 mM h^{-1}	V_{max} = 3.35 ± 0.97 mM h^{-1}
R^2 = 0.806	R^2 = 0.957

Table 3.6 Maximum rate of conversion with standard deviation over three independent repeats extracted from Figure 5, **B** with a trendline.



Ligand B_1	Ligand B_2	Ligand C
V_{lag} = 2.05 ± 0.28 mM h^{-1}	V_{max} = 4.64 ± 0.25 mM h^{-1}	V_{max} = 23.0 ± 0.63 mM h^{-1}
R^2 = 0.987	R^2 = 1	R^2 = 0.986

Table 3.7 Maximum rate of conversion with standard deviation over three independent repeats extracted from Figure 5, **C** with a trendline, where B_1 is from data points during the lag period and B_2 is after the lag period.

3.8 References

1 E. A. J. Post and S. P. Fletcher, Controlling the Kinetics of Self-Reproducing Micelles by Catalyst Compartmentalization in a Biphasic System, *J. Org. Chem.*, 2019, **84**, 2741–2755.

2 U. Brinker and J. Mieusset, *Molecular Encapsulation*, John Wiley & Sons, Ltd, Chichester, UK, 2010.

3 D. M. Vriezema, M. C. Aragonès, J. A. A. W. Elemans, J. J. L. M. Cornelissen, A. E. Rowan and R. J. M. Nolte, Self-assembled nanoreactors, *Chem. Rev.*, 2005, **105**, 1445–1489.

4 O. D. K. Maddocks, C. F. Labuschagne and K. H. Vousden, Localization of NADPH Production: A Wheel within a Wheel, *Mol. Cell*, 2014, **55**, 158–160.

5 C. Clark and C. B. Newgard, in *Mechanisms of Insulin Action*, Springer New York, New York, NY, 2012, pp. 90–109.

6 M. F. Utter and D. T. Chuang, Gluconeogenesis as a Compartmentalized Activity, *Biochem. Soc. Trans.*, 1978, **6**, 11–16.

7 B. H. Lipshutz, Synthetic chemistry in a water world. New rules ripe for discovery, *Curr. Opin. Green Sustain. Chem.*, 2018, **11**, 1–8.

8 P. Stano, P. Carrara, Y. Kuruma, T. Pereira de Souza and P. L. Luisi, Compartmentalized reactions as a case of soft-matter biotechnology: synthesis of proteins and nucleic acids inside lipid vesicles, *J. Mater. Chem.*, 2011, **21**, 18887.

9 J. J. Kozak, in *Advances in Chemical Physics*, 2000, vol. 115, pp. 245–406.

10 T. Litschel, K. A. Ganzinger, T. Movinkel, M. Heymann, T. Robinson, H. Mutschler and P. Schwille, Freeze-thaw cycles induce content exchange between cell-sized lipid vesicles, *New J. Phys.*, 2018, **20**, 055008.

11 N. Nuti, P. E. Verboket and P. S. Dittrich, Multivesicular droplets: a cell model system to study compartmentalised biochemical reactions, *Lab Chip*, 2017, **17**, 3112–3119.

12 T. Hamada, R. Fujimoto, S. F. Shimobayashi, M. Ichikawa and M. Takagi, Molecular behavior of DNA in a cell-sized compartment coated by lipids, *Phys. Rev. E - Stat. Nonlinear, Soft Matter Phys.*, 2015, **91**, 1–5.

13 T. Tanaka and M. Yamazaki, Membrane Fusion of Giant Unilamellar Vesicles of Neutral Phospholipid Membranes Induced by La 3+, *Langmuir*, 2004, **20**, 5160–5164.

14 M. Andes-Koback and C. D. Keating, Complete Budding and Asymmetric Division of Primitive Model Cells To Produce Daughter Vesicles with Different Interior and Membrane Compositions, *J. Am. Chem. Soc.*, 2011, **133**, 9545–9555.

15 S. Tsuda, T. Sakakura, S. Fujii, H. Suzuki and T. Yomo, Shape Transformations of Lipid Vesicles by Insertion of Bulky-Head Lipids, *PLoS One*, 2015, **10**, e0132963.

16 B. C. Buddingh' and J. C. M. van Hest, Artificial Cells: Synthetic Compartments

with Life-like Functionality and Adaptivity, *Acc. Chem. Res.*, 2017, **50**, 769–777.

17 H. H. Zepik, E. Blöchliger and P. L. Luisi, A Chemical Model of Homeostasis, *Angew. Chemie Int. Ed.*, 2001, **40**, 199–202.

18 K. Kurihara, M. Tamura, K. Shohda, T. Toyota, K. Suzuki and T. Sugawara, Self-reproduction of supramolecular giant vesicles combined with the amplification of encapsulated DNA, *Nat. Chem.*, 2011, **3**, 775–781.

19 J. W. Szostak, D. P. Bartel and P. L. Luisi, Synthesizing life, *Nature*, 2001, **409**, 387–390.

20 K. Takakura, T. Toyota and T. Sugawara, A novel system of self-reproducing giant vesicles, *J. Am. Chem. Soc.*, 2003, **125**, 8134–8140.

21 P. S. Donnelly, S. D. Zanatta, S. C. Zammit, J. M. White and S. J. Williams, ' Click ' cycloaddition catalysts : copper (I) and copper (II) tris (triazolylmethyl) amine complexes w, 2008, **233**, 2459–2461.

22 T. R. Chan, R. Hilgraf, K. B. Sharpless and V. V Fokin, Polytriazoles as Copper(I)-Stabilizing Ligands in Catalysis, *Org. Lett.*, 2004, **6**, 2853–2855.

23 S. N. Semenov, L. Belding, B. J. Cafferty, M. P. S. Mousavi, A. M. Finogenova, R. S. Cruz, E. V. Skorb and G. M. Whitesides, Autocatalytic Cycles in a Copper-Catalyzed Azide–Alkyne Cycloaddition Reaction, *J. Am. Chem. Soc.*, 2018, **140**, 10221–10232.

24 R. J. Brea and N. K. Devaraj, Continual reproduction of self-assembling oligotriazole peptide nanomaterials, *Nat. Commun.*, 2017, **8**, 730.

25 M. D. Hardy, J. Yang, J. Selimkhanov, C. M. Cole, L. S. Tsimring and N. K. Devaraj, Self-reproducing catalyst drives repeated phospholipid synthesis and membrane growth, *Proc. Natl. Acad. Sci.*, 2015, **112**, 8187–8192.

26 S. I. Presolski, V. Hong, S. Cho and M. G. Finn, Tailored Ligand Acceleration of the Cu-Catalyzed Azide - Alkyne Cycloaddition Reaction : Practical and Mechanistic Implications, *J. Am. Chem. Soc.*, 2010, **132**, 14570–14576.

27 B. R. Buckley, S. E. Dann, D. P. Harris, H. Heaney and E. C. Stubbs, Alkynylcopper(i) polymers and their use in a mechanistic study of alkyne-azide click reactions, *Chem. Commun.*, 2010, **46**, 2274–2276.

28 M. Meldal and C. W. Tornøe, Cu-Catalyzed Azide−Alkyne Cycloaddition, *Chem. Rev.*, 2008, **108**, 2952–3015.

29 J. E. Hein and V. V. Fokin, Copper-catalyzed azide-alkyne cycloaddition (CuAAC) and beyond: New reactivity of copper(i) acetylides, *Chem. Soc. Rev.*, 2010, **39**, 1302–1315.

30 L. Li and Z. Zhang, Development and applications of the copper-catalyzed azide-alkyne cycloaddition (CuAAC) as a bioorthogonal reaction, *Molecules*, 2016, **21**, 1–22.

31 R. Evans, Z. Deng, A. K. Rogerson, A. S. McLachlan, J. J. Richards, M. Nilsson and G. A. Morris, Quantitative interpretation of diffusion-ordered NMR spectra: Can we rationalize small molecule diffusion coefficients?, *Angew. Chemie - Int. Ed.*, 2013, **52**, 3199–3202.

32 C. C. Miller, The Stokes-Einstein Law for Diffusion in Solution, *Proc. R. Soc. A Math. Phys. Eng. Sci.*, 1924, **106**, 724–749.

33 T. Hashimoto and K. Maruoka, in *Asymmetric Phase Transfer Catalysis*, Wiley-VCH Verlag GmbH & Co. KGaA, Weinheim, Germany, 2008, pp. 1–8.

34 C. M. Starks, C. L. Liotta and M. E. Halpern, in *Phase-Transfer Catalysis*, Springer Netherlands, Dordrecht, 1994, pp. 23–47.

35 I. A. Esikova, Y. Sasson and R. Neumann, *Handbook of Phase Transfer Catalysis*, Springer Netherlands, Dordrecht, 1997.

36 P. A. Bachmann, P. L. Luisi and J. Lang, Autocatalytic self-replicating micelles as models for prebiotic structures, *Nature*, 1992, **357**, 57–59.

37 T. Buhse, D. Lavabre, R. Nagarajan and J. C. Micheau, Origin of autocatalysis in the biphasic alkaline hydrolysis of C-4 to C-8 ethyl alkanoates, *J. Phys. Chem. A*, 1998, **102**, 10552–10559.

38 T. Buhse, R. Nagarajan, D. Lavabre and J. C. Micheau, Phase-transfer model for the dynamics of '"micellar autocatalysis"', *J. Phys. Chem. A*, 1997, **101**, 3910–3917.

39 R. Berg and B. F. Straub, Advancements in the mechanistic understanding of the copper-catalyzed azide-alkyne cycloaddition, *Beilstein J. Org. Chem.*, 2013, **9**, 2715–2750.

40 L. Jin, D. R. Tolentino, M. Melaimi and G. Bertrand, Isolation of bis(copper) key intermediates in Cu-catalyzed azide-alkyne 'click reaction', *Sci. Adv.*, 2015, **1**, e1500304–e1500304.

41 W. G. Lewis, F. G. Magallon, V. V. Fokin and M. G. Finn, Discovery and Characterization of Catalysts for Azide−Alkyne Cycloaddition by Fluorescence Quenching, *J. Am. Chem. Soc.*, 2004, **126**, 9152–9153.

42 C. Nolte, P. Mayer and B. F. Straub, Isolation of a Copper(I) Triazolide: A "Click" Intermediate, *Angew. Chemie Int. Ed.*, 2007, **46**, 2101–2103.

43 V. V. Rostovtsev, L. G. Green, V. V. Fokin and K. B. Sharpless, A Stepwise Huisgen Cycloaddition Process: Copper(I)-Catalyzed Regioselective "Ligation" of Azides and Terminal Alkynes, *Angew. Chemie Int. Ed.*, 2002, **41**, 2596–2599.

44 V. O. Rodionov, V. V. Fokin and M. G. Finn, Mechanism of the Ligand-Free CuI-Catalyzed Azide-Alkyne Cycloaddition Reaction, *Angew. Chemie Int. Ed.*, 2005, **44**, 2210–2215.

45 V. D. Bock, H. Hiemstra and J. H. van Maarseveen, CuI-Catalyzed Alkyne-Azide "Click" Cycloadditions from a Mechanistic and Synthetic Perspective, *European J. Org. Chem.*, 2006, 51–68.

46 V. O. Rodionov, S. I. Presolski, D. Díaz Díaz, V. V. Fokin and M. G. Finn, Ligand-Accelerated Cu-Catalyzed Azide−Alkyne Cycloaddition: A Mechanistic Report, *J. Am. Chem. Soc.*, 2007, **129**, 12705–12712.

47 D. G. Blackmond, An Examination of the Role of Autocatalytic Cycles in the Chemistry of Proposed Primordial Reactions, *Angew. Chemie Int. Ed.*, 2009, **48**, 386–390.

48 W. A. Loughlin, I. D. Jenkins, N. D. Karis and P. C. Healy, Discovery of new nanomolar inhibitors of GPa: Extension of 2-oxo-1,2-dihydropyridinyl-3-yl amide-based GPa inhibitors, *Eur. J. Med. Chem.*, 2017, **127**, 341–356.

49 H. A. Michaels and L. Zhu, in *Encyclopedia of Reagents for Organic Synthesis*, John Wiley & Sons, Ltd, Chichester, UK, 2011, pp. 1–7.

50 V. Hong, S. I. Presolski, C. Ma and M. G. Finn, Analysis and optimization of copper-catalyzed azide-alkyne cycloaddition for bioconjugation., *Angew. Chem. Int. Ed. Engl.*, 2009, **48**, 9879–83.

51 W. Li, A. a Jaroń-Becker, C. W. Hogle, V. Sharma, X. Zhou, A. Becker, H. C. Kapteyn and M. M. Murnane, Visualizing electron rearrangement in space and time during the transition from a molecule to atoms., *Proc. Natl. Acad. Sci.*, 2010, **107**, 20219–20222.

52 G. Hu and T. Emrick, Functional Choline Phosphate Polymers, *J. Am. Chem. Soc.*, 2016, **138**, 1828–1831.

53 E. Y. Zeynep, D. Antoine, C. Brice, B. Frank and J. Christine, Double hydrophilic polyphosphoester containing copolymers as efficient templating agents for calcium carbonate microparticles, *J. Mater. Chem. B*, 2015, **3**, 7227–7236.

54 L. Liu, M. E. Lee, P. Kang and M. G. Choi, Revisit to Synthesis of Allyl- and Propargyl-Phosphorylcholines: Crystal Structure of Allyl-Phosphorylcholine, *Phosphorus, Sulfur Silicon Relat. Elem.*, 2015, **190**, 1525–1534.

Chapter 4 Out-of-Equilibrium Self-Reproducing Protocells: Competition, Inhibition and Secondary Metabolism

The results of this chapter have been submitted for publication in *Chemical Science*. All experiments were designed and performed by Elias Post under the supervision of Prof. Stephen Fletcher. Part of the supramolecular characterisation of the protocells was performed in the Katsonis lab at University of Twente.

4.1 Introduction

The system of physical autocatalysis driven by CuAAC developed in Chapter 2, combined with the mechanistic understanding obtained in Chapter 3 on how to control reactivity through catalyst compartmentalisation, laid the groundwork for a more advanced self-reproducing system. Research in the Fletcher group had focused mainly on micellar autocatalysis, since aggregate formation is well-behaved and requires simple starting materials.[1–5] However, a system of self-reproducing vesicles may be designed to study more dynamic and complex behaviour and to model biological cells more faithfully. Section 1.3 discussed the importance of creating a protocell model that exhibits core-and-shell reproduction to further our understanding of abiogenesis and to develop a truly living system.

We believed that our system of physical autocatalysis driven by CuAAC would be ideally suited to take on the task of shell reproduction in an artificial cell. The robust nature of the CuAAC reaction was expected to tolerate vesicle-forming coupling partners and to be compatible with orthogonal chemistry taking place within the vesicle. We therefore set out to develop a system of self-reproducing protocells driven by CuAAC that could be used as a platform to subsequently introduce orthogonal chemistry and dynamic kinetic behaviour.

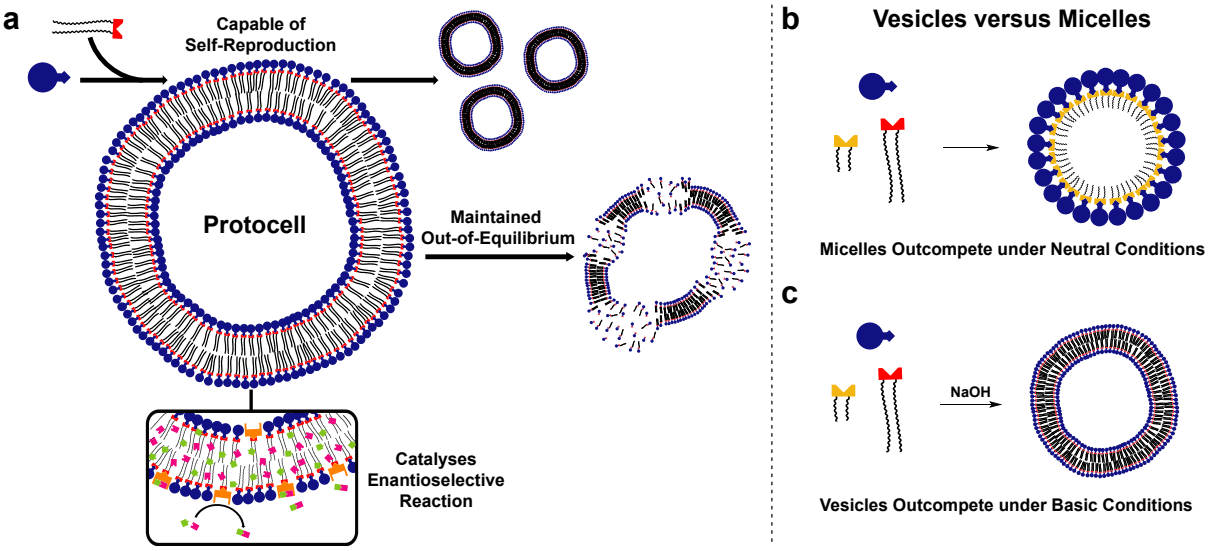


Figure 4.1 A protocell system featuring several emergent functionalities. **a.** Schematic representation of a protocell that is capable of self-reproduction, can be maintained out-of-equilibrium, and can catalyse enantioselective reactions. Competition experiments between two replicators select for micellar aggregates under neutral conditions (**b**) and vesicular aggregates under basic conditions (**c**).

This chapter reports the study of self-reproducing phospholipid vesicles generated from phase-separated reagents *via* CuAAC. This coupling reaction has previously been used as a biomimetic method to drive *de novo* vesicular membrane assembly.[6–8] The system can self-reproduce while in an out-of-equilibrium steady-state, out-competes a faster micellar replicator under specific reaction conditions, and is able to generate an organocatalyst with orthogonal reactivity (Figure 4.1a). Out-of-equilibrium self-reproduction is achieved by establishing conditions in which phospholipid product is formed but also subsequently destroyed by hydrolysis. Rudimentary selection processes are observed for micelle- and vesicle-based autocatalysts competing for a common feedstock. Environmental conditions determine which species dominates: Under pH-neutral conditions micelles are selected for *via* a mechanism in which vesicle formation is inhibited (Figure 4.1b), whilst under basic conditions the formation of vesicles is favoured over micellar aggregates (Figure 4.1c). Additionally, a secondary metabolism within vesicle protocells is enabled by catalysing the *in situ* formation of an amphiphilic organocatalyst which, after embedding in the vesicle bilayer, becomes catalytically active. Subsequently, the protocell functions as an enantioselective nanoreactor, enabling

downstream orthogonal chemical reactivity. Overall, self-reproducing protocells with several emergent, life-like properties are generated *in situ* from simple chemical building blocks.

4.2 Results and discussion

4.2.1 Designing a system of self-reproducing protocells

The protocell systems reported here operate through a mechanism of physical autocatalysis driven by CuAAC analogous to the systems described in Chapter 2 and 3.[4,5,9,10] Compound **4.1** was selected as azide coupling partner with two oleic ester chains as hydrophobic tails. The azide was installed on the centre carbon of glycerol to afford a prochiral substrate, thereby circumventing potential regioisomer formation, which could complicate analysis. Meanwhile, phosphocholine **4.2** was used as alkyne-containing hydrophilic headgroup. Phospholipid **4.3** is obtained when **4.1** and **4.2** react at the interface *via* a CuAAC with a hydrophobic copper-ligand complex (step i, Figure 4.2). This surfactant is analogous in structure to naturally occurring glycerophospholipids that make up biological membranes,[11] but differs by its prochiral nature as the phosphocholine moiety is connected to the central glycerol carbon.

Product **4.3** aggregates into vesicles, as opposed to micelles, once a critical aggregation concentration (CAC) of surfactant is reached (step ii). The two-tailed surfactant **4.3** takes up the volume of a truncated cone, inducing vesicle formation, while the formation of micelles requires a conal shape.[12] Vesicles can take up hydrophobic **4.1** and Cu-complex from the organic phase into the hydrophobic bilayer and act as phase-transfer catalyst (step iii) to facilitate reaction with phase-separated **4.2**. This accelerates the formation of **4.3**, with self-reproduction closing the autocatalytic cycle (step iv).

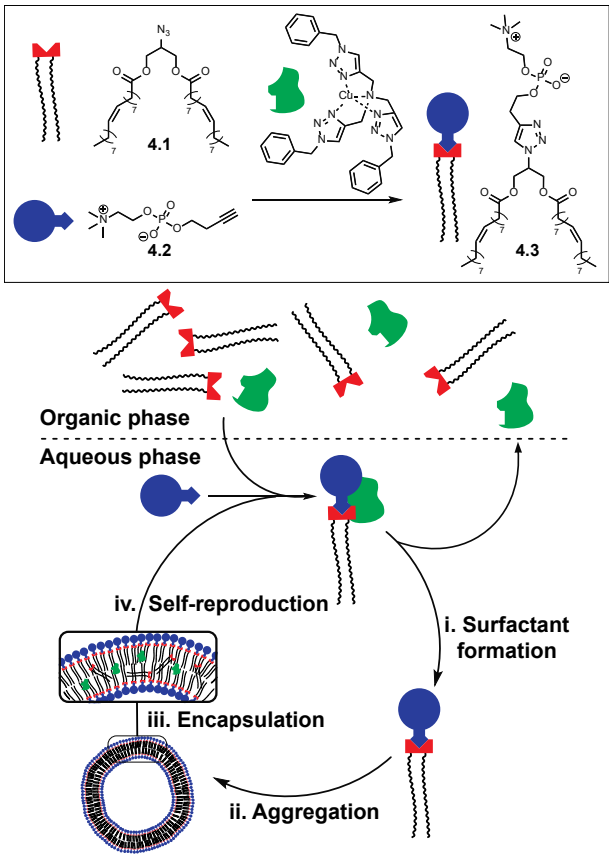


Figure 4.2 Schematic representation of the mechanism of self-reproducing protocells. Two-tailed azide **4.1** reacts with phosphocholine **4.2** to form phospholipid **4.3** catalysed by a hydrophobic copper complex. Surfactant **4.3** aggregates into vesicles and encapsulates any hydrophobic substrates in the bilayer. This facilitates phase-transfer and interaction with hydrophilic azide **4.2**, accelerating the reaction.

4.2.2 Characterisation of supramolecular properties

The large size and stability of vesicular aggregates enabled the study of the supramolecular properties of **4.3** by a wide variety of analytical techniques not available to us in the previous systems (Chapters 2 and 3). Fluorimetry measurements indicated a CAC of 0.68 μM for **4.3**, much lower than that of micellar systems studied previously (Section 4.8.3, Figure 4.14). Dynamic light scattering (DLS) measurements confirmed the presence of aggregates that increase in size with increasing concentration, from diameter of 300 nm at 40 μM, to micron sized vesicles at 4 mM (Section 4.8.4, Figure 4.16). The aggregates decreased in size when the same samples were stirred, possibly due to shearing forces. UV-VIS absorption measurements showed a wavelength-independent increase in absorption with increasing concentration, suggesting an increase in turbidity

due to the formation of more and larger aggregates that diffract light (Section 4.8.5). Spherical aggregates with diameters mostly in the range of 1-30 nm, but with outliers up to 180 nm, were observed by TEM analysis of **4.3** at 4 mM (Section 4.8.6, Figure 4.25). Confocal microscopy of **4.3** at different concentrations showed multilaminar vesicles that increased in size and density with increasing concentration (Section 4.8.7, Figure 4.29-4.37).

4.2.3 Kinetic investigation

Reaction conditions were optimised by screening stirring speed, catalyst loading and reaction concentration to obtain a sigmoidal rate profile for the formation of **4.3** at convenient time scales. Azide **4.1** is significantly more hydrophobic than previously studied hydrophobic coupling partners due to the two 18-carbon tails, which meant that a higher catalyst loading (10%) and stirring speed (1000 rpm) were required to get an appreciable rate of product formation. Furthermore, when hydrophilic ligand **B** from Chapter 3 was employed the reaction was slowed down to such a significant degree that no product formation was observed after 5 days.

Kinetic analysis of the unseeded reaction under the optimised conditions (Section 4.8.2) revealed a lag period of approximately 6 hours followed by a period with faster formation of **4.3** (Figure 4.3, red squares). Seeding the reaction at $t = 0$ with **4.3** at a concentration (4 mM) above the CAC reduced the length of the lag period to 4 hours and increased the rate of product formation (blue diamonds), suggestive of a physical autocatalytic mechanism. However, the lag period was not completely eliminated as is normally observed in seeded micellar autocatalytic systems.[2–5,9] The unseeded reaction was repeated in a 1:1 water/*tert*-butanol solvent mixture, leading to an elimination of the lag

period and complete conversion in 1.5 hours (Section 4.8.9, Figure 4.50). This confirms that phase separation is responsible for the lag period and non-linear kinetics.

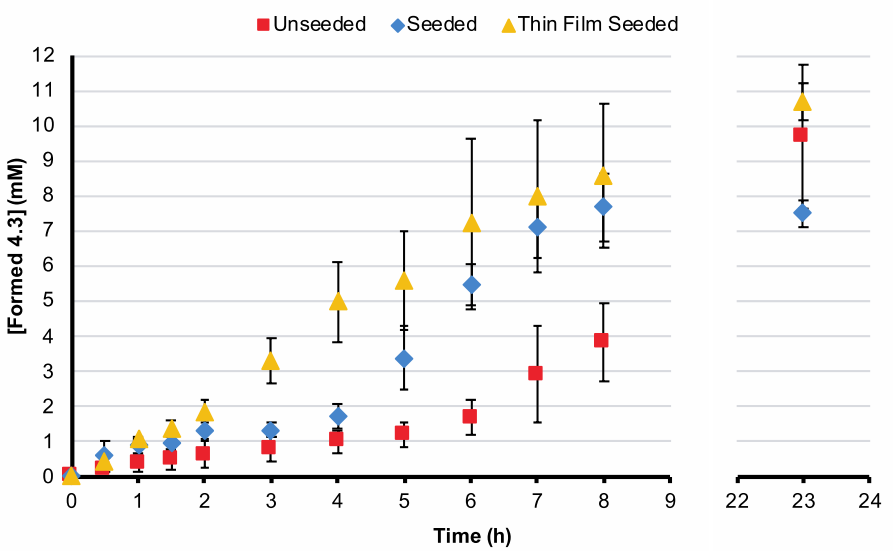


Figure 4.3 Kinetic results showing autocatalytic formation of **4.3** over time under unseeded (red squares), seeded (4 mM, blue diamonds) conditions. Seeded through a different method of thin-film hydration (4 mM, yellow triangles) fully eliminated the lag period, as further discussed below. Reactions are monitored by UPLC-analysis. Points are the mean of three independent experiments and the error bars indicate the standard deviation (n=3).

Changes in the supramolecular structure of the aggregates were monitored throughout the reaction. TEM analysis of aliquots of the unseeded reaction at $t = 0$ showed no aggregates (only salt crystals of the negative stain), but analyses at later time points (after **4.3** had formed) indicated the presence of increasingly larger aggregates (Figure 4.4a and 4.27 for additional time points). When the same aliquots were studied by confocal microscopy, only stained oil droplets of **4.1** were observed at $t = 0$, whereas later time points showed largely unilaminar vesicles of <5 micron size (Figure 4.4b and 4.39 for additional time points). DLS analysis indicated a population of micron sized vesicles that grew over time when analysed based on intensity of scattering (Figure 4.4c). However, this is a biased result as large particles give a high scattering signal despite being few in number. DLS analysis by particle number indicated that the majority of vesicles did not become larger than 30 - 100 nm in size regardless of reaction time (Figure 4.19), possibly due to the shearing forces introduced by stirring the reaction.

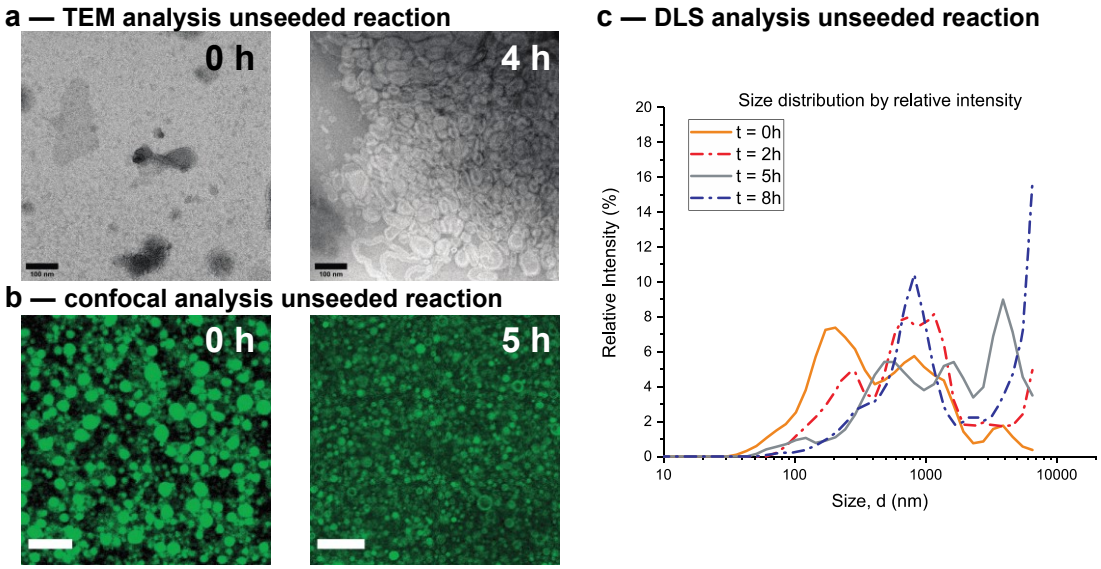


Figure 4.4 Supramolecular characterisation of vesicles in unseeded reaction (Figure 4.3, red squares). **a.** TEM images at different time points of aliquots of the unseeded reaction (negatively stained with 2% uranyl acetate solution). Scale bar, 100 nm and 0.5 μm. **b.** Confocal images at different time points of aliquots of the unseeded reaction (stained with 5 μM Coumarin 6 solution). Scale bar, 10 μm. **c.** Size distribution by intensity of the aggregates in aliquots of the unseeded reaction at different time points measured by DLS.

Supramolecular analysis of the seeded reactions confirmed the presence of aggregates at $t = 0$ by both TEM and confocal analysis (Figure 4.5a and b). Vesicles with sizes of >20 micron were observed by TEM (Figure 4.28 for additional time points), while confocal microscopy indicated that vesicles became multilaminar to such a degree that no aqueous interior is visible; they appeared to be completely filled with stained multilaminar membrane (Figure 4.39 for additional time points). DLS analysis of these samples by intensity showed a growing population of aggregates in the 1-10 micron range (Figure 4.5c) but, as with the unseeded reaction, analysis by number indicates that the majority of vesicles remained in the 20-100 nm range independent of reaction time when analysed by number (Figure 4.20).

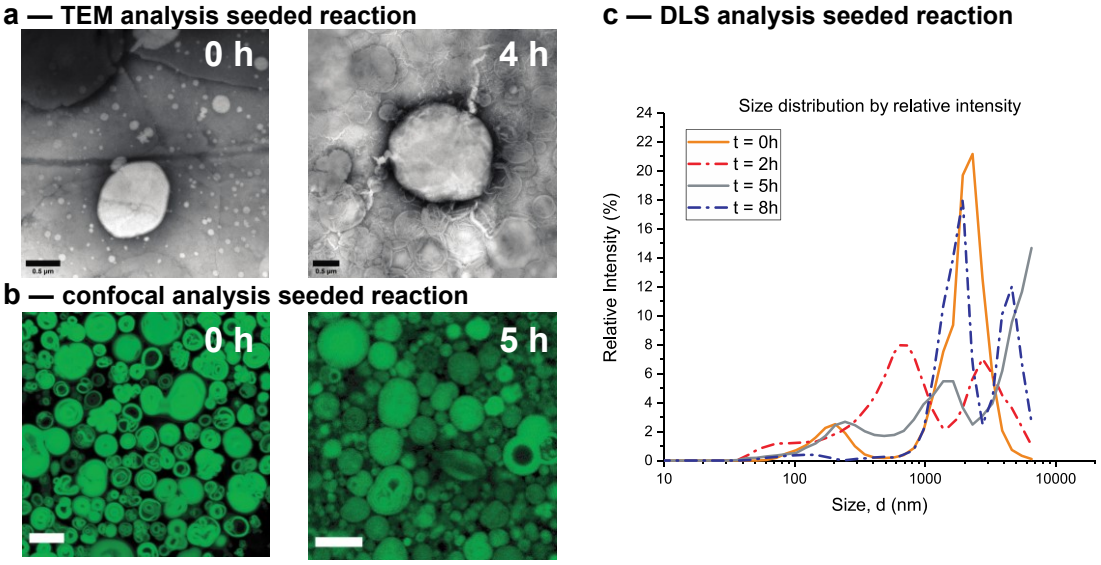


Figure 4.5 Supramolecular characterization of vesicles in seeded reaction (Figure 4.3, blue diamonds). **a.** TEM images at different time points of aliquots of the seeded reaction (negatively stained with 2% uranyl acetate solution). Scale bar, 100 nm and 0.5 μm respectively. **b.** Confocal images at different time points of aliquots of the seeded reaction respectively (stained with 5 μM Coumarin 6 solution). Scale bar, 10 μm. **c.** Size distribution by intensity of the aggregates in aliquots of the reaction at different time points measured by DLS.

Overall, unseeded and seeded experiments show differences in supramolecular structure of the vesicles. Aggregates formed *in situ* stay small and unilaminar throughout the reaction, whereas seeded aggregates are large and multilaminar throughout the reaction without significant formation of additional small, unilaminar vesicles. The multilaminar nature of seeded vesicles might be the reason for the low efficiency of autocatalysis: the catalyst complex or hydrophobic substrate **4.1** sequestered in inner layers of the multilaminar aggregates could be physically separated from hydrophilic **4.2** and thus unable to form **4.3**. Furthermore, inner layers might not be able to take up new material and participate in the transfer between phases. This might cause the lag period observed for seeded reactions, where the seeded product is an ineffective autocatalyst, unable to efficiently accelerate the reaction (Figure 4.3).

Giant unilaminar vesicles (GUV) of **4.3** were generated through the hydration of a thin film,[13–15] as opposed to simple dissolution of purified **4.3**, to test the hypothesis that multilaminarity decreases catalytic efficiency. Confocal analysis showed unilaminar

aggregates (Figure 4.38) and DLS indicated a decrease in size compared to normal dissolution of **4.3** (Figure 4.17). Seeding the reaction with GUVs fully eliminated the lag period and led to a more significant rate acceleration (Figure 4.3, yellow triangles). Confocal micrographs of aliquots indicated that unilaminar vesicles were still present at later time points (Figure 4.41), while the majority of aggregates are 20 nm in diameter according to DLS analysis by number (Figure 4.21). We conclude that variations in supramolecular morphology of the vesicles heavily influences the efficiency of the autocatalyst and the kinetics of the overall reaction.

4.3 Out-of-equilibrium self-reproduction

Maintaining a system in an out-of-equilibrium state by the continuous consumption of chemical energy is important to accurately mimic self-assembly and reproduction processes occurring in nature, as discussed in Section 1.4. Our self-reproducing system could transition into an out-of-equilibrium regime by introducing conditions that result in transient formation of the replicator.[2,3] An autocatalyst that is under the continuous pressure of degradation while constantly being regenerated will not reach thermodynamic equilibrium and allows for study of the system in an out-of-equilibrium state.

Increasing the basicity of the aqueous phase enabled destructive hydrolysis of the ester moieties in the phospholipid, making **4.3** transient. Meanwhile, esters in hydrophobic **4.1** do not hydrolyse over the time scale of the reaction due to phase-separation as determined by ^{1}H NMR spectroscopic analysis. The hydrolysis of one or two ester moieties in **4.3** gives degradation product **4.4** or **4.5** respectively, in addition to oleate as a side product (Figure 4.6). Hydrolysis should not only lead to destruction of the monomers but also of the supramolecular structure of the vesicles, affecting the system's capacity to self-reproduce. A second prerequisite for out-of-equilibrium reproduction is continuous

regeneration of the transient replicator through constant supply of starting material. This was achieved through the continuous addition of hydrophobic (Figure 4.6b; syringe i) and hydrophilic (syringe ii) coupling partners, and removal of by-products (syringe iii) from the reaction flask with syringe pumps. This setup forms a continuously stirred-tank reactor (CSTR) which prevents the reaction from fully equilibrating, maintaining the system in an out-of-equilibrium state.

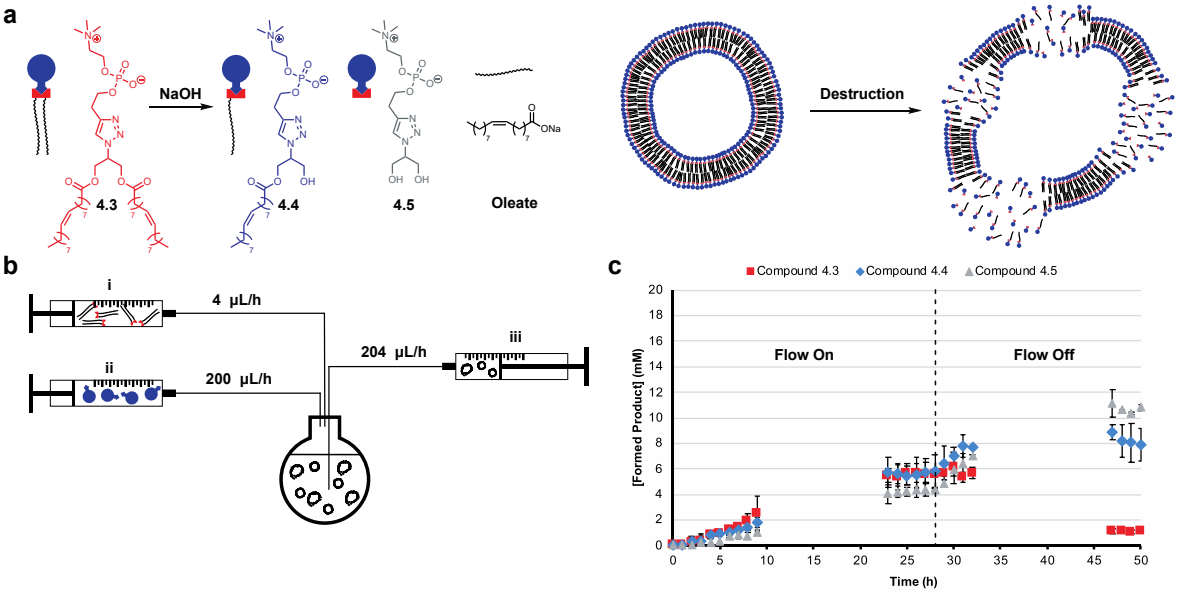


Figure 4.6 Formation of a transient out-of-equilibrium replicator. **a.** Schematic representation of the destruction of vesicle forming compound **4.3** to hydrolysis products **4.4** and **4.5**. **b.** Schematic representation of the continuously stirred-tank reactor (CSTR) setup. **c.** Kinetic results showing an out-of-equilibrium state of metastable **4.3** with 100 mM NaOH when flow through the CSTR is maintained, followed by degradation when the flow is turned off. Each point is the mean of two independent experiments and the error bars represent the standard deviation (n=2).

The reaction was reoptimised for kinetic analysis under hydrolysing conditions, as the formation of **4.3** was significantly slowed down. This can likely be attributed to the destruction of the autocatalyst which is no longer able to accelerate the reaction. When the loading of copper catalyst was quadrupled, significant product formation was observed at convenient timescales (Figure 4.51). The concentration of NaOH as base was optimised to induce the required degree of hydrolysis of **4.3**. DLS analysis indicated that aggregates decreased in size as the concentration of NaOH was increased (Figure 4.22). Overall, slower reaction rates were observed, and increased hydrolysis occurred with

incremental increases in the concentration of NaOH from 0 mM to 50 mM (Figure 4.52-54). However, the majority of base is consumed to reach the equilibrium composition at these concentrations and when the flow was turned off no further hydrolysis of **4.3** was observed, indicating that the system was not truly out-of-equilibrium. By further increasing the concentration to 100 mM NaOH, an out-of-equilibrium composition of **4.3** at t = 23 h was achieved (Figure 4.6c) which was maintained for 6 hours in the CSTR. When the flow was turned off, the system returned to thermodynamic equilibrium through degradation of any remaining **4.3** to **4.4** and **4.5**, with almost complete destruction after 47 hours.

The out-of-equilibrium state could not be reached during a control experiment under homogeneous conditions. Complete conversion with immediate hydrolysis to **4.5** occurred within 5 hours and turning of the flow led to no further change in the system (Figure 4.55). This indicates that phase-separation and supramolecular aggregation are required to achieve out-of-equilibrium self-reproduction.

Analysis of aliquots of the reaction in Figure 4.6c by DLS showed that the size of the protocells remained below 100 nm throughout the reaction (Figure 4.23). These sizes are below the detection limit of conventional confocal microscopy and could therefore not be observed with this technique. Confocal microscopy confirmed the presence of a mixture of vesicles with amorphous material at earlier time points (<8h), whereas only oil droplets were observed for aliquots taken after 24 hours indicating decomposition of larger vesicles (Figure 4.42). Overall, introduction of base to the system facilitated transient formation of **4.3** which could be utilised to maintain the system in an out-of-equilibrium state by performing the reaction in a CSTR setup.

4.4 Reaction conditions select the winner of competition experiments

A fundamental trait of all living systems is their capability to undergo Darwinian evolution (Section 1.1); this involves selection for specific traits by external pressures. The graded autocatalysis replication domain (GARD) model states that selection among heterogeneous amphiphile assemblies of differing composition can occur due to changes in the environment,[16–18] which might be viewed as a rudimentary form of evolution. We set out to test the GARD model in its most simplified form by employing two amphiphiles analogous in structure but differing in supramolecular morphology: one forms vesicles and the other micelles. The two compounds competed for a common substrate and the basicity of the reaction mixture was tuned to apply an external pressure.

4.4.1 A micellar phospholipid autocatalyst

A novel micellar replicator was developed by employing shorter-tailed azide **4.6** which couples to phosphocholine **4.2** to form phospholipid **4.7** as product (Figure 4.7). This surfactant is analogous in structure to **4.3**, but the length of the hydrophobic chains is shorter. These shorter chains give a cone, as opposed to a truncated cone, shape to **4.7**, and induce aggregation into micelles.[19] DLS and TEM measurements showed the formation of aggregates of 10 nm in size (Figure 4.18 and 4.26). In contrast to **4.3**, the size of these aggregates is constant and independent of the concentration. The critical micelle concentration (CMC) of **4.7** is 27.6 μM as measured by fluorimetry (Figure 4.18). When **4.7** is exposed to base, a single hydrolysis event yields **3.8**, whereas hydrolysis of the second ester affords **3.5**. Hexanoate is obtained as a sideproduct.

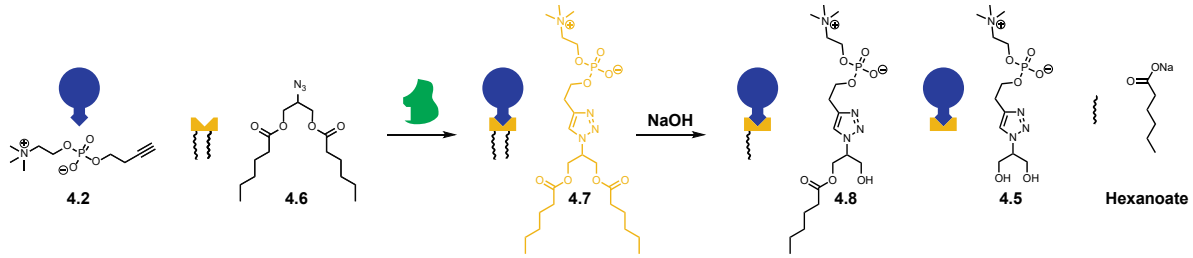


Figure 4.7 Schematic representation of micelle forming **4.7** produced from azide **4.6** and **4.2**, which is degraded by hydrolysis to form **4.5**, **4.8** and hexanoate.

Reaction conditions for this replicator had to be reoptimized due to the high rate of product formation under standard conditions (Figure 4.56). This faster rate could be attributed to the higher solubility of shorter tailed **4.6** in the aqueous phase, similar to the trend observed in Chapter 2. Lowering the stirring speed from 1000 to 400 rpm resulted in a lag period of one hour for the unseeded formation of **4.7** (Figure 4.8, yellow circles). Seeding the reaction at t = 0 with **4.7** at a concentration (4 mM) above the CMC eliminated the lag period and increased the rate of product formation (yellow crosses). When the unseeded reaction was performed in a 1:1 water/*tert*-butanol mixture to facilitate phase mixing, the lag period was eliminated, and complete conversion was observed in 15 minutes (Figure 4.50). Overall, these results are consistent with the autocatalytic formation of **4.7** in a phase-separated system.

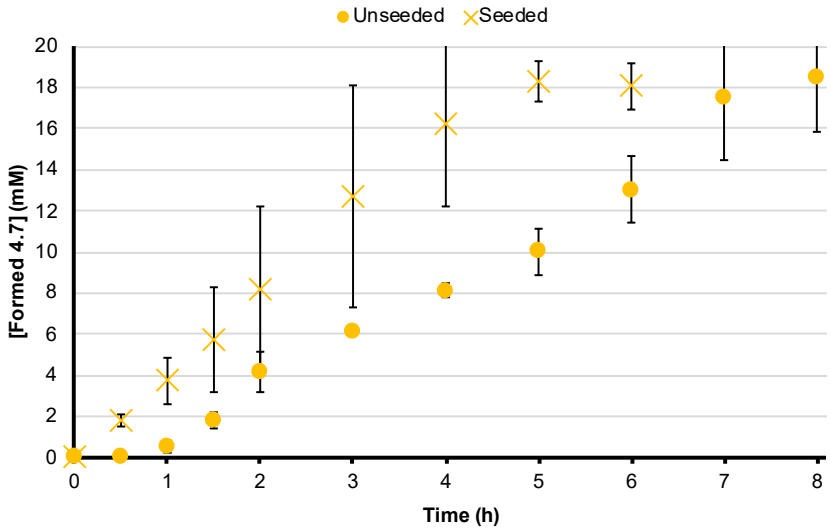


Figure 4.8 Reaction kinetics for the formation of surfactant **4.7** when unseeded (yellow circles), and seeded (yellow crosses) with product **4.7** (4 mM). The unseeded reaction (yellow circles) shows a lag period of 1 hour and complete conversion in 8 hours whereas the seeded reaction (yellow crosses) has no lag period

and is complete in 5 hours. Experimental conditions: performed in batch with a 2 mM copper(I) catalyst loading while stirring at 400 rpm. Points are the mean of three independent experiments and the error bars represent the standard deviation (n=3).

4.4.2 Competition experiments

During an initial competition experiment between azide **4.1** and **4.6** for reaction with alkyne **4.2** under neutral conditions, only product **4.7** was observed, with no formation of **4.3** (Figure 4.9a). However, when the basicity was increased by the addition of 50 mM NaOH both **4.7** and **4.3** formed, and **4.3** reached a higher relative concentration at completion of the reaction (Figure 4.9b; see Figure 4.57 for hydrolysis products).

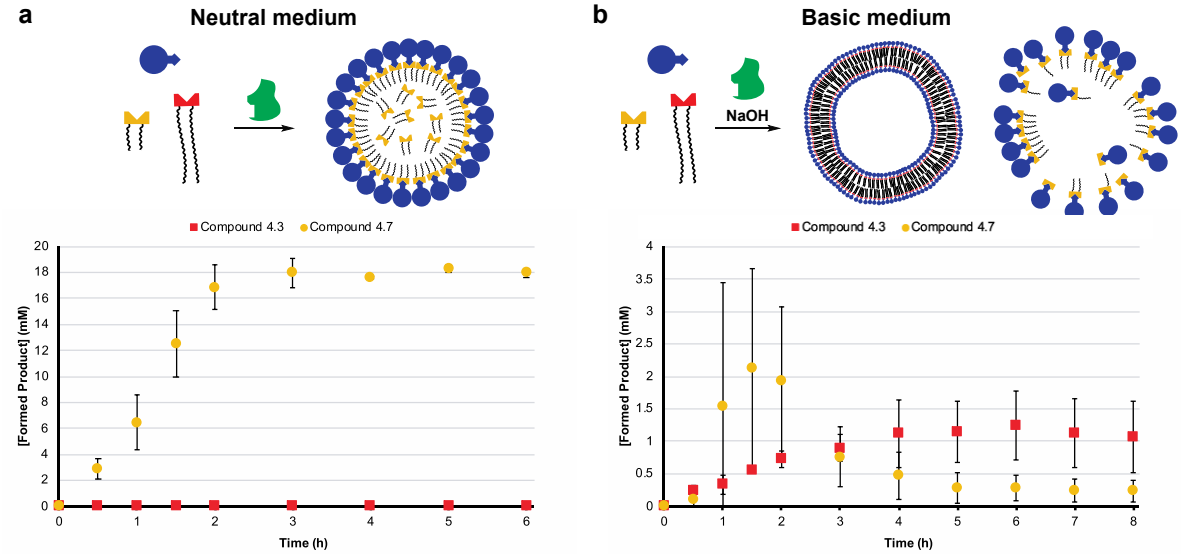


Figure 4.9 Competition experiments between a self-reproducing protocell and a micellar replicator. **a.** Competition between two azides (**4.1** and **4.6**) with alkyne **4.2** to yield **4.3** and **4.7** respectively under neutral conditions. **b.** Competition between **4.1** and **4.6** to give **4.3** and **4.7** in the presence of 50 mM NaOH. Points are the mean of three independent experiments and the error bars are the standard deviation (n=3).

When the competition reaction was repeated in a CSTR setup under basic conditions, an out-of-equilibrium steady-state was reached after 5 hours and was maintained for a further 20 hours. During this period the concentration of **4.3** was higher than **4.7** (Figure 4.10 and 4.58) and when the flow was turned off **4.7** completely degraded whereas **4.3** remained stable.

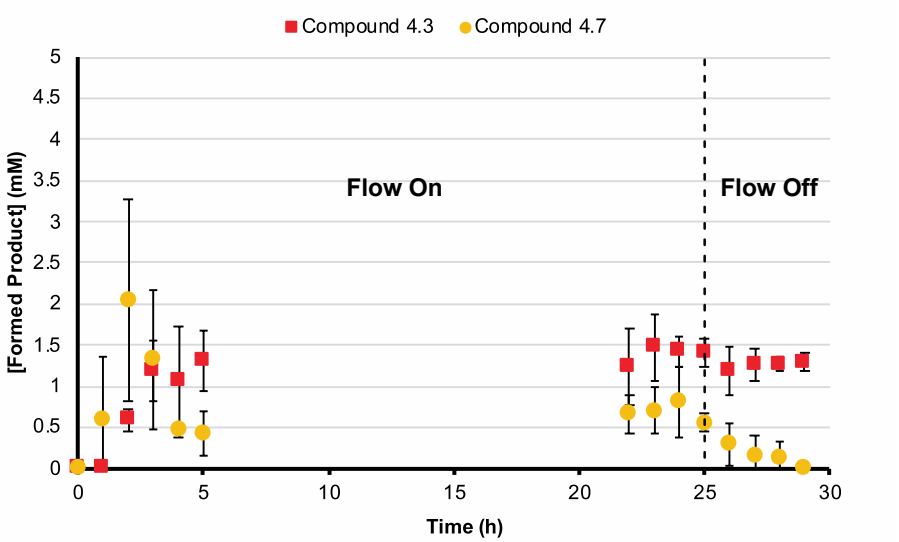


Figure 4.10 Competition between azides **4.1** and **4.6** to give **4.3** and **4.7** with 50 mM NaOH in a CSTR setup. The flow is turned off after 25 hours. Points are the mean of three independent experiments and the error bars are the standard deviation (n=3).

4.4.3 Cross seeding experiments

A reaction to produce **4.3** was seeded with **4.7** and *vice versa* in cross seeding experiments to probe how competing surfactants affect self-reproduction. The formation of **4.7** displayed a similar kinetic profile when seeded with **4.3** or **4.7**, there appeared to be no difference in the degree of acceleration whether micelle or vesicle forming surfactants are employed as catalyst (c.f. Figure 4.8 and 4.59).

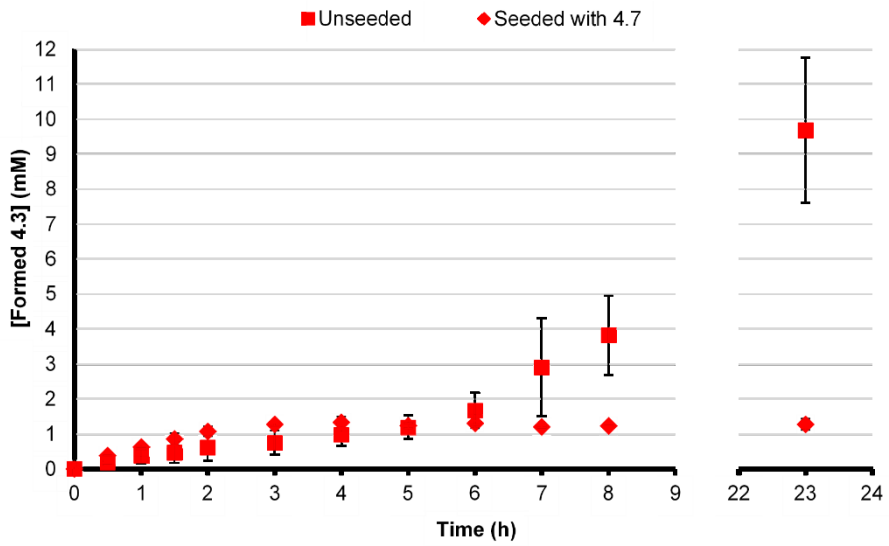


Figure 4.11 Cross-seeding experiment between azide **4.1** and alkyne **4.2** to give **4.3** unseeded (red squares) and seeded with **4.7** (4 mM, red diamonds). All reactions were monitored by UPLC-analysis. Points are the mean of three independent experiments and the error bars are the standard deviation (n=3).

Unexpectedly, seeding the formation of long tailed **4.3** with micelles of **4.7** halted the reaction prematurely, conversion stopped after two hours at around 1 mM, though the lag period was eliminated (Figure 4.11). The addition of **4.7**, after briefly accelerating formation of **4.3**, inhibits any further reaction. This agrees with what was observed during the competition experiments (Figure 4.9a); in the absence of base only **4.7** and no **4.3** is generated. Meanwhile, at increased basicity **4.7** cannot inhibit formation of **4.3** (Figure 4.9b) as it is continuously degraded through hydrolysis, whereas vesicles of **4.3** are less labile towards hydrolysis (Figure 4.60). Overall, this results in a concentration of **4.3** higher than **4.7** in the final reaction composition under basic conditions in both batch and CSTR setups.

4.5 Mechanisms of selection and inhibition

The mechanisms underpinning the outcome of these competition experiments were investigated to understand what leads to autocatalyst selection and what causes the unique inhibitory behaviour. On setting out to perform these competition experiments, we expected micelles to have different reproducing behaviour from vesicles. The supramolecular composition of micelles instils different physical properties: they are fluid and rapidly exchange micellar components with the surrounding solvent in contrast to phospholipid vesicles which are less dynamic and relatively inert.[20,21] Furthermore, micelles lack an aqueous interior and have no inner layers of membrane, whereas multilaminar vesicles have bilayers impermeable to polar compounds which subsequently cannot reach any inner layers of membrane.[22]

Based on these two properties, phospholipid vesicles were expected to be more stable towards hydrolysis than micelles as this requires interaction with water and a polar base. Sutherland and co-workers observed a similar trend, where acylation and hydrolysis

cycling selected for longer-chain acylglycerol-phosphates,[23] which self-assembled into vesicles more stable towards hydrolysis than short chain compounds. Boekhoven and co-workers observed a selection mechanism where shorter-tailed anhydrides are hydrolysed preferentially over longer-tailed anhydrides which phase-separated into oil droplets stabilising them to hydrolysis.[24]

4.5.1 Stability towards hydrolysis

The stability of the aggregates towards hydrolysis was probed by exposing 20 mM of **4.3** or **4.7** to 50 mM of aqueous NaOH. This resulted in limited decomposition of **4.3**, whereas **4.7** was completely hydrolysed in 15 minutes. (Figure 4.60 and 4.61). Repeating the hydrolysis experiment for **4.3** in a 1:1 water/*tert*-butanol mixture, where no aggregation into vesicles occurs, gave complete hydrolysis of **4.3** to **4.4** and **4.5** within 30 minutes (Figure 4.62). Generating either **4.3** or **4.7** *in situ* in 50 mM NaOH leads to similar behaviour, with **4.7** degrading while **4.3** dominates (Figure 4.51 and 4.63). Based on these experiments, vesicles of **4.3** indeed appear to be more stable to hydrolysis than micelles of **4.7**, as long the surfactants are in an aggregated state.

4.5.2 DOSY study

The relative stability towards hydrolysis does not fully explain why **4.3** reached a higher concentration than **4.7** during the competition experiment under basic conditions (Figure 4.9b). This cannot simply be attributed to relative stability as **4.3** never forms under neutral conditions; **4.7** must additionally inhibit formation of **4.3**. Diffusion ordered spectroscopy (DOSY) experiments were performed to probe the mechanism through which inhibition might occur (Table 4.1).

Diffusion coefficients were recorded for all reaction components at the concentrations present in the system during the synthesis of **4.7** in water. The diffusion rates are

consistent with the phase behaviour observed in Chapter 2 and 3: hydrophobic components are solubilized by surfactant aggregates and hydrophilic components do not associate with micelles of **4.7**.

The low CMC of **4.7** (27.6 μM) made it impossible to get ^{1}H NMR measurements at concentrations below this value. However, the diffusion coefficient (*D*) for the aggregated surfactant **4.7** at 4 mM is in agreement with that of micelles analysed in previous chapters[4,5] and decreases with increasing concentration (20 mM), indicating a greater ratio of aggregated to free surfactant (Table 4.1, Entries A-B). Control experiments show that azide **4.6** is insoluble in the absence of surfactant and associates strongly with micelles of **4.7** (Entries C−E). However, long-tailed azide **4.1** is only solubilized at high concentrations of **4.7** (20 mM) and is not observed in the absence, or at lower concentrations, of **4.7** (Entries F−H). The hydrophobic ligand **C** is insoluble in water even at high concentrations of **4.7** (Entries I-K), in contrast to the previous systems investigated, where micelles were able to solubilize this compound. However, when the ligand is coordinated to copper strong association with **4.7** is observed (Entries L-N). Hydrophilic alkyne **4.2** is soluble without **4.7** and does not associate with micelles (Entries O−Q).

Phase-behaviour of aggregates of **4.3** in D_2O could not be studied by ^{1}H NMR due to the ill-defined broad peaks in the spectra that were obtained, likely due to long relaxation times. The rigid stacking of individual molecules of **4.3** in the vesicle bilayer, and the slow movement of large aggregates, might prevent spin relaxation after excitation, leading to broader resonances.[25]

Entry	Species present	*D* (4.7)	*D* (4.6)	*D* (4.1)	*D* (C)	*D* (4.2)
A	**4.7** (4 mM) = *	3.4	-	-	-	-
B	**4.7** (20 mM) = **	2.8	-	-	-	-
C	**4.6** (saturated)	-	ND	-	-	-
D	* + **4.6** (saturated)	3.4	3.3	-	-	-
E	** + **4.6** (saturated)	2.7	0.44	-	-	-
F	**4.1** (saturated)	-	-	ND	-	-
G	* + **4.1** (saturated)	3.3	-	ND	-	-
H	** + **4.1** (saturated)	2.7	-	0.12	-	-
I	**C** (saturated)	-	-	-	ND	-
J	* + **C** (saturated)		-	-	ND	-
K	** + **C** (saturated)	2.5	-	-	ND	-
L	[Cu-**C**] (saturated)	-	-	-	ND	-
M	* + [Cu-**C**] (saturated)	2.8			3.0	-
N	** + [Cu-**C**] (saturated)	1.4	-	-	0.82	-
O	**4.2** (20 mM)	-	-	-	-	5.5
P	* + **4.2** (20 mM)	3.4	-	-	-	5.4
Q	** + **4.2** (20 mM)	2.8	-	-	-	5.2

Table 4.1 Legend: * = **4.7** (4 mM) and ** = **4.7** (20 mM). Diffusion coefficients extracted from DOSY experiments. The diffusion coefficients were recorded for all reaction components at the concentrations present in the system during the synthesis of **4.7** in water. *D* values reported in 10^{-10} m^2s^{-1}. A decrease in the diffusion coefficient in the presence of surfactant **4.7** above the CMC indicates a strong association with the micelle. ND indicates that the diffusion coefficient could not be extracted because of the limited solubility of the compound in water. For entries L-N sodium ascorbate (24 mM) was added to reduce $CuSO_4$.

4.5.3 Proposed inhibition mechanism

The most striking result from these experiments is that the diffusion rates suggest that **4.7** is not capable of effectively solubilizing **4.1**. At lower concentrations of **4.7** (4 mM), azide **4.1** is restricted to the organic phase (Table 4.1, Entry G), whereas the hydrophobic Cu-ligand complex is encapsulated and solubilised into the aqueous phase (Figure 4.12, step 1). Micelles of **4.7** might not be able to take up **4.1** because of the longer length of the hydrophobic tails. This larger size could disrupt packing of **4.7** into micelles, whose hydrophobic interior is restricted in size due to its shorter tails.

A second contribution to the inhibition mechanism might be the sequestering of the active catalyst into the aqueous phase by micelles (Figure 4.12, step 2), which readily associates

with the copper-ligand complex (Table 4.1, Entry M). This causes a three-phase separation between the catalyst in the micelles, **4.1** in the organic phase, and **4.2** in the aqueous phase, which consequently prevents turnover and formation of **4.3** (step 3).

This hypothesis was tested by performing the cross-seeding experiment in a 1:1 water/*tert*-butanol mixture which gave full conversion in 45 minutes (Figure 4.64). No inhibition occurred under these homogeneous conditions: phase separation and aggregation are required for the inhibition mechanism to operate.

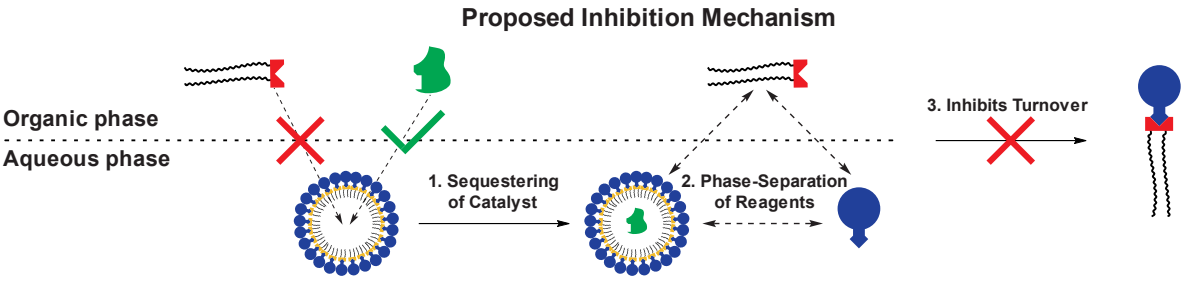
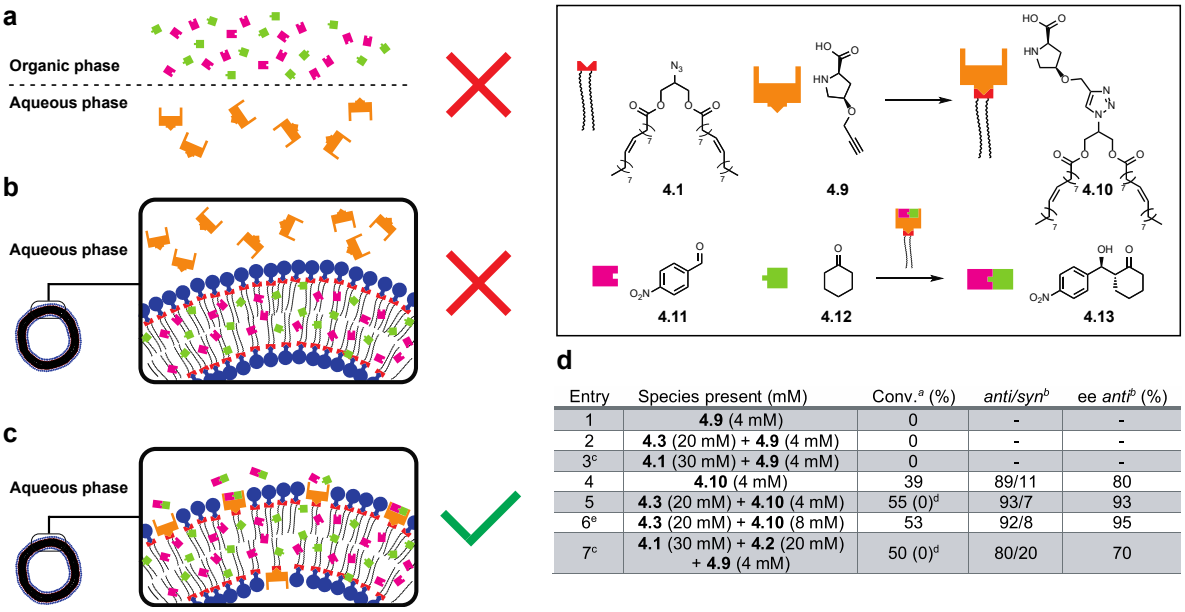


Figure 4.12 Proposed mechanism by which micelles of **4.7** inhibit the formation of **4.3** through selective sequestering of the catalyst in the micelle interior. Phase-separation between azide, alkyne and copper catalyst inhibits turnover to hospholipid **4.3**.

When the supramolecular properties of mixtures of **4.3** and **4.7** were studied by confocal microscopy it became apparent that aggregates were no longer limited to spherical morphologies – tubular structures and fused vesicles are also observed (Figure 4.43). This is reminiscent of work by Szostak where seeding multilamellar fatty acid vesicles with fatty acid micelles led to a transformation into long thread-like vesicles.[26] Analysis of the hydrolysing competition reaction (Figure 4.9b) by confocal microscopy showed clusters of large oil droplets (up to 40 micron) at t = 1h, likely emulsified by the small amounts of **4.3** and **4.7** present,[27] while later time points showed clusters of vesicles <2 micron in size combined with amorphous material (Figure 4.44).

4.6 Metabolism through orthogonal reactivity

Life depends on interconnected reactions that together constitute metabolism.[28] Living organisms have achieved metabolic closure, meaning that from a limited set of building blocks they can generate, through various metabolic intermediates, all the components needed to maintain and generate more of themselves. A network of linked reactions was introduced to our system by linking protocell formation to the *in situ* generation of a catalytically active surfactant. Once embedded in the vesicle bilayer it could function as an organocatalyst[29–32] to drive an enantioselective aldol reaction between phase separated substrates to synthesise a downstream, secondary metabolite.



d

Entry	Species present (mM)	Conv.[a] (%)	*anti/syn*[b]	ee *anti*[b] (%)
1	**4.9** (4 mM)	0	-	-
2	**4.3** (20 mM) + **4.9** (4 mM)	0	-	-
3[c]	**4.1** (30 mM) + **4.9** (4 mM)	0	-	-
4	**4.10** (4 mM)	39	89/11	80
5	**4.3** (20 mM) + **4.10** (4 mM)	55 (0)[d]	93/7	93
6[e]	**4.3** (20 mM) + **4.10** (8 mM)	53	92/8	95
7[c]	**4.1** (30 mM) + **4.2** (20 mM) + **4.9** (4 mM)	50 (0)[d]	80/20	70

Figure 4.13. Enantioselective catalysis by a self-reproducing protocell nanoreactor. **a**. Schematic representation of entry 1 in table **d** where **4.9** is phase separated from **4.11** and **4.12**, and no aldol reaction occurs. **b**. Schematic representation of entry 2 where **4.9** is phase separated from **4.11** and **4.12** which are encapsulated in the bilayer of **4.3**, and no aldol reaction occurs. **c**. Schematic representation of entry 5 where **4.10** is embedded in the bilayer of **4.3** with **4.11** and **4.12** enabling the formation **4.13**. **d.** Table showing the experimental results of aldol experiments. All reactions were carried out at room temperature in the presence of **4.11** (13.3 mM) and **4.12** (66.6 mM) in 1 mL of H_2O while stirring at 1000 rpm for 10 days. [a]Determined by ^{1}H-NMR spectroscopy of crude reaction mixture. [b]Determined by SFC on a chiral non-racemic stationary phase. [c]$CuSO_4$ (8 mM), TBTA (8 mM) and sodium ascorbate (24 mM) were also present in 5 mL of H_2O. [d]Conversion observed when the reaction was performed in a *t*BuOH:H_2O (1:1) mixture. [e]26.6 mM **4.11**, 133.2 mM **4.12** and 6 days of reaction time.

Proline is known to catalyse aldol reactions enantioselectively[11] and was considered a good candidate to drive secondary reactivity in our protocell system. The polar nature of

the amino acid indicated that an amphiphile catalyst might be generated from a water-soluble precatalyst. Hydroxyproline was appended with an alkyne moiety to give precatalyst **4.9**, allowing *in situ* generation of amphiphilic organocatalyst **4.10** through CuAAC with **4.1** enabled by protocells of **4.3** (Figure 4.13). Compound **4.10** subsequently catalysed an enantioselective aldol reaction between nitrobenzaldehyde **4.11** and cyclohexane **4.12** to give enantioenriched β-hydroxyketone **4.13**.

Control reactions showed that **4.9** alone does not catalyse formation of **4.13**, likely due to phase separation between substrates and catalyst (Figure 4.13a and 4.13d; Entry 1). Addition of amphiphile **4.3** facilitated solubilisation of **4.11** and **4.12**, but precatalyst **4.9** was still unable to generate **4.13** (Figure 4.13b and 4.13d, Entry 2). We attribute this lack of reactivity to the polarity of **4.9**, which renders it unable to penetrate the hydrophobic lipid bilayer of vesicles and interact with the aldol reagents. Attempts at reacting **4.1** with **4.9** in water under CuAAC conditions to generate **4.10** *in situ* failed, and consequently no aldol product was obtained (Entry 3). It appears that formation of **4.10** is not autocatalytic and that phase separation between **4.1** and **4.9** prevents overall reactivity.

Surprisingly, addition of preformed catalyst **4.10** as a solid to an aqueous mixture of **4.11** and **4.12** did not yield **4.13**. Solubility of **4.10** in water was low and the catalyst largely remained a solid throughout the reaction, possibly contributing to its limited reactivity. The reaction was repeated by generating a thin film of **4.10** on the flask, to facilitate dissolution and to increase the surface area of organocatalyst available for reaction. Under these conditions formation of **4.13** was observed (Entry 4, 39% conversion, 89:11 *anti:syn* ratio, 80% ee of *anti*).

When **4.10** is combined with **4.3**, a vesicle-assembly is obtained where the organocatalyst is embedded in the lipid bilayer. This nanoreactor can perform the aldol reaction with a

drastically increased efficiency and selectivity: aldol product **4.13** is formed at higher conversion (55%), with higher 93:7 *anti:syn*-selectivity and 93%ee (Figure 4.13c and 4.13d, Entry 5). Reaction time is further reduced and ee is increased to 95% when loading of aldol reagents and catalyst **4.10** is doubled (Entry 6).

Since **4.3** and **4.10** are both products from CuAAC, a fully functional system with autocatalytic behaviour and orthogonal enantioselective catalysis can be generated *in situ* from the catalytically inactive starting materials **4.1**, **4.2** and **4.9** (Entry 7). Under these conditions formation of **4.13** from **4.11** and **4.12** was observed: the protocell not only enhances the efficiency of the aldol reaction but also facilitates formation of catalyst **4.10**, otherwise prevented by phase separation of the precursors *(c.f.* Entry 3). The *anti*/*syn* ratio and ee of **4.13** are reduced compared to Entry 6, which may be caused by binding of copper to the proline moiety, hindering effective catalysis of the aldol reaction. Slower formation of **4.3** under these conditions corroborates that proline affects the activity of copper.

Surprisingly, when the experiments from entries 5 and 7 were repeated in a 1:1 water/*tert*-butanol mixture (conversion value shown in brackets) no formation of **4.13** occurred at the time scale of the reaction. In this solvent mixture aggregation into vesicles does not occur. However, phase-mixing is facilitated which should accelerate interaction between aldol substrates and organocatalyst. Thus, we expected faster rates for the aldol reaction. We attribute the lack of reactivity to the fact that reagents are no longer encapsulated in the bilayer and the aldol reaction is no longer compartmentalised. Compartmentalisation increases the local concentration of substrates, accelerates reaction times, and appears to be a vital prerequisite for a successful aldol reaction in this system. Overall, a network of reactions was developed reminiscent of metabolic networks: *in situ* generated protocells facilitate the synthesis of an organocatalyst, which, upon incorporation in the bilayer,

forms a nanoreactor that catalyses the enantioselective formation of a secondary metabolite.

4.7 Conclusions

The work in this chapter reports on the experimental realisation of a system of self-assembling, self-reproducing protocells generated from simple, phase-separated chemical building blocks. A destructive step was introduced to the autocatalytic system by applying hydrolysing conditions which enabled the transient formation of surfactants. The system could be maintained in an out-of-equilibrium steady-state, mimicking natural self-assembly processes, by running the reaction in a CSTR setup. The basicity of the reaction mixture acted as a selection pressure during competition experiments between vesicular and micellar replicators for a common feedstock and controlled which species predominated. At neutral conditions micelle formation was favoured through a unique selection mechanism where micelles inhibit the formation of vesicle-forming surfactants by effectively phase-separating all reagents preventing reaction. Under basic conditions vesicular surfactants predominate because inhibitory micelles are quickly degraded, allowing formation of vesicles that are less prone to hydrolysis. A network of linked reactions was incorporated into the protocell system with orthogonal downstream reactivity. Vesicles facilitated formation of an organocatalyst imbedded in the bilayer which subsequently catalysed formation of enantioenriched secondary metabolites. Overall, the system merges multiple, emergent properties into a functioning, dynamic protocell. We have shown that through a bottom-up synthetic approach a simple molecular system can exhibit complex, life-like behaviour.

This chapter linked CuAAC based autocatalysis to enantioselective reactivity. Chapter 5 describes an approach towards asymmetric autocatalysis driven by CuAAC. Asymmetric

CuAAC conditions are applied to a racemising allylic azide to generate a chiral triazole ligand that can perform enantioselective reactions.

4.8 Experimental

4.8.1 General Information

The general information for the work reported in this chapter is as described in Section 2.5.1.

Dynamic Light Scattering: Dynamic Light Scattering (DLS) measurements were recorded using a Microtrac Nanotrac Wave W3043 (University of Twente) and Malvern Zetasizer Nano S (University of Oxford) instruments and analysed with Origin software.

Transmission Electron Microscopy: Transmission Electron Microscopy (TEM) measurements were performed with a Philips CM300ST-FEG Transmission Electron Microscope with a GATAN Ultrascan1000 (2kx2k CCD camera), GATAN Tridiem energy filter (2kx2k CCD camera) and Noran System Six EDX analyser Nanotrace detector. The samples were deposited on a copper grid and stained with 2% uranyl acetate.

Confocal micrography: Confocal micrographs were captured with a Nikon A1plus confocal microscope (University of Twente) and Olympus FV1200 laser scanning microscope (University of Oxford) with the laser set at 488 nm. All the samples were stained with the dye Coumarin 6 by adding 1 μL of a 1 mM solution of dye in THF to 200 μL of sample giving a final concentration of 5 μM.

Image processing: Image processing of all micrographs was done with Fiji ImageJ software. Segmentation and thresholding were performed by training classifiers with the Trainable Weka Segmentation plugin. Particles were counted with the analyse particles function and diameters were calculated from the counted areas.

Ultra Performance Liquid Chromatography: Ultra performance liquid chromatography (UPLC) analyses were performed using a Waters Acquity ultra performance liquid chromatography H-Class system with photodiode array (PDA) detector. Instrument control and data processing were performed using Empower software. An Acquity® UPLC BEH Amide column (130 Å, 1.7 µm, 2.1 mm × 150 mm) was used. Conditions: Flow rate: 0.6 ml/min. Gradient: H_2O:MeCN:MeOH with a gradient of 0:95:5 to 30:65:5 in 0 to 2.5 min; 30:65:5 isocratically 2.5 to 4 min; 0:95:5 isocratically from 4 to 5 min. λ_{det} = 214.5 nm.

Supercritical Fluid Chromatography: Supercritical fluid chromatography (SFC) separations were conducted with a chiral non-racemic stationary phase on a Waters Acquity UPC2 system using Waters Empower software. A Chiralpak® IE column (3 µm, 150×3 mm) was used. Conditions: Flow rate: 1.5 ml/min. Gradient: CO_2:MeOH with a gradient of 99:1 to 60:40 in 0 to 5 min; gradient of 60:40 to 40:60 in 5 to 5.5 min; 40:60 isocratically from 5.5 to 7 min; 100:0 isocratically from 7 to 8 min. λ_{det} = 266.8 nm.

4.8.2 Experimental Procedures and Characterisation of Compounds

Representative procedure for kinetic analysis of reactions

The concentrations of all UV active reaction species in aliquots removed from reaction were monitored by UPLC using an external standard. The external standard solution was first prepared by the dissolution of ethyl benzoate (50 µL, 0.35 mmol) in MeCN (500 mL) giving an overall concentration of 0.7 µM. To monitor the reactions a small volume (~25 µL) of the reaction mixture was withdrawn at specified time points by plastic syringe. A 20 µL aliquot of this withdrawn solution was then measured by microsyringe and injected into 500 µL of the standard solution in an MS vial. Five microliter of the resultant solution was the standard injection volume for analysis by UPLC. Concentration of compounds

were calculated from the peak area using the UPLC calibration curves reported in this Supplemental Information.

Representative procedure for setup of kinetic experiments (Figure 4.3)

A solution of alkyne **4.2** (23.5 mg, 0.10 mmol, 1 eq, 1 mL of 100 mM standard solution in H_2O), $CuSO_4 \cdot 5H_2O$ (2.5 mg, 0.01 mmol, 0.1 eq, 250 μL of 40 mM standard solution in H_2O) (and surfactant **4.3** (17.6 mg, 0.02 mmol, 0.2 eq) for the seeded reactions) were added to H_2O (3.75 mL) to give a total volume of 5 mL in a round bottom flask (25 mL) with a stirrer bar of an identical size (4.5 mm diameter and 12 mm length) for each experiment. Subsequently TBTA (5.3 mg, 0.01 mmol, 0.1 eq), azide **4.1** (100 μL, 0.156 mmol, 1.56 eq) were added and the flask was capped with a septum and the solution was degassed by bubbling argon through it for 30 minutes. Afterwards sodium ascorbate (6.0 mg, 0.03 mmol, 0.3 eq) was added to initiate the reaction. The reaction mixture was stirred at 1000 rpm under a continuous flow of argon.

Note: For the thin film seeded reaction surfactant **4.3** (17.6 mg, 0.04 mmol, 0.4 eq) was first dissolved in a minimum of MeOH and then concentrated *in vacuo* to generate a thin film of the compound on the flask. This was hydrated in H_2O (3 mL) before addition of the other reagents.

Note 2: For figure 4.9a, azide **4.1** (100 μL, 0.156 mmol, 1.56 eq) and azide **4.6** (45 μL, 0.156 mmol, 1.56 eq) were added to the reaction mixture. The reaction was stirred at 1000 rpm.

Note 3: These reactions are very sensitive to physical parameters, so changing the flask size, stirrer bar or adding compounds at different time points during the degassing process might affect the overall kinetics of the reaction.

Representative procedure for setup of hydrolysis experiments (Figure 4.51)

A solution of alkyne **4.2** (23.5 mg, 0.10 mmol, 1 eq, 1 mL of 100 mM standard solution in H_2O) and of $CuSO_4 \cdot 5H_2O$ (10 mg, 0.04 mmol, 0.4 eq, 1 mL of 40 mM standard solution in H_2O) were added to H_2O (2.5 mL) in a round bottom flask (25 mL) with a stirrer bar of an identical size (4.5 mm diameter and 12 mm length) for each experiment. Subsequently TBTA (21 mg, 0.04 mmol, 0.1 eq), azide **4.1** (100 µL, 0.156 mmol, 1.56 eq) were added and the flask was capped with a septum and the solution was degassed by bubbling argon through it for 30 minutes. Subsequently, 0.5 mL of a degassed, aqueous NaOH (500 mM) solution was added to give a final reaction volume of 5 mL with 50 mM of NaOH. Afterwards sodium ascorbate (24.0 mg, 0.12 mmol, 1.2 eq) was added to initiate the reaction. The reaction mixture was stirred at 1000 rpm under a continuous flow of argon.

Note: For figure 4.9b, azide **4.1** (100 µL, 0.156 mmol, 1.56 eq) and azide **4.6** (45 µL, 0.156 mmol, 1.56 eq) were added to the reaction mixture.

Representative procedure for setup of hydrolysis experiments in a continuously stirred tank reactor (Figure 4.6)

A solution of alkyne **4.2** (70.5 mg, 0.30 mmol, 1 eq, 3 mL of 100 mM standard solution in H_2O) and of $CuSO_4 \cdot 5H_2O$ (30 mg, 0.12 mmol, 0.4 eq, 3 mL of 40 mM standard solution in H_2O) were added to H_2O (6 mL) in a round bottom flask (25 mL) with a stirrer bar of an identical size (4.5 mm diameter and 12 mm length) for each experiment. Subsequently TBTA (63 mg, 0.12 mmol, 0.1 eq) was added and the flask was capped with a septum and the solution was degassed by bubbling argon through it for 30 minutes. Afterwards 3 mL of a degassed, aqueous NaOH (500 mM) solution and sodium ascorbate (72.0 mg, 0.36 mmol, 1.2 eq) were added to give a final reaction volume of 15 mL with 100 mM of

NaOH. Of this solution 10 mL was withdrawn into a 10 mL syringe which was subsequently installed into a syringe pump set at a flow of 200 μL/h. In a second syringe pump a 1 mL syringe with 200 μL of azide **4.1** was installed with a flow rate of 4 μL/h. A third syringe pump had an empty 10 mL syringe installed and was set at withdrawal rate of 204 μL/h. Azide **4.1** (100 μL, 0.156 mmol, 1.56 eq) was added to the reaction mixture and the pumps were turned on to initiate the reaction. The reaction mixture was stirred at 1000 rpm under a continuous flow of argon.

Note: During the periods that the reaction was monitored the withdrawal rate was lowered to 180 μL/h to compensate for the amount of reaction mixture removed by taking aliquots.

Note 2: For figure 4.10, a syringe with a mixture of azide **4.1** (100 μL, 0.156 mmol, 1.56 eq) and azide **4.6** (45 μL, 0.156 mmol, 1.56 eq) was installed in syringe pump 2 which was set at 5.8 μL/h. The withdrawal pump was set at of 205.8 μL/h. A mixture of azide **4.1** (100 μL, 0.156 mmol, 1.56 eq) and azide **4.6** (45 μL, 0.156 mmol, 1.56 eq) was added to the reaction mixture to initiate the reaction.

Representative procedure for setup of enantioselective aldol reaction in a self-replicating protocell (Figure 4.13d, Entry 7)

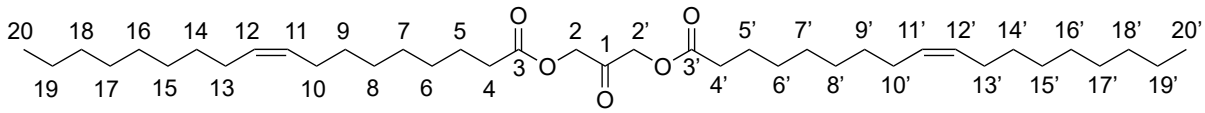
A solution of alkyne **4.2** (23.5 mg, 0.10 mmol, 1 eq, 1 mL of 100 mM standard solution in H_2O), $CuSO_4 \cdot 5H_2O$ (10 mg, 0.04 mmol, 0.4 eq, 1 mL of 40 mM standard solution in H_2O) were added to H_2O (3 mL) to give a total volume of 5 mL in a round bottom flask (25 mL) with a stirrer bar of an identical size (4.5 mm diameter and 12 mm length) for each experiment. Subsequently TBTA (21 mg, 0.040 mmol, 0.40 eq), azide **4.1** (100 μL, 0.156 mmol, 1.56 eq) were added and the flask was capped with a septum and the solution was degassed by bubbling argon through it for 30 minutes. Afterwards sodium ascorbate (24 mg, 0.12 mmol, 1.2 eq), precatalyst **4.9** (3.4 mg, 0.020 mmol, 0.20 eq),

nitrobenzaldehyde **4.11** (10 mg, 0.066 mmol, 0.66 eq) and cyclohexanone **4.12** (34 μL, 0.33 mmol, 3.3 eq) were added to initiate the reaction. The reaction mixture was stirred at 1000 rpm under a continuous flow of argon.

Note: Entry 3 was performed in an identical manner however alkyne **4.2** was not added.

Note 2: Entry 1, 2, 4, 5 and 6 were performed by simply stirring the reported substrates at the reported concentrations in 1 mL of H_2O. Compounds **4.3** and **4.10** were first dissolved in a minimum of MeOH and then concentrated *in vacuo* to generate a thin film of the compound on the flask. This was hydrated in H_2O (1 mL) before addition of the other reagents.

2-Oxopropane-1,3-diyl dioleate (4.14)

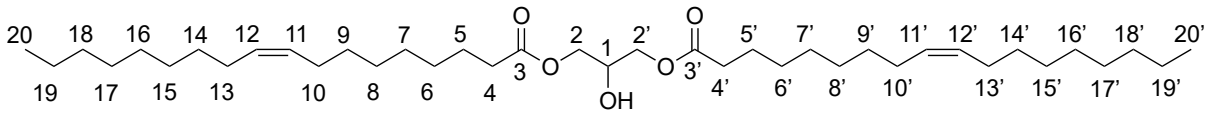


Chemical Formula: $C_{39}H_{70}O_5$
Molecular Weight: 618.9840

Synthesised according to procedure adapted from Li *et al*.[33] To a solution of 1,3-dihydroxylacetone (7.20 g, 79.7 mmol, 1.00 eq) in $CHCl_3$ (300 mL), oleoyl chloride (60.0 ml, 159 mmol, 2.00 eq, 89% pure) was added, followed by dropwise addition of pyridine (14.4 mL, 179 mmol, 2.20 eq). The reaction mixture was stirred at room temperature overnight and was subsequently washed with 5% aqueous HCl (300 mL), saturated aqueous $NaHCO_3$ (300 mL), and brine (300 mL). The organic layer was dried (Na_2SO_4) and concentrated *in vacuo*. The crude product was recrystallized from hot 2-propanol (25 mL/g). The crystals were collected by filtration and purified by flash column chromatography (10% EtOAc in hexane) to yield diester **4.14** (41.76 g, 67.47 mmol, 85%) as a white, waxy solid.

^{1}H NMR (400 MHz, $CDCl_3$) δ 5.39 – 5.29 (m, 4H, C<u>H</u>-11;C<u>H</u>-11';C<u>H</u>-12;C<u>H</u>-12'), 4.75 (s, 4H, C<u>H</u>$_2$-2;C<u>H</u>$_2$-2'), 2.42 (t, *J* = 7.6 Hz, 4H, C<u>H</u>$_2$-4;C<u>H</u>$_2$-4'), 2.08 – 1.95 (m, 8H, C<u>H</u>$_2$-10;C<u>H</u>$_2$-10';C<u>H</u>$_2$-13;C<u>H</u>$_2$-13'), 1.66 (p, *J* = 7.4 Hz, 4H, C<u>H</u>$_2$-5;C<u>H</u>$_2$-5'), 1.39 – 1.20 (m, 40H, (C<u>H</u>$_2$)$_4$-6-9;(C<u>H</u>$_2$)$_4$-6'-9';(C<u>H</u>$_2$)$_6$-14-19;(C<u>H</u>$_2$)$_6$-14'-19'), 0.92 – 0.83 (m, 6H, C<u>H</u>$_3$-20;C<u>H</u>$_3$-20'); **^{13}C{^{1}H} NMR** (101 MHz, $CDCl_3$) δ 198.3, 173.1 (2C), 130.2 (2C), 129.9 (2C), 66.3 (2C), 33.9 (2C), 32.1 (2C), 29.9 (2C), 29.8 (2C), 29.7 (2C), 29.5 (4C), 29.3 (2C), 29.2 (2C), 29.2 (2C), 27.4 (2C), 27.3 (2C), 25.0 (2C), 22.8 (2C), 14.3 (2C); **HRMS** (ESI) *m/z* calcd for $C_{39}H_{70}O_5Na$ $[M+Na]^+$: 641.5116, found: 641.5114. Consistent with reported literature values.[33]

2-Hydroxypropane-1,3-diyl dioleate (4.15)

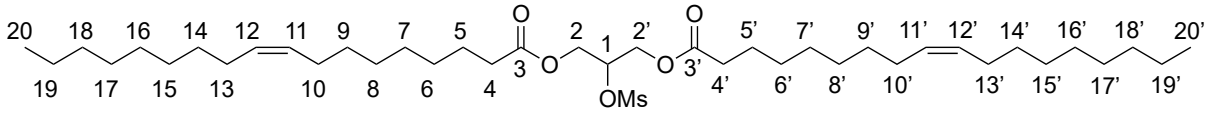


Chemical Formula: $C_{39}H_{72}O_5$
Molecular Weight: 621.0000

Synthesised according to procedure adapted from Li *et al*.[33] $NaBH_4$ (2.77 g, 73.2 mmol, 1.50 eq) in water (a minimum quantity) was slowly added to a solution of diester **4.14** (30.2 g, 48.8, 1 eq) in THF (500 mL) at 0 °C. The reaction mixture was stirred at 0 °C for 30 min and quenched by addition of 5% HCl (10 mL). H_2O (300 mL) was added, and the mixture was extracted with $CHCl_3$ (600 mL). The organic layer was washed sequentially with H_2O (400 mL), saturated aqueous $NaHCO_3$ (300 mL), and brine (400 mL). The organic layer was dried (Na_2SO_4), concentrated *in vacuo* and purified by flash column chromatography (5% EtOAc in hexane) to yield alcohol **4.15** (27.29 g, 43.95 mmol, 89%) as a transparent oil. Some of the regioisomer is formed during the reaction due to transesterifaction.

^{1}H NMR (400 MHz, $CDCl_3$) δ 5.45 – 5.26 (m, 4H, C<u>H</u>-11;C<u>H</u>-11';C<u>H</u>-12;C<u>H</u>-12'), 4.21 – 4.04 (m, 5H, C<u>H</u>-1;C<u>H$_2$</u>-2;C<u>H$_2$</u>-2'), 2.43 (d, *J* = 4.8 Hz, 1H, CH-O<u>H</u>-1), 2.34 (t, *J* = 7.6 Hz, 4H, C<u>H$_2$</u>-4;C<u>H$_2$</u>-4'), 2.07 – 1.94 (m, 8H, C<u>H$_2$</u>-10;C<u>H$_2$</u>-10';C<u>H$_2$</u>-13;C<u>H$_2$</u>-13'), 1.62 (p, *J* = 7.2 Hz, 4H, C<u>H$_2$</u>-5;C<u>H$_2$</u>-5'), 1.39 – 1.19 (m, 40H, (C<u>H$_2$</u>)$_4$-6-9;(C<u>H$_2$</u>)$_4$-6'-9';(C<u>H$_2$</u>)$_6$-14-19;(C<u>H$_2$</u>)$_6$-14'-19'), 0.94 – 0.83 (m, 6H, C<u>H$_3$</u>-20;C<u>H$_3$</u>-20'); **^{13}C{^{1}H} NMR** (101 MHz, $CDCl_3$) δ 174.0 (2C), 130.2 (2C), 129.9 (2C), 68.6, 65.2 (2C), 34.2 (2C), 32.1 (2C), 29.9 (2C), 29.8 (2C), 29.7 (2C), 29.5 (4C), 29.3 (2C), 29.2 (4C), 27.4 (2C), 27.3 (2C), 25.0 (2C), 22.8 (2C), 14.3 (2C); **HRMS** (ESI) *m/z* calcd for $C_{39}H_{72}O_5Na$ $[M+Na]^+$: 643.5272, found: 643.5274. Consistent with reported literature values.[33]

2-((Methylsulfonyl)oxy)propane-1,3-diyl dioleate (4.16)



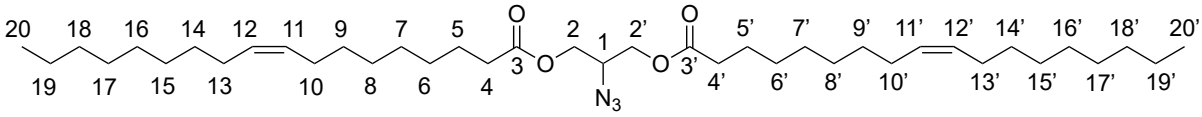
Chemical Formula: $C_{40}H_{74}O_7S$
Molecular Weight: 699.0850

To a solution of alcohol **4.15** (27.29 g, 43.95 mmol, 1 eq) and triethylamine (9.19 mL, 65.9 mmol, 1.5 eq) in anhydrous CH_2Cl_2 (200 mL) was added methanesulfonyl chloride (3.74 mL, 48.4, 1.1 eq) at 0 °C under argon atmosphere. After 2 hours the reaction mixture was washed with 5% aqueous HCl (200 mL), saturated aqueous $NaHCO_3$ (200 mL), and brine (200 mL). The organic layer was dried (Na_2SO_4), concentrated *in vacuo* and purified by flash column chromatography (2.5% EtOAc in hexane) to afford mesylate **4.16** (20.92 g, 29.93 mmol, 68%) as a transparent oil.

^{1}H NMR (400 MHz, $CDCl_3$) δ 5.40 – 5.29 (m, 4H, C<u>H</u>-11;C<u>H</u>-11';C<u>H</u>-12;C<u>H</u>-12'), 5.02 (tt, *J* = 6.4, 3.8 Hz, 1H, C<u>H</u>-1), 4.36 (dd, *J* = 12.3, 3.9 Hz, 2H, C<u>H$_a$</u>H$_b$-2;C<u>H$_a$</u>H$_b$-2'), 4.22 (dd, *J* = 12.3, 6.5 Hz, 2H, CH$_a$<u>H$_b$</u>-2;CH$_a$<u>H$_b$</u>-2'), 3.08 (s, 3H, SO_2C<u>H$_3$</u>-21), 2.35 (t, *J* = 7.6

Hz, 4H, C$\underline{H}_2$-4;C$\underline{H}_2$-4'), 2.05 – 1.94 (m, 8H, C$\underline{H}_2$-10;C$\underline{H}_2$-10';C$\underline{H}_2$-13;C$\underline{H}_2$-13'), 1.67 – 1.59 (m, 4H, C$\underline{H}_2$-5;C$\underline{H}_2$-5'), 1.38 – 1.21 (m, 40H, (C$\underline{H}_2$)$_4$-6-9;(C$\underline{H}_2$)$_4$-6'-9';(C$\underline{H}_2$)$_6$-14-19;(C$\underline{H}_2$)$_6$-14'-19'), 0.90 – 0.85 (m, 6H, C$\underline{H}_3$-20;C$\underline{H}_3$-20'); **^{13}C{^{1}H} NMR** (101 MHz, $CDCl_3$) δ 173.2 (2C), 130.2 (2C), 129.8 (2C), 76.8, 62.4 (2C), 38.8, 34.1 (2C), 32.0 (2C), 29.9 (2C), 29.8 (2C), 29.7 (2C), 29.5 (4C), 29.3 (2C), 29.2 (2C), 29.2 (2C), 27.4 (2C), 27.3 (2C), 24.9 (2C), 22.8 (2C), 14.3 (2C); **HRMS** (ESI) *m/z* calcd for $C_{40}H_{74}O_7NaS$ $[M+Na]^+$: 721.5048, found: 721.5045.

2-Azidopropane-1,3-diyl dioleate (4.1)



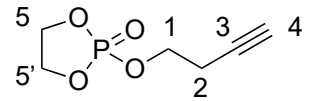
Chemical Formula: $C_{39}H_{71}N_3O_4$
Molecular Weight: 646.0140

To a solution of mesylate **4.16** (15.43 g, 22.08 mmol, 1 eq) in DMF (100 mL) was added sodium azide (5.73 g, 88.2 mmol, 4 eq). The reaction mixture was heated to 90 °C for 18 hours and was then concentrated *in vacuo* to remove the majority of DMF. The crude was dissolved in CH_2Cl_2 (100 mL) and washed with saturated aqueous $NaHCO_3$ (3 × 100 mL). The organic layer was dried (Na_2SO_4), concentrated *in vacuo* and purified by flash column chromatography (10% EtOAc in hexane) to afford azide **4.1** (9.81 g, 15.2 mmol, 69%) as a transparent oil.

^{1}H NMR (400 MHz, $CDCl_3$) δ 5.40 – 5.28 (m, 4H, C$\underline{H}$-11;C$\underline{H}$-11';C$\underline{H}$-12;C$\underline{H}$-12'), 4.23 (dd, *J* = 11.6, 4.6 Hz, 2H, C$\underline{H}_a$H$_b$-2;C$\underline{H}_a$H$_b$-2'), 4.14 (dd, *J* = 11.6, 6.8 Hz, 2H, CH$_a\underline{H}_b$-2;CH$_a\underline{H}_b$-2'), 3.87 (tt, *J* = 6.8, 4.6 Hz, 1H, C$\underline{H}$-1), 2.35 (t, *J* = 7.5 Hz, 4H, C$\underline{H}_2$-4;C$\underline{H}_2$-4'), 2.07 – 1.97 (m, 8H, C$\underline{H}_2$-10;C$\underline{H}_2$-10';C$\underline{H}_2$-13;C$\underline{H}_2$-13'), 1.69 – 1.57 (m, 4H, C$\underline{H}_2$-5;C$\underline{H}_2$-5'), 1.38 – 1.20 (m, 40H, (C$\underline{H}_2$)$_4$-6-9;(C$\underline{H}_2$)$_4$-6'-9';(C$\underline{H}_2$)$_6$-14-19;(C$\underline{H}_2$)$_6$-14'-19'), 0.94 – 0.80 (m, 6H, C$\underline{H}_3$-20;C$\underline{H}_3$-20'); **^{13}C{^{1}H} NMR** (101 MHz, $CDCl_3$) δ 173.4 (2C),

130.2 (2C), 129.9 (2C), 63.2 (2C), 58.8, 34.1 (2C), 32.1 (2C), 29.9 (2C), 29.8 (2C), 29.7 (2C), 29.5 (4C), 29.3 (2C), 29.2 (4C), 27.4 (2C), 27.3 (2C), 24.9 (2C), 22.8 (2C), 14.3 (2C); **HRMS** (ESI) *m/z* calcd for $C_{39}H_{71}O_4N_3Na$ $[M+Na]^+$: 668.5337, found: 668.5332; **IR** (ATR) ν (cm^{-1}) thin film, CH_2Cl_2: 2923 (s), 2858 (s), 2122 (w), 1745 (s), 1463 (w), 1240 (w), 1161 (m), 723 (w).

2-(But-3-yn-1-yloxy)-1,3,2-dioxaphospholane 2-oxide (4.17)

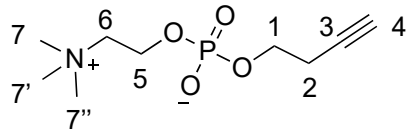


Chemical Formula: $C_6H_9O_4P$
Molecular Weight: 176.1078

Synthesised according to adapted procedure from Emrick *et al*.[34] To a solution of 3-butyn-1-ol (1.06 mL, 14.0 mmol, 1 eq) in anhydrous THF (20 mL) was added triethylamine (2.15 mL, 15.4 mmol, 1.1 eq) at 0 °C under argon atmosphere. After slow addition of 2-chloro-2-oxo-1,3,2-dioxaphospholane (1.29 mL, 14.0 mmol, 1 eq), the mixture was warmed to room temperature and stirred for 2 hours. The white suspension was filtered over a sintered funnel, and the filtrate was concentrated by rotary evaporation and dried in vacuo to give phospholane **4.17** (2.30 g, 13.1 mmol, 93%) as a yellow oil. This was used without further purification due to decomposition of **4.17** on silica.

^{1}H NMR (400 MHz, $CDCl_3$) δ 4.50 – 4.32 (m, 4H, C$\underline{H}_2$-5;C$\underline{H}_2$-5'), 4.24 (dt, *J* = 9.5, 6.8 Hz, 2H, C$\underline{H}_2$-1), 2.62 (td, *J* = 6.8, 2.7 Hz, 2H, C$\underline{H}_2$-2), 2.04 (t, *J* = 2.7 Hz, 1H, C$\underline{H}$-4); **^{13}C{^{1}H} NMR** (101 MHz, $CDCl_3$) δ 79.2, 70.6, 66.4 (d, J_{CP} = 5.7 Hz), 66.2 (d, J_{CP} = 3.1 Hz, 2C), 20.9 (d, J_{CP} = 6.6 Hz); **^{31}P NMR** (162 MHz, $CDCl_3$) δ 17.38. Consistent with reported literature values.[35]

But-3-yn-1-yl (2-(trimethylammonio)ethyl) phosphate (4.2)

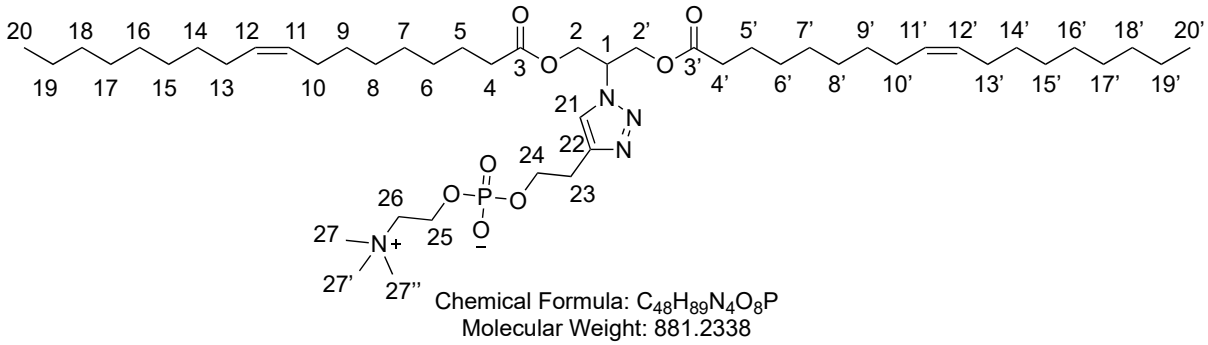


Chemical Formula: $C_9H_{18}NO_4P$
Molecular Weight: 235.2198

Synthesized according to adapted procedure from Choi *et al*.[36] Crude phospholane **4.20** (2.30 g, 13.1 mmol) was dissolved in dry MeCN (20 mL) in a 100 mL flame dried flask under argon. After trimethylamine (21 mL, 21 mmol, 1.6 eq, 1 M in THF) was added, the flask was closed and heated to 70 °C for 48 h. The crude mixture was concentrated *in vacuo* and purified by flash column chromatography (10% H_2O and 40% MeOH in CH_2Cl_2) to yield phosphocholine **4.2** (2.42 g, 10.3 mmol, 79%) as a transparent oil that crystallized in the freezer.

^{1}H NMR (400 MHz, CD_3OD) δ 4.34 – 4.24 (m, 2H, C$\underline{H}_2$-5), 3.96 (q, J = 7.0 Hz, 2H, C$\underline{H}_2$-1), 3.66 – 3.60 (m, 2H, C$\underline{H}_2$-6), 3.23 (s, 9H, C$\underline{H}_3$-7;C$\underline{H}_3$-7';C$\underline{H}_3$-7''), 2.53 (td, J = 6.8, 2.7 Hz, 2H, C$\underline{H}_2$-2), 2.31 (t, J = 2.7 Hz, 1H, C$\underline{H}_2$-4); **^{13}C{^{1}H} NMR** (101 MHz, CD_3OD) δ 81.8, 71.0, 67.5 – 67.3 (m, J_{CN}^+ and J_{CP}), 65.0 (d, J_{CP} = 5.6 Hz), 60.4 (d, J_{CN}^+ = 4.9 Hz), 54.8 – 54.6 (m, J_{CN}^+, 3C), 49.8, 30.7, 24.2, 21.6 (d, J_{CP} = 7.9 Hz); **^{31}P NMR** (162 MHz, CD_3OD) δ -0.55; **HRMS** (ESI) *m/z* calcd for $C_9H_{19}NO_4P$ $[M+H]^+$: 236.1046, found: 236.1045; **IR** (ATR) ν (cm^{-1}) thin film, MeOH: 3273 (broad m), 2361 (w), 1654 (w), 1479 (w) 1229 (m), 1083 (s), 1051 (s), 970 (w), 926 (w).

2-(1-(1,3-Bis(oleoyloxy)propan-2-yl)-1*H*-1,2,3-triazol-4-yl)ethyl (2-(trimethylammonio)ethyl) phosphate (4.3)

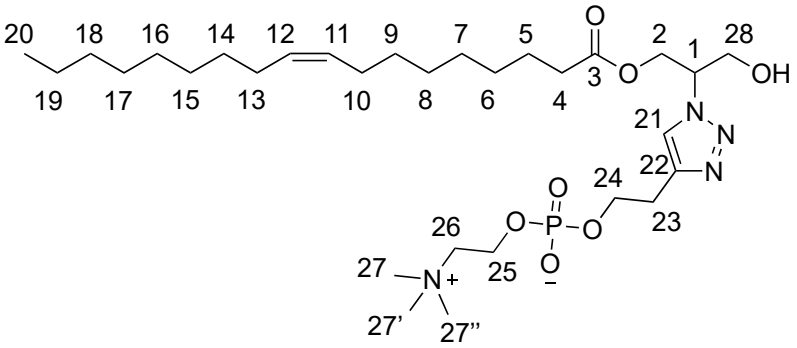


To a solution of alkyne **4.2** (203 mg, 0.863 mmol, 1.00 eq), $CuSO_4 \cdot 5H_2O$ (20 mg, 0.080 mmol, 0.090 eq) in Milli-Q H_2O (2.5 mL) and *t*-BuOH (2.5 mL) was added TBTA (42 mg, 0.080 mmol, 0.090 eq) and azide **4.1** (600 μL, 0.938 mmol, 1.09 eq), and the flask capped with a septum. The solution was degassed by bubbling argon through it for 30 minutes. Afterwards sodium ascorbate (48 mg, 0.25 mmol, 0.27 eq) was added to initiate the reaction. The reaction mixture was stirred at 1000 rpm under a continuous flow of argon. The crude mixture was concentrated *in vacuo* and purified by flash column chromatography (2% H_2O and 48% MeOH in CH_2Cl_2). The obtained compound was dissolved in a minimum of MeOH and filtered through a PTFE syringe filter to remove any silica particles and concentrated *in vacuo* to yield surfactant **4.3** (584 mg, 0.662 mmol, 77%) as a transparent viscous oil.

^{1}H NMR (400 MHz, CD_3OD) δ 7.95 (s, 1H, C<u>H</u>-21), 5.34 – 5.23 (m, 4H, C<u>H</u>-11;C<u>H</u>-11';C<u>H</u>-12;C<u>H</u>-12'), 5.10 (p, *J* = 6.1 Hz, 1H, C<u>H</u>-1), 4.50 (d, *J* = 6.1 Hz, 4H, C<u>H$_2$</u>-2;C<u>H$_2$</u>-2'), 4.22 – 4.16 (m, 2H, C<u>H$_2$</u>-25), 4.08 (q, *J* = 6.5 Hz, 2H, C<u>H$_2$</u>-24), 3.60 – 3.54 (m, 2H, C<u>H$_2$</u>-26), 3.17 (s, 9H, C<u>H$_3$</u>-27;C<u>H$_3$</u>-27';C<u>H$_3$</u>-27''), 3.00 (t, *J* = 6.4 Hz, 2H, C<u>H$_2$</u>-23), 2.26 (t, *J* = 7.4 Hz, 4H, C<u>H$_2$</u>-4;C<u>H$_2$</u>-4'), 2.10 – 1.96 (m, 8H,C<u>H$_2$</u>-10;C<u>H$_2$</u>-10';C<u>H$_2$</u>-13;C<u>H$_2$</u>-13'), 1.51 (p, *J* = 6.6, 6.0 Hz, 4H, C<u>H$_2$</u>-5;C<u>H$_2$</u>-5'), 1.36 – 1.14 (m, 40H, (C<u>H$_2$</u>)$_4$-6-

9;(C<u>H</u>$_2$)$_4$-6'-9';(C<u>H</u>$_2$)$_6$-14-19;(C<u>H</u>$_2$)$_6$-14'-19'), 0.90 – 0.79 (m, 6H, C<u>H</u>$_3$-20;C<u>H</u>$_3$-20'); **^{13}C{^{1}H} NMR** (101 MHz, CD_3OD) δ 174.5 (2C), 130.9 (2C), 130.89 (2C), 124.0, 67.7 – 67.4 (m, J_{CN}^+ and J_{CP}), 65.5 (d, J_{CP} = 5.8 Hz), 64.4, 63.59 (2C), 60.3 (d, J_{CN}^+ = 4.8 Hz), 60.2, 55.0 – 54.5 (m, J_{CN}^+, 3C), 34.7 (2C), 33.1 (2C), 30.9 (2C), 30.8 (2C), 30.6 (2C), 30.5 (2C), 30.4 (2C), 30.3 (2C), 30.2 (2C), 30.1 (2C), 28.2 (d, J_{CP} = 7.7 Hz, 1C), 28.1 (4C), 25.9 (2C), 23.7 (2C), 14.5 (2C); **^{31}P NMR** (162 MHz, CD_3OD) δ -0.71; **HRMS** (ESI) *m/z* calcd for $C_{48}H_{90}O_8N_4P$ $[M+H]^+$: 881.6491, found: 881.6488; **IR** (ATR) ν (cm^{-1}) thin film, MeOH: 3367 (broad w), 2924 (s), 2853, (m), 1741 (m), 1655 (w), 1465 (w) 1229 (m), 1086 (s), 970 (w).

2-(1-(1-Hydroxy-3-(oleoyloxy)propan-2-yl)-1*H*-1,2,3-triazol-4-yl)ethyl (2-(trimethylammonio)ethyl) phosphate (4.4)

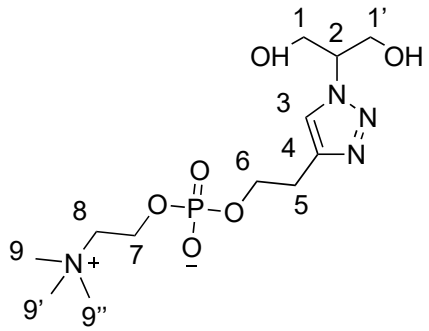


Chemical Formula: $C_{30}H_{57}N_4O_7P$
Molecular Weight: 616.7808

This compound was recovered for characterization from experiments as described in the representative procedure for setup of hydrolysis experiments. The crude reaction mixture of multiple experiments were combined, concentrated *in vacuo* and purified by flash column chromatography (5% H_2O and 45% MeOH in CH_2Cl_2). The obtained compound was dissolved in a minimum of MeOH and filtered through a PTFE syringe filter to remove any silica particles and concentrated *in vacuo* to yield compound **4.4** as a transparent viscous oil.

^{1}H NMR (400 MHz, CD_3OD) δ 7.92 (s, 1H, C<u>H</u>-21), 5.34 – 5.22 (m, 2H, C<u>H</u>-11;C<u>H</u>-12), 4.88 – 4.82 (m, 1H, C<u>H</u>-1), 4.46 (dt, *J* = 5.6, 2.7 Hz, 2H, C<u>H$_2$</u>-2), 4.07 (q, *J* = 6.2 Hz, 4H, C<u>H$_2$</u>-24;C<u>H$_2$</u>-25), 3.97 – 3.86 (m, 2H, C<u>H$_2$</u>-28), 3.54 – 3.48 (m, 2H, C<u>H$_2$</u>-26), 3.13 (s, 9H, C<u>H$_3$</u>-27;C<u>H$_3$</u>-27';C<u>H$_3$</u>-27''), 2.98 (t, *J* = 6.2 Hz, 2H, C<u>H$_2$</u>-23), 2.21 (t, *J* = 7.4 Hz, 2H, C<u>H$_2$</u>-4), 1.96 (q, *J* = 6.4 Hz, 4H, C<u>H$_2$</u>-10;C<u>H$_2$</u>-13), 1.46 (p, *J* = 7.2 Hz, 2H, C<u>H$_2$</u>-5), 1.41 – 1.22 (m, 20H, (C<u>H$_2$</u>)$_4$-6-9;(C<u>H$_2$</u>)$_6$-14-19), 0.87 – 0.81 (m, 3H, C<u>H$_3$</u>-20); **^{13}C{^{1}H} NMR** (101 MHz, CD_3OD) δ 174.7, 145.7, 130.9, 130.8, 124.0, 67.8 – 67.3 (m, J_{CN}^{+} and J_{CP}), 65.5 (d, J_{CP} = 5.5 Hz), 63.9, 63.5, 62.1, 60.3 (d, J_{CN}^{+} = 5.0 Hz), 55.2 – 54.3 (m, J_{CN}^{+}, 3C), 34.7, 33.0, 30.8, 30.8, 30.6, 30.4, 30.3, 30.2, 30.1, 30.1, 28.3 (d, J_{CP} = 8.0 Hz), 28.1, 25.9, 23.7, 14.5; **^{31}P NMR** (162 MHz, CD_3OD) δ -0.45; **HRMS** (ESI) *m/z* calcd for $C_{30}H_{58}O_7N_4P$ $[M+H]^+$: 617.4039, found: 617.4038; **IR** (ATR) ν (cm^{-1}) thin film, MeOH: 3352 (broad m), 2924 (m), 2854, (w), 1741 (w), 1655 (w), 1465 (w) 1229 (s), 1086 (s), 970 (w), 929 (w). 790 (w).

2-(1-(1,3-dihydroxypropan-2-yl)-1*H*-1,2,3-triazol-4-yl)ethyl (2-(trimethylammonio) ethyl phosphate (4.5)



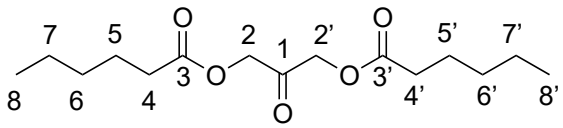
Chemical Formula: $C_{12}H_{25}N_4O_6P$
Molecular Weight: 352.3278

This compound was recovered for characterization from experiments as described in the representative procedure for setup of hydrolysis experiments. The crude reaction mixture of multiple experiments were combined, concentrated *in vacuo* and purified by flash

column chromatography (10% H_2O and 40% MeOH in CH_2Cl_2). The obtained compound was dissolved in a minimum of MeOH and filtered through a PTFE syringe filter to remove any silica particles and concentrated *in vacuo* to yield compound **4.5** as a transparent viscous oil.

^{1}H NMR (400 MHz, CD_3OD) δ 7.89 (s, 1H, C<u>H</u>-3), 4.66 – 4.57 (m, 1H, C<u>H</u>-2), 4.07 (q, J = 6.1 Hz, 2H, C<u>H</u>$_2$-6), 4.04 – 3.98 (m, 2H, C<u>H</u>$_2$-7), 3.94 – 3.84 (m, 4H, C<u>H</u>-1;C<u>H</u>-1'), 3.51 – 3.44 (m, 2H, C<u>H</u>$_2$-8), 3.15 (d, J = 4.5 Hz, 1H, CHO<u>H</u>-1;CHO<u>H</u>-1'), 3.11 (s, 9H, C<u>H</u>$_3$-9;C<u>H</u>$_3$-9';C<u>H</u>$_3$-9''), 2.98 (t, J = 6.2 Hz, 3H, C<u>H</u>$_2$-5); **^{13}C{^{1}H} NMR** (101 MHz, CD_3OD) δ 145.6, 124.2, 67.6 – 67.3 (m, J_{CN}^+ and J_{CP}), 66.8, 65.6 (d, J_{CP} = 5.5 Hz), 62.3 (2C), 60.3 (d, J_{CN}^+ = 4.9 Hz), 55.0 – 54.6 (m, J_{CN}^+, 3C), 49.9, 28.2 (d, J_{CP} = 8.0 Hz); **^{31}P NMR** (162 MHz, CD_3OD) δ -0.44; **HRMS** (ESI) *m/z* calcd for $C_{12}H_{26}O_6N_4P$ $[M+H]^+$: 353.1585, found: 353.1583; **IR** (ATR) ν (cm^{-1}) thin film, MeOH: 3263 (broad m), 2966 (w), 1655 (w), 1478 (w) 1224 (s), 1081 (s), 970 (m), 929 (m). 790 (m).

2-Oxopropane-1,3-diyl dihexanoate (4.18)



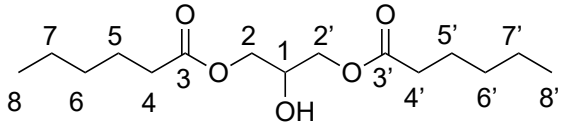
Chemical Formula: $C_{15}H_{26}O_5$
Molecular Weight: 286.3680

To a solution of 1,3-dihydroxylacetone (6.00 g, 66.5 mmol, 1.00 eq) in $CHCl_3$ (150 mL), hexanoyl chloride (20.50 ml, 146.7 mmol, 2.200 eq) was added, followed by dropwise addition of pyridine (12.00 mL, 149.0 mmol, 2.200 eq). The reaction mixture was stirred at room temperature overnight and was subsequently washed with 5% aqueous HCl (150 mL), saturated aqueous $NaHCO_3$ (150 mL), and brine (150 mL). The organic layer was dried (Na_2SO_4) and concentrated *in vacuo* and was purified by flash column

chromatography (10% EtOAc in hexane) to yield diester **4.18** (16.3 g, 56.9 mmol, 86%) as a white waxy solid.

^{1}H NMR (400 MHz, $CDCl_3$) δ 4.75 (s, 4H, C$\underline{H}_2$-2;C$\underline{H}_2$-2'), 2.48 – 2.38 (m, 4H, C$\underline{H}_2$-4;C$\underline{H}_2$-4'), 1.73 – 1.62 (m, 4H, C$\underline{H}_2$-5;C$\underline{H}_2$-5'), 1.39 – 1.28 (m, 8H, C$\underline{H}_2$-6;C$\underline{H}_2$-6'; C$\underline{H}_2$-7;C$\underline{H}_2$-7'), 0.95 – 0.87 (m, 6H, C$\underline{H}_3$-8;C$\underline{H}_3$-8'); **^{13}C{^{1}H} NMR** (101 MHz, $CDCl_3$) δ 198.3, 173.1 (2C), 66.3 (2C), 33.9 (2C), 31.3 (2C), 24.6 (2C), 22.4 (2C), 14.0 (2C); **HRMS** (ESI) *m/z* calcd for $C_{15}H_{26}O_5Na$ $[M+Na]^+$: 309.1673, found: 309.1672.

2-hydroxypropane-1,3-diyl dihexanoate (4.19)



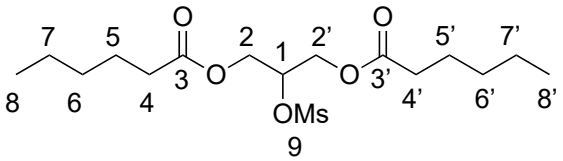
Chemical Formula: $C_{15}H_{28}O_5$
Molecular Weight: 288.3840

$NaBH_4$ (1.90 g, 50.2 mmol, 2.60 eq) in water (a small quantity) was slowly added to a solution of diester **4.18** (5.51 g, 19.2 mmol, 1.00 eq) in THF (300 mL) at 0 °C. The reaction mixture was stirred at 0 °C for 30 min and quenched by addition of 5% HCl (10 mL). H_2O (300 mL) was added, and the mixture was extracted with $CHCl_3$ (400 mL). The organic layer was washed sequentially with H_2O (300 mL), saturated aqueous $NaHCO_3$ (300 mL), and brine (300 mL). The organic layer was dried (Na_2SO_4), concentrated *in vacuo* and purified by flash column chromatography (20% EtOAc in hexane) to yield alcohol **4.19** (3.40 g, 11.8 mmol, 61%) as a transparent oil. A significant amount of the regioisomer is formed during the reaction due to transesterifaction.

^{1}H NMR (400 MHz, $CDCl_3$) δ 4.22 – 4.02 (m, 5H, C$\underline{H}$-1;C$\underline{H}_2$-2;C$\underline{H}_2$-2'), 2.53 (d, J = 4.8 Hz, 1H, CHO$\underline{H}$-1), 2.34 (t, J = 7.6 Hz, 4H, C$\underline{H}_2$-4;C$\underline{H}_2$-4'), 1.69 – 1.57 (m, 4H, C$\underline{H}_2$-5;C$\underline{H}_2$-5'), 1.38 – 1.22 (m, 8H, C$\underline{H}_2$-6;C$\underline{H}_2$-6'; C$\underline{H}_2$-7;C$\underline{H}_2$-7'), 0.93 – 0.85 (m, 6H, C$\underline{H}_3$-8;C$\underline{H}_3$-8'); **^{13}C{^{1}H} NMR** (101 MHz, $CDCl_3$) δ 174.1 (2C), 68.5, 65.2 (2C), 34.2 (2C),

31.4 (2C), 24.7 (2C), 22.5 (2C), 14.1 (2C); **HRMS** (ESI) *m/z* calcd for $C_{15}H_{28}O_5Na$ $[M+Na]^+$: 311.1829, found: 311.1827. Consistent with reported literature values.[37]

2-((methylsulfonyl)oxy)propane-1,3-diyl dihexanoate (4.20)

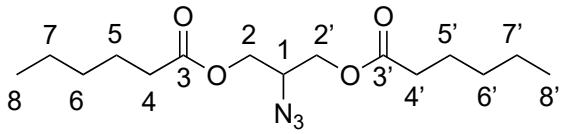


Chemical Formula: $C_{16}H_{30}O_7S$
Molecular Weight: 366.4690

To a solution of alcohol **4.19** (3.40 g, 11.8 mmol, 1.00 eq) and triethylamine (2.50 mL, 17.7 mmol, 1.50 eq) in anhydrous CH_2Cl_2 (50 mL) was added methanesulfonyl chloride (1.00 mL, 12.9 mmol, 1.10 eq) at 0 °C under argon atmosphere. After 2 hours the reaction mixture was washed with 5% aqueous HCl (50 mL), saturated aqueous $NaHCO_3$ (50 mL), and brine (50 mL). The organic layer was dried (Na_2SO_4), concentrated *in vacuo* and purified by flash column chromatography (10% EtOAc in hexane) to afford mesylate **4.20** (3.60 g, 9.82 mmol, 83%) as a transparent oil.

^{1}H NMR (400 MHz, $CDCl_3$) δ 5.02 (tt, *J* = 6.5, 3.8 Hz, 1H, C$\underline{H}$-1), 4.36 (dd, *J* = 12.3, 3.8 Hz, 2H, C$\underline{H}_a$H$_b$-2;CH$_a$H$_b$-2'), 4.22 (dd, *J* = 12.3, 6.5 Hz, 2H, CH$_a\underline{H}_b$-2;CH$_a\underline{H}_b$-2'), 3.08 (s, 3H, $SO_2C\underline{H}_3$-9), 2.35 (t, *J* = 7.6 Hz, 4H, C$\underline{H}_2$-4;C$\underline{H}_2$-4'), 1.69 – 1.57 (m, 4H, C$\underline{H}_2$-5;C$\underline{H}_2$-5'), 1.38 – 1.24 (m, *J* = 4.1, 3.7 Hz, 8H, C$\underline{H}_2$-6;C$\underline{H}_2$-6';C$\underline{H}_2$-7;C$\underline{H}_2$-7'), 0.94 – 0.84 (m, 6H, C$\underline{H}_3$-8;C$\underline{H}_3$-8'); **^{13}C{^{1}H} NMR** (101 MHz, $CDCl_3$) δ 173.3 (2C), 76.8, 62.4 (2C), 38.9, 34.1 (2C), 31.4 (2C), 24.6 (2C), 22.5 (2C), 14.0 (2C); **HRMS** (ESI) *m/z* calcd for $C_{15}H_{27}O_4$ $[M-OMs]^+$: 271.1904, found: 271.1905.

2-azidopropane-1,3-diyl dihexanoate (4.6)

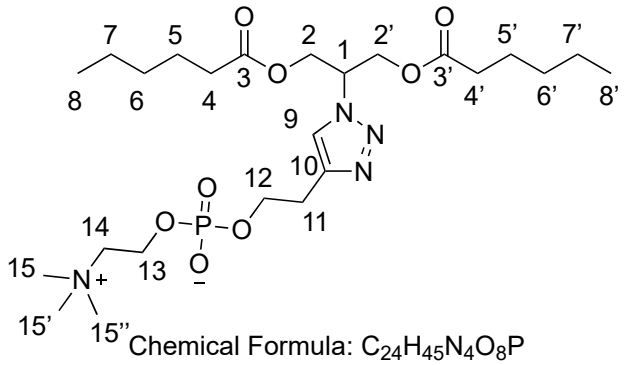


Chemical Formula: $C_{15}H_{27}N_3O_4$
Molecular Weight: 313.3980

To a solution of mesylate **4.20** (3.60 g, 9.82 mmol, 1 eq) in DMF (50 mL) was added sodium azide (2.78 g, 42.8 mmol, 4.40 eq). The reaction mixture was heated to 90 °C for 18 hours and was then concentrated *in vacuo* to remove the majority of DMF. The crude was dissolved in CH_2Cl_2 (50 mL) and washed with saturated aqueous $NaHCO_3$ (3 × 50 mL). The organic layer was dried (Na_2SO_4), concentrated *in vacuo* and purified by flash column chromatography (10% EtOAc in hexane) to afford azide **4.6** (2.76 g, 8.80 mmol, 90%) as a transparent oil.

^{1}H NMR (400 MHz, $CDCl_3$) δ 4.23 (dd, *J* = 11.6, 4.7 Hz, 2H, C$\underline{H}_a$H$_b$-2;C$\underline{H}_a$H$_b$-2'), 4.14 (dd, *J* = 11.6, 6.8 Hz, 2H, CH$_a$$\underline{H}_b$-2;CH$_a$$\underline{H}_b$-2'), 3.88 (tt, *J* = 6.8, 4.6 Hz, 1H, C$\underline{H}$-1), 2.35 (t, *J* = 7.6 Hz, 4H, C$\underline{H}_2$-4;C$\underline{H}_2$-4'), 1.68 – 1.59 (m, 4H, C$\underline{H}_2$-5;C$\underline{H}_2$-5'), 1.41 – 1.23 (m, 8H, C$\underline{H}_2$-6;C$\underline{H}_2$-6';C$\underline{H}_2$-7;C$\underline{H}_2$-7'), 0.95 – 0.86 (m, 6H, C$\underline{H}_3$-8;C$\underline{H}_3$-8'); **^{13}C{^{1}H} NMR** (101 MHz, $CDCl_3$) δ 173.4 (2C), 63.1 (2C), 58.8, 34.1 (2C), 31.4 (2C), 24.6 (2C), 22.4 (2C), 14.0 (2C); **HRMS** (ESI) *m/z* calcd for $C_{15}H_{27}O_4N_3Na$ $[M+Na]^+$: 336.1894, found: 336.1893; **IR** (ATR) ν (cm^{-1}) thin film, CH_2Cl_2: 2957 (w), 2932 (w), 2872 (w), 2118 (w), 1741 (s), 1460 (w), 1242 (m), 1159 (s), 1099 (m), 734 (w).

2-(1-(1,3-bis(hexanoyloxy)propan-2-yl)-1*H*-1,2,3-triazol-4-yl)ethyl (2-(trimethylammonio)ethyl) phosphate (4.7)

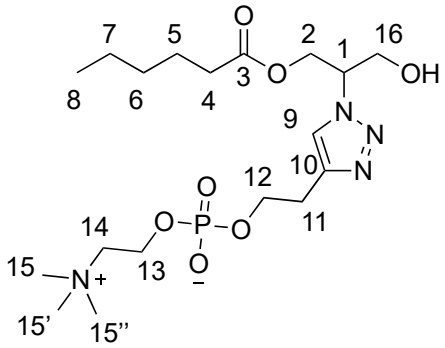


To a solution of alkyne **4.2** (200 mg, 0.850 mmol, 1.00 eq), $CuSO_4 \cdot 5H_2O$ (2.5 mg, 0.010 mmol, 0.010 eq) in Milli-Q H_2O (2.5 mL) and *t*-BuOH (2.5 mL) was added TBTA (5.2 mg, 0.010 mmol, 0.010 eq) and azide **4.6** (300 μL, 1.00 mmol, 1.18 eq), and the flask was capped with a septum. The solution was degassed by bubbling argon through it for 30 minutes. Afterwards sodium ascorbate (6.0 mg, 0.030 mmol, 0.040 eq) was added to initiate the reaction. The reaction mixture was stirred at 1000 rpm under a continuous flow of argon. The crude mixture was concentrated *in vacuo* and purified by flash column chromatography (2% H_2O and 48% MeOH in CH_2Cl_2). The obtained compound was dissolved in a minimum of MeOH and filtered through a PTFE syringe filter to remove any silica particles and concentrated *in vacuo* to yield surfactant **4.7** (342 mg, 0.620 mmol, 73%) as a transparent viscous oil.

^{1}H NMR (400 MHz, CD_3OD) δ 8.02 (s, 1H, C<u>H</u>-9), 5.16 (p, *J* = 6.1 Hz, 1H, C<u>H</u>-1), 4.62 – 4.51 (m, 4H, C<u>H</u>$_2$-2;C<u>H</u>$_2$-2’), 4.22 (dt, *J* = 7.1, 3.6 Hz, 2H, C<u>H</u>$_2$-13), 4.14 (q, *J* = 6.5 Hz, 2H, C<u>H</u>$_2$-12), 3.66 – 3.59 (m, 2H, C<u>H</u>$_2$-14), 3.22 (s, 9H, C<u>H</u>$_3$-15;C<u>H</u>$_3$-15’;C<u>H</u>$_3$-15’’), 3.05 (t, *J* = 6.4 Hz, 2H, C<u>H</u>$_2$-11), 2.30 (t, *J* = 7.4 Hz, 4H, C<u>H</u>$_2$-4;C<u>H</u>$_2$-4’), 1.55 (p, *J* = 7.4

Hz, 4H, C$\underline{H}_2$-5;C$\underline{H}_2$-5'), 1.38 – 1.19 (m, 8H, C$\underline{H}_2$-6;C$\underline{H}_2$-6';C$\underline{H}_2$-7;C$\underline{H}_2$-7'), 0.90 (t, J = 7.1 Hz, 6H, C$\underline{H}_3$-8;C$\underline{H}_3$-8'); **^{13}C{^{1}H} NMR** (101 MHz, CD_3OD) δ 174.5 (2C), 145.9, 124.0, 67.8 – 67.4 (m, J_{CN}^+ and J_{CP}), 65.5 (d, J_{CP} = 5.3 Hz), 63.5 (2C), 60.4 – 60.3 (m, J_{CN}^+, 2C), 54.9 – 54.6 (m, J_{CN}^+, 3C), 34.6 (2C), 32.3 (2C), 28.3 (d, J_{CP} = 8.0 Hz), 25.6 (2C), 23.3 (2C), 14.2 (2C); **^{31}P NMR** (162 MHz, CD_3OD) δ -0.56; **HRMS** (ESI) *m/z* calcd for $C_{24}H_{46}O_8N_4P$ $[M+H]^+$: 549.3048, found: 549.3047; **IR** (ATR) ν (cm^{-1}) thin film, MeOH: 3378 (broad w), 2958 (w), 2872 (w), 1742 (s), 1468 (w) 1230 (s), 1165 (m), 1086 (s), 970 (w), 786 (w).

2-(1-(1-(Hexanoyloxy)-3-hydroxypropan-2-yl)-1*H*-1,2,3-triazol-4-yl)ethyl (2-(trimethylammonio)ethyl) phosphate (4.8)

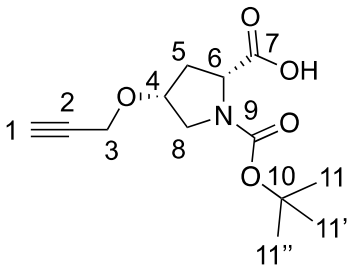


Chemical Formula: $C_{18}H_{35}N_4O_7P$
Molecular Weight: 450.4728

Compound **4.8** was recovered for characterization from experiments as described in the representative procedure for setup of hydrolysis experiments. The crude reaction mixture of multiple experiments were combined, concentrated *in vacuo* and purified by flash column chromatography (5% H_2O and 45% MeOH in CH_2Cl_2). The obtained compound was dissolved in a minimum of MeOH and filtered through a PTFE syringe filter to remove any silica particles and concentrated *in vacuo* to yield compound **4.4** as a transparent viscous oil.

^{1}H NMR (400 MHz, CD_3OD) δ 7.99 (s, 1H, C<u>H</u>-9), 4.95 – 4.89 (m, 1H, C<u>H</u>-1), 4.59 – 4.48 (m, 2H, C<u>H</u>$_2$-2), 4.13 (q, *J* = 6.4 Hz, 4H, C<u>H</u>$_2$-6;C<u>H</u>$_2$-7), 4.04 – 3.92 (m, 2H, C<u>H</u>$_2$-16), 3.62 – 3.53 (m, 2H, C<u>H</u>$_2$-14), 3.24 – 3.22 (m, 1H, CHO<u>H</u>-16), 3.20 (s, 9H, C<u>H</u>$_3$-15;C<u>H</u>$_3$-15';C<u>H</u>$_3$-15''), 3.05 (t, *J* = 6.3 Hz, 2H, C<u>H</u>$_2$-11), 2.28 (t, *J* = 7.4 Hz, 2H, C<u>H</u>$_2$-4), 1.53 (p, *J* = 7.4 Hz, 2H, C<u>H</u>$_2$-5), 1.37 – 1.16 (m, 4H, C<u>H</u>$_2$-6;C<u>H</u>$_2$-7), 0.89 (t, *J* = 7.1 Hz, 3H, C<u>H</u>$_3$-8); **^{13}C{^{1}H} NMR** (101 MHz, CD_3OD) δ 174.7, 124.0, 73.9, 67.8 – 67.2 (m, J_{CN}^{+} and J_{CP}), 65.5 (d, J_{CP} = 5.6 Hz), 64.4, 63.9, 63.5, 62.2, 60.3 (d, J_{CN}^{+} = 5.0 Hz), 54.8 – 54.7 (m, J_{CN}^{+}, 3C), 34.7, 32.3, 28.2 (d, J_{CP} = 7.6 Hz), 25.6, 23.3, 14.2; **^{31}P NMR** (162 MHz, CD_3OD) δ -0.43; **HRMS** (ESI) *m/z* calcd for $C_{18}H_{36}O_7N_4P$ $[M+H]^+$: 451.2316, found: 451.2315; **IR** (ATR) ν (cm^{-1}) thin film, MeOH: 3345 (broad w), 2958 (w), 1736 (w), 1477 (w) 1225 (s), 1082 (broad s), 970 (w), 790 (w).

(2*R*,4*R*)-1-(*tert*-butoxycarbonyl)-4-(prop-2-yn-1-yloxy)pyrrolidine-2-carboxylic acid (4.21)



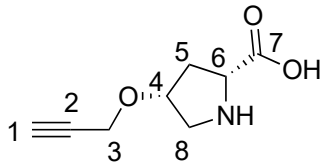
Chemical Formula: $C_{13}H_{19}NO_5$
Molecular Weight: 269.30

Synthesized according to adapted procedure from van Oers *et al*.[31] N-Boc-cis-4-hydroxy-D-proline (2.00 g, 4.32 mmol, 1.00 eq) was dissolved in anhydrous THF (20 mL) at RT. Sodium hydride (346 mg of a 60 wt. % dispersion in mineral oil, 8.65 mmol, 2.00 equiv) was added in small portions and the solution was stirred for 10 min. Next, an additional amount of THF (20 mL) was added, followed by the addition of propargyl bromide (963 μL of a 80 wt. % in toluene, 8.65 mmol, 2.00 equiv). The solution was stirred for 18 h.

Afterwards, the solution was cooled to 0 °C, quenched with 5 mL water, and allowed to warm up to ambient temperature. The reaction was quenched by slow addition of H_2O (5 mL) and the mixture was acidified to pH 2 with 1 M HCl solution. The product was extracted with CH_2Cl_2 (3 × 25 mL), after which the resulting organic fractions were dried (Na_2SO_4), concentrated *in vacuo* and purified by flash column chromatography (1% AcOH and 39% EtOAc in hexane) yielded alkyne **4.21** (823 mg, 3.06 mmol, 71%) as a white crystalline solid.

^{1}H NMR (400 MHz, CD_3OD, mixture of rotamers) δ 4.37 – 4.25 (m, 2H, C<u>H</u>-4;C<u>H</u>-6), 4.18 – 4.11 (m, 2H, C<u>H$_2$</u>-3), 3.64 (dd, *J* = 11.7, 5.5 Hz, 1H, C<u>H$_a$H$_b$</u>-8), 3.44 (ddd, *J* = 11.6, 3.0, 1.1 Hz, 1H, CH$_a$<u>H$_b$</u>-8), 2.83 (t, *J* = 2.4 Hz, 1H, C<u>H</u>-1), 2.41 (dddd, *J* = 29.7, 14.1, 9.2, 5.2 Hz, 1H, C<u>H$_a$H$_b$</u>-5), 2.32 – 2.18 (m, 1H, CH$_a$<u>H$_b$</u>-5), 1.47 (s, 3H, C<u>H$_3$</u>-11;C<u>H$_3$</u>-11';C<u>H$_3$</u>-11''), 1.43 (s, 6H, C<u>H$_3$</u>-11;C<u>H$_3$</u>-11';C<u>H$_3$</u>-11''); **^{13}C{^{1}H} NMR** (101 MHz, CD_3OD, mixture of rotamers) δ 175.7, 155.9, 81.6, 80.4, 77.7 (rotamer), 76.8, 76.0, 76.0 (rotamer), 59.0, 58.6 (rotamer), 57.0, 56.9 (rotamer), 53.1 (rotamer), 52.5, 36.7, 35.8 (rotamer), 28.7 (C3, rotamer), 28.5 (C3); **HRMS** (ESI) *m/z* calcd for $C_{13}H_{19}O_5NNa$ $[M+Na]^+$: 292.1155, found: 292.1155; **IR** (ATR) ν (cm^{-1}) thin film, $CHCl_3$: 3267 (w), 2978 (w), 1697 (broad s), 1407 (board strong), 1368 (m), 1164 (s), 1090 (s), 900 (w), 770 (w), 670 (w); **[α]**$^{25}_D$ = +61.0 (c = 1.00, $CHCl_3$). Consistent with reported literature values.[38]

(2*R*,4*R*)-4-(prop-2-yn-1-yloxy)pyrrolidine-2-carboxylic acid (4.9)

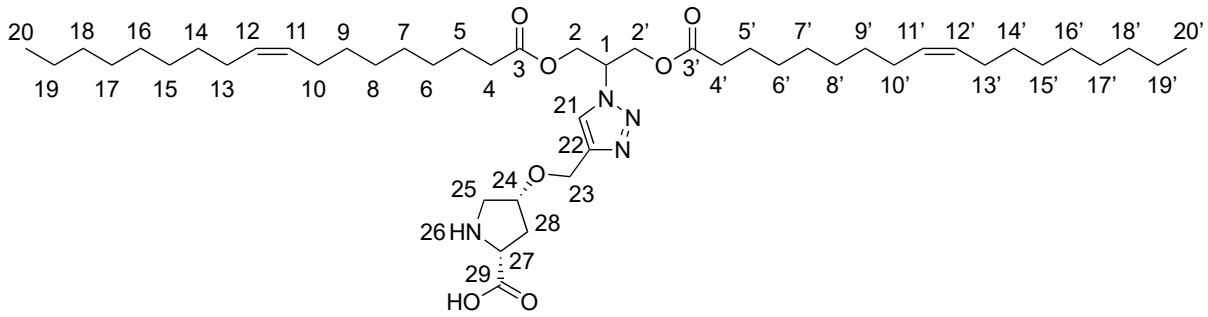


Chemical Formula: $C_8H_{11}NO_3$
Molecular Weight: 169.18

Synthesized according to adapted procedure from van Wang *et al*.[39] Alkyne **4.21** (500 mg, 1.86 mmol) was suspended in water and heated to reflux for 2 hours. The solution was concentrated *in vacuo* and the resultant solid was triturated with CH_2Cl_2 to yield deprotected alkyne **4.9** (284 mg, 1.68 mmol, 90%) as a crystalline white solid.

^{1}H NMR (400 MHz, CD_3OD) δ 4.53 – 4.44 (m, 1H, C<u>H</u>-4), 4.26 – 4.13 (m, 2H, C<u>H$_2$</u>-3), 4.05 (dd, *J* = 9.7, 4.6 Hz, 1H, C<u>H</u>-6), 3.58 (dt, *J* = 12.3, 1.7 Hz, 1H, C<u>H$_a$</u>H$_b$-8), 3.36 – 3.31 (m, 2H, CH$_a$<u>H$_b$</u>-8;N<u>H</u>), 2.91 (t, *J* = 2.4 Hz, 1H, C<u>H</u>-1), 2.48 (ddd, *J* = 12.3, 4.6, 2.3 Hz, 1H, C<u>H$_a$</u>H$_b$-5), 2.42 (ddd, *J* = 14.3, 9.8, 4.7 Hz, 1H, CH$_a$<u>H$_b$</u>-5); **^{13}C{^{1}H} NMR** (101 MHz, CD_3OD) δ 173.6, 79.9, 77.0, 76.5, 61.2, 56.7, 51.9, 35.2; **HRMS** (ESI) *m/z* calcd for $C_8H_{12}O_3N$ $[M+H]^+$: 170.0812, found: 170.0812; **IR** (ATR) ν (cm^{-1}) thin film, CH_3OH: 3260 (w), 3199 (w), 3099 (w), 2343 (broad w), 2111 (w), 1617 (s), 1395 (m), 1369 (m), 1307 (w), 1081 (s), 1060 (s), 1039 (m), 874 (m), 707 (w), 666 (w); **[α]**$^{25}_D$ = +26.2 (c = 1.00, CH_3OH).

(2*R*,4*R*)-4-((1-(1,3-bis(oleoyloxy)propan-2-yl)-1*H*-1,2,3-triazol-4-yl)methoxy)pyrrolidine-2-carboxylic acid (4.10)



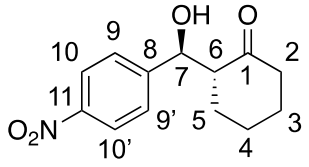
Chemical Formula: $C_{47}H_{82}N_4O_7$
Molecular Weight: 815.19

To a solution of alkyne **4.9** (30.0 mg, 0.177 mmol, 1.00 eq), $CuSO_4 \cdot 5H_2O$ (10 mg, 0.040 mmol, 0.23 eq) in Milli-Q H_2O (2.5 mL) and *t*-BuOH (2.5 mL) was added TBTA (21 mg, 0.040 mmol, 0.23 eq) and azide **4.1** (130 μL, 0.203 mmol, 1.15 eq), and the flask was capped with a septum. The solution was degassed by bubbling argon through it for 30

minutes. Afterwards sodium ascorbate (24 mg, 0.12 mmol, 0.69 eq) was added to initiate the reaction. The reaction mixture was stirred at 1000 rpm under a continuous flow of argon. The crude mixture was concentrated *in vacuo* and purified by flash column chromatography (1→30% MeOH in CH_2Cl_2) to yield organocatalyst **4.10** (136 mg, 0.167 mmol, 94%) as a transparent viscous oil.

^{1}H NMR (400 MHz, CD_3OD) δ 8.11 (s, 1H, C<u>H</u>-21), 5.41 – 5.28 (m, 4H, C<u>H</u>-11;C<u>H</u>-11';C<u>H</u>-12;C<u>H</u>-12'), 5.18 (p, *J* = 6.0 Hz, 1H, C<u>H</u>-1), 4.65 – 4.59 (m, 2H, C<u>H$_2$</u>-23), 4.57 (d, *J* = 5.8 Hz, 4H, C<u>H$_2$</u>-2;C<u>H$_2$</u>-2'), 4.36 – 4.28 (m, 1H, C<u>H</u>-24), 4.09 – 4.00 (m, 1H, C<u>H</u>-27), 3.57 (d, *J* = 12.2 Hz, 1H, C<u>H$_a$</u>H$_b$-25), 3.27 (dd, *J* = 12.9, 4.6 Hz, 1H, CH$_a$<u>H$_b$</u>-25), 2.55 (d, *J* = 14.1 Hz, 1H, C<u>H$_a$</u>H$_b$-28), 2.42 – 2.34 (m, 1H, CH$_a$<u>H$_b$</u>-28), 2.30 (t, *J* = 7.4 Hz, 4H, C<u>H$_2$</u>-4;C<u>H$_2$</u>-4'), 2.03 (q, *J* = 6.4 Hz, 8H, C<u>H$_2$</u>-10;C<u>H$_2$</u>-10';C<u>H$_2$</u>-13;C<u>H$_2$</u>-13'), 1.55 (p, *J* = 7.4 Hz, 4H, C<u>H$_2$</u>-5;C<u>H$_2$</u>-5'), 1.43 – 1.22 (m, 40H, (C<u>H$_2$</u>)$_4$-6-9;(C<u>H$_2$</u>)$_4$-6'-9';(C<u>H$_2$</u>)$_6$-14-19;(C<u>H$_2$</u>)$_6$-14'-19'), 0.93 – 0.86 (m, 6H, C<u>H$_3$</u>-20;C<u>H$_3$</u>-20'); **^{13}C{^{1}H} NMR** (126 MHz, CD_3OD) δ 174.4 (2C), 145.8, 130.9 (2C), 130.8 (2C), 124.9, 77.9, 63.4, 63.4, 62.8, 61.1, 60.5, 52.0, 35.4, 34.7 (2C), 33.1 (2C), 30.9 (2C), 30.8 (2C), 30.6 (2C), 30.5 (2C), 30.4 (2C), 30.3 (2C), 30.2 (2C), 30.1 (2C), 28.1 (4C), 25.9 (2C), 23.8 (2C), 14.5 (2C); **HRMS** (ESI) *m/z* calcd for $C_{47}H_{83}O_7N_4$ $[M+H]^+$: 815.6256, found: 815.6254; **IR** (ATR) ν (cm^{-1}) thin film, $CHCl_3$: 2924 (s), 2854 (m), 2361 (w), 1745 (s), 1604 (board m), 1457 (m), 1378 (m), 1162 (m), 1162 (m), 1084 (m), 775 (w), 695 (w); **[α]$^{25}_D$** = −1.0 (c = 1.00, $CHCl_3$).

(*R*)-2-((*S*)-Hydroxy(4-nitrophenyl)methyl)cyclohexan-1-one (4.13)



Chemical Formula: $C_{13}H_{15}NO_4$
Molecular Weight: 249.27

Enantioenriched variant of **4.13** was prepared according to the general procedure reported above.

The racemate of **4.13** was synthesised in the following manner: A solution of 4-nitrobenzaldehyde (150 mg, 0.990 mmol, 1.00 eq) and pyrrolidine (8.0 μL, 0.096 mmol, 0.10 eq) in cyclohexanone (520 μL, 5.02 mmol, 5.00 eq) was stirred overnight. The crude reaction mixture was purified by flash column chromatography (30% EtOAc in hexane) to yield racemic *anti* aldol product **4.13** (85 mg, 0.34 mmol, 34%) as an off-white solid.

^{1}H NMR (400 MHz, $CDCl_3$) δ 8.22 – 8.11 (m, 2H, C<u>H</u>-10; C<u>H</u>-10'), 7.53 – 7.44 (m, 2H, C<u>H</u>-9; C<u>H</u>-9'), 4.88 (dd, *J* = 8.3, 2.8 Hz, 1H, C<u>H</u>-7), 4.08 (d, *J* = 3.2 Hz, 1H, CHO<u>H</u>-7), 2.58 (dddd, *J* = 12.8, 8.3, 5.5, 1.2 Hz, 1H, C<u>H</u>-6), 2.50 – 2.43 (m, 1H, C<u>H</u>$_a$H$_b$-2), 2.35 (tdd, *J* = 13.6, 6.1, 1.2 Hz, 1H, CH$_a$<u>H</u>$_b$-2), 2.09 (ddt, *J* = 12.0, 5.8, 3.0 Hz, 1H, C<u>H</u>$_a$H$_b$-3), 1.85 – 1.77 (m, 1H, C<u>H</u>$_a$H$_b$-4), 1.72 – 1.51 (m, 3H, CH$_a$<u>H</u>$_b$-3;CH$_a$<u>H</u>$_b$-4;C<u>H</u>$_a$H$_b$-5), 1.42 – 1.29 (m, 1H, CH$_a$<u>H</u>$_b$-5); **^{13}C{^{1}H} NMR** (101 MHz, $CDCl_3$) δ 214.7, 148.6, 147.6, 128.0 (2C), 123.6 (2C), 74.0, 57.3, 42.7, 30.8, 27.7, 24.7; **HRMS** (ESI) *m/z* calcd for $C_{13}H_{14}O_4N$ $[M-H]^-$: 248.0928, found: 248.0926; **[α]**$^{25}_D$ = – 6.7 (c = 0.60, $CHCl_3$). Negative optical rotation is in agreement with the (2*R*,1'*S*) absolute stereochemistry.[40]

Enantiomeric excess was determined by SFC with a Chiralpak® IE column (3 μm, 150×3 mm). Conditions: Flow rate: 1.5 ml/min. Gradient: CO_2:MeOH with a gradient of 99:1 to 60:40 in 0 to 5 min; gradient of 60:40 to 40:60 in 5 to 5.5 min; 40:60 isocratically from 5.5 to 7 min; 100:0 isocratically from 7 to 8 min. λ_{det} = 266.8 nm. Retention time: $t_{(2S,1'R)}$ = 5.16 min (minor), $t_{(2R,1'S)}$ = 5.36 min (major).

Consistent with reported literature values.[41]

4.8.3 Fluorimetry Data

The critical micelle concentrations of surfactant **4.3** and **4.7** were determined as described in Section 2.5.3.

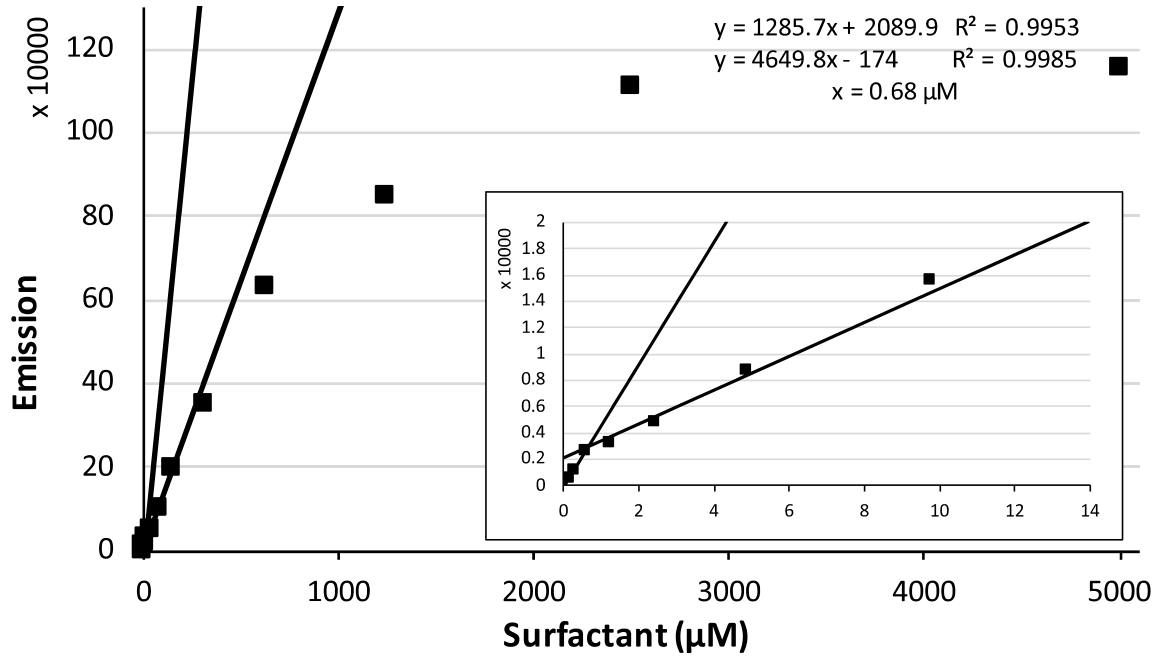


Figure 4.14 Determination of CAC by fluorimetry measurements. A CAC of 0.68 µM was extracted from a plot of fluorescence measurements at various concentration for surfactant **4.3**.

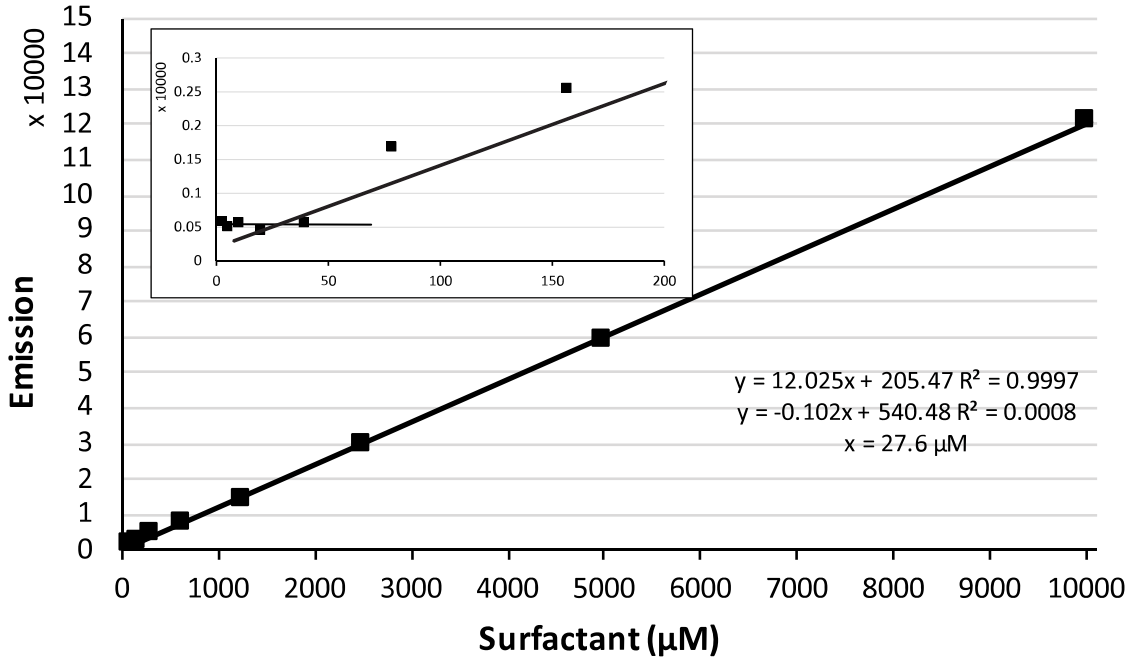


Figure 4.15 Determination of CMC by fluorimetry measurements. A CMC of 27.6 µM was extracted from a plot of fluorescence measurements at various concentration for surfactant **4.7**.

4.8.4 DLS Data

Samples were prepared by dissolving the surfactant in 1 mL of ultrapure Milli-Q water at the reported concentrations. In the case of reaction monitoring by DLS an aliquot was taken from the reaction mixture and this was directly measured by DLS. When the sample concentration is too low (i.e. t = 0 h), the scattering from the particles is weak and there is greater influence of noise from unwanted sources e.g. dust particles or oil droplets which gives biased results.

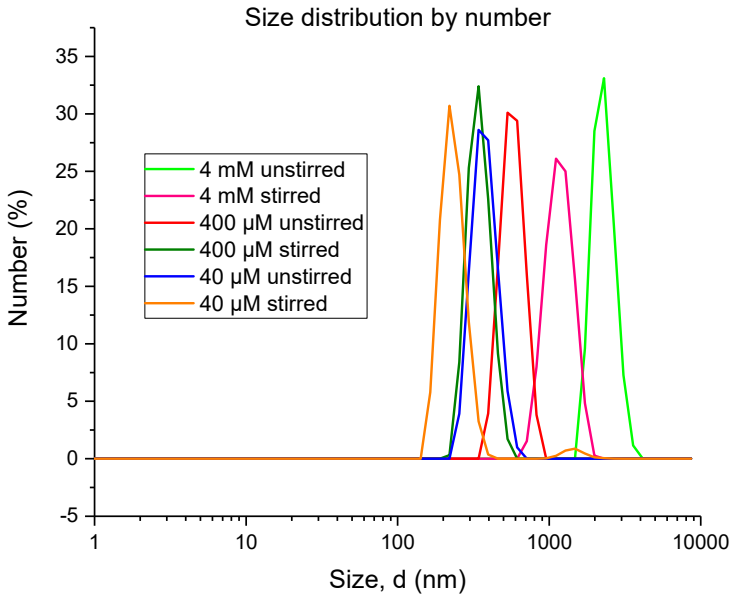


Figure 4.16 Determination of size and the effect of stirring on aggregates of **4.3**. The size distribution by number of DLS measurements of surfactant **4.3** at 40 µM, 400 µM and 4 mM under stirred and unstirred conditions indicates a reduction in aggregate size at lower concentrations and when exposed to stirring conditions.

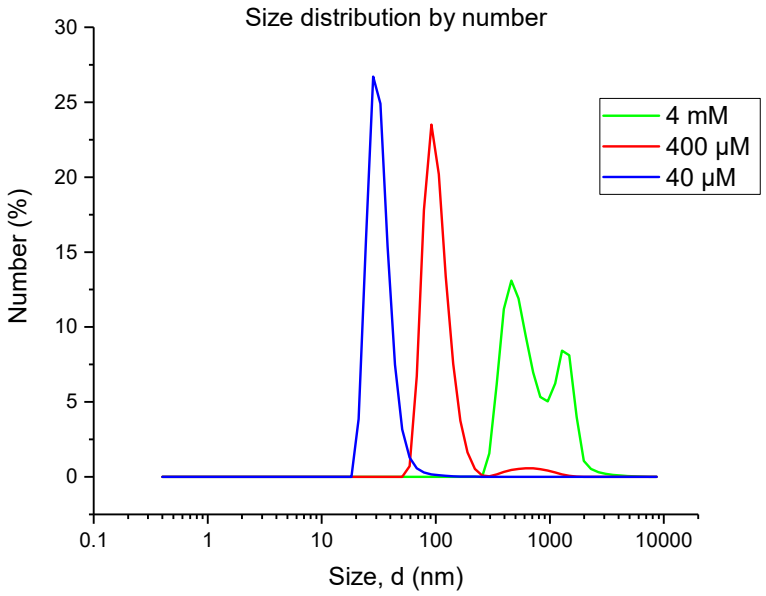


Figure 4.17 Determination of aggregate size of **4.3** by number after thin film hydration. The size distribution by number of DLS measurements of vesicles **4.3** at 40 µM, 400 µM and 4 mM formed through thin film hydration indicates aggregation into vesicles of smaller size than normal dissolution of **4.3**.

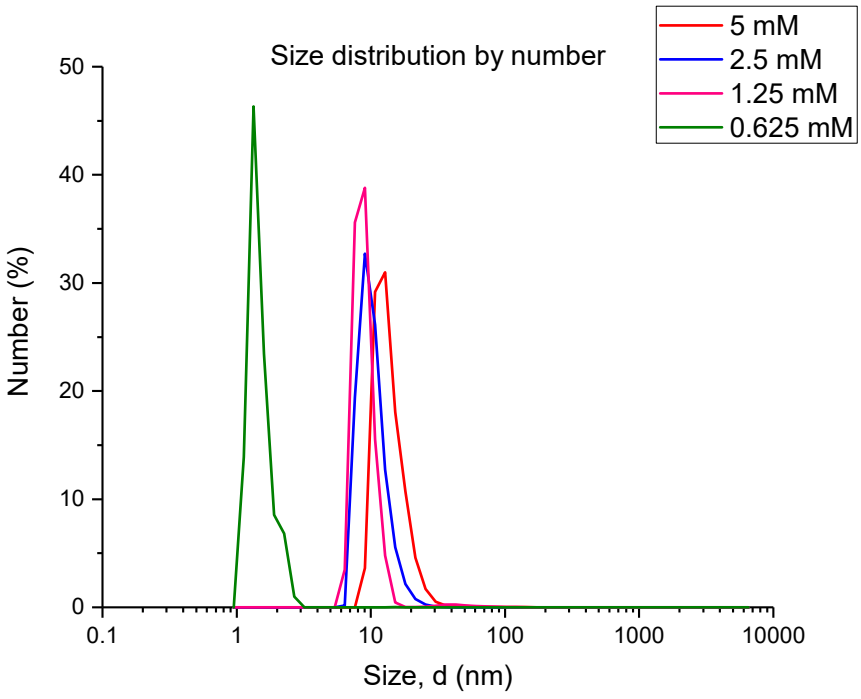


Figure 4.18 Determination of aggregate size of **4.7** by number. The size distribution by number of DLS measurements of surfactant **4.7** at 0.625 mM to 5 mM indicates aggregation into micelles with a consistent size around 10 nm independent of concentration.

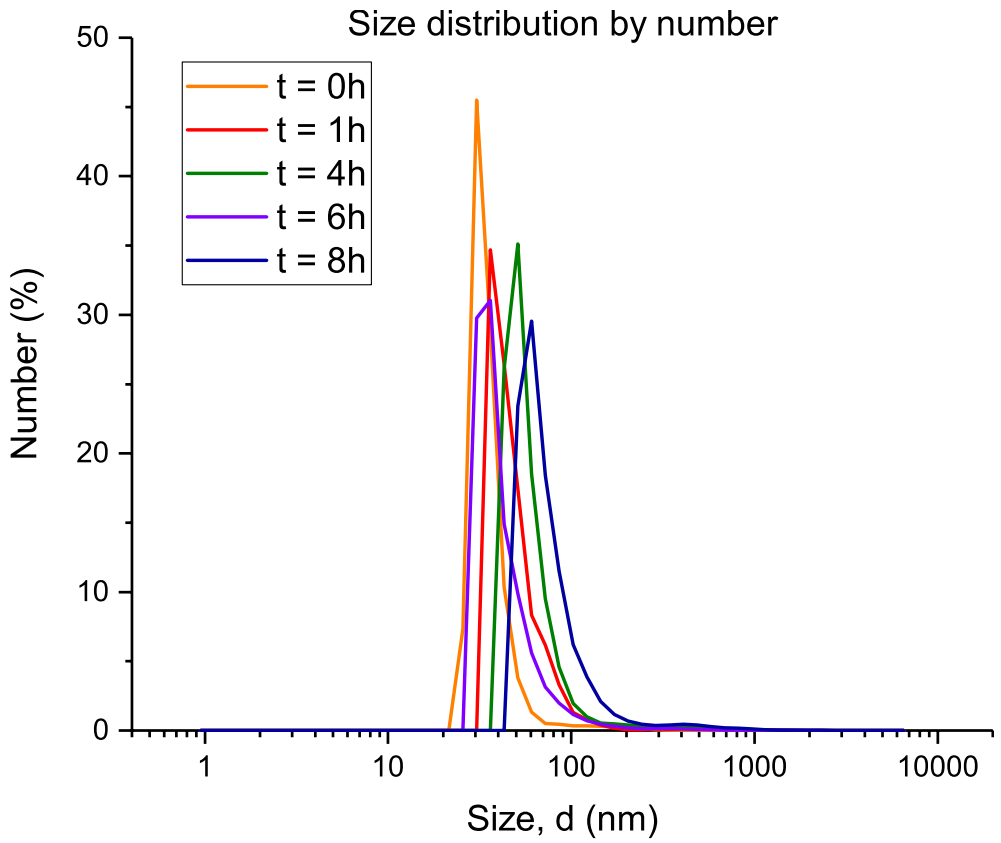


Figure 4.19 Determination of aggregate size of **4.3** in unseeded reaction by number. Size distribution by number of the aggregates in aliquots of the unseeded reaction (Fig. 4.3, red squares) at different time points measured by DLS.

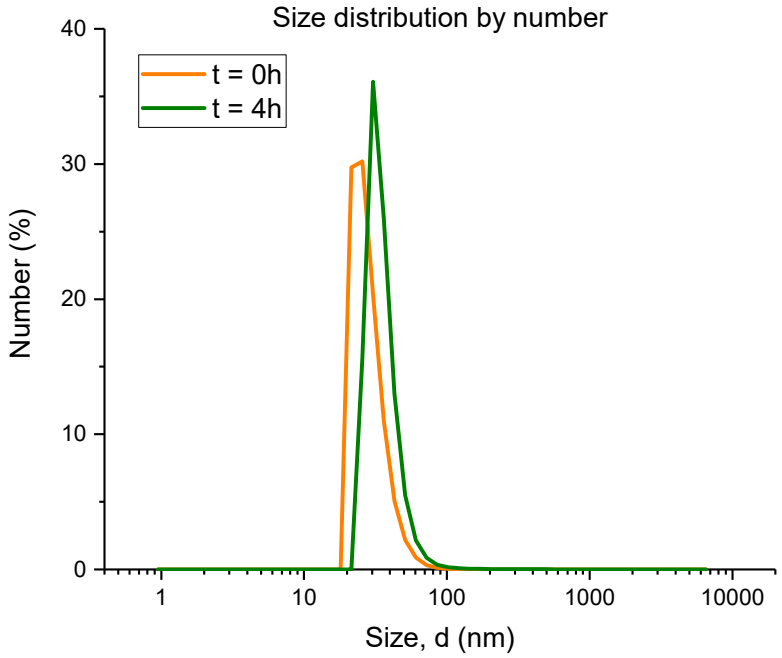


Figure 4.20 Determination of aggregate size of **4.3** in seeded reaction by number. Size distribution by number of the aggregates in aliquots of the seeded reaction (Figure 4.3, blue diamonds) at different time points measured by DLS.

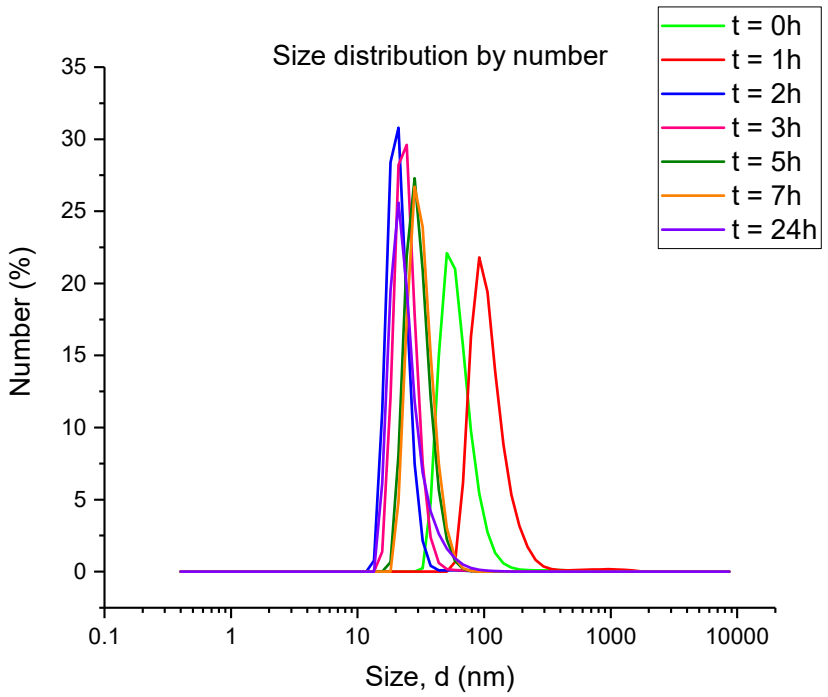


Figure 4.21 Determination of aggregate size of **4.3** in thin film seeded reaction by number. Size distribution by number of the aggregates in aliquots of the thin film seeded reaction (Fig. 4.3, yellow triangles) at different time points measured by DLS.

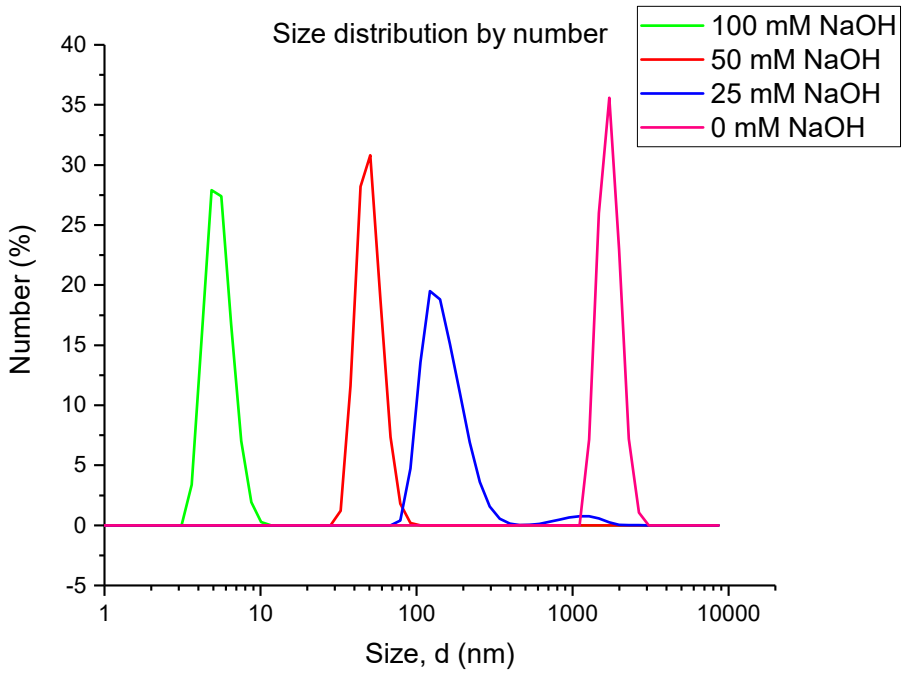


Figure 4.22 Determination of influence of NaOH concentration on aggregate size. Exposure of 4 mM of surfactant **4.3** to increasing concentrations of NaOH results in smaller aggregates due to higher degrees of hydrolysis: 25 mM NaOH yields 2.7 mM of **4.3** and 1.3 mM of **4.4**; 50 mM NaOH yields 1 mM of **4.3**, 2.3 mM of **4.4** and 0.7 mM of **4.5**; 100 mM NaOH yields 4 mM of **4.5**.

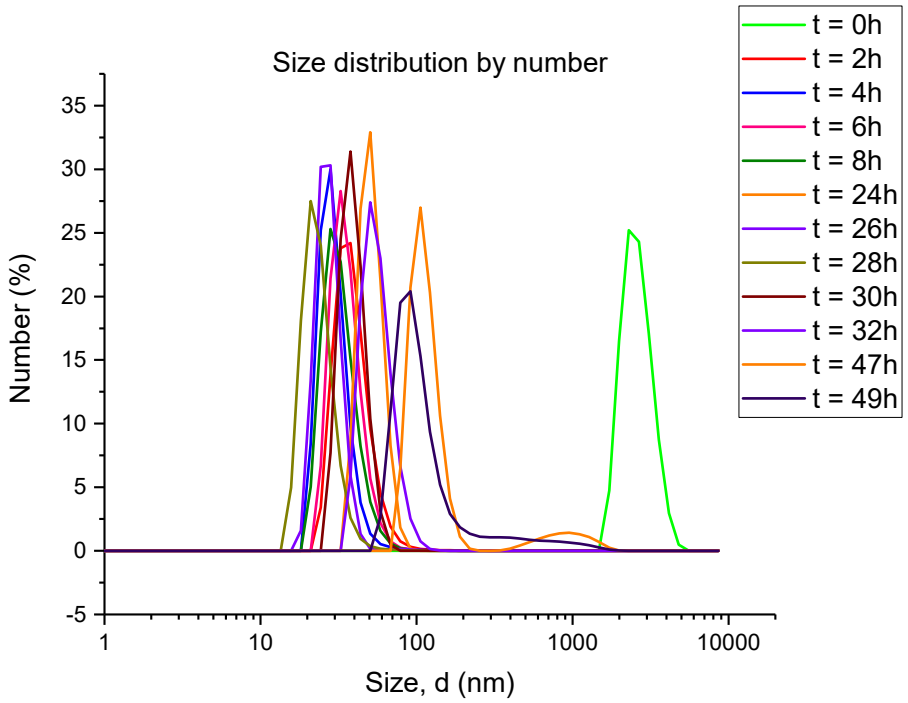


Figure 4.23 Determination of aggregate size under out-of-equilibrium conditions. Size distribution by number of the aggregates in aliquots of out-of-equilibrium reaction (Figure 4.6c) at different time points measured by DLS.

4.8.5 Turbidity Measurements



Figure 4.24 A wavelength-independent increase in absorbance was observed with increasing concentration of **4.3** indicating an increase in turbidity of the solution.

4.8.6 TEM Data

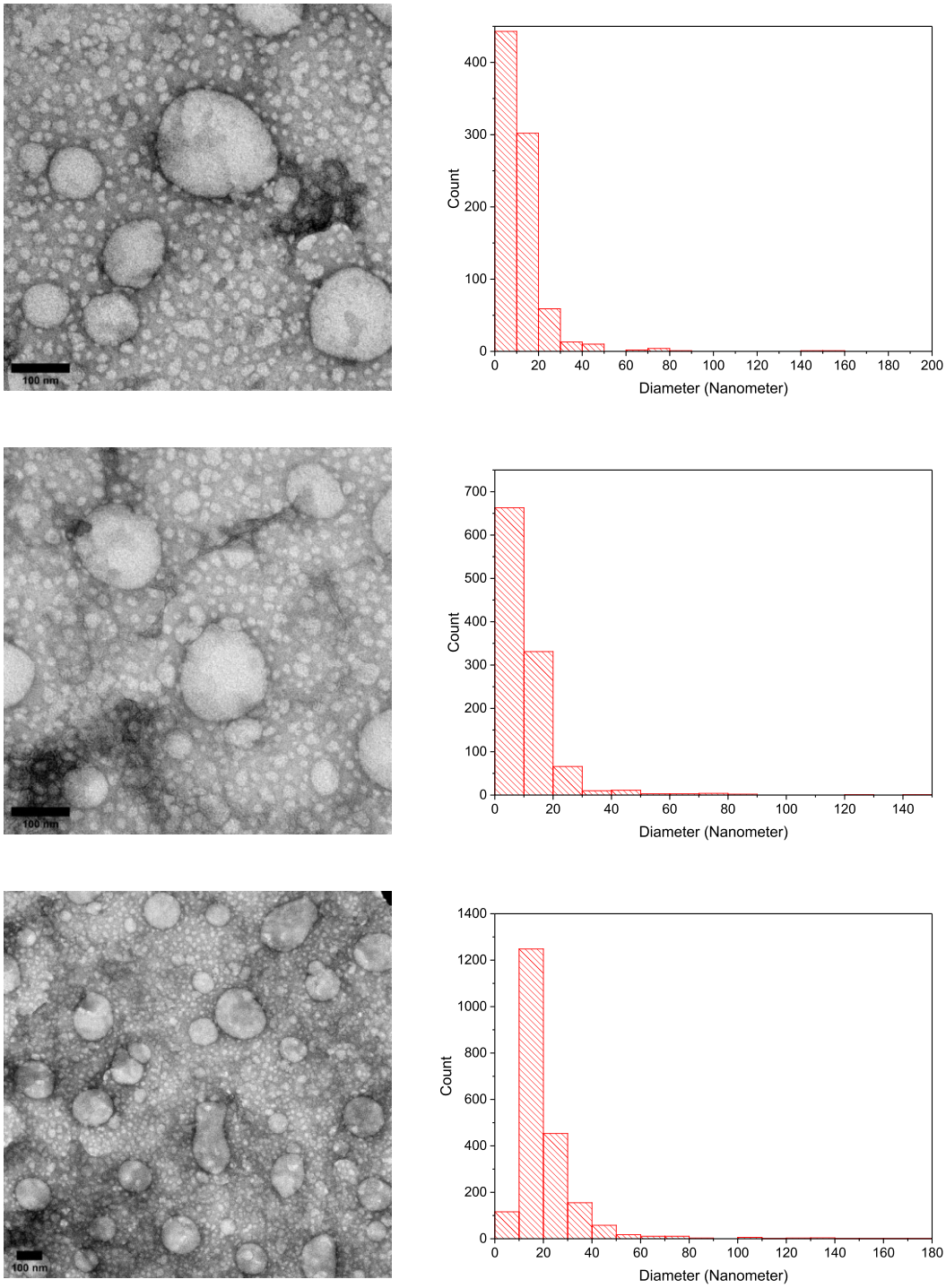


Figure 4.25 TEM micrographs of **4.3** (4 mM) deposited on a copper grid and stained with 2% uranyl acetate. Aggregates in the range 1-40 nm and some up to 40-180 nm are observed. Scale bar, 100 nm.

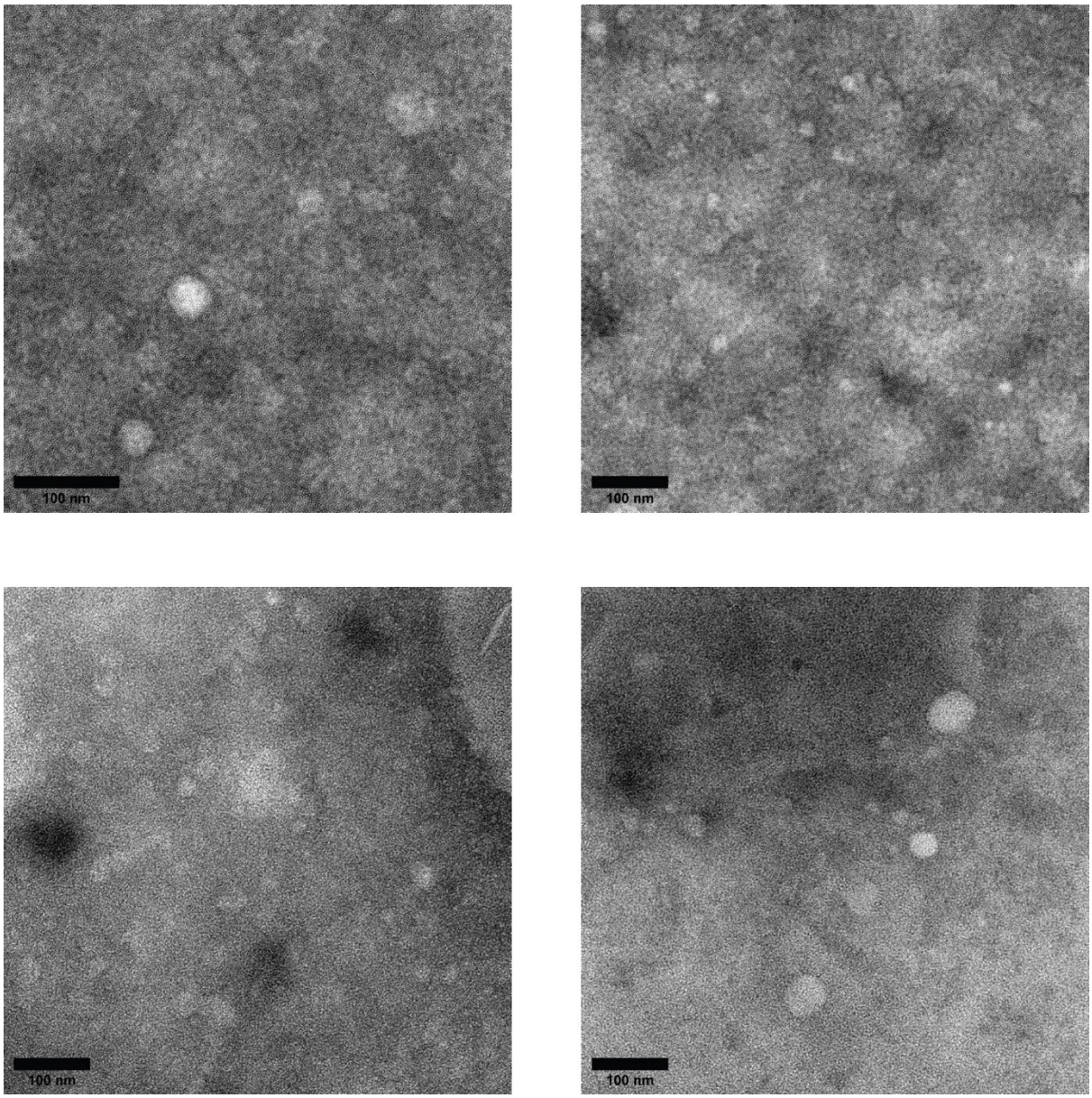


Figure 4.26 TEM micrographs of **4.7** (4 mM) deposited on a copper grid and stained with 2% uranyl acetate. Micelles largely in the 10-30 nm range are observed. Scale bar, 100 nm.

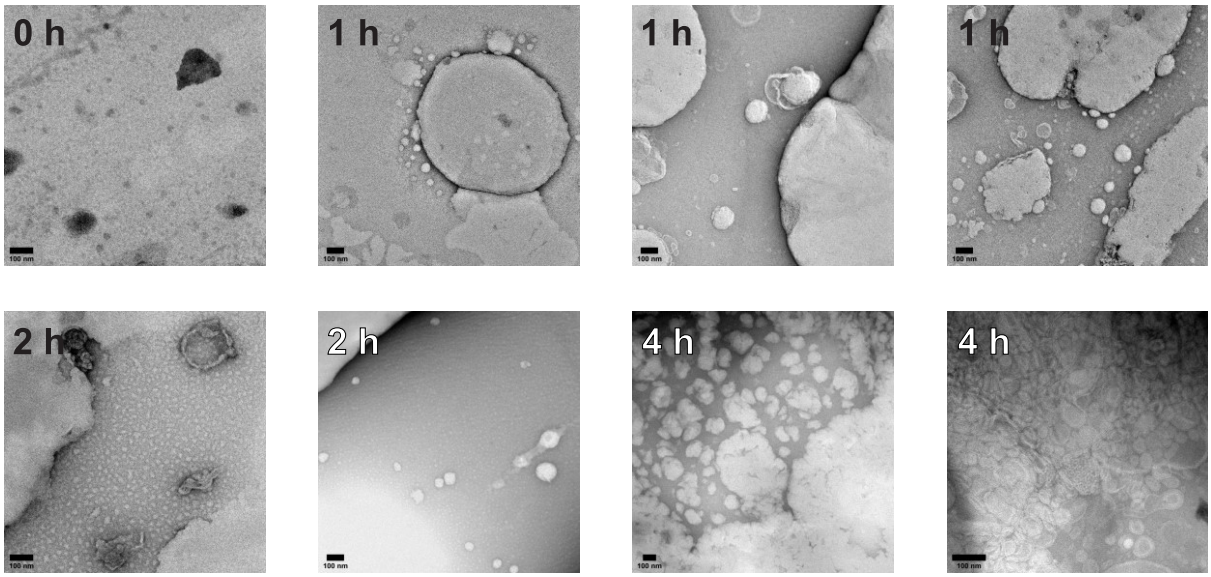


Figure 4.27 Additional TEM micrographs to Figure 4.4a of aliquots of the unseeded reaction. Scale bar, 100 nm.

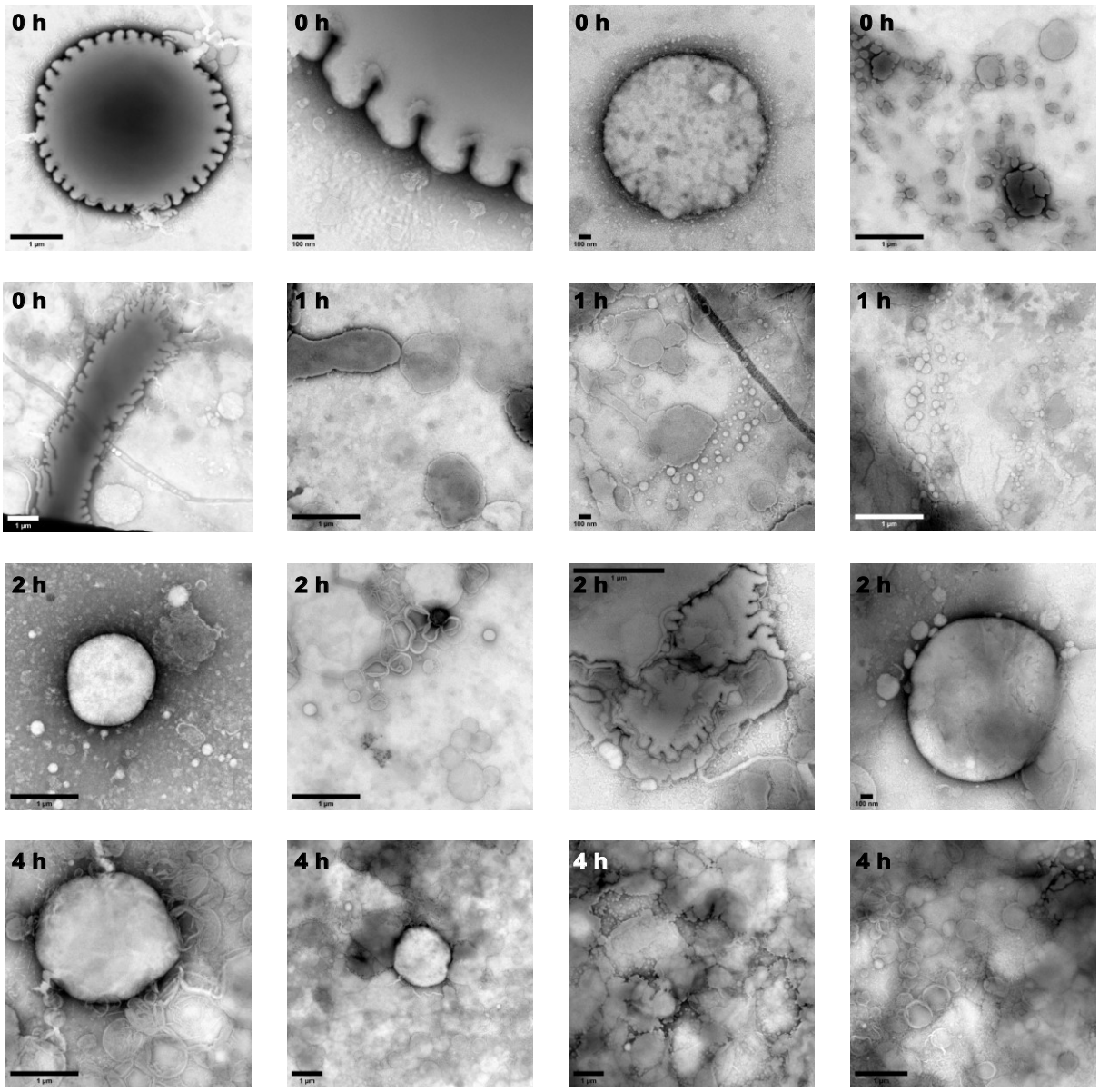


Figure 4.28 Additional TEM micrographs to Figure 4.5a of aliquots of the seeded reaction. Scale bars, 1 μm and 100 nm.

4.8.7 Confocal Microscopy

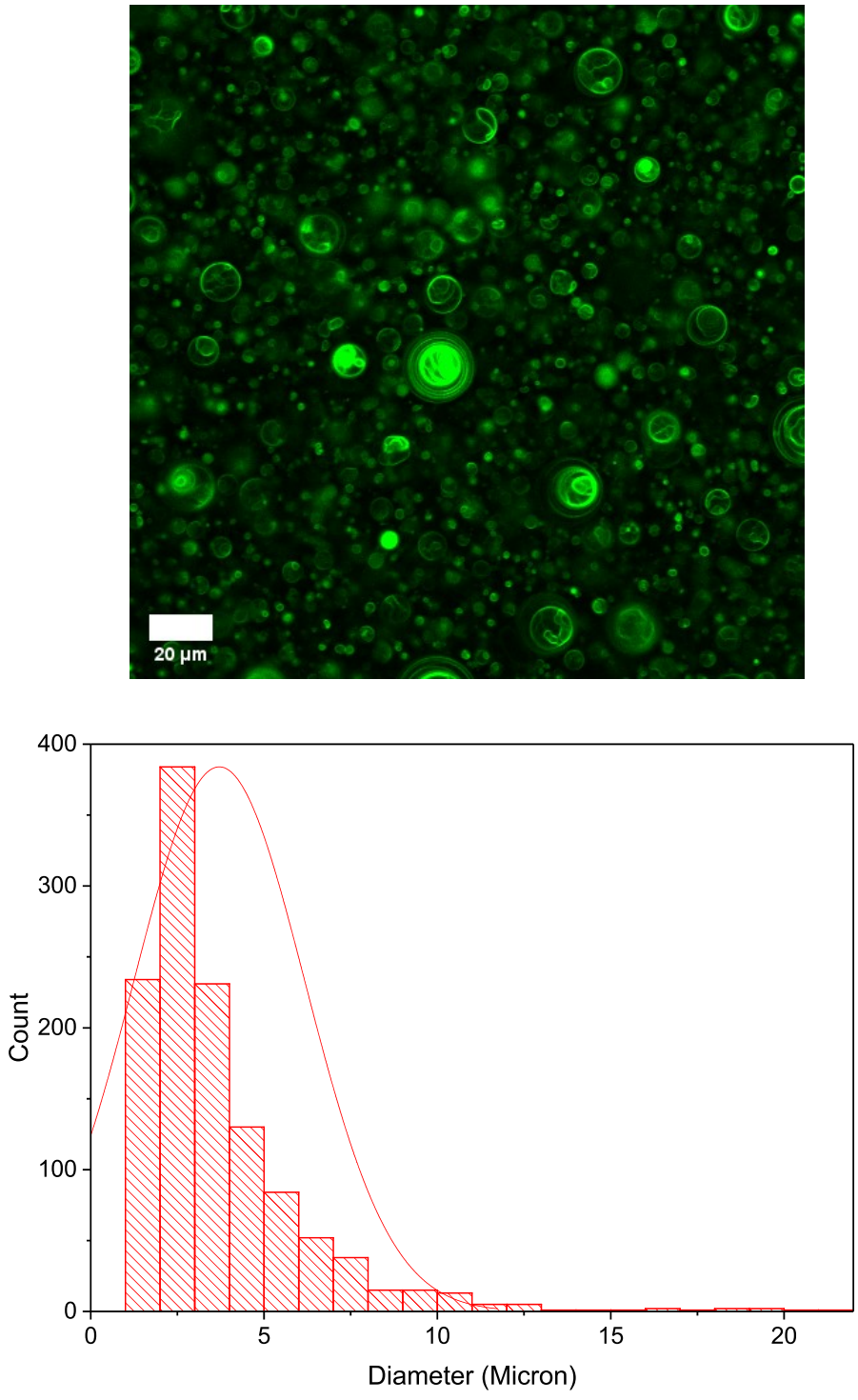


Figure 4.29 Confocal image of phospholipid vesicles of **4.3** (4 mM). A polydisperse range of multilaminar vesicles up to 20 µm is observed. Scale bar, 20 µm.

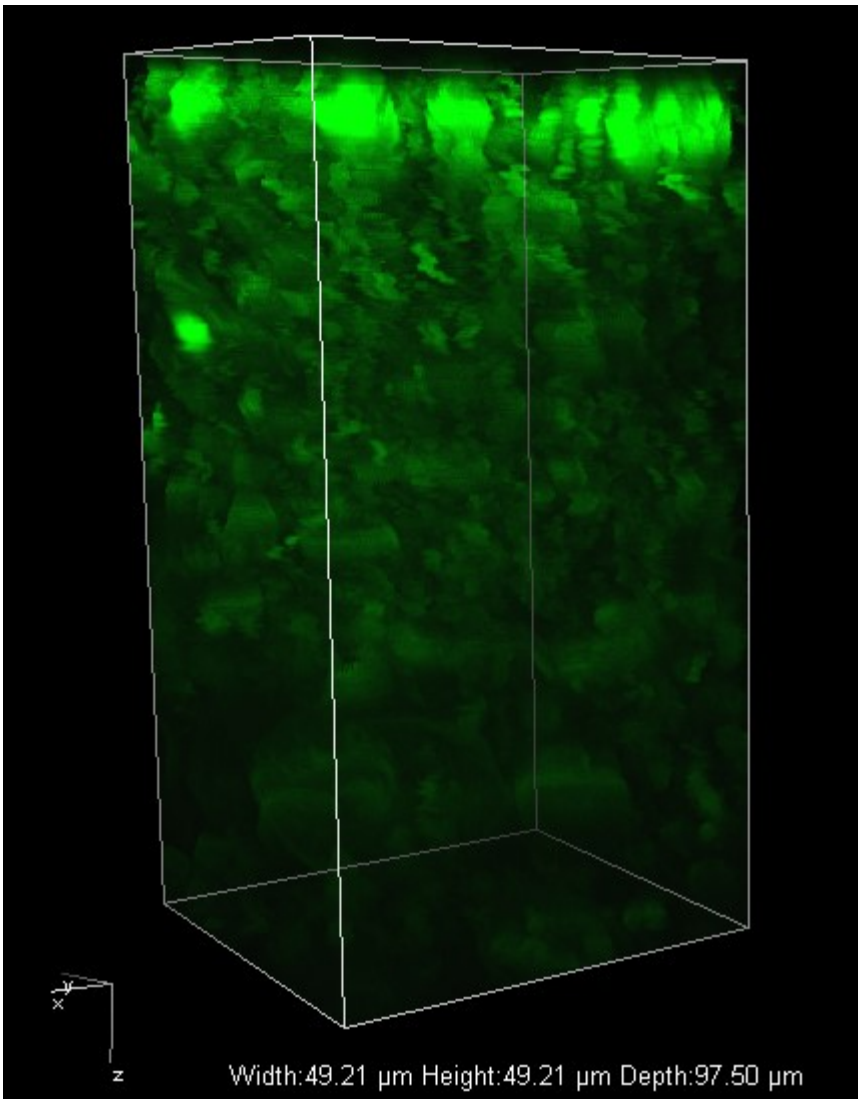


Figure 4.30 A Z-stack image of phospholipid vesicles of **4.3** (4 mM) after the sample has been left to sediment on to the coverslip overnight. A layer of about 100 µm that decreases in density as the distance to the coverslip increases is observed.

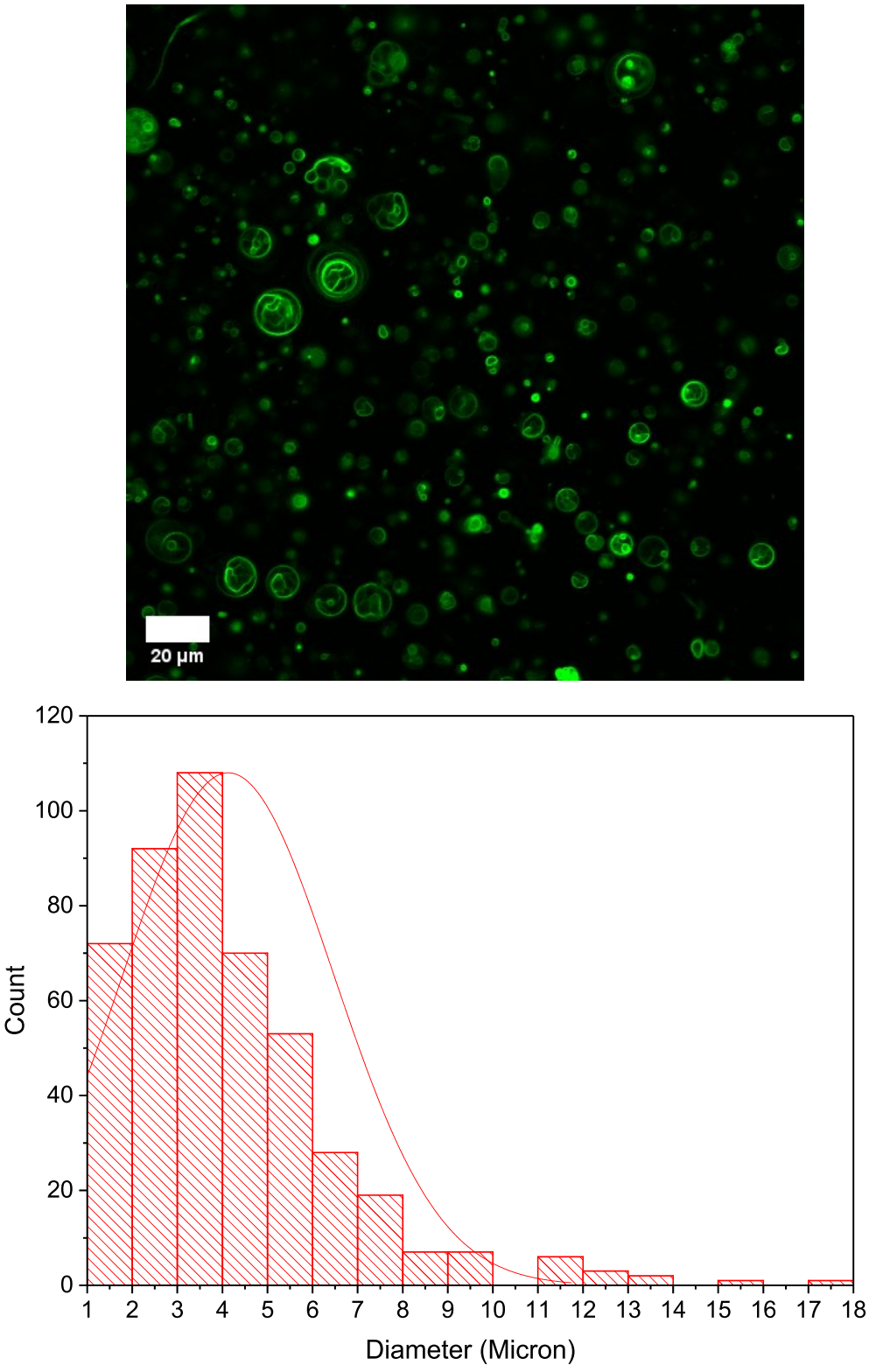


Figure 4.31 Confocal image of phospholipid vesicles of **4.3** (400 µM). A less dense and smaller range of multilaminar vesicles up to 18 µm is observed at this lower concentration. Scale bar, 50 µm.

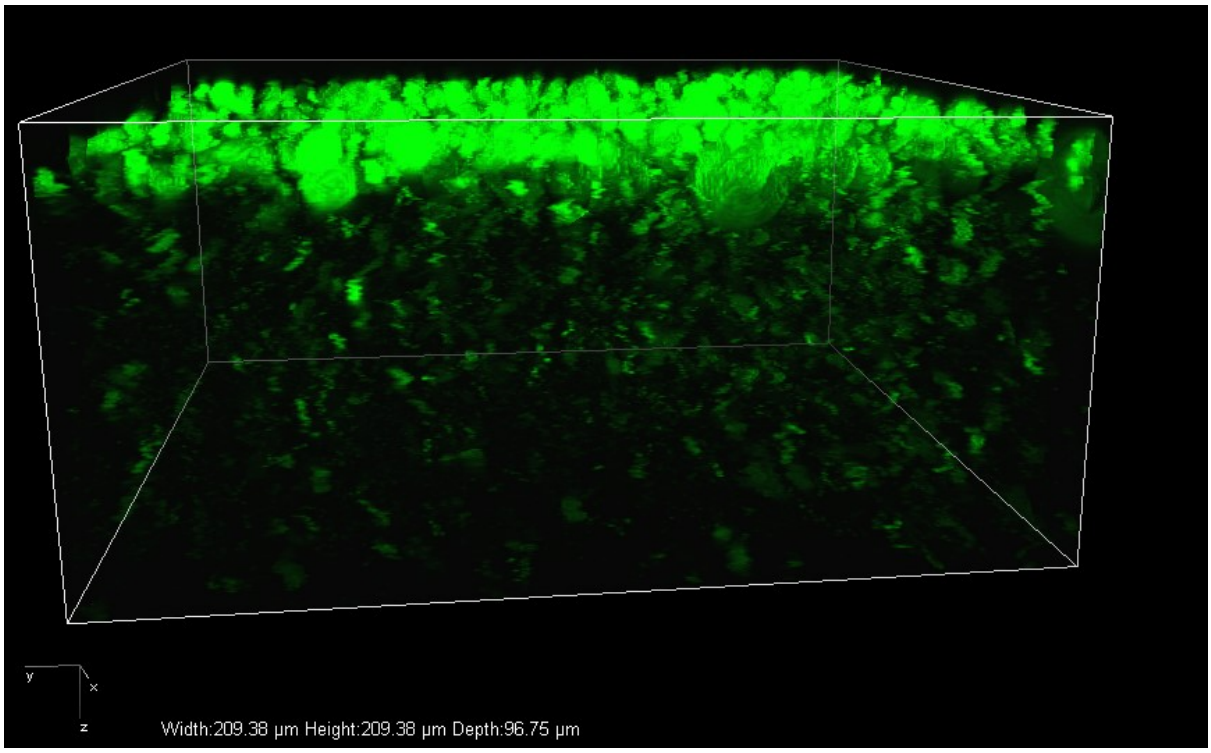


Figure 4.32 A Z-stack image of phospholipid vesicles of **4.3** (400 µM) after the sample has been left to sediment on to the coverslip overnight. A thinner layer of about 30 µm that decreases in density as the distance to the coverslip increases is observed at this concentration.

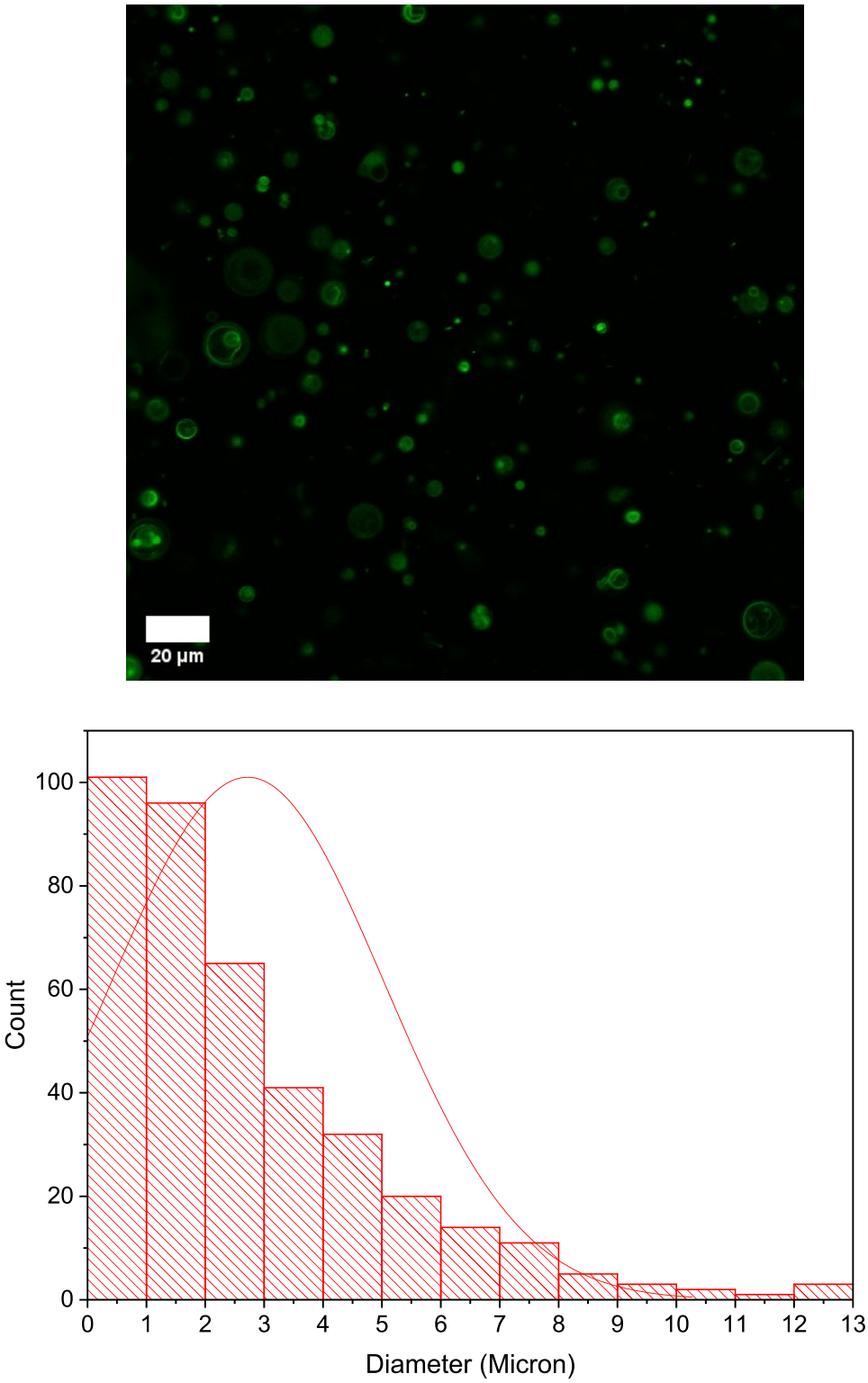


Figure 4.33 Confocal image of phospholipid vesicles of **4.3** (40 µM) in solution. A very dilute and smaller population of mainly <5 µm vesicles is observed at this concentration in solution. Scale bar, 20 µm.

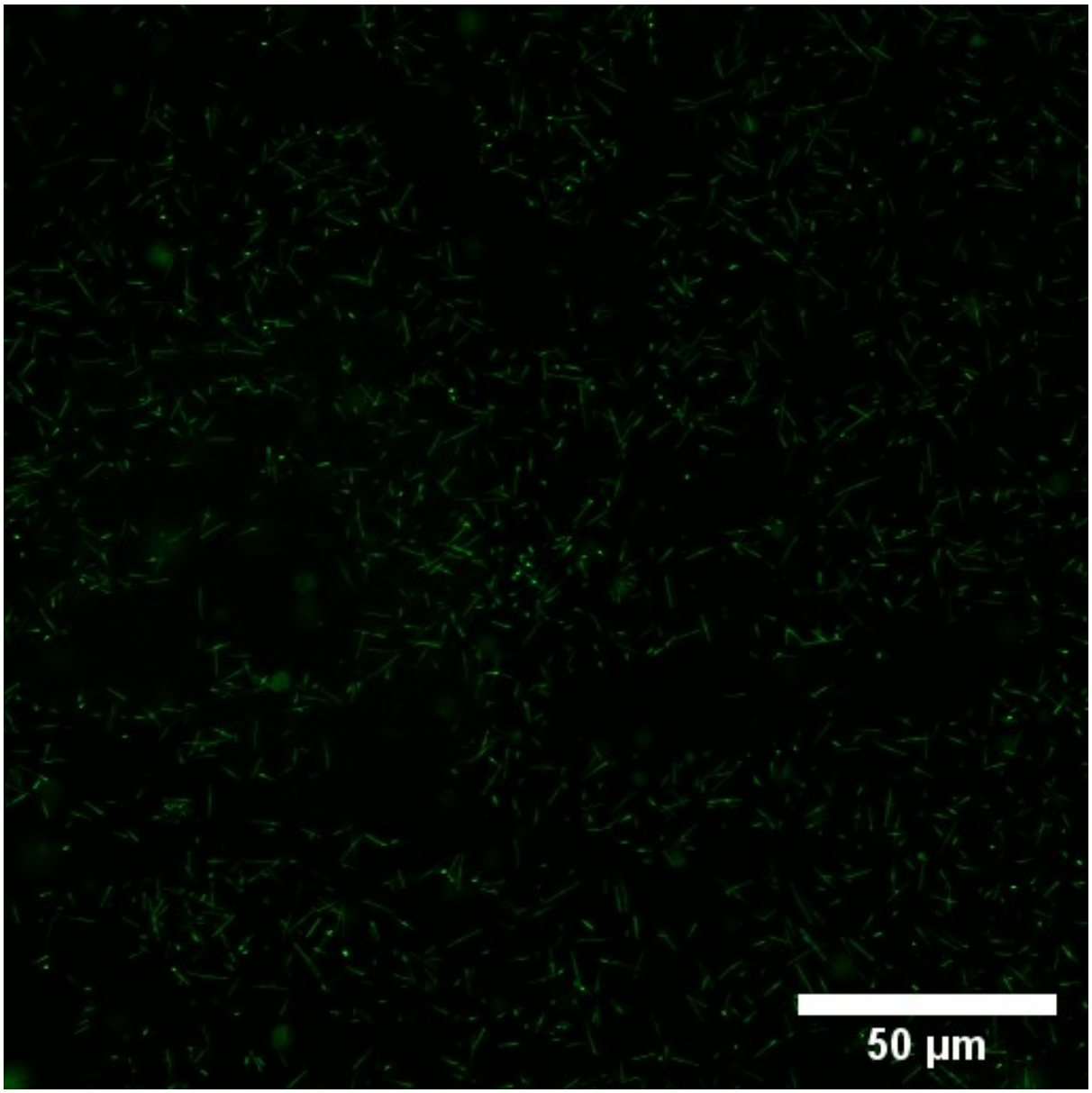


Figure 4.34 Confocal image of phospholipid vesicles of **4.3** (40 µM) on the coverslip. Rod-like structures of 1 µm width and 2-6 µm length are observed. Scale bar, 50 µm.

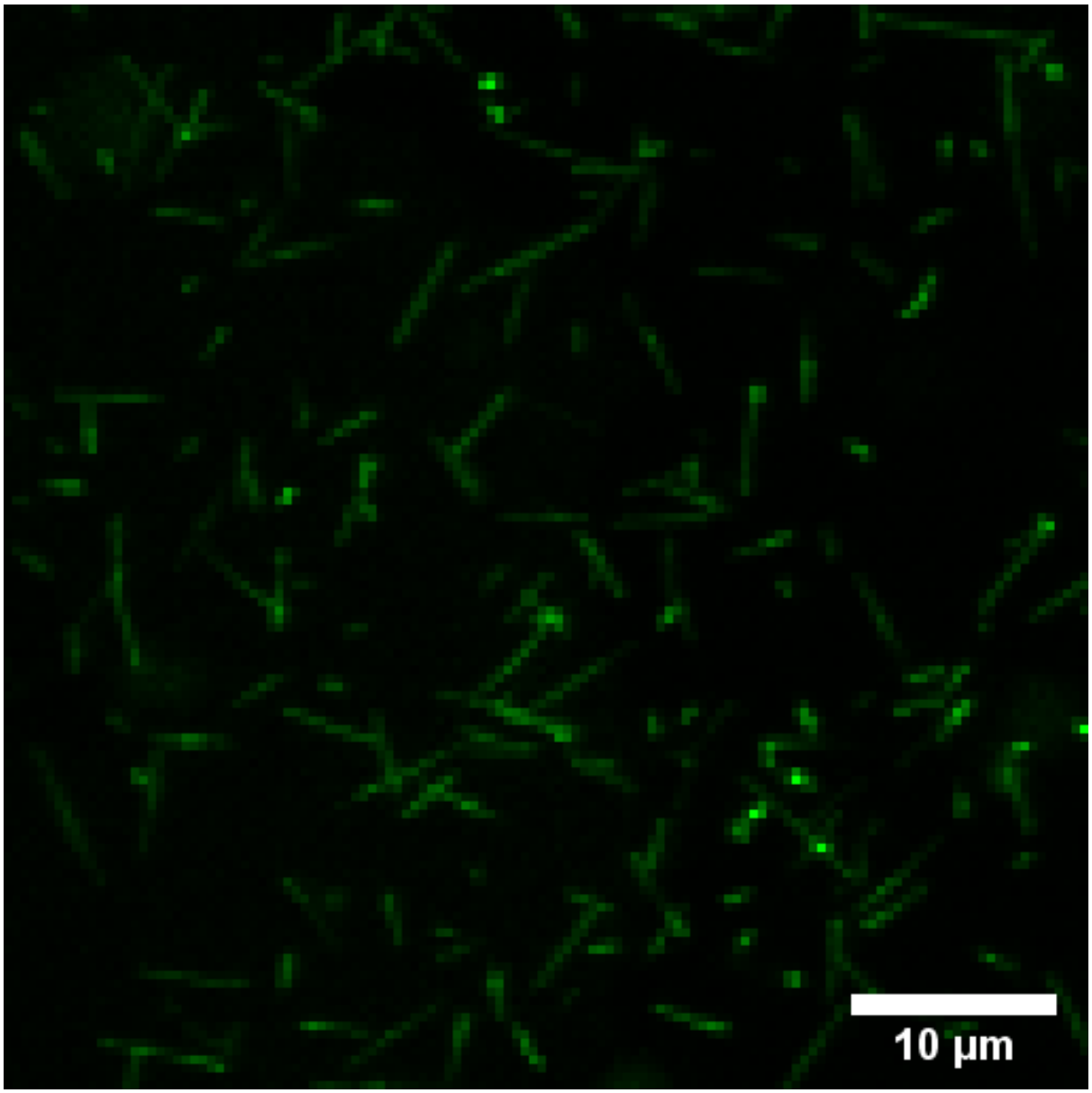


Figure 4.35 Zoomed in area of Figure 34.

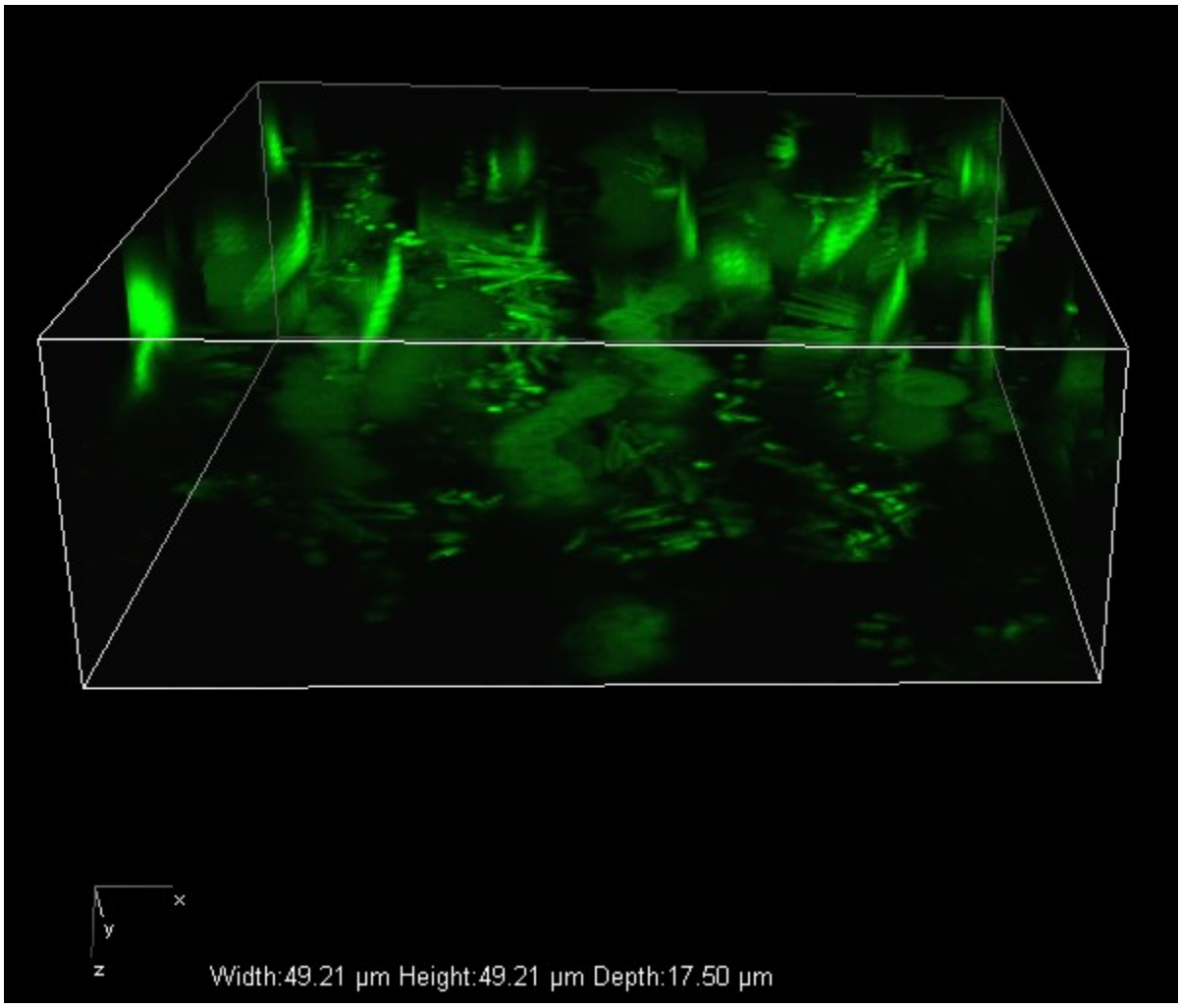


Figure 4.36 A Z-stack image of phospholipid vesicles **4.3** (40 µM) after the sample has been left to sediment on to the coverslip overnight. A very thin layer of about 10 µm is observed. The Z-stack also captured the "wiggling" motion of the rod-like structures at the coverslip.

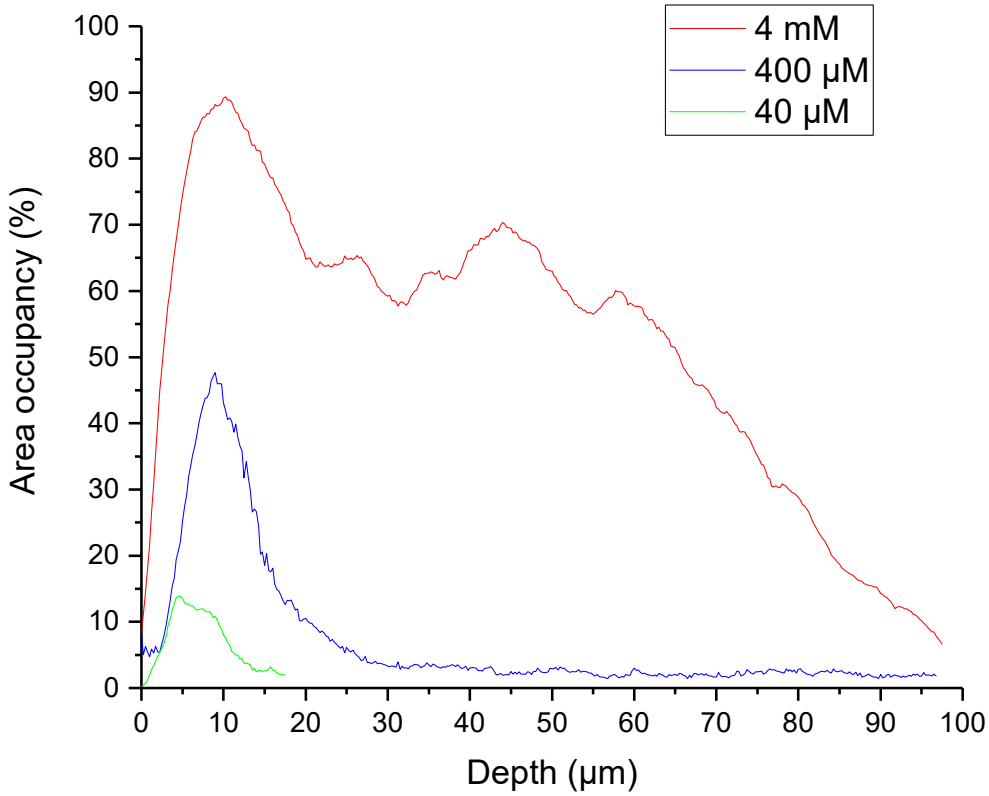


Figure 4.37 A threshold limit for the pixel intensity was set to calculate the number of green pixels relative to black pixels in the Z-stacks of Figure 3.30, 3.32 and 3.36. This allowed us to quantify the occupancy of stained membrane of **4.3** at each slice of the Z-stack. The graph shows that at higher concentrations the layer of sedimented vesicles is not only thicker but the amount of membrane present at each depth is higher as well.

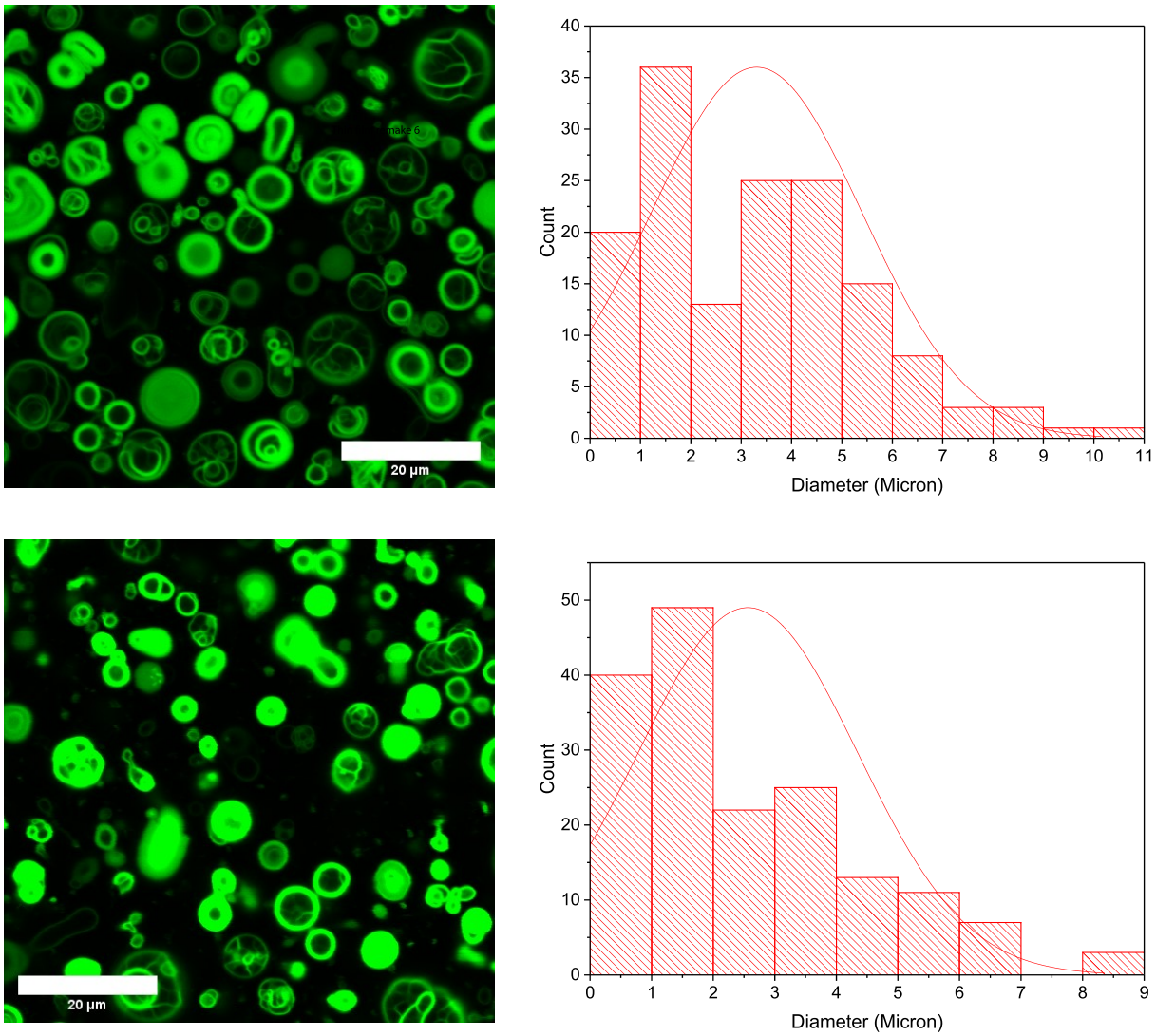


Figure 4.38 Confocal image thin film hydrated phospholipid vesicles of **4.3** (4 mM). Largely unilaminar vesicles up to 9 µm in size were observed. Scale bar, 20 µm.

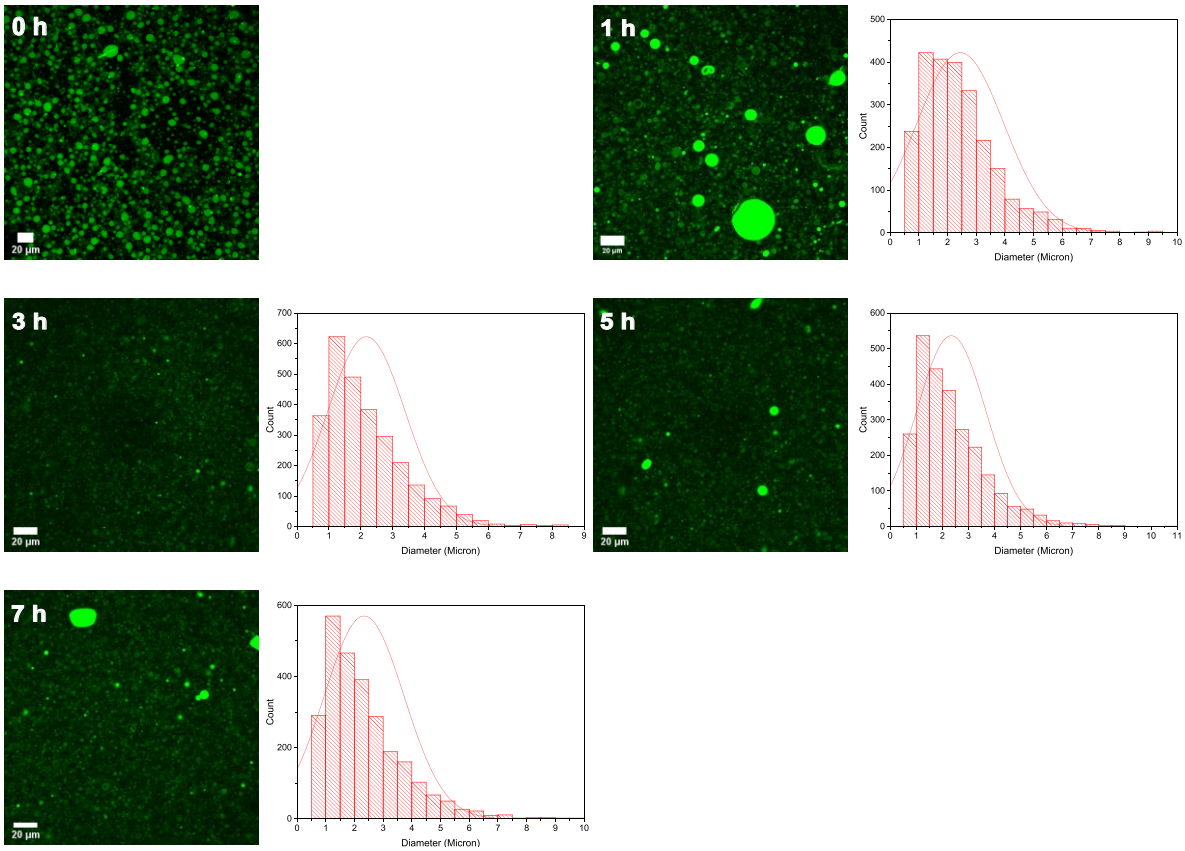


Figure 4.39 Additional confocal micrographs to Figure 4.4b of aliquots of the unseeded reaction. Scale bar, 20 µm.

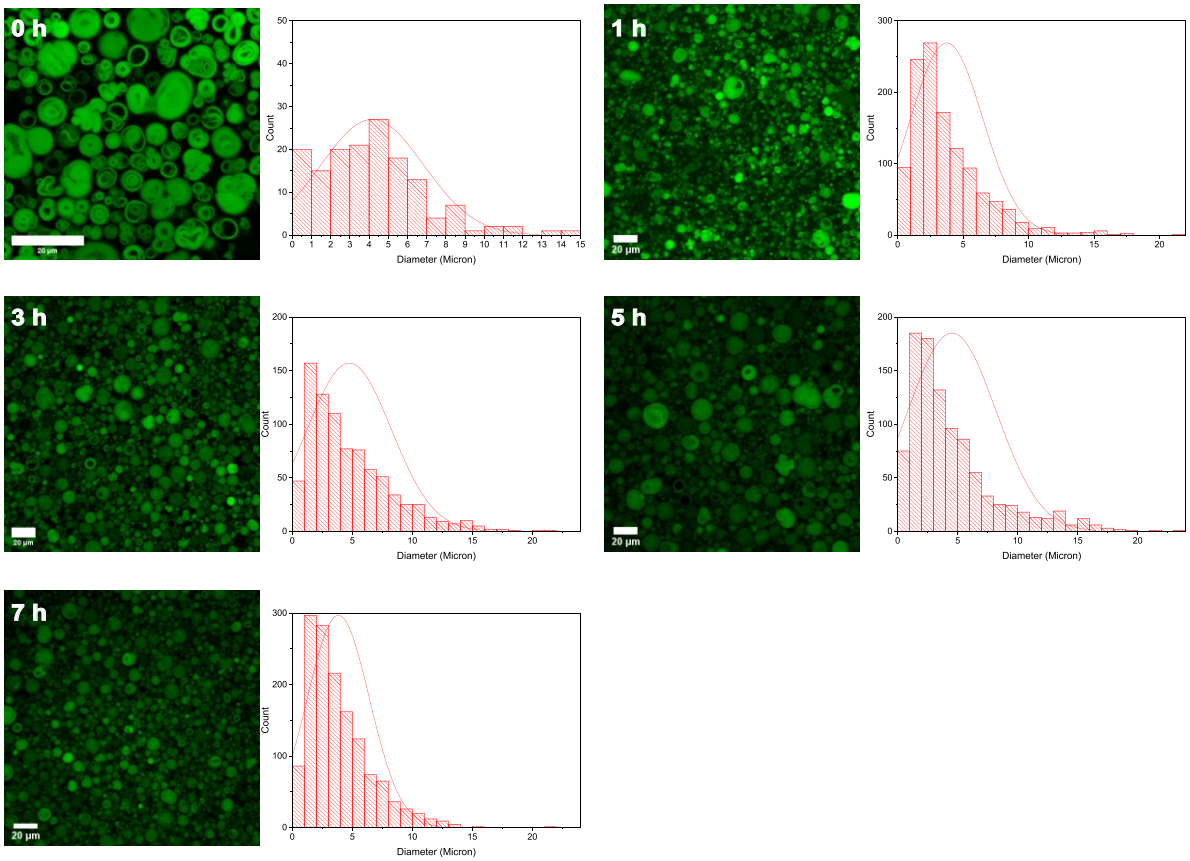


Figure 4.40 Additional confocal micrographs to Figure 4.5b of aliquots of the seeded reaction. Scale bar, 20 µm.

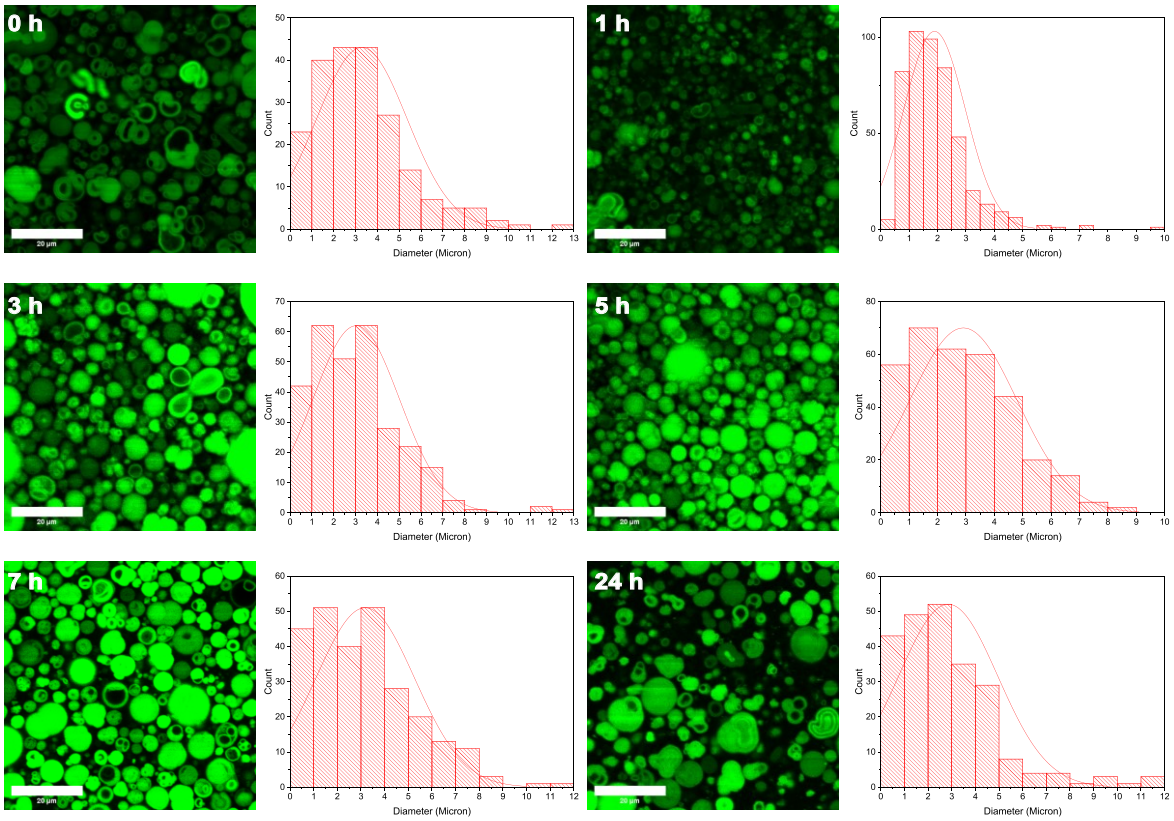


Figure 4.41 Confocal micrographs of aliquots of the thin film seeded reaction (yellow triangles in Figure 4.3). Scale bar, 20 μm.

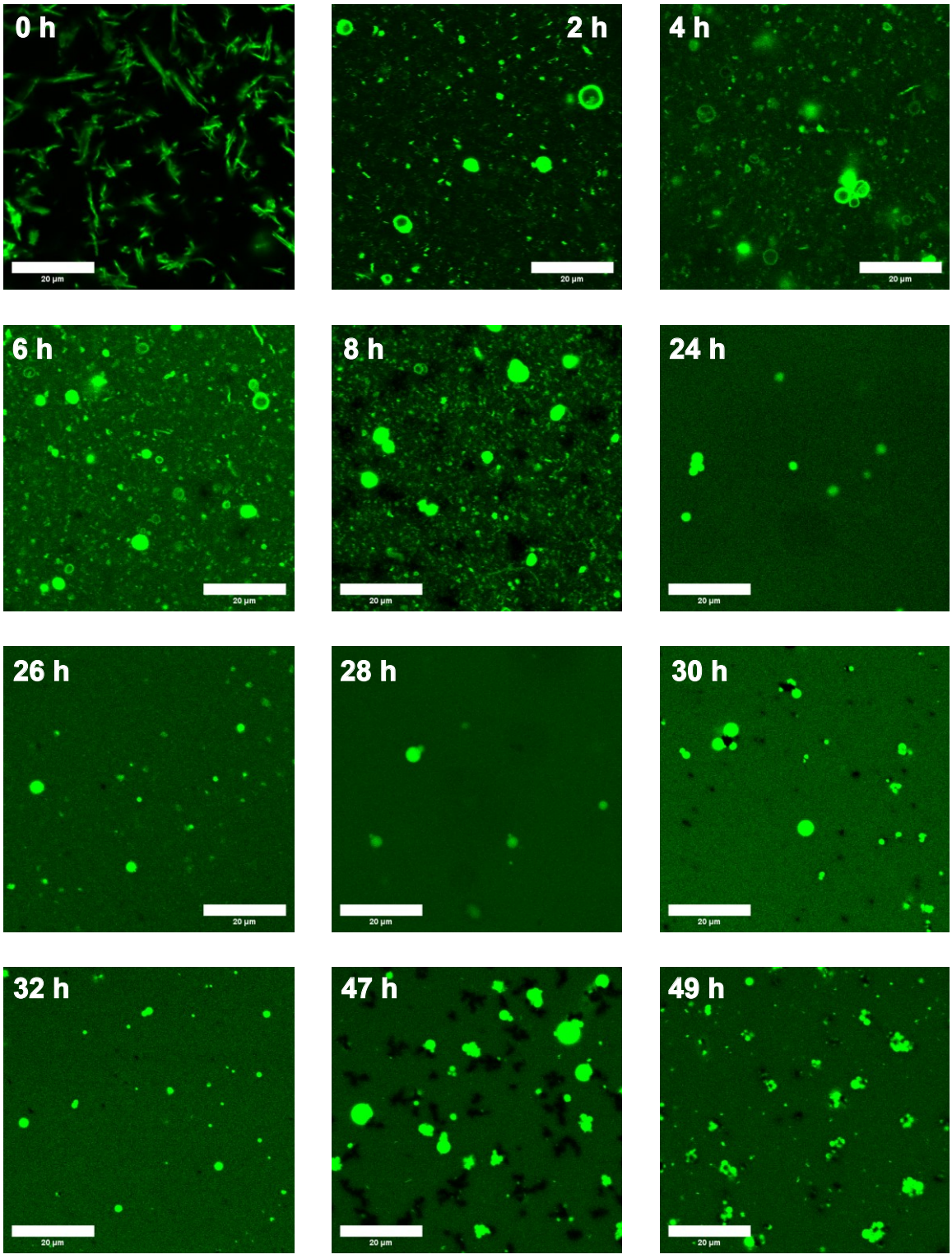


Figure 4.42 Confocal micrographs of aliquots of the out-of-equilibrium reaction (Figure 4.6). Scale bar, 20 µm. At t = 0 h amorphous oil of **4.1** is observed. From t = 2 to 8 h an mixture of vesicles and amorphous material is observed, at later time points (after t= 24 h) when the out-of-equilibrium steady state is reached only oil droplets are observed. Any aggregates present at these later time points are of sizes below the detection limit of confocal microscopy.

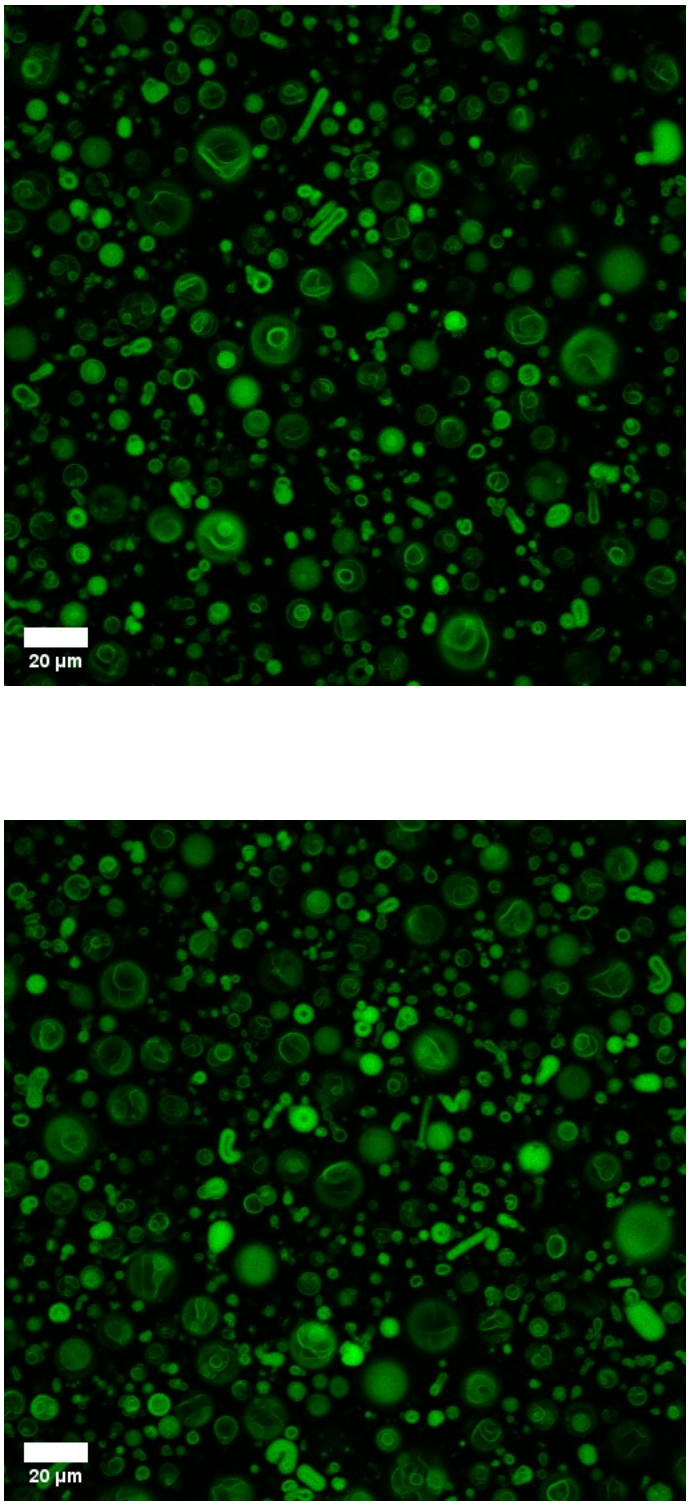


Figure 4.43 Confocal images of phospholipid vesicles of a mixture of **4.3** (4 mM) with **4.7** (10 mM). Not only spherical but also tubular vesicles are observed as are cases where multiple vesicles appear to be fused together. Scale bar, 20 µm.

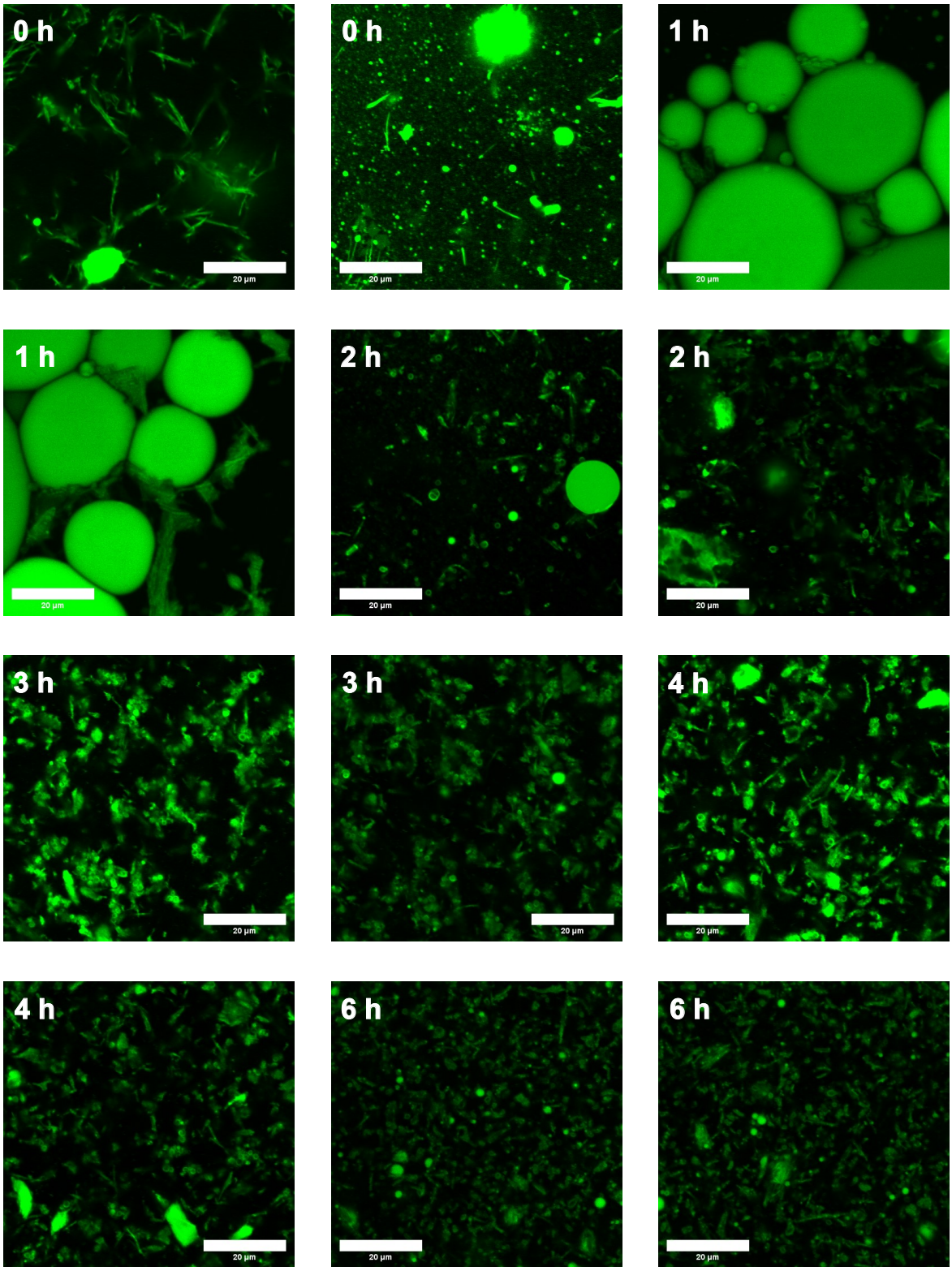


Figure 4.44 Confocal micrographs of aliquots of the competition reaction (Figure 4.9b) for the formation of compound **4.3** and **4.7** in the presence of 50 mM NaOH. Scale bar, 20 µm. Initially oil droplets stabilized by surfactants are observed, followed by the formation of amorphous aggregates and clusters of vesicles.

4.8.8 UPLC Calibration Curves

A calibration plot was prepared for the various compounds that were analysed by UPLC by plotting the peak area against the concentration of pure compound and fitting a trendline through the data points. These curves were used to calculate the concentration of compounds in the aliquots during kinetic monitoring of the reactions.

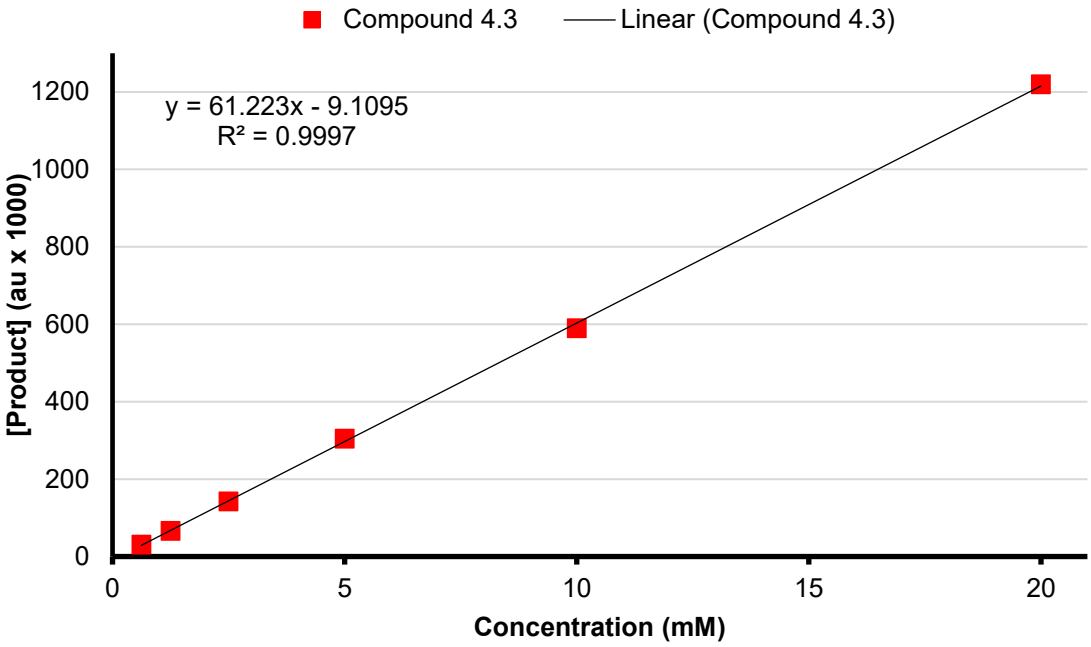


Figure 4.45 A linear calibration curve through data points of the area of pure **4.3** at different concentrations. Experimental conditions: 20 µL of aqueous sample diluted in 500 µL of standard solution of MeCN containing 0.7 mM of ethyl benzoate as internal standard. λ_{det} = 214.5 nm, injection volume = 5 µL, retention time: $t_{(4.3)}$ = 2.27 min.

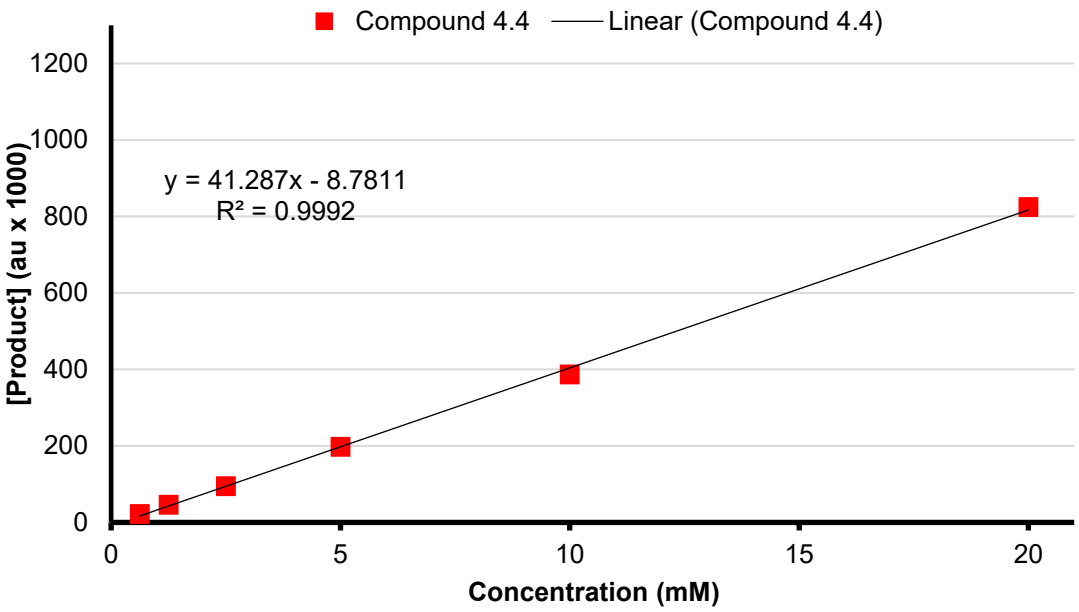


Figure 4.46 A linear calibration curve through data points of the area of pure **4.4** at different concentrations. Experimental conditions: 20 µL of aqueous sample diluted in 500 µL of standard solution of MeCN containing 0.7 mM of ethyl benzoate as internal standard. λ_{det} = 214.5 nm, injection volume = 5 µL, retention time: $t_{(4.4)}$ = 2.74 min.

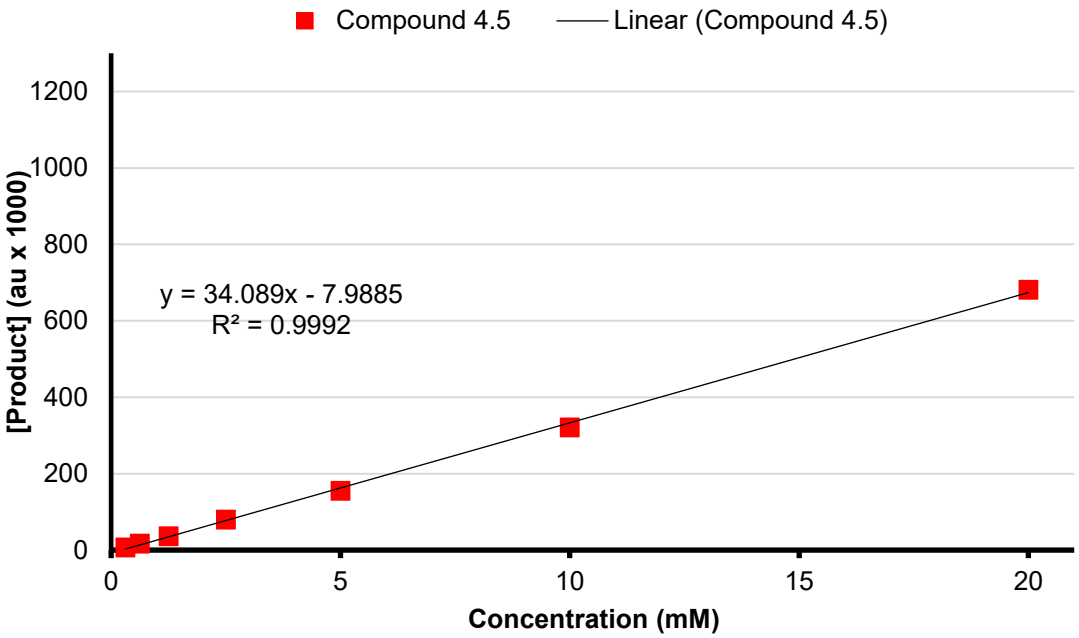


Figure 4.47: A linear calibration curve through data points of the area of pure **4.5** at different concentrations. Experimental conditions: 20 µL of aqueous sample diluted in 500 µL of standard solution of MeCN containing 0.7 mM of ethyl benzoate as internal standard. λ_{det} = 214.5 nm, injection volume = 5 µL, retention time: $t_{(4.5)}$ = 3.86 min.

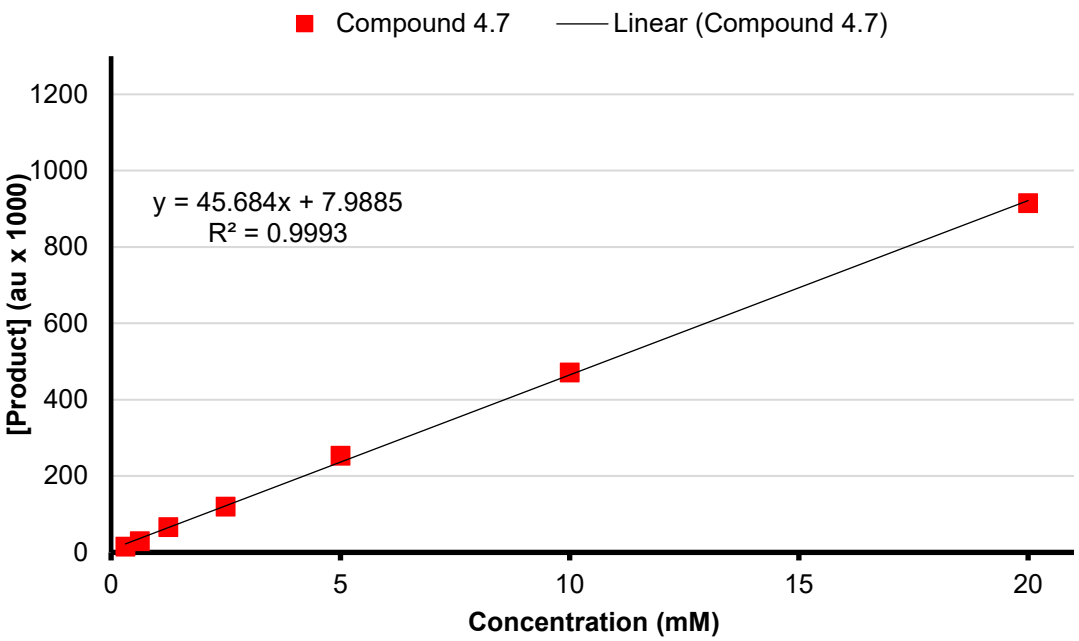


Figure 4.48: A linear calibration curve through data points of the area of pure **4.7** at different concentrations. Experimental conditions: 20 µL of aqueous sample diluted in 500 µL of standard solution of MeCN containing 0.7 mM of ethyl benzoate as internal standard. λ_{det} = 214.5 nm, injection volume = 5 µL, retention time: $t_{(4.7)}$ = 2.62 min.

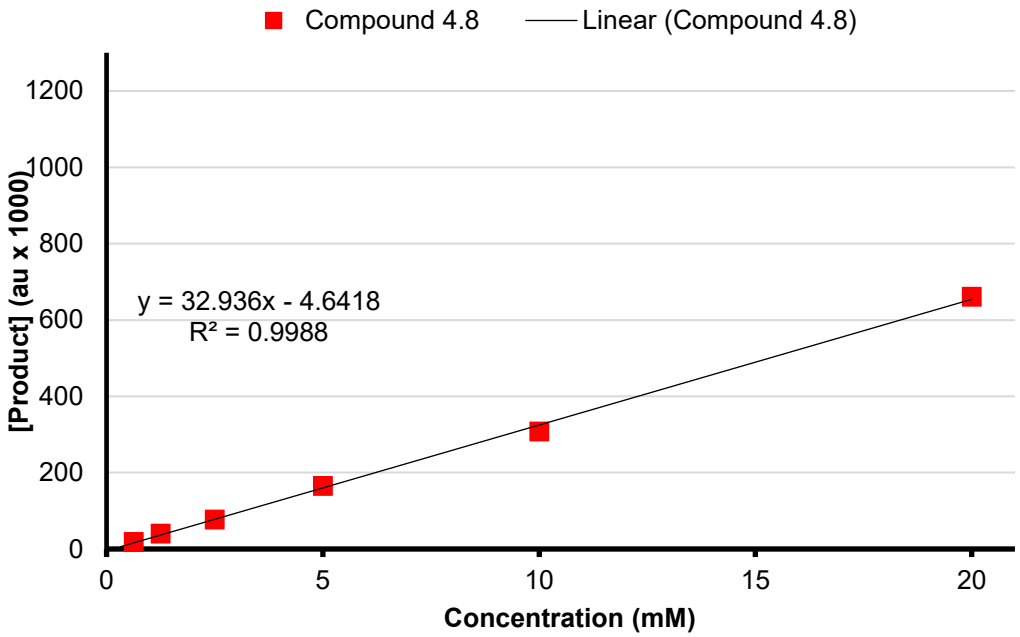


Figure 4.49 A linear calibration curve through data points of the area of pure **4.8** at different concentrations. Experimental conditions: 20 µL of aqueous sample diluted in 500 µL of standard solution of MeCN containing 0.7 mM of ethyl benzoate as internal standard. λ_{det} = 214.5 nm, injection volume = 5 µL, retention time: $t_{(4.8)}$ = 3.02 min.

4.8.9 Kinetic Data

This section contains addition kinetic data acquired supplemental to the main text.

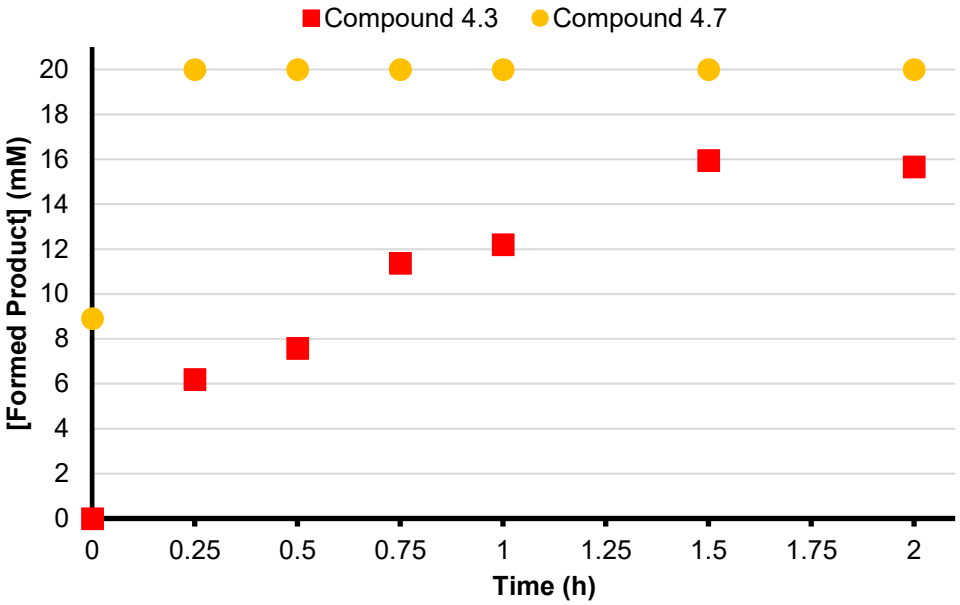


Figure 4.50 Reaction kinetics for the formation of surfactant under *t*BuOH/H_2O (1:1) conditions. Compound **4.3** (red squares) shows no lag period and complete conversion in 1.5 hours. Compound **4.7** (yellow circles) shows complete conversion in 15 minutes. Experimental conditions: Performed in batch in the presence with a 2 mM copper(I) catalyst loading while stirring at 1000 rpm for formation of **4.3** and stirring at 400 rpm for **4.7**.

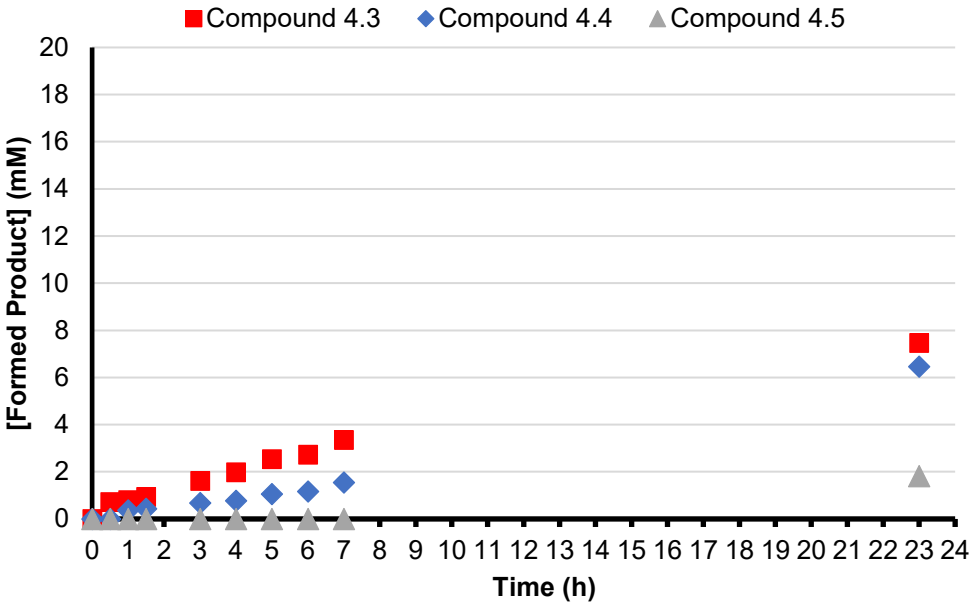


Figure 4.51 Reaction kinetics for the formation of compound **4.3** (red squares), **4.4** (blue diamonds) and **4.5** (grey triangles). Results indicate that **4.3** is relatively stable to hydrolysis but that a higher catalyst loading is required to obtain significant product formation at convenient time scales. Experimental conditions: Performed in batch in the presence of 50 mM NaOH with 8 mM copper(I) catalyst loading while stirring at 1000 rpm.

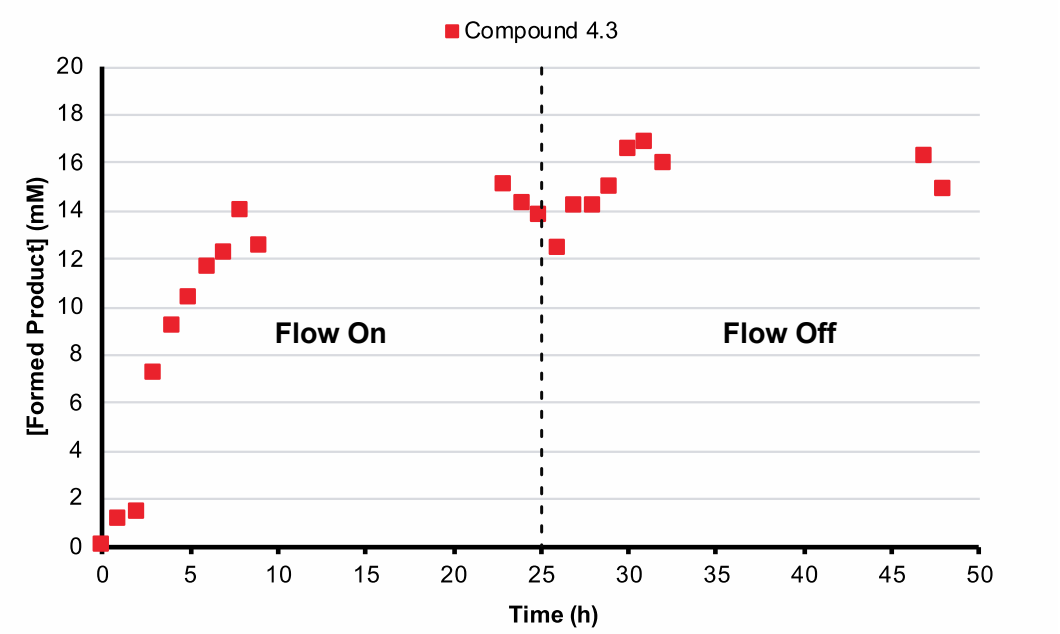


Figure 4.52 Reaction kinetics for the formation of compound **4.3** (red squares) in CSTR setup. Results indicate that no out-of-equilibrium steady-state can be obtained at 0 mM NaOH. Experimental conditions: Performed in CSTR setup in the presence of 0 mM NaOH with 8 mM copper(I) catalyst loading while stirring at 1000 rpm. The flow was turned off at $t = 25$ h.

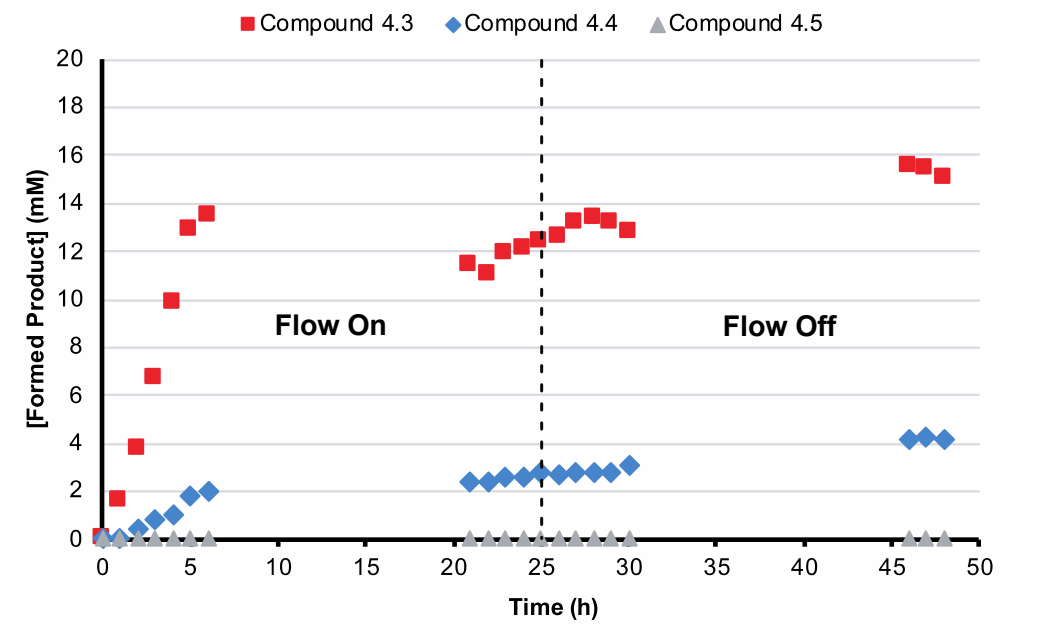


Figure 4.53 Reaction kinetics for the formation of compound **4.3** (red squares), **4.4** (blue diamonds) and **4.5** (grey triangles) in CSTR setup. Results indicate that no out-of-equilibrium steady-state can be obtained at 25 mM NaOH. Experimental conditions: Performed in CSTR setup in the presence of 25 mM NaOH with a 8 mM copper(I) catalyst loading while stirring at 1000 rpm. The flow was turned off at $t = 25$ h.

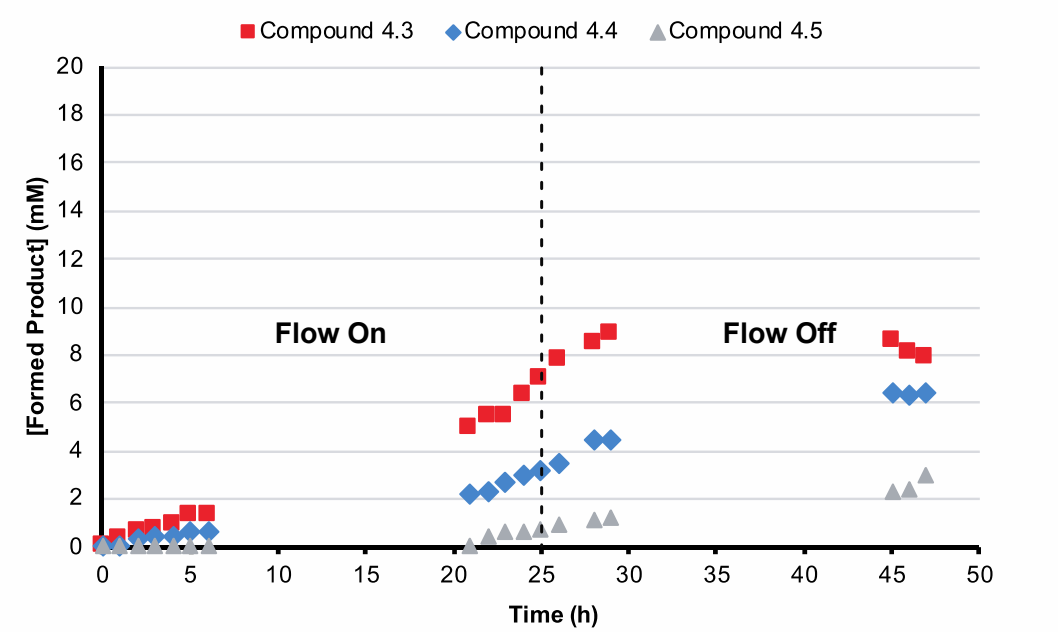


Figure 4.54 Reaction kinetics for the formation of compound **4.3** (red squares), **4.4** (blue diamonds) and **4.5** (grey triangles) in CSTR setup. Results indicate that no out-of-equilibrium steady-state can be obtained at 50 mM NaOH. Experimental conditions: Performed in CSTR setup in the presence of 50 mM NaOH with a 8 mM copper(I) catalyst loading while stirring at 1000 rpm. The flow was turned off at t = 25 h.

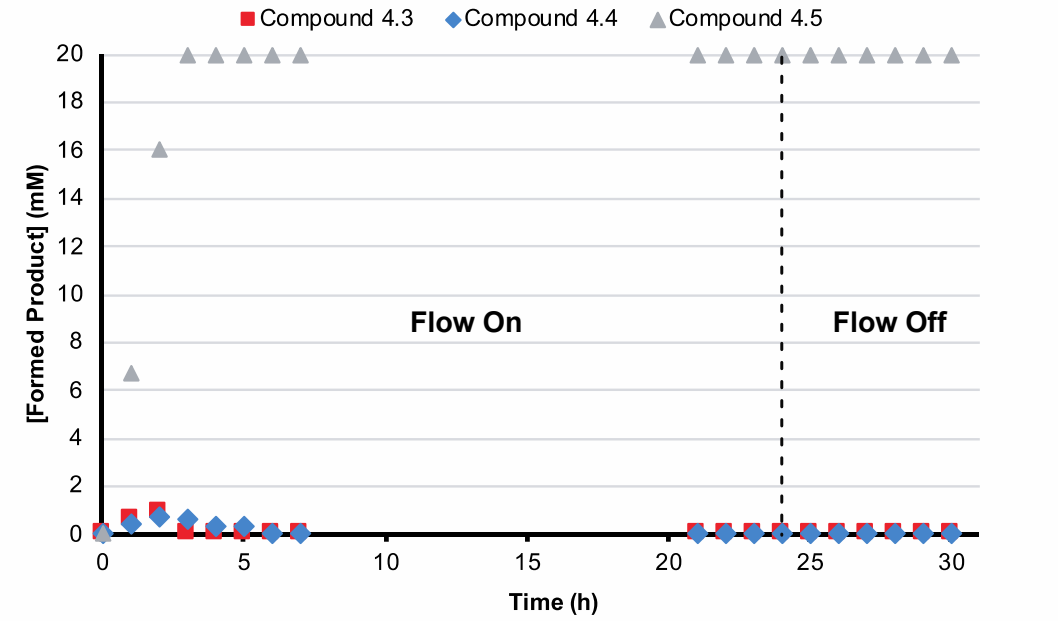


Figure 4.55 Reaction kinetics for the formation of compound **4.3** (red squares), **4.4** (blue diamonds) and **4.5** (grey triangles) in CSTR setup. Complete conversion to **4.5** is observed within 5 hours and turning of the flow at t = 24 h does not lead to a change in composition. This shows that an out-of-equilibrium steady-state requires phase separation, and hence product aggregation, allowing the autocatalytic mechanism to operate. Experimental conditions: Performed in flow in the presence of 100 mM NaOH with 8 mM copper(I) catalyst loading while stirring at 1000 rpm in *t*BuOH/H_2O (1:1). The flow was turned off at t = 24h.

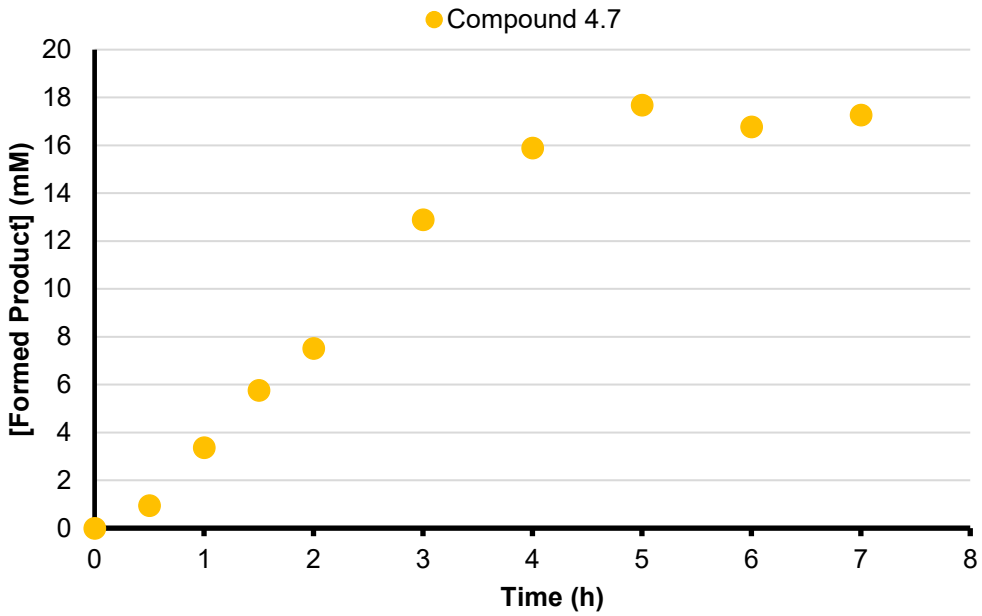


Figure 4.56 Reaction kinetics for the unseeded formation of compound **4.7** (yellow circles). Results indicate that formation of **4.7** is too fast when stirred at 1000 rpm resulting in no visible lag period. Experimental conditions: Performed in batch with 2 mM copper(I) catalyst loading while stirring at 1000 rpm.

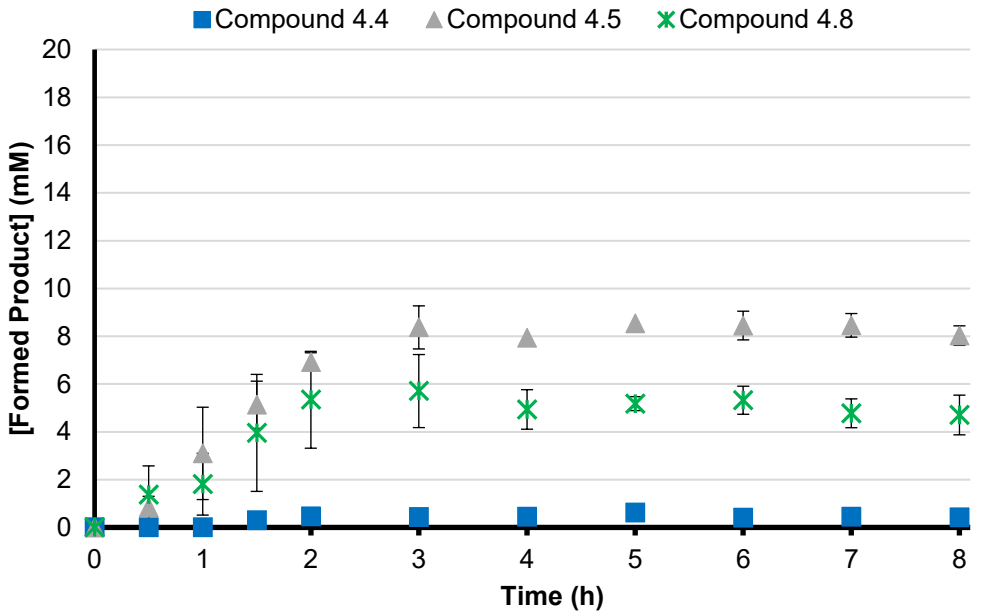


Figure 4.57 Complementary figure to Figure 4.9b showing the formation of hydrolysis products **4.4** (blue squares), **4.5** (grey triangles) and **4.8** (green stars). Results indicate significant formation of hydrolysis products **4.5** and **4.8** but not of **4.4** indicating hydrolysis of **4.7** but not of **4.3**. Experimental conditions: Performed in batch in the presence of 50 mM NaOH with 8 mM copper(I) catalyst loading while stirring at 1000 rpm. Points are the mean of three independent experiments and the error bars are the standard deviation (n=3).

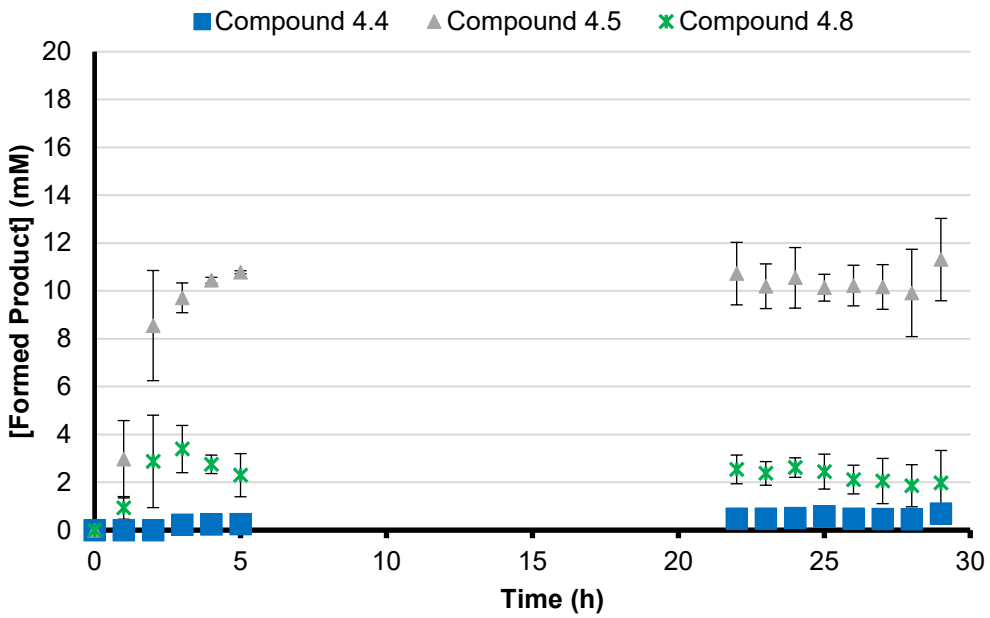


Figure 4.58 Complementary figure to Figure 4.10 showing the formation of hydrolysis products **4.4** (blue squares), **4.5** (grey triangles) and **4.8** (green stars) in CSTR setup**.** Results indicate significant formation of hydrolysis products **4.5** and **4.8** but not of **4.4** indicating hydrolysis of **4.7** but not of **4.3**. Experimental conditions: Performed in CSTR setup in the presence of 50 mM NaOH with 8 mM copper(I) catalyst loading while stirring at 1000 rpm. The flow was turned off at t = 25 h. Points are the mean of three independent experiments and the error bars are the standard deviation (n=3).

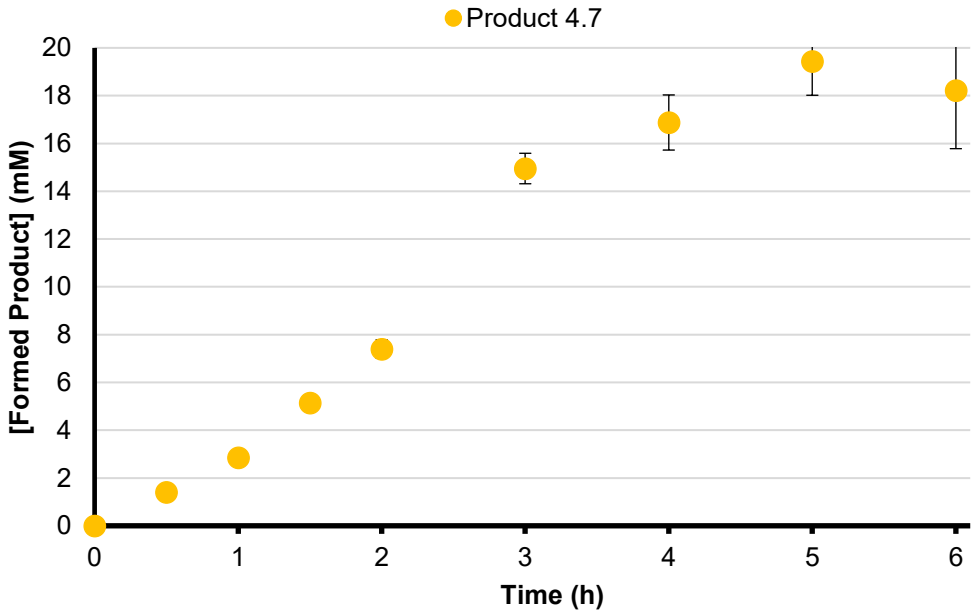


Figure 4.59 Reaction kinetics for the formation of compound **4.7** (yellow circles) when cross-seeded with 4 mM of **4.3**. Results indicate that vesicles of **4.3** have a similar efficiency at accelerating formation of **4.7** as micelles of **4.7**. Experimental conditions: Performed in batch with 8 mM copper(I) catalyst loading while stirring at 400 rpm, related to Figure 4e. Points are the mean of three independent experiments and the error bars are the standard deviation (n=3).

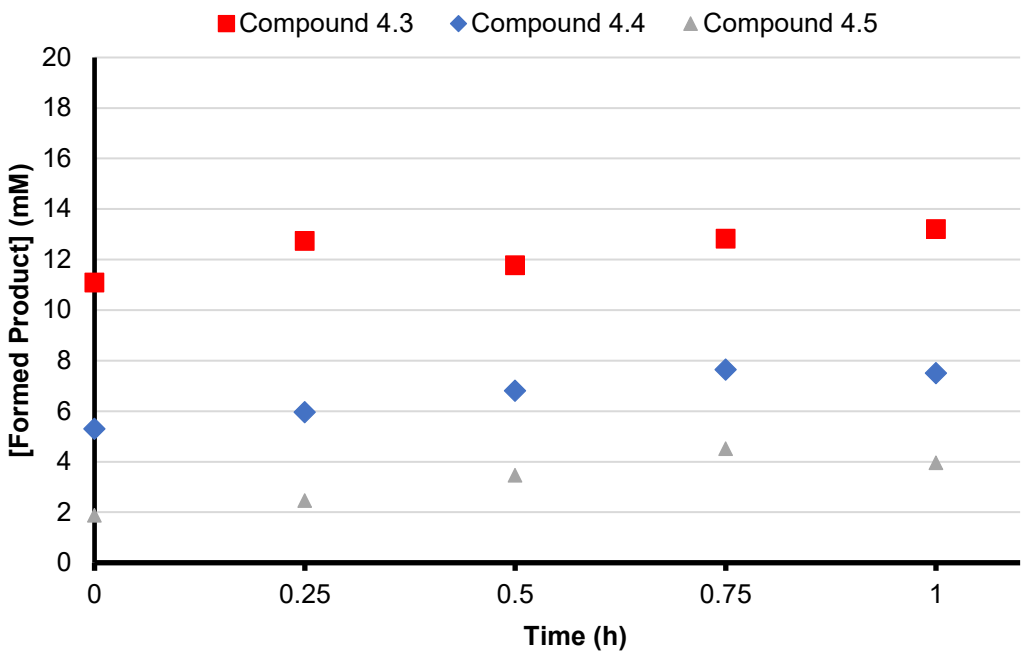


Figure 4.60 Reaction kinetics for the hydrolysis of compound **4.3** (red squares) to **4.4** (blue diamonds) and **4.5** (grey triangles). Results indicate the relative stability of **4.3** to hydrolysis. Experimental conditions: Performed in batch by stirring 20 mM of **4.3** in the presence of 50 mM NaOH at 1000 rpm.

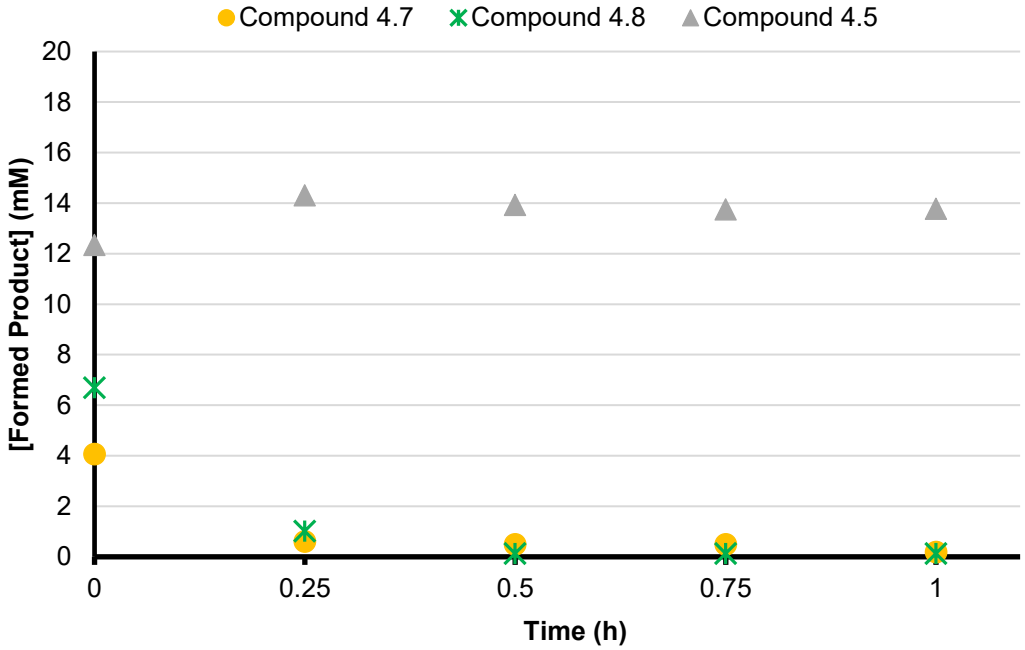


Figure 4.61 Reaction kinetics for the hydrolysis of compound **4.7** (yellow circles) to **4.8** (green stars) and **4.5** (grey triangles). Results show the instability of compound **4.7** to hydrolysis. Experimental conditions: Performed in batch by stirring 20 mM of **4.7** in the presence of 50 mM NaOH at 1000 rpm.

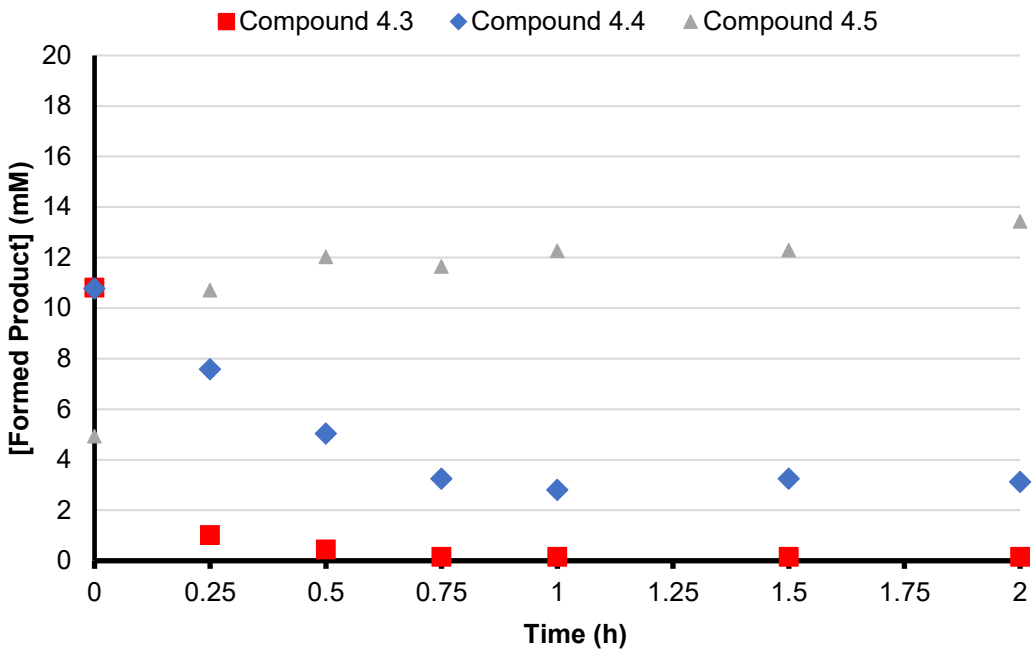


Figure 4.62 Reaction kinetics for the hydrolysis of compound **4.3** (red squares) to **4.4** (blue diamonds) and **4.5** (grey triangles) under *t*BuOH/H_2O (1:1) conditions. Results show that **4.3** becomes unstable to hydrolysis when in its unaggregated form. Experimental conditions: Performed in batch by stirring 20 mM of **4.3** in the presence of 50 mM NaOH at 1000 rpm in a 1:1 water/*tert*-butanol mixture.

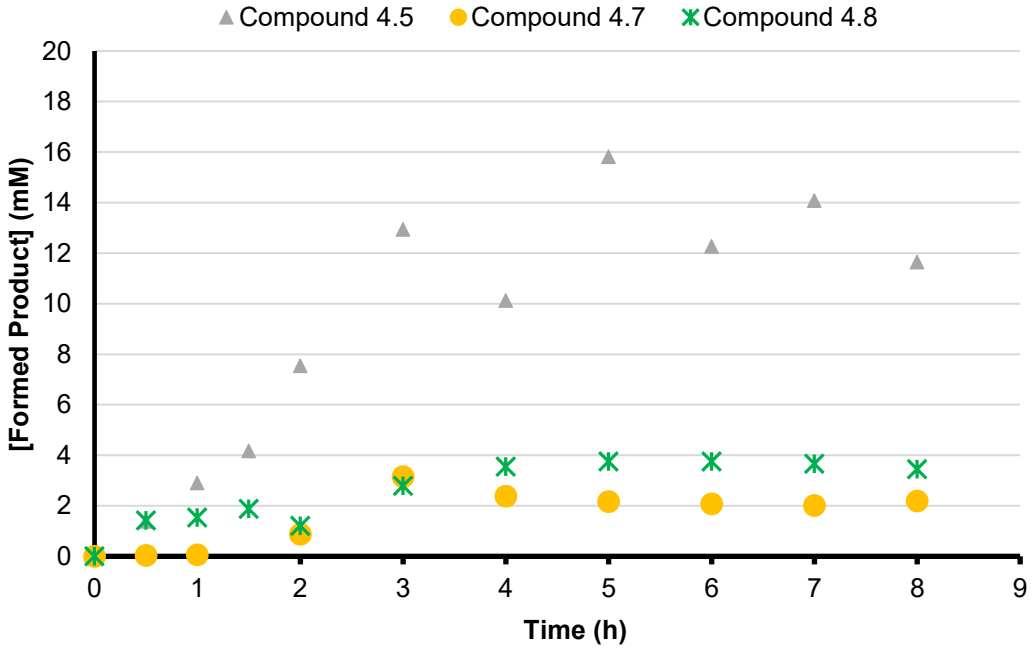


Figure 4.63 Reaction kinetics for the formation of compound **4.7** (yellow circles), **4.8** (green stars) and **4.5** (grey triangles) under hydrolysing conditions. Results show that in situ generated **4.7** is unstable to hydrolysis. Experimental conditions: Reaction between compound **4.2** and **4.6** performed in batch in the presence of 50 mM NaOH with a 8 mM copper(I) catalyst loading while stirring at 1000 rpm.

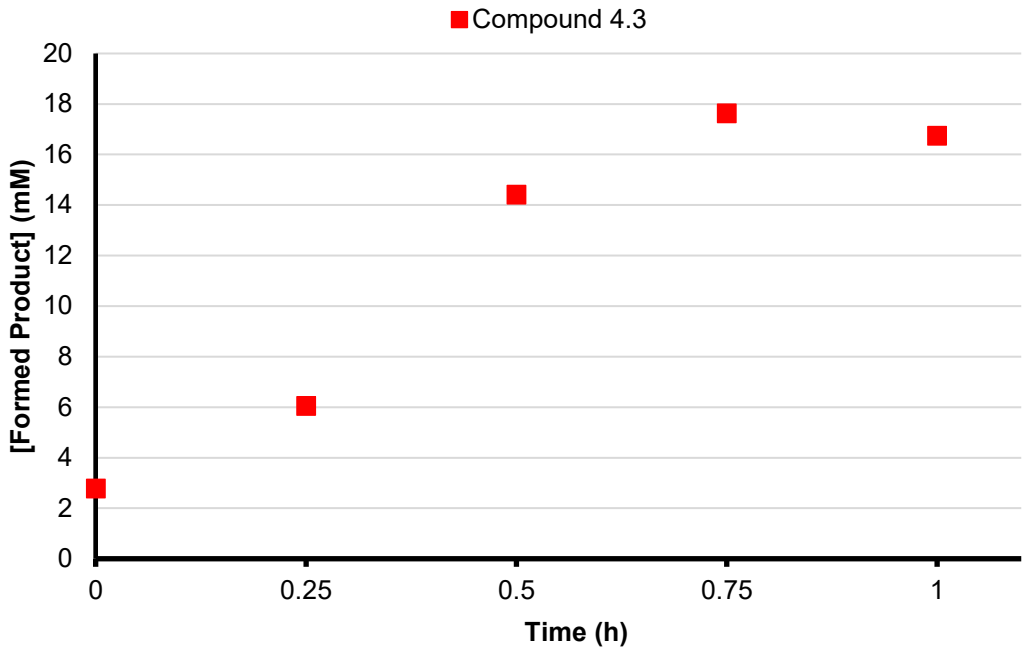


Figure 4.64 Reaction kinetics for the formation of compound **4.3** (red squares) when seeded with 4 mM of **4.7** under *t*BuOH/H_2O (1:1) conditions. Results show that **4.7** does not inhibit formation of **4.3** when there is no phase separation and supramolecular aggregation. Experimental conditions: Performed in batch with 8 mM copper(I) catalyst loading while stirring at 1000 rpm in *t*BuOH/H_2O (1:1).

4.9 References

1 A. J. Bissette, B. Odell and S. P. Fletcher, Physical autocatalysis driven by a bond-forming thiol–ene reaction, *Nat. Commun.*, 2014, **5**, 4607.

2 S. M. Morrow, I. Colomer and S. P. Fletcher, A chemically fuelled self-replicator, *Nat. Commun.*, 2019, **10**, 1011.

3 I. Colomer, S. M. Morrow and S. P. Fletcher, A transient self-assembling self-replicator, *Nat. Commun.*, 2018, **9**, 2239.

4 E. A. J. Post, A. J. Bissette and S. P. Fletcher, Self-reproducing micelles coupled to a secondary catalyst, *Chem. Commun.*, 2018, **54**, 8777–8780.

5 E. A. J. Post and S. P. Fletcher, Controlling the Kinetics of Self-Reproducing Micelles by Catalyst Compartmentalization in a Biphasic System, *J. Org. Chem.*, 2019, **84**, 2741–2755.

6 I. Budin and N. K. Devaraj, Membrane Assembly Driven by a Biomimetic Coupling Reaction, *J. Am. Chem. Soc.*, 2012, **134**, 751–753.

7 M. D. Hardy, D. Konetski, C. N. Bowman and N. K. Devaraj, Ruthenium photoredox-triggered phospholipid membrane formation, *Org. Biomol. Chem.*, 2016, **14**, 5555–5558.

8 M. D. Hardy, J. Yang, J. Selimkhanov, C. M. Cole, L. S. Tsimring and N. K. Devaraj, Self-reproducing catalyst drives repeated phospholipid synthesis and membrane growth, *Proc. Natl. Acad. Sci.*, 2015, **112**, 8187–8192.

9 P. A. Bachmann, P. L. Luisi and J. Lang, Autocatalytic self-replicating micelles as models for prebiotic structures, *Nature*, 1992, **357**, 57–59.

10 A. J. Bissette, B. Odell and S. P. Fletcher, Physical autocatalysis driven by a bond-forming thiol-ene reaction., *Nat. Commun.*, 2014, **5**, 4607.

11 B. List, Proline-catalyzed asymmetric reactions, *Tetrahedron*, 2002, **58**, 5573–5590.

12 D. Lombardo, M. A. Kiselev, S. Magazù and P. Calandra, Amphiphiles Self-Assembly: Basic Concepts and Future Perspectives of Supramolecular Approaches, *Adv. Condens. Matter Phys.*, 2015, **2015**, 1–22.

13 A. Jesorka, N. Stepanyants, H. Zhang, B. Ortmen, B. Hakonen and O. Orwar, Generation of phospholipid vesicle-nanotube networks and transport of molecules therein, *Nat. Protoc.*, 2011, **6**, 791–805.

14 M. Karlsson, K. Sott, M. Davidson, A.-S. Cans, P. Linderholm, D. Chiu and O. Orwar, Formation of geometrically complex lipid nanotube-vesicle networks of higher-order topologies, *Proc. Natl. Acad. Sci.*, 2002, **99**, 11573–11578.

15 M. Karlsson, K. Nolkrantz, M. J. Davidson, A. Strömberg, F. Ryttsén, B. Åkerman and O. Orwar, Electroinjection of Colloid Particles and Biopolymers into Single Unilamellar Liposomes and Cells for Bioanalytical Applications, *Anal. Chem.*, 2000, **72**, 5857–5862.

16 D. Lancet, R. Zidovetzki and O. Markovitch, Systems protobiology: origin of life

in lipid catalytic networks, *J. R. Soc. Interface*, 2018, **15**, 20180159.

17 D. Segré, D. Ben-Eli, D. W. Deamer and D. Lancet, The Lipid World, *Orig. Life Evol. Biosph.*, 2001, **31**, 119–145.

18 D. Segré, D. Ben-Eli and D. Lancet, Compositional genomes: Prebiotic information transfer in mutually catalytic noncovalent assemblies, *Proc. Natl. Acad. Sci. U. S. A.*, 2000, **97**, 4112–4117.

19 C. Tanford, *The hydrophobic effect: Formation of micelles and biological membranes*, Wiley-Interscience, New York, 1980.

20 J. C. Blain and J. W. Szostak, Progress Toward Synthetic Cells, *Annu. Rev. Biochem.*, 2014, **83**, 615–640.

21 R. M. Garavito and S. Ferguson-Miller, Detergents as Tools in Membrane Biochemistry, *J. Biol. Chem.*, 2001, **276**, 32403–32406.

22 I. A. Chen and P. Walde, From Self-Assembled Vesicles to Protocells, *Cold Spring Harb. Perspect. Biol.*, 2010, **2**, a002170.

23 C. Bonfio, C. Caumes, C. D. Duffy, B. H. Patel, C. Percivalle, M. Tsanakopoulou and J. D. Sutherland, Length-Selective Synthesis of Acylglycerol-Phosphates through Energy-Dissipative Cycling, *J. Am. Chem. Soc.*, 2019, **141**, 3934–3939.

24 M. Tena-Solsona, C. Wanzke, B. Riess, A. R. Bausch and J. Boekhoven, Self-selection of dissipative assemblies driven by primitive chemical reaction networks, *Nat. Commun.*, 2018, **9**, 2044.

25 G. Da Costa, L. Mouret, S. Chevance, E. Le Rumeur and A. Bondon, NMR of molecules interacting with lipids in small unilamellar vesicles, *Eur. Biophys. J.*, 2007, **36**, 933–942.

26 T. F. Zhu and J. W. Szostak, Coupled Growth and Division of Model Protocell Membranes, *J. Am. Chem. Soc.*, 2009, **131**, 5705–5713.

27 M. J. Rosen and J. T. Kunjappu, *Surfactants and Interfacial Phenomena*, John Wiley & Sons, Inc., Hoboken, 4th edn., 2012.

28 J. C. Letelier, M. L. Cárdenas and A. Cornish-Bowden, From L'Homme Machine to metabolic closure: Steps towards understanding life, *J. Theor. Biol.*, 2011, **286**, 100–113.

29 Y. Hayashi, S. Aratake, T. Okano, J. Takahashi, T. Sumiya and M. Shoji, Combined proline-surfactant organocatalyst for the highly diastereo- and enantioselective aqueous direct cross-aldol reaction of aldehydes, *Angew. Chemie - Int. Ed.*, 2006, **45**, 5527–5529.

30 J. Huang, X. Zhang and D. W. Armstrong, Highly efficient asymmetric direct stoichiometric aldol reactions on/in water, *Angew. Chemie - Int. Ed.*, 2007, **46**, 9073–9077.

31 M. C. M. van Oers, W. S. Veldmate, J. C. M. van Hest and F. P. J. T. Rutjes, Aqueous asymmetric aldol reactions in polymersome membranes, *Polym. Chem.*, 2015, **6**, 5358–5361.

32 B. H. Lipshutz and S. Ghorai, Organocatalysis in Water at Room Temperature with

In-Flask Catalyst Recycling, *Org. Lett.*, 2012, **14**, 422–425.

33 S. Li, L. Bouzidi and S. S. Narine, Synthesis, crystallization, and melting behavior of metathesis-like triacylglycerol oligomers: Effects of saturation, isomerism, and size, *Ind. Eng. Chem. Res.*, 2014, **53**, 14579–14591.

34 G. Hu and T. Emrick, Functional Choline Phosphate Polymers, *J. Am. Chem. Soc.*, 2016, **138**, 1828–1831.

35 E. Y. Zeynep, D. Antoine, C. Brice, B. Frank and J. Christine, Double hydrophilic polyphosphoester containing copolymers as efficient templating agents for calcium carbonate microparticles, *J. Mater. Chem. B*, 2015, **3**, 7227–7236.

36 L. Liu, M. E. Lee, P. Kang and M. G. Choi, Revisit to Synthesis of Allyl- and Propargyl-Phosphorylcholines: Crystal Structure of Allyl-Phosphorylcholine, *Phosphorus, Sulfur Silicon Relat. Elem.*, 2015, **190**, 1525–1534.

37 Y. Wang, B. A. Aleiwi, Q. Wang and M. Kurosu, Selective Esterifications of Primary Alcohols in a Water-Containing Solvent, *Org. Lett.*, 2012, **14**, 4910–4913.

38 S. E. Northfield, S. J. Mountford, J. Wielens, M. Liu, L. Zhang, H. Herzog, N. D. Holliday, M. J. Scanlon, M. W. Parker, D. K. Chalmers and P. E. Thompson, Propargyloxyproline Regio- and Stereoisomers for Click-Conjugation of Peptides: Synthesis and Application in Linear and Cyclic Peptides, *Aust. J. Chem.*, 2015, **68**, 1365–1372.

39 J. Wang, Y. L. Liang and J. Qu, Boiling water-catalyzed neutral and selective N-Boc deprotection, *Chem. Commun.*, 2009, 5144–5146.

40 S. Luo, H. Xu, J. Li, L. Zhang and J.-P. Cheng, A Simple Primary−Tertiary Diamine−Brønsted Acid Catalyst for Asymmetric Direct Aldol Reactions of Linear Aliphatic Ketones, *J. Am. Chem. Soc.*, 2007, **129**, 3074–3075.

41 Z. An, Y. Guo, L. Zhao, Z. Li and J. He, L-Proline-Grafted Mesoporous Silica with Alternating Hydrophobic and Hydrophilic Blocks to Promote Direct Asymmetric Aldol and Knoevenagel–Michael Cascade Reactions, *ACS Catal.*, 2014, **4**, 2566–2576.

Chapter 5 Asymmetric Autocatalytic Copper-Catalysed Alkyne-Azide Cycloadditions

The results of this chapter are from an on-going research project and have not been submitted for publication. All experiments were designed and performed by Elias Post under the supervision of Prof. Stephen Fletcher.

5.1 Introduction

The previous three chapters explored how copper can be linked to physical autocatalysis through catalysis of alkyne-azide cycloadditions of phase-separated components. This reaction was used to model and investigate emergent, life-like properties in self-reproducing systems. Chirality was linked to physical autocatalysis driven by CuAAC through *in situ* generation of a chiral organocatalyst which subsequently catalysed an aldol reaction enantioselectively (Chapter 4). However, the origin and propagation of chirality in living systems must be properly addressed to model life accurately. Many of life's building blocks are not achiral or racemic but exist as single enantiomers such as L-amino acids and D-sugars. Homochirality is considered a universal hallmark of life and must have played an important part in the origin of life.[1]

Asymmetric autocatalysis is considered a plausible pathway through which asymmetry might have been amplified after an initial chiral symmetry breaking event to reach the homochiral state seen in nature (Section 1.5).[2] The Soai reaction is so far the only experimental realisation of absolute asymmetric autocatalysis, where small chiral imbalances can be amplified to enantiopure states through mutual antagonism between the minor and major enantiomer.[3,4] The mechanism of the Soai reaction is extremely sensitive to variations in substrate structure and the reaction is therefore limited in scope.

A discovery of a novel absolute asymmetric autocatalytic reaction with a wide substrate scope that operates under prebiotically plausible conditions, such as through organocatalysis,[5] would be desirable in furthering our understanding of biological homochirality. However, not a single asymmetric autocatalytic reaction has been discovered since the first report on the Soai reaction in 1995.[6] The development of a novel method of asymmetric autocatalysis would represent a breakthrough in the field, even if

this reaction was not prebiotically plausible and did not exhibit mutual antagonism causing e.e. to slowly erode over time:

5.2 Asymmetric CuAAC

At first sight, CuAAC is not an obvious candidate to perform an asymmetric reaction, let alone an asymmetric autocatalytic reaction. The azide and alkyne coupling partners both have sp hybridisation and are thus linear, whereas the triazole product is sp^2 hybridised and is therefore geometrically flat: at no point during the reaction is a new stereogenic centre installed (Figure 5.1a). Furthermore, CuAAC is an extremely fast reaction so an asymmetric variant would have to outcompete this efficient racemic background reaction. It comes as no surprise that asymmetric CuAAC is an under-studied area of asymmetric catalysis but some work has been done on desymmetrisation of prochiral substrates and on kinetic resolution of racemic coupling partners (Figure 5.1b and c).[7]

There is thus precedence for generating chirality using CuAAC. However, the reactions tend to be substrate specific, and are either plagued by competitive bis-product formation during desymmetrisations or are inherently limited to a maximum theoretical yield of 50% for kinetic resolutions. Recently, an asymmetric CuAAC reaction was reported that utilised racemising allyl azides to perform a dynamic kinetic resolution (DKR) to obtain enantioenriched allylic triazoles (Figure 5.1d).[8] This reaction was demonstrated on a wide variety of allylic azides with a maximum theoretical yield of 100% for the chiral triazole product.

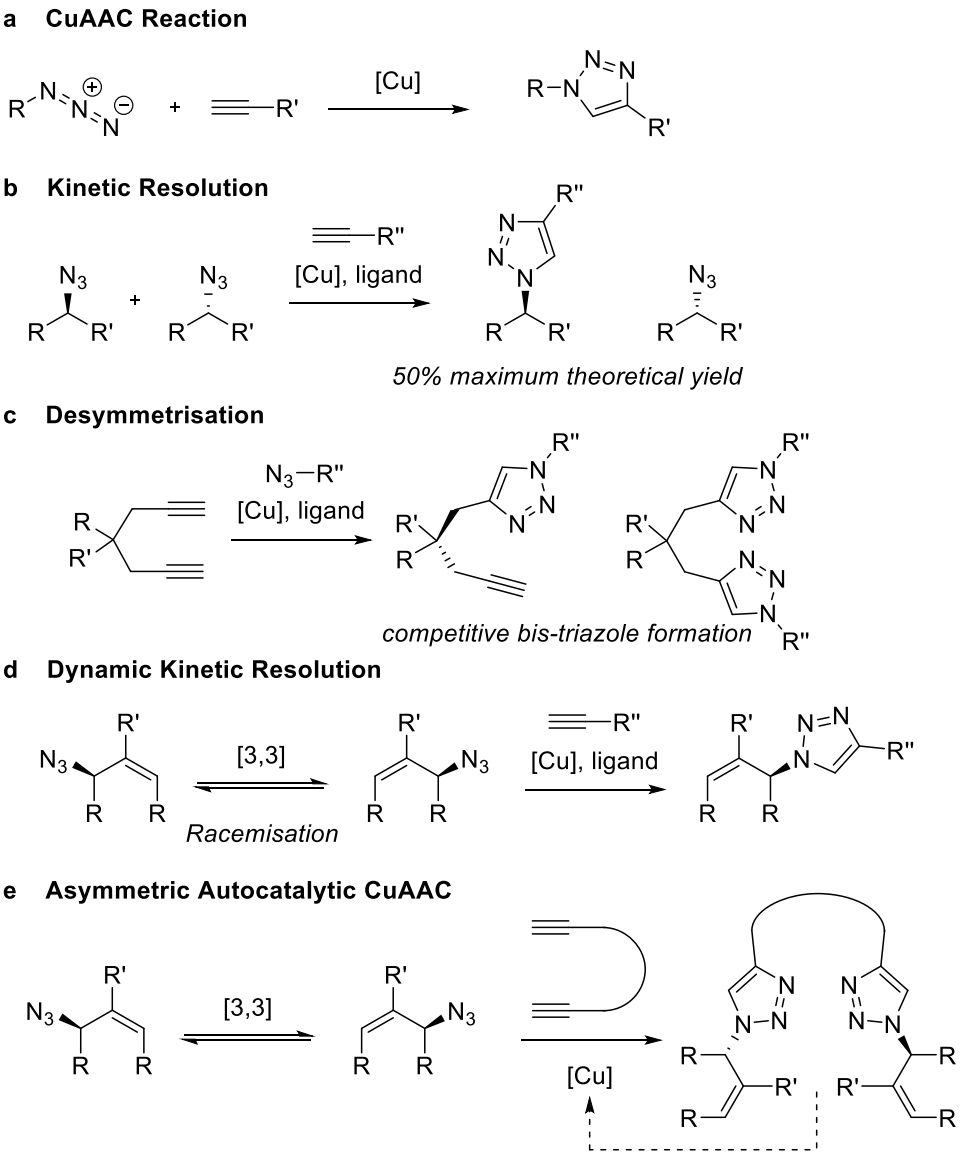


Figure 5.1 Different approaches towards performing an asymmetric CuAAC reaction.

We hypothesised that this enantioselective CuAAC reaction enabled by DKR could be an ideal candidate for asymmetric autocatalysis. Polytriazole compounds are known ligands for the CuAAC reaction, and their formation can be autocatalytic as discussed in Chapter 3. Through DKR a compound could be synthesised that contains multiple chiral allylic triazole moieties that might function as a chiral ligand in asymmetric CuAAC (Figure 5.1e). If this new class of copper ligand can induce chirality effectively it might be used to synthesise more of itself asymmetrically and thus facilitate an asymmetric autocatalytic reaction cycle.

5.2.1 CuAAC kinetic resolution strategies

One approach towards performing an asymmetric CuAAC reaction involves kinetic resolution of a racemic mixture of starting materials. If a chiral copper-catalyst complex reacts faster with one enantiomer over the other, both starting material and product will become enantioenriched.[9] The ratio between the rate of fast-reacting enantiomer and slow-reacting enantiomer is called the selectivity factor and is considered a metric of the efficiency of a kinetic resolution. If the selectivity factor is sufficiently high, product can be isolated in high ee. However, the maximum enantiopure yield will never be above 50% as the racemic mixture only contains 50% of each enantiomer. Additionally, kinetic resolution by CuAAC can be used to generate enantioenriched azides or alkynes as unreacted starting material can be recovered upon completion of the reaction.

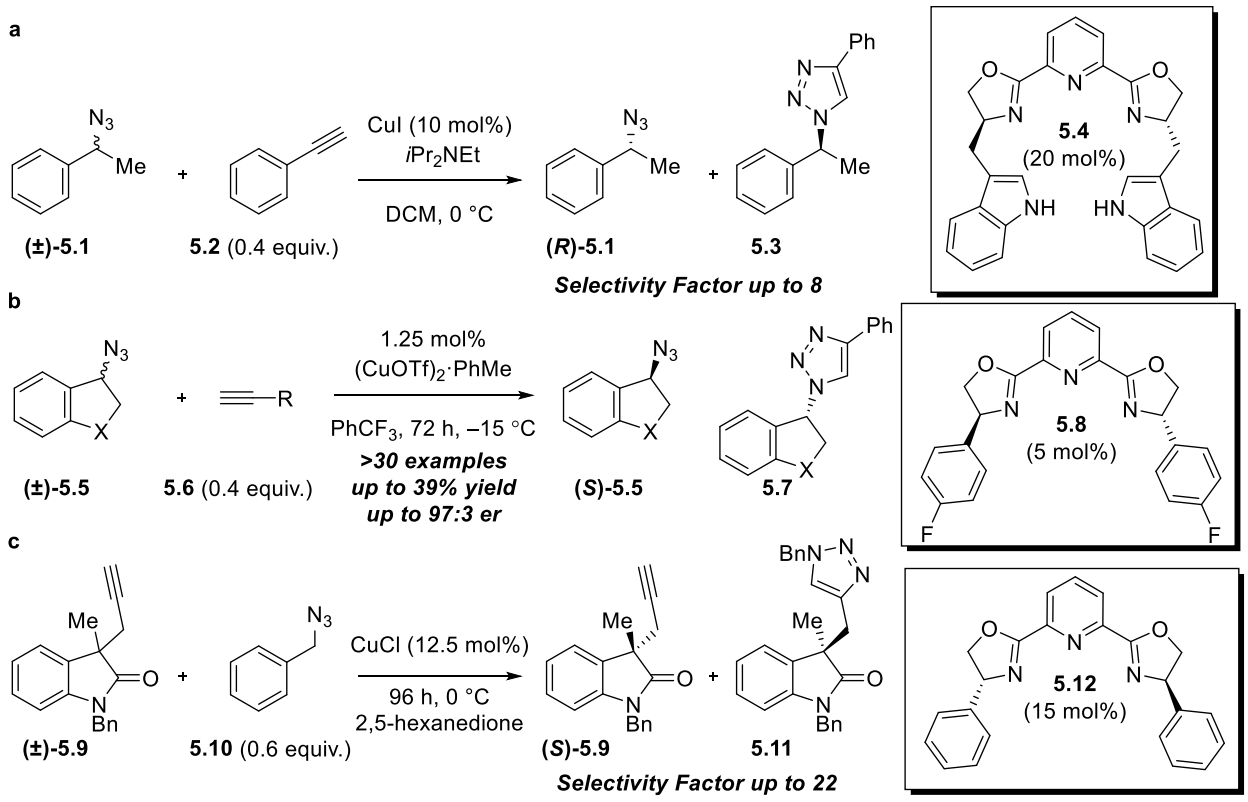


Figure 5.2 Methods of achieving kinetic resolution of racemic azides (a and b) or alkynes (c).

The first kinetic resolution of racemic azides (Figure 5.2a) was reported by Fokin and Finn,[10] the developers of polytriazole ligands.[11] CuAAC between α-benzylic azide **5.1**

and phenyl acetylene **5.2** afforded enantioenriched triazole **5.3** in the presence of copper(I) iodide and indole-derived PYBOX **5.4**. The selectivity factor of this reaction was relatively low at 8 and they were unable to expand the scope of azide substrates. Attempts at resolving various α-benzylic alkynes were unsuccessful with selectivity factors of 1. It was hypothesised that this might be due to the linear nature of alkynes which places the resolvable stereogenic centre too far out of the chiral influence of the catalyst complex.

More recently, the scope of kinetic resolution of racemic azides was significantly expanded using cyclic secondary azides **5.5** (Figure 5.2b).[12] A wide variety of chiral ligands were investigated but similar to the previous report only aryl-PYBOX ligands provided good enantioselectivity, where ligand **5.8** performed the best. Various alkynes could be employed and different heterocyclic azides could be resolved. Interestingly, unreacted scalemic azide could be recovered and racemised by subsequent exposure to catalytic $AgPF_6$ and then subjected to a second kinetic resolution cycle.

A successful resolution of terminal alkynes was reported with alkyne-appended oxindole **5.9** as the substrate (Figure 5.2c).[13] Enantioenriched triazole **5.7** was obtained when **5.9** was coupled to benzyl azide **5.10** in combination with copper(I) chloride and phenyl-derived PYBOX **5.12** in the uncommon solvent system 2,5-hexanedione. Ketone solvents appeared to play a pivotal role in obtaining high enantioselectivity and yield. The authors propose that this strong solvent dependency could be indicative of a mechanism that relies on a polynuclear catalyst complex which provides an environment that enables linear alkynes to be affected by distant chiral ligands, overcoming the problem postulated by Fokin and Finn.

5.2.2 CuAAC desymmetrisation strategies

A different way to achieve asymmetric CuAAC is through desymmetrisation of achiral starting materials. This involves the modification of a compound which results in the loss of a symmetry element which turns a prochiral substrate into a chiral product. With this approach towards asymmetric CuAAC prochiral substrates, such as geminal azides or alkynes, can be converted to a single enantiomer of triazole product with a theoretical maximum yield of 100%. A drawback of this approach is that the product can undergo competing side reaction to afford achiral bistriazole sideproduct, reducing the yield of enantioenriched product.

The paper that described the kinetic resolution of α-benzylic azide **5.1** also reported on desymmetrisation of geminal azide **5.13** to enantioenriched triazole **5.14** under similar conditions (Figure 5.3a).[10] However, this reaction proceeded with concomitant overreaction to bis-triazole **5.15**. Although the selectivity was moderate, it was the first and only successful demonstration of desymmetrisation of geminal azides.

The first of desymmetrisation of bis-alkynes was based on oxindole **5.16** that could be coupled to a range of azides (**5.17**) to desymmetrise triazole **5.18** with minimal bis-triazole **5.19** formation (Figure 5.3b).[14] Conditions in this system are similar to those reported in Figure 5.3a where PYBOX ligand **5.12** and 2,5-hexanedione were required to achieve high yield and selectivity. Variations in oxindole substitution, azide and N-protecting group were tolerated. A negative non-linear effect was observed between ee of product **5.18** and ee of ligand **5.12**, indicating that homochiral catalyst complex could be less reactive that the heterochiral complex.

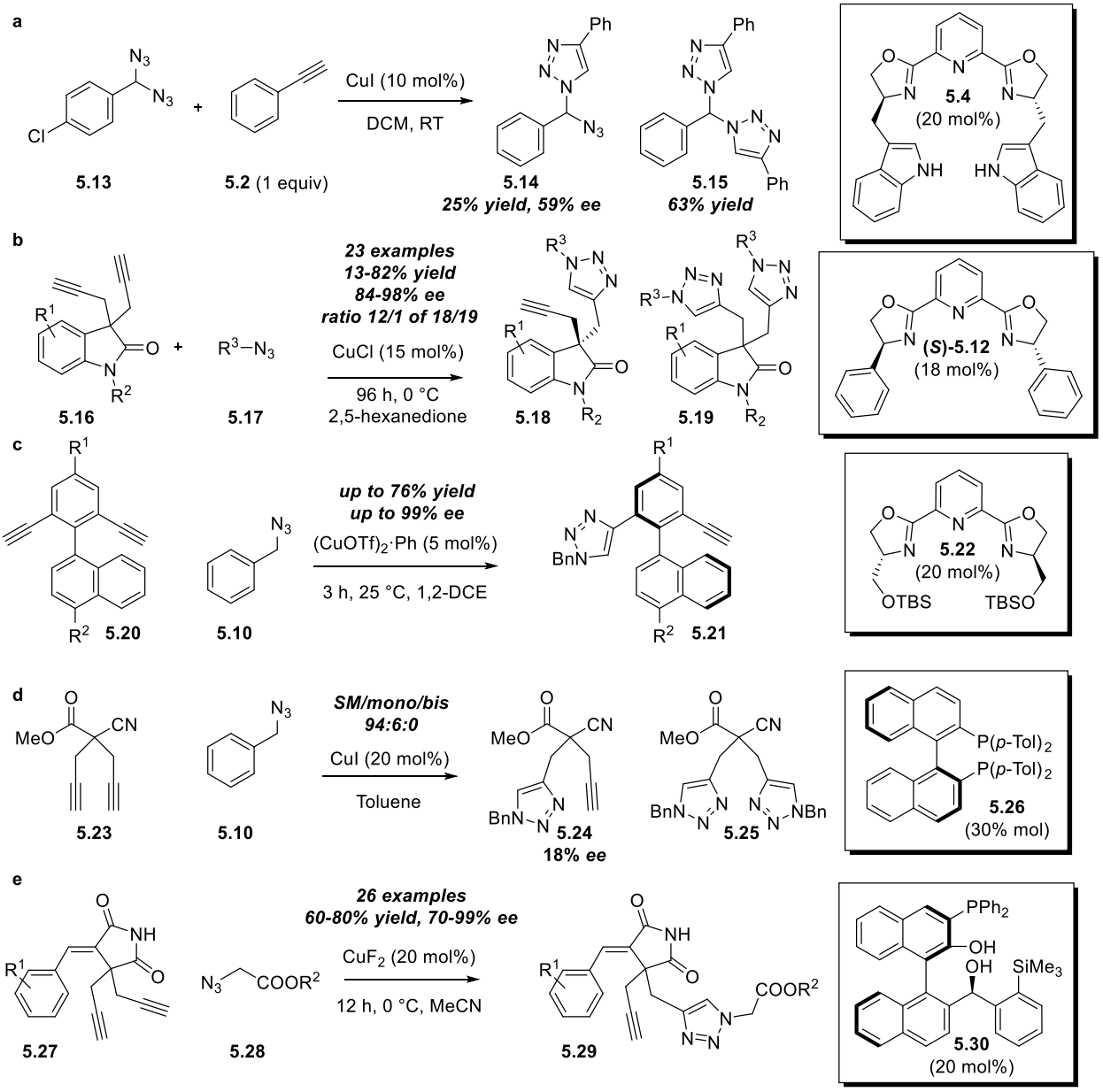


Figure 5.3 Desymmetrisation strategies for geminal azides (a) or bis-alkynes (b-e). An unique amplification effect occurred during formation of **5.21**, where the minor enantiomer preferentially reacts to form bis-triazole side product increasing the overall enantioselectivity of the reaction.

Desymmetrisation through asymmetric CuAAC was used to generate single atropisomers (Figure 5.3c).[15] Bis-alkyne biaryl **5.20** was coupled to benzyl azide **5.10** to generate atropisomer **5.21** in high ee by utilising PYBOX ligand **5.22** and copper(I) triflate as copper source. Azides other than benzyl azide were not tolerated in this reaction. Mechanistic investigation indicated that increasing equivalents of **5.10** improved enantioselectivity. Two sequential asymmetric processes appeared to be operating; initial

desymmetrisation was followed by kinetic resolution of **5.21**, where the minor enantiomer preferentially reacts to form bis-triazole side product.

More challenging acyclic substrates have also been desymmetrised albeit in low yield and low ee (Figure 5.3d). Benzyl azide **5.10** underwent asymmetric CuAAC with 2,2-diyne **5.23** in combination with phosphine ligand **5.26** and copper(I) iodide to afford enantioenriched triazole **5.24**. In this linear system significant over reaction occurred to bis-triazole **5.25**, possibly due to the rotational freedom of this substrate in contrast to the previous cyclic systems, so the reaction had to be halted at low conversions. The authors acknowledged that although a wide-range of phosphine ligands were screened their reaction still under performed compared to the other reported systems that employed PYBOX ligands.

Following this report, Song *et al* performed an exhaustive screen of phosphine ligands and discovered a new class of chiral ligands containing silicon bulky groups that performed well in the desymmetrisation of maleimide-based bis-alkynes (Figure 5.3e).[16] Compound **5.27** could be desymmetrised through coupling with azide **5.28** to generate triazole **5.29** in good yield and high enantioselectivity. Mechanistic studies indicated formation of a polynuclear catalyst species and that both phosphine centre and diol moiety in ligand **5.30** were indispensable for high yield and enantioselectivity.

5.2.3 Enantioselective CuAAC by dynamic kinetic resolution

The previous examples of kinetic resolution and desymmetrisation have shown that asymmetric CuAAC reactions are possible, however, they come with significant drawbacks of a 50% theoretical yield and competitive *bis*-triazole formation respectively. Recently Topczewski reported an alternative approach towards asymmetric CuAAC: a dynamic kinetic resolution (DKR) where allylic azides, that rapidly racemise, were

combined with an enantioselective functionalisation.[8] The reaction conditions were optimised with allylic azide **5.31** and *tert*-butyl propiolate **5.32** as coupling partners to afford allylic triazole **5.33** (Figure 5.4). During screening it was observed that cationic copper sources such as $Cu(OTf)_2 \cdot PhMe$ increased the yield and enantioselectivity of the reaction. Various ligands including bidentate and tridentate phosphorus and nitrogen ligands were screened, and Aryl-PYBOX ligands appeared to be the most effective with **5.34** giving the highest selectivity. Interestingly, an increase in temperature resulted in increased enantioselectivity of asymmetric CuAAC, likely by accelerating the relative rate of racemisation of the allylic azide through a sigmatropic pathway.

A wide range of allylic azides was tolerated in the scope of asymmetric CuAAC through DKR affording allylic triazoles in high yield and ee. The scope of alkyne coupling partners was quite broad including electron rich and deficient aryl alkynes in addition to aliphatic and heterocyclic alkynes.

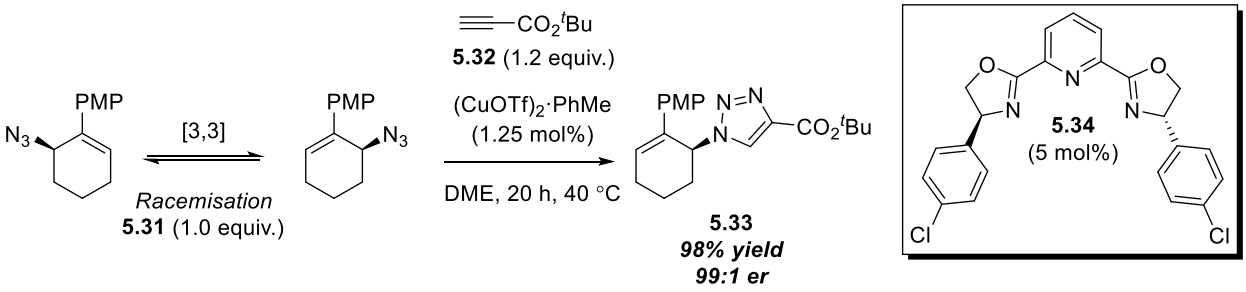


Figure 5.4 The optimised reaction conditions for asymmetric CuAAC by dynamic kinetic resolution.

5.3 Project aim

As discussed, development and study of novel asymmetric autocatalytic reactions is important to furthering our understanding of biological homochirality, and could open up new ways to incorporate chirality in bottom-up chemical models of living systems. Despite widespread interest in this field there is no known reaction other than the Soai reaction that exhibits asymmetric autocatalysis and amplification of chirality.

Based on prior literature, we believed that asymmetric CuAAC could be a good candidate for development of a new asymmetric autocatalytic reaction. Polytriazole compounds are widely used and highly effective ligands in CuAAC.[17] Furthermore, their synthesis involves a CuAAC reaction that exhibits autocatalytic kinetics.[11,18] Asymmetric CuAAC driven by DKR has shown to tolerate a wide substrate scope and can generate chiral triazole products in high yield and high enantioselectivity.[8] Chiral polytriazole ligands could be a new class of ligands suitable for asymmetric CuAAC. Mechanistic studies have shown that both CuAAC and asymmetric CuAAC reactions involve polynuclear catalyst complexes. This could facilitate amplification of chirality through mutual antagonism if homochiral complexes are better catalysts than their heterochiral counterparts. The mechanism of the Soai reaction proceeds through a homochiral tetrameric substrate-catalyst complex, whereas the heterochiral tetramer complex is catalytically inactive.[19]

Additionally, the presence of multiple stereocenters on polytriazole ligands could be beneficial to amplification of chirality. Multiple consecutive stereospecific reactions with moderate selectivity could still lead to high enantiomeric excess in the final product composition e.g. a high ratio between (*R,R,R*)- and (*S,S,S*)-enantiomers might be obtained through concomitant formation of undesired (*R,S,S*)- and (*S,R,R*)-diastereomers. Furthermore, kinetic resolution of the intermediates could occur: (*R*)-monoadduct might react faster to form (*R,R*)-bisadduct than (*S*)-intermediate could form (*S,R*)-bisadduct resulting in higher enantioselectivity. Finally, the undesired (*S,R,R*)-diastereomer might still exhibit limited (*R*)-selectivity preventing significant erosion of e.e. through sideproduct formation.

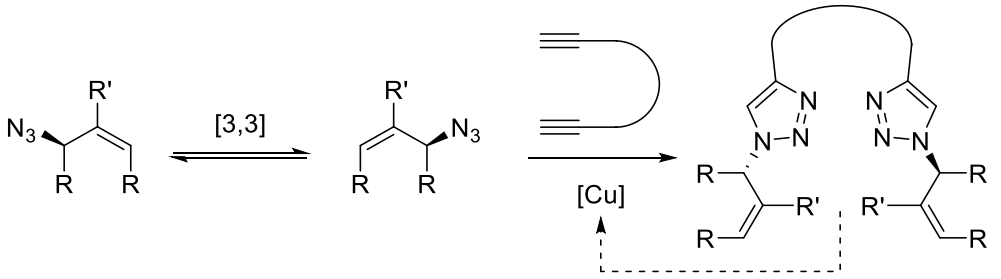


Figure 5.5 Proposed system to achieve asymmetric autocatalysis: DKR of allylic azides by asymmetric CuAAC affords enantioenriched polytriazole compounds that act as chiral ligands for their own formation.

The aim of this project is to use asymmetric CuAAC DKR conditions to synthesise chiral polytriazole compounds (Figure 5.5). Once enantiopure polytriazoles are obtained, they will be tested as chiral ligands in asymmetric CuAAC reactions to study their ability to coordinate to copper and their capacity to induce enantioselectivity. When a suitable polytriazole ligand and optimal reaction conditions are found, asymmetric autocatalytic synthesis of the polytriazole ligand will be investigated.

5.4 System design

The correct polytriazole structure must to be selected for study to optimise our chances of successfully developing an asymmetric autocatalytic reaction. Based on prior literature, it became apparent that triazole-based ligands require multiple triazole moieties combined with a central aromatic or aliphatic nitrogen to effectively coordinate to copper.[11,20,21]

With these constraints in hand, two structurally different ligands were selected for study. Tris-triazole **3.35** with a central tertiary amine is analogous in structure to polytriazole ligands commonly used in CuAAC (Figure 5.6a), such as THPTA and TBTA in Chapter 3 and 4. This structural design is known to accelerate CuAAC reactions, however it is unclear if the flexible structure combined with distant chiral centres will be able to induce chirality in asymmetric CuAAC. A similarly structured chiral Cu(II)-tris(oxazoline)

complex with a central amine was employed for the enantioselective allyl oxidation of cycloalkenes and afforded excellent enantioselectivity.[22]

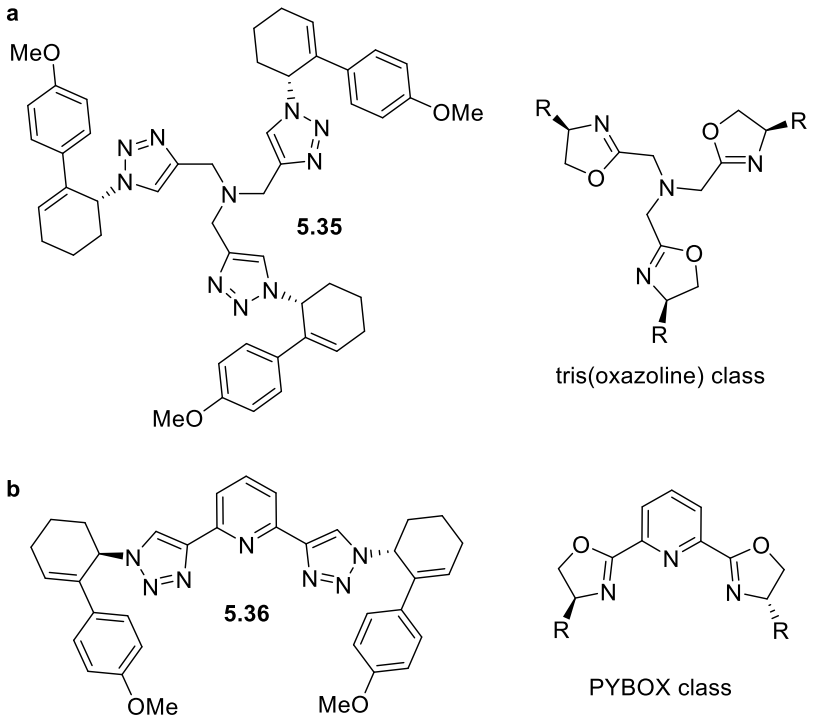


Figure 5.6 Proposed chiral polytriazole ligand structures for asymmetric autocatalysis.

The second ligand selected for study was bis-triazole **5.36** which contains a central pyridine ring flanked by two triazoles (Figure 5.6b) and derives its structure from the PYBOX class of ligands which have proven to be very effective at asymmetric CuAAC. However, it is unclear if replacing oxazoline groups with triazoles will still impart the same degree of enantioselectivity to this ligand.

5.5 Testing conditions for asymmetric CuAAC *via* DKR

The reproducibility and effectiveness of asymmetric CuAAC by DKR through racemising allylic azides was first tested in our hands. The standard reaction conditions reported by Topczewski[8] were selected for study combined with their best performing coupling partners namely azide **5.31** and alkyne **5.32** to synthesise enantioenriched **5.33** with PYBOX ligand **5.34** (Figure 5.7). The authors noted the importance of a cationic copper

source and used copper(I) triflate toluene complex as the metal source. This type of copper salt is extremely sensitive to oxygen and will quickly decompose upon exposure to air. Therefore, their general setup involved preparation of the active catalyst complex inside a glovebox.

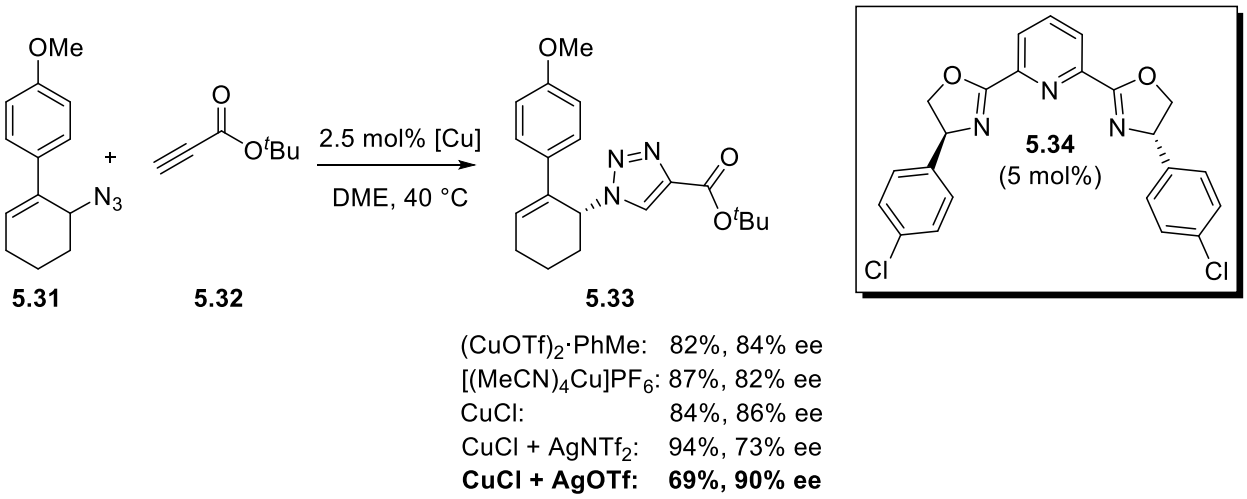


Figure 5.7 Results of a test of the standard conditions for asymmetric CuAAC by DKR with various copper sources.

Due to practical considerations, we were interested in finding conditions that afforded good enantioselectivity under Schlenk conditions without the need for a glovebox. When $(CuOTf)_2 \cdot PhMe$ was weighted out under open atmosphere a yield of 82% with 84% ee was obtained (Figure 5.7). These are lower than the reported yield of 98% and 98% ee, possibly due to oxidation of copper under these conditions. Furthermore, quick decomposition of this copper salt was observed when stored on the benchtop under argon. Other copper salts, such as $[(MeCN)_4Cu]PF_6$ and CuCl, were tested and afforded similar lower ee's.

The Fletcher group has extensive experience with asymmetric copper chemistry and often uses more Lewis acidic copper(I) triflate or triflimide in their reactions.[23–26] These are usually generated *in situ* via salt metathesis from bench-stable silver salts and CuCl by precipitating out AgCl. When copper(I) triflate was generated *via* this method for

asymmetric CuAAC a lower yield of 69% with a good enantioselectivity of 90% ee could be obtained for **5.33** without a glovebox.

5.6 Asymmetric synthesis of chiral tris-triazole ligands

The standard route of synthesis for tris-triazole compounds was selected for ligand **5.35** starting from tripropargylamine **5.37** combined with allylic azide **5.31**, which performed the best for asymmetric CuAAC (Figure 5.8). It should be noted that the original scope of asymmetric CuAAC by DKR did not contain an unprotected tertiary amine: they only tested a N-Boc protected secondary amine whose lone pair is delocalized, and it was appreciated that the aliphatic nitrogen lone pair in **5.37** might disrupt asymmetric CuAAC through coordination to copper.

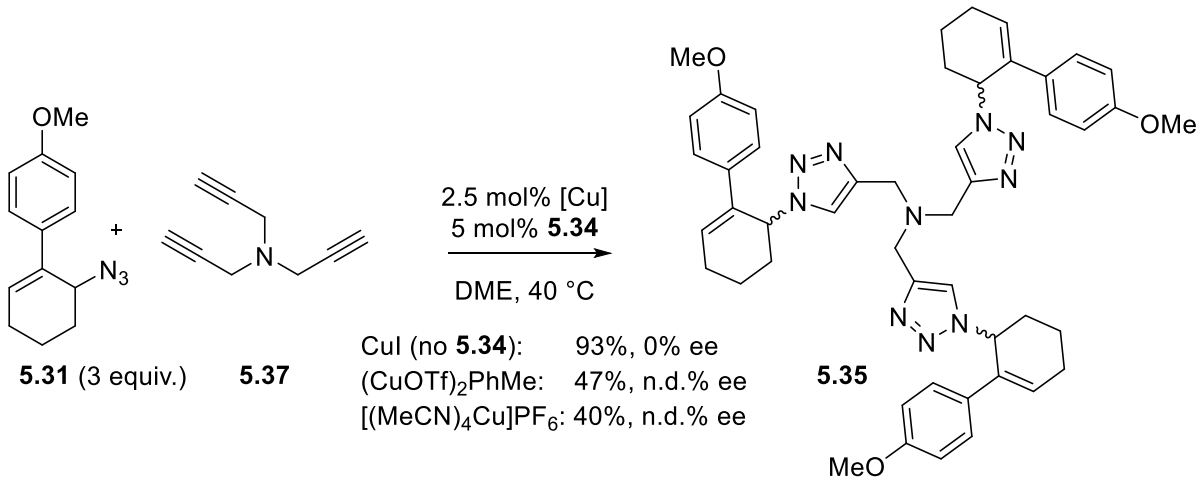


Figure 5.8 Applying asymmetric CuAAC conditions to allylic **5.31** and tripropargyl **5.37** affords a diastereomeric mixture of tris-triazole **5.35** that is inseparable by SFC or flash column chromatography.

CuAAC conditions successfully generated racemic **5.35** in the absence of a chiral ligand (Figure 5.8). However, we encountered several problems during asymmetric synthesis of **5.35**. Firstly, the ligand contains three chiral centres and the statistical distribution between desired (*S,S,S*)- and (*R,R,R*)-enantiomers relative to unwanted (*R,S,S*)- and (*S,R,R*)-diastereomers will lean towards the undesired sideproducts in a 1 : 3 ratio due to C_3 symmetry (confirmed by integration of the ^{1}H NMR OMe resonances). Due to the

polar nature of this compound and the structural similarity between the diastereomers, the desired product could not be isolated by flash column chromatography. Before this ligand can be used, the undesired diastereomer must be completely removed as it would likely have a lower or unwanted enantioselectivity in asymmetric CuAAC. Furthermore, contamination would complicate kinetic and enantiomeric analysis of autocatalytic formation of **5.35** down the line.

Secondly, we were unable to find screening conditions for supercritical fluid chromatography (SFC) which could effectively separate all enantiomers and diastereomers present in the reaction mixture to reliably calculate any enantiomeric excess obtained during asymmetric CuAAC. The chiral columns tested were not suitable for separation of compounds with multiple basic nitrogens such as **5.35**. A reversed-phase chiral column suitable for this class of compounds on a UPLC system would likely give better separation but was unavailable to us. Furthermore, preliminary tests employing asymmetric conditions did not show a decrease in the undesired diastereomer by ^{1}H NMR indicating that enantioenrichment was likely not occurring.

5.6.1 An alternative route towards chiral tris-triazoles

Due to the problems mentioned above, an alternative route towards chiral tris-triazoles was devised that incorporates chiral triazole moiety at an earlier step in the synthesis before the central basic amine is installed (Figure 5.9). This approach ensured that asymmetric CuAAC can proceed with high enantioselectivity as simpler alkyne substrates can be tested and their enantiomeric excess determined. The final tris-triazole product is expected to retain the same ee as allylic triazoles do not racemise. Furthermore, this enantioenriched chiral triazole precursor might be used to generate a wide range of polytriazole ligands that could be tested for asymmetric CuAAC.

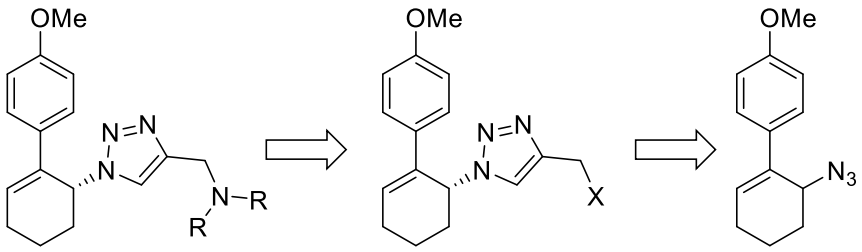


Figure 5.9 An alternative route towards enantioenriched poly-triazole ligands.

Several different functionalised propargyl compounds were screened for asymmetric CuAAC (Figure 5.10). Reaction of azide **5.31** with propargyl alcohol **5.38** afforded triazole **5.39** in low ee, likely due to interference by the alcohol group. Propargyl bromide **5.40** and propargyl tosylate **5.41** were unreactive and did not form any triazole product under the reaction conditions even at increased temperatures. TBS-protected propargyl alcohol **5.42** yielded enantioenriched triazole **5.43** in 86% ee when copper(I) triflate was generated *in situ*. Synthesis of **5.43** was included in the scope of the original report where it was obtained in 88% ee.[8]

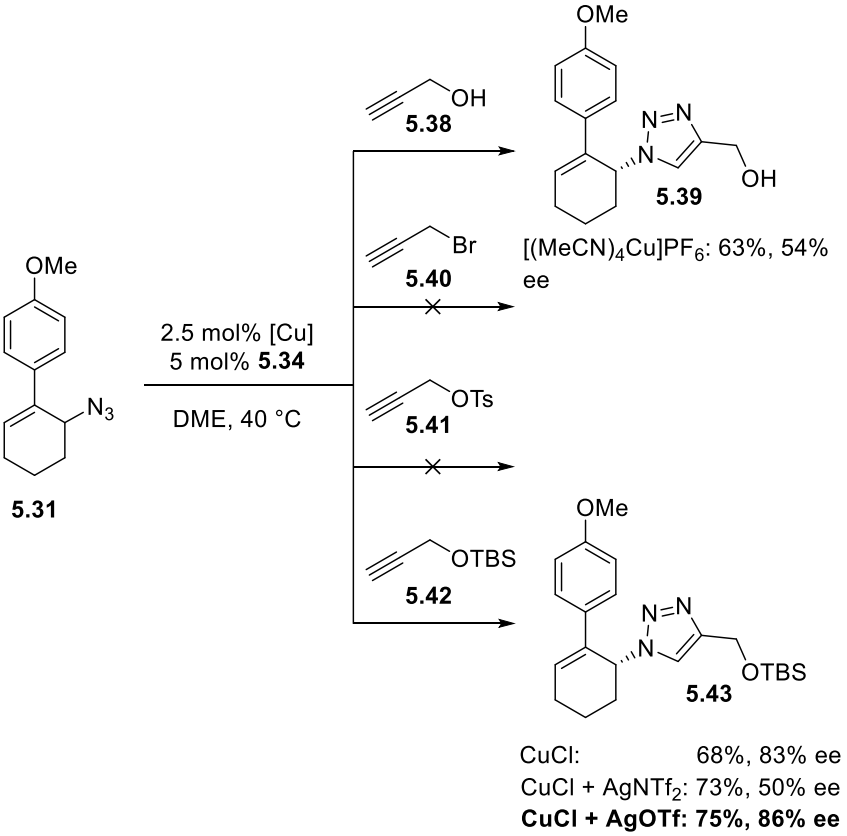


Figure 5.10 Synthesis of functionalised enantioenriched allylic triazoles.

Treatment with TBAF removed the TBS-protecting group from **5.43** to generate alcohol **5.39** in 89% ee (Figure 5.11). Attempts at activating the alcohol group of **5.39** through tosylation or mesylation were unsuccessful but a preliminary test reaction indicated that a bromide could be installed to give compound **5.44** using Appel conditions. A larger scale synthesis of enantioenriched **5.44** is currently underway and routes towards ligand **5.35** or other polytriazole compounds such as substitution by ammonium salts or cross-coupling reactions will be explored.

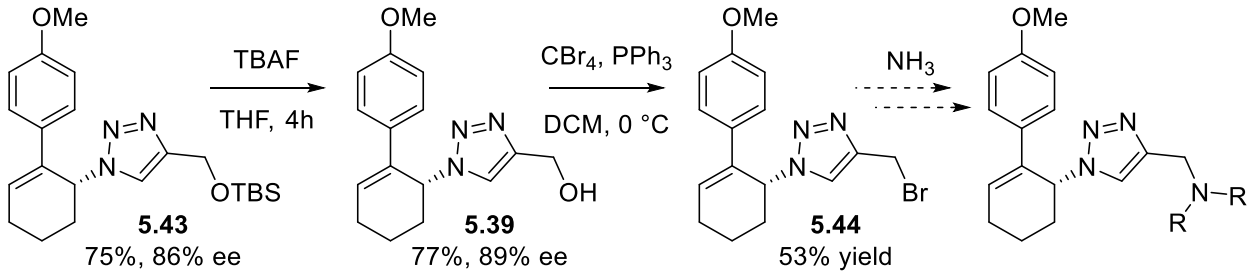


Figure 5.11 Synthesis of bromide **5.44** that might be used to create enantioenriched polytriazole ligands.

5.7 Asymmetric synthesis of chiral bis-triazole ligands

Bis-triazole ligands were derived from bis-alkyne precursor **5.46** which could be made from the corresponding 2,6-dibromopyridine **5.44** through Sonogashira coupling to afford **5.45** followed by TMS-deprotection (Figure 5.12).

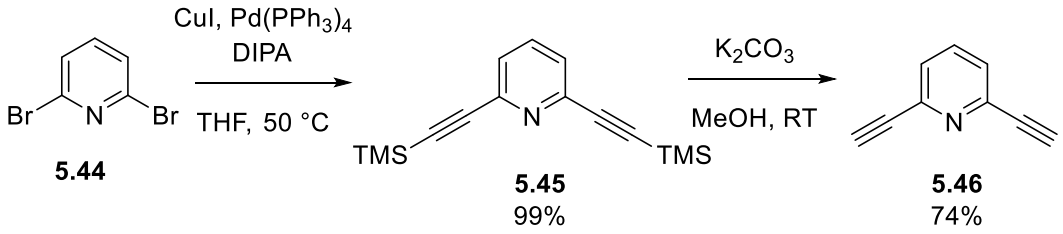


Figure 5.12 Synthesis of bis-alkyne precursor **5.46** from dibromide **5.44** via deprotection of **5.45.**

Racemic CuAAC conditions successfully generated bis-triazole **5.36** from bis-alkyne **5.46** and allylic azide **5.31** as confirmed by mass spectrometry analysis (Figure 5.13). However, several issues were encountered during characterisation of this compound that are of note.

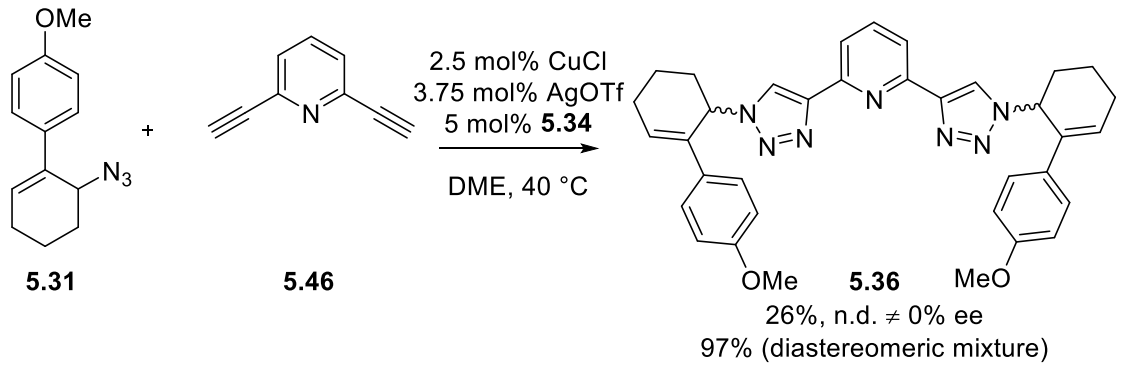


Figure 5.13 Synthesis of enantioenriched bis-triazole **5.36** from allylic azide **5.31** and bis-alkyne **5.46**.

During ^{1}H NMR analysis of **5.36** broad ill-defined resonances were obtained, albeit around the expected chemical shifts (Figure 5.14a). Two separate singlets with chemical shifts in the range for methoxy-groups (3.6-3.7 ppm) were observed indicating the presence of at least two isomers.

The paramagnetic nature of residual copper(II) could significantly reduce T_2 relaxation times leading to broad ill-defined resonances.[27] Therefore, the reaction mixture was thoroughly extracted with an aqueous solution of NH_3 (17% w/w) in 0.1 M sodium-ethylenediaminetetraacetate to ensure that no residual copper remained coordinated to **5.36** after purification by column chromatography. However, this did not observably improve the ^{1}H NMR spectrum of **5.36**.

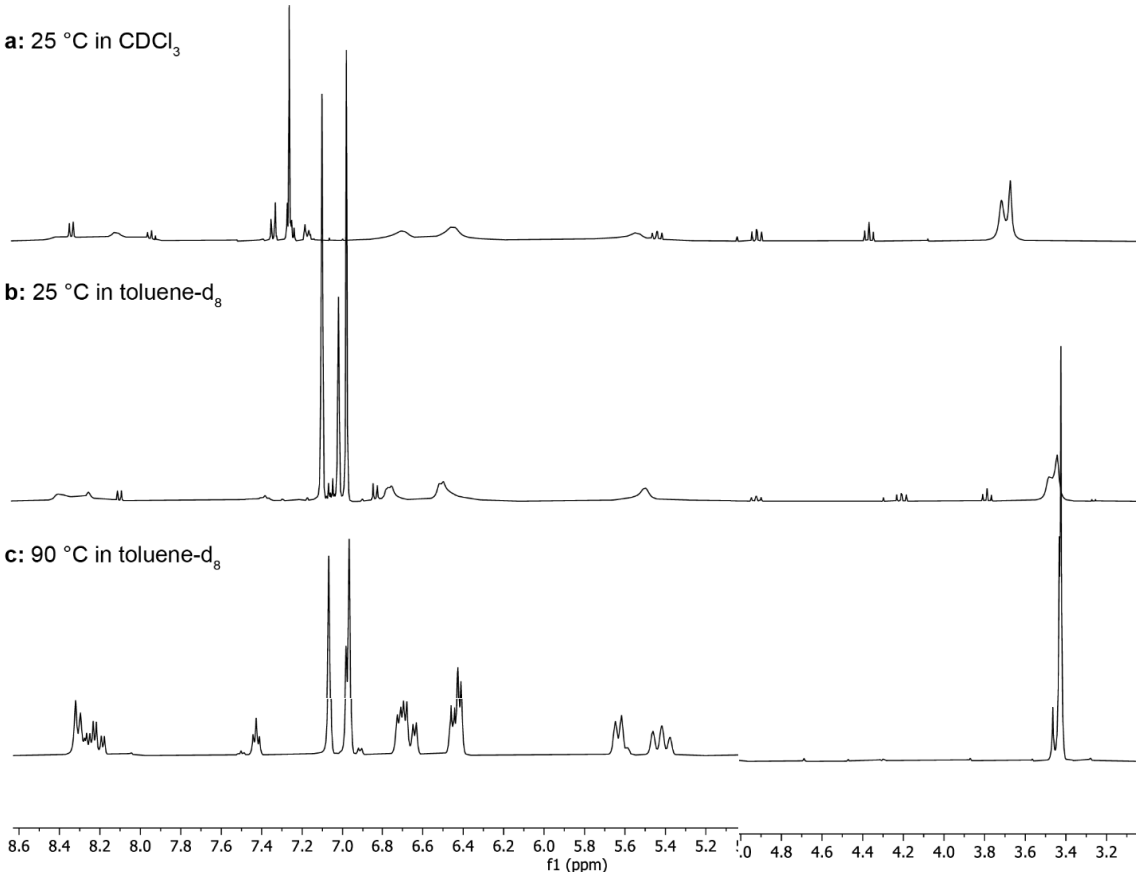


Figure 5.14 ^{1}H NMR spectrum of **5.36** in $CDCl_3$ at 25 °C (a), toluene-d_8 at 25 °C (b) and toluene-d_8 at 90 °C (c).

Interestingly, sharper peaks were observed during ^{1}H NMR analysis when **5.36** was dissolved in toluene-d_8 (Figure 5.14b) and a subsequent increase of the probe temperature to 90 °C afforded a well-defined spectrum revealing a third methoxy-resonance (Figure 5.14c). This temperature dependence is indicative of a barrier to rotation around a bond in **5.36** which enables observation of multiple stable conformers of each diastereomer. The presence of a third smaller methoxy-resonance at higher temperatures corroborates this hypothesis.

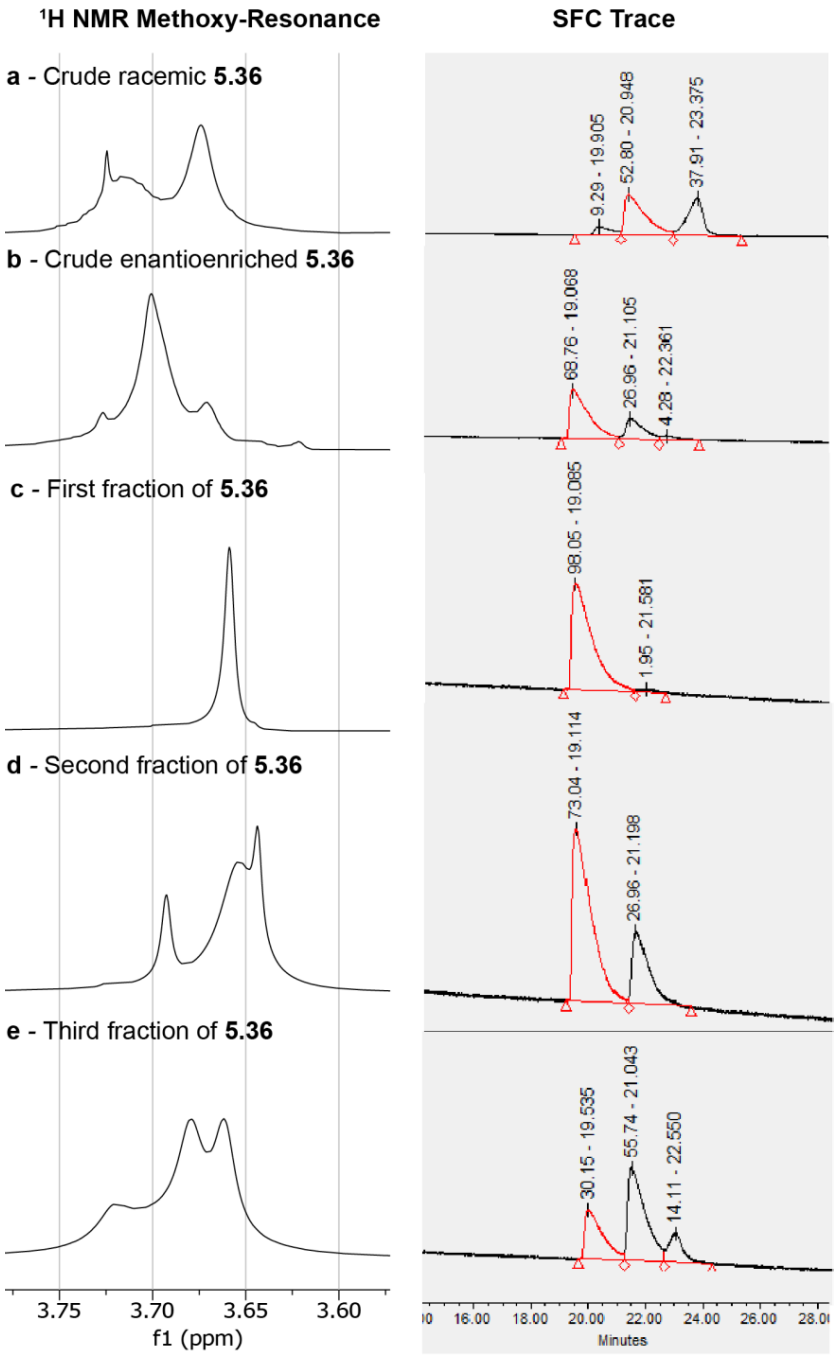


Figure 5.15 ^{1}H NMR spectrum ($CDCl_3$, 25 °C) of methoxy-resonances, and SFC traces of crude racemic **5.36** (a), crude enantioenriched **5.36** (b), and (c-d) fractions of enantioenriched **5.36** collected after flash column chromatography.

The presence of multiple conformers complicated enantiomeric analysis as more than three different isomers of **5.36** could be present in the final product composition. Three individual peaks were observed during SFC analysis, however these peaks did not integrate to the expected statistical ratio of 1:2:1 for (*R,R*):(*R,S*):(*S,S*) isomers (Figure 5.15a).

We were hopeful that through enantioenrichment of **5.36** the desired enantiomer could be isolated during SFC analysis and flash column chromatography as smaller relative amounts of undesired enantio- and diastereomers would make separation more facile. To our delight, employing the optimised conditions for asymmetric CuAAC resulted in a significant enrichment of a minor isomer as confirmed by SFC analysis and was accompanied by reduction of undesired diastereomers as confirmed by ^{1}H NMR analysis (Figure 5.15a and b).

Analysis of the fractions, obtained after column flash chromatography of crude enantioenriched **5.36**, by SFC and ^{1}H NMR indicated enrichment in the minor isomer (Figure 5.15b-e). The first fraction contained a single diastereomer of **5.36** as confirmed by a single methoxy-resonance during ^{1}H NMR analysis, whereas SFC analysis indicated that only the enriched isomer was present is this fraction (Figure 5.15c). The second and third fraction on the other hand contained additional undesired diastereomers (Figure 5.15d and e).

Unfortunately, the enantiomeric excess of the sample could not be determined. The single peak observed during SFC analysis in the first fraction could represent two overlapping enantiomers and thus does not fully confirm enantioenrichment as we did not achieve complete separation of all isomers in the racemic sample. The optical rotation of the first fraction of **5.36** was measured to ensure that enantioenrichment had occurred. A non-zero value for the optical rotation was obtained and confirmed enrichment of an enantiomer of **5.36** ($[\alpha]^{25}_{D}$ = + 30.7 (c = 0.30, $CHCl_3$)).

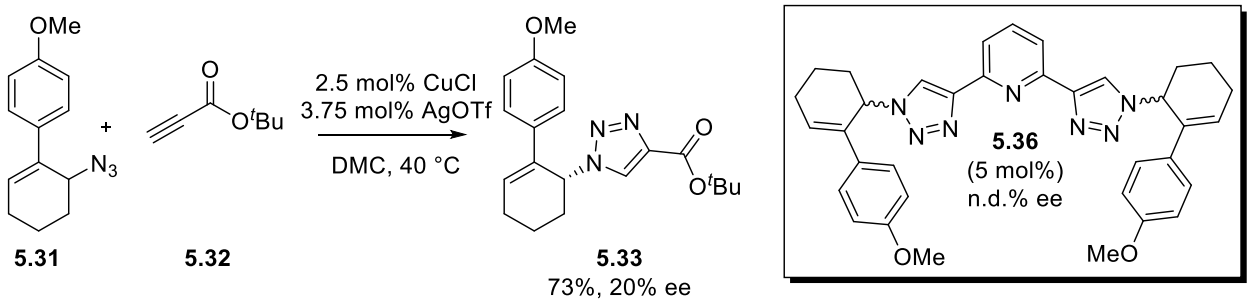
A synthesis of the opposite enantiomer of **5.36** utilising the opposite enantiomer of **5.34** as ligand is underway to further confirm enantioenrichment. A different method for separation, potentially reverse phase UPLC-conditions combined with a chiral column

suitable for this class of compounds, will be required to get full separation of all isomers and this is the only way to determine the level of enantiomeric enrichment with any confidence. Additionally, X-ray diffraction crystallography measurements of a sufficiently enantioenriched fraction could generate at crystal structure of **5.36** and could provide an unambiguous determination of the absolute configuration of this isomer.

Overall, by employing optimised asymmetric CuAAC conditions bis-triazole **5.36** was synthesised in an enantioenriched state and was isolated from undesired diastereomers.

5.7.1 Testing chiral bis-triazole ligands in asymmetric CuAAC

With an enantioenriched sample of ligand **5.36** in hand albeit of unknown conformation, the efficacy of the bis-triazole-pyridine motif in asymmetric CuAAC could be tested. Two conditions must be fulfilled before **5.36** can function as an effective ligand in this reaction: the ligand must capable of coordinating strongly to copper and once the copper-ligand complex has formed, the chiral centres of the ligand must be in proximity of the substrates and intermediates to induce asymmetry during the CuAAC reaction.



5.31 **5.32** **5.33** 73%, 20% ee

Figure 5.16 Test of the efficacy of enantioenriched **5.36** as a ligand in asymmetric CuAAC.

The standard substrates, allylic azide **5.31** and alkyne **5.32**, were selected to test the efficacy of **5.36** in asymmetric CuAAC (Figure 5.16). DCM was used as solvent, as **5.36** is insoluble in DME, combined with *in situ* generated copper(I) triflate as catalyst. This preliminary, unoptimised reaction afforded triazole **5.33** in promising 20% ee. This result indicates that **5.36** and possibly analogous compounds bearing a bis-triazole-pyridine

motif have the potential to be effective catalysts in asymmetric CuAAC and could potentially become a new class of chiral copper ligand with utility in other areas of asymmetric copper chemistry.

Further optimisation is required to investigate if the enantiomeric excess of this reaction can be increased and if an asymmetric autocatalytic variant of this reaction can be developed to prepare **5.36**. Asymmetric CuAAC has shown to be highly sensitive to temperature, solvent system, copper source and ligand structure, therefore a wide range of variables should be screened and optimised.

When optimised conditions for asymmetric autocatalytic CuAAC have been found, kinetic study of the reaction should be performed. Enantiomeric excess and conversion could be followed over time and repeating the reaction with varying enantiopurity of the ligand might indicate if non-linear effects are present. A positive non-linear effect could be an indicator that homochiral catalyst complexes are more efficient catalysts and that asymmetric amplification of chirality could be possible through mutual antagonism if heterochiral catalyst complexes are unreactive.

5.8 Conclusions

Over the course of this project, synthetic routes towards two structurally different enantioenriched polytriazole ligands were explored for their ultimate application in an asymmetric autocatalytic CuAAC reaction.

Direct synthesis of enantioenriched tris-triazole ligand **5.35** through asymmetric CuAAC *via* DKR was unsuccessful due to complications during purification and determination of enantiomeric excess (Section 5.6). However, an alternative route towards tris-triazole ligand **5.35** and potentially other polytriazole ligands starting from an activated enantioenriched triazole precursor appeared to be promising. Bromide-appended triazole

5.44 was obtained and might readily be converted to polytriazole compounds through nucleophilic attack by a nitrogen-bearing substrate.

Bis-triazole **5.36** was generated in an enantioenriched state and was isolated from undesired diastereomers. However, the enantiomeric excess of this sample of **5.36** could not be determined with confidence due to rotamer formation. A preliminary test for the efficacy of **5.36** as a chiral ligand in DKR through asymmetric CuAAC promisingly afforded allylic triazole **5.36** in 20% ee. This result confirmed that chiral polytriazole ligands are capable of binding to copper and inducing chirality, and thus can be used as ligands in asymmetric CuAAC reactions.

The results reported in this chapter have laid the groundwork for the development of an asymmetric autocatalytic CuAAC reaction. Reaction conditions for asymmetric CuAAC with **5.36** as ligand will have to be optimised and conditions for separation of all possible isomers of **5.36** must be found. How this might be achieved and how this research project might be brought to fruition will be discussed in more depth in the future work section of Chapter 6.

5.9 Experimental

5.9.1 General Information

The general information for the work reported in this chapter is as described in Section 2.5.1 and 4.8.1.

5.9.2 Experimental Procedures and Characterisation of Compounds

General procedure 1: Racemic Triazole Preparation

A flame-dried flask (5 mL) was charged with CuCl (0.5 mg, 0.005 mmol, 0.025 eq) and 2,2'-bipyridine (1.6 mg, 0.01 mmol, 0.05 eq) followed by addition of anhydrous DME (1

mL) under argon atmosphere. After the resulting solution had stirred at ambient temperature for 30 mins, allylic azide (0.20 mmol, 1 eq) and alkyne (0.24 mmol, 1.2 eq) were added. The flask was sealed by a septum and heated to 40 ˚C. After 16 hours, the reaction was cooled and concentrated *in vacuo*. The resulting crude was purified by flash column chromatography (eluent specified below) to afford the desired racemic triazole compound.

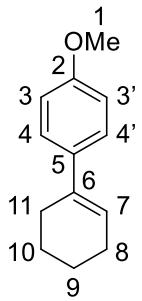
General procedure 2: Enantioselective Triazole Preparation

Flask **A**: A flame-dried flask (5 mL) was charged with CuCl (0.5 mg, 0.005 mmol, 0.025 eq) and PYBOX **5.34** (4.3 mg, 0.01 mmol, 0.05 eq). Anhydrous DME (1 mL) was added under argon atmosphere and the resulting solution was stirred at 40 ˚C for 30 min. AgOTf (1.6 mg, 0.0055 mmol, 0.0275 eq) was then added and stirred for a further 15 mins. A pale brown suspension formed.

Flask **B**: A separate flame-dried flask (5 mL) was charged with allylic azide (0.20 mmol, 1 eq) and alkyne (0.24 mmol, 1.2 eq) under argon atmosphere.

The contents of flask **A** were transferred into flask *B* using a syringe equipped with a Camlab PTFE syringe filter (13 mm size, pore diameter 0.22 μm) to remove precipitated AgCl. The combined mixture was left to stir at 40 ˚C in the absence of light. After 18 hours, the reaction was cooled and concentrated *in vacuo*. The resulting crude was purified by flash column chromatography (eluent specified below) to afford the desired enantioenriched triazole compound.

1-(4-Methoxyphenyl)cyclohexene (5.47)



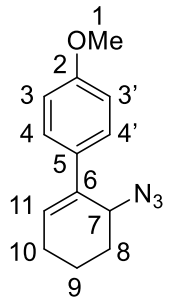
Chemical Formula: $C_{13}H_{16}O$
Molecular Weight: 188.2700

Synthesised according to method adapted from Lui *et al*.[8] A flame-dried flask sealed under argon was charged with anhydrous THF (50 mL) and *n*-butyllithium (18.0 mL, 2.5 M in hexanes, 45.0 mmol, 1.125 eq) while cooled in an acetone/dry ice bath. 4-bromoanisole (5.00 mL, 40.0 mmol, 1 eq) was added dropwise to the flask over 5 min. After 1 h, cyclohexanone (4.56 mL, 44.0 mmol, 1.1 eq) was added dropwise via a syringe and the reaction was gradually warmed to room temperature. After 1 h, the reaction was quenched by addition of water (30 mL). The resulting solution was diluted with water (100 mL) and extracted with hexane (3 × 100 mL). The combined organic solution was washed with brine, dried (Na_2SO_4), filtered, and concentrated *in vacuo* to afford crude 1-(4-methoxyphenyl)cyclohexanol which was used without further purification. The crude intermediate (assuming 40 mmol) was dissolved in toluene (50 mL) followed by addition of *p*-toluenesulfonic acid (40 mg, 0.20 mmol. 0.005 eq) and the reaction was heated to reflux. After 1 h, the reaction was cooled and solid $MgSO_4$ was added. The resulting suspension was filtered, concentrated *in vacuo* and purified by flash column chromatography (0 - 10%, EtOAc in hexane) to afford 1-(4-methoxyphenyl)cyclohexene **5.47** as a white solid (5.09 g, 27.03 mmol, 68% over two steps).

^{1}H NMR (400 MHz, $CDCl_3$) δ 7.36 – 7.28 (m, 2H, C<u>H</u>-4;C<u>H</u>-4'), 6.90 – 6.81 (m, 2H, C<u>H</u>-3;C<u>H</u>-3'), 6.08 – 6.00 (m, 1H, C<u>H</u>-7), 3.81 (s, 3H, C<u>H</u>$_3$-1), 2.44 – 2.34 (m, 2H, C<u>H</u>$_2$-11), 2.25 – 2.15 (m, 2H, C<u>H</u>$_2$-8), 1.84 – 1.73 (m, 2H, C<u>H</u>$_2$-10), 1.66 (s, 2H, C<u>H</u>$_2$-9); **^{13}C{^{1}H} NMR** (101 MHz, $CDCl_3$) δ 158.6, 136.1, 135.5, 126.1 (2C), 123.3, 113.7 (2C),

55.4, 27.6, 26.0, 23.3, 22.4; **HRMS** (ESI) *m/z* calcd for $C_{13}H_{15}O$ $[M-H]^-$: 187.1117, found: 187.1119. Consistent with reported literature values.[28]

2-Azido-4'-methoxy-2,3,4,5-tetrahydro-1,1'-biphenyl (5.31)



Chemical Formula: $C_{13}H_{15}N_3O$
Molecular Weight: 229.2830

Synthesised according to method adapted from Lui *et al*.[8] To a solution of cyclohexene **5.47** (5.09 g, 27.0 mmol, 1.00 eq) in acetone (120 mL) and water (40 mL) at 0 °C was added portion wise solid *N*-bromosuccinimide (4.81 g, 27.0 mmol, 1.00 eq). After 1 h, the reaction was diluted with water (50 mL) and extracted with hexane (3 × 100 mL). The combined organic solution was washed with sodium bicarbonate solution (1 × 100 mL), brine (1 × 100 mL), dried (Na_2SO_4), filtered, and concentrated *in vacuo*. The resulting bromohydrin was used without further purification because of instability.

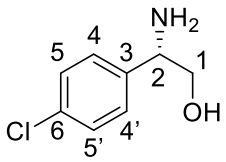
To a solution crude bromohydrin (assuming 27.0 mmol) in hexane (50 mL) at 0 °C was added a sulfuric acid solution (80 mL, 20% v/v in AcOH). After 10 min, the reaction was quenched with ice water and the resulting solution was extracted with hexane (3 × 100 mL). The combined organic solution was washed with saturated sodium bicarbonate solution (1 × 100 mL), brine (1 × 100 mL), dried (Na_2SO_4), filtered, and concentrated *in vacuo*. The resulting 6-bromo-1-(4- methoxyphenyl)cyclohexene was used without further purification because of instability.

To a solution of crude allylic bromide (assuming 27.0 mmol) in DMF (60 mL) was added sodium azide (7.00 g, 108 mmol, 4.00 eq) and the reaction was heated to 90 °C. After 30

min, the reaction was cooled and excess DMF was removed *in vacuo*. The crude oil was dissolved in hexane (50 mL) and washed with sodium bicarbonate solution (1 × 100 mL), dried (Na_2SO_4), filtered, concentrated *in vacuo* and purified by flash column chromatography (0 - 2%, EtOAc in hexane) to afford allylic azide **5.31** (2.56 g, 11.1 mmol, 41% over 3 steps) as a colourless oil that crystallises in the fridge.

^{1}H NMR (400 MHz, $CDCl_3$) δ 7.41 – 7.34 (m, 2H, C<u>H</u>-4;C<u>H</u>-4'), 6.94 – 6.86 (m, 2H, C<u>H</u>-3;C<u>H</u>-3'), 6.26 (dd, *J* = 4.8, 3.2 Hz, 1H, C<u>H</u>-11), 4.36 – 4.27 (m, 1H, C<u>H</u>-7), 3.82 (s, 3H, C<u>H</u>$_3$-1), 2.38 – 2.27 (m, 1H, C<u>H</u>$_a$H$_b$-10), 2.26 – 2.17 (m, 1H, CH$_a$<u>H</u>$_b$-10), 2.17 – 2.09 (m, 1H, C<u>H</u>$_a$H$_b$-8), 1.96 – 1.86 (m, 1H, CH$_a$<u>H</u>$_b$-8), 1.81 – 1.73 (m, 2H, C<u>H</u>$_2$-9); **^{13}C{^{1}H} NMR** (101 MHz, $CDCl_3$) δ 159.2, 134.2, 132.7, 129.1, 127.0 (2C), 114.1 (2C), 57.0, 55.4, 29.7, 25.7, 17.6. Consistent with reported literature values.[8]

(*S*)-2-amino-2-(4-chlorophenyl)ethan-1-ol (5.48)



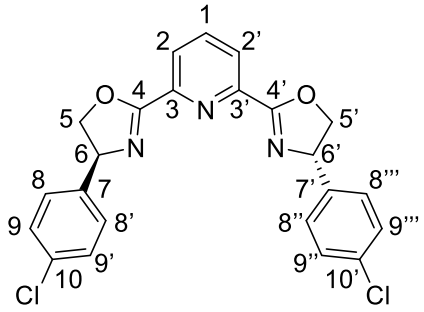
Chemical Formula: $C_8H_{10}ClNO$
Molecular Weight: 171.6240

Synthesised according to the method adapted from Lui *et al*.[8] A flame-dried flask sealed under argon was charged with (*S*)-2-amino-2-(4-chlorophenyl)acetic acid (1.85 g, 10.0 mmol, 1.00 eq), and sodium borohydride (953 mg, 25.2 mmol, 2.52 eq). The flask was cooled in an ice bath and anhydrous THF (150 mL) was added. After 10 min, a solution of iodine (3.12 g, 12.3 mmol, 1.23 eq) in THF (20 mL) was added dropwise and the reaction was heated to reflux. After 16 h, the reaction was cooled, and methanol was added dropwise until the suspension turned to a clear solution. After stirring at room temperature for an additional 30 min., a sodium hydroxide solution (40 mL, 3 M in water) was added. After an additional 4 h, the solution was concentrated *in vacuo* and the

resulting suspension was extracted with DCM (3 × 50 mL). The combined organic solution was washed with brine (1 × 50 mL), dried (Na_2SO_4), filtered, and concentrated *in vacuo*. The resulting aminoalcohol **5.48** was obtained in (1.54 g, 8.97 mmol, 90%) as a yellow solid. **5.48** was used without further purification.

^{1}H NMR (400 MHz, $CDCl_3$) δ 7.34 – 7.26 (m, 4H, C<u>H</u>-4;C<u>H</u>-4';C<u>H</u>-5;C<u>H</u>-5'), 4.03 (dd, *J* = 8.1, 4.3 Hz, 1H, C<u>H</u>-2), 3.70 (dd, *J* = 10.8, 4.3 Hz, 1H, C<u>H$_a$</u>H$_b$-1), 3.52 (dd, *J* = 10.8, 8.0 Hz, 1H, CH$_a$<u>H$_b$</u>-1), 2.34 (bs, 3H, CH-2-N<u>H$_2$</u>;CH$_2$-1-O<u>H</u>); **^{13}C{^{1}H} NMR** (101 MHz, $CDCl_3$) δ 141.2, 133.3, 128.8 (2C), 128.0 (2C), 67.9, 56.9; **HRMS** (ESI) *m/z* calcd for $C_8H_{11}ON^{35}Cl$ $[M+H]^+$: 172.0524, found: 172.0524; calcd for $C_8H_{11}ON^{37}Cl$ $[M+H]^+$: 174.0494, found: 174.0496. Consistent with reported literature values.[22]

2,6-bis((*S*)-4-(4-chlorophenyl)-4,5-dihydrooxazol-2-yl)pyridine (5.34)



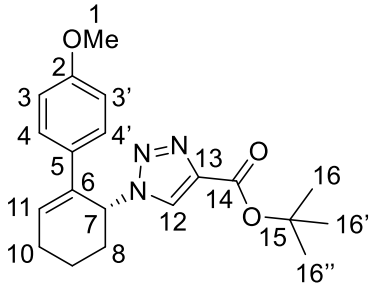
Chemical Formula: $C_{23}H_{17}Cl_2N_3O_2$
Molecular Weight: 438.3080

Synthesised according to the method adapted from Lui *et al*.[8] Sodium methoxide (7.2 mg, 0.10 mmol, 0.10 eq) was added to a solution of 2,6-pyridinedicarbonitrile (130 mg, 1.00 mmol, 1.00 eq) in methanol (2.0 mL). After stirring at ambient temperature for 24 h, the reaction was quenched with acetic acid (12 μL). The solvent was removed *in vacuo* and the flask was refilled anhydrous DCM (10 mL) under argon. Aminoalcohol **5.48** was added to the flask and the reaction was heated to reflux. After 48 h, the reaction was cooled to ambient temperature, concentrated *in vacuo* and purified by flash column

chromatography (0-20% MeCN in toluene) afforded PYBOX **5.34** (388 mg, 0.885 mmol, 89%).

^{1}H NMR (400 MHz, $CDCl_3$) δ 8.33 (d, *J* = 7.8 Hz, 2H, C<u>H</u>-2;C<u>H</u>-2'), 7.94 (t, *J* = 7.9 Hz, 1H, C<u>H</u>-1), 7.36 – 7.32 (m, 4H, C<u>H</u>-9;C<u>H</u>-9';C<u>H</u>-9'';C<u>H</u>-9'''), 7.26 (dq, *J* = 4.4, 2.2 Hz, 4H, C<u>H</u>-8;C<u>H</u>-8';C<u>H</u>-8'';C<u>H</u>-8'''), 5.44 (dd, *J* = 10.3, 8.5 Hz, 2H, C<u>H</u>-6,C<u>H</u>-6'), 4.92 (dd, *J* = 10.4, 8.7 Hz, 2H, C<u>H$_a$</u>H$_b$-5;C<u>H$_a$</u>H$_b$-5'), 4.37 (t, *J* = 8.6 Hz, 2H, CH$_a$<u>H$_b$</u>-5;CH$_a$<u>H$_b$</u>-5'); **^{13}C{^{1}H} NMR** (101 MHz, $CDCl_3$) δ 163.8 (2C), 146.8 (2C), 140.3 (2C), 137.7, 133.8 (2C), 129.1 (4C), 128.3 (4C), 126.5 (2C), 75.5 (2C), 69.8 (2C); **HRMS** (ESI) *m/z* calcd for $C_{23}H_{18}O_2N_3{}^{35}Cl_2$ $[M+H]^+$: 438.0771, found: 438.0765; calcd for $C_{23}H_{18}O_2N_3{}^{37}Cl$ $[M+H]^+$: 440.0742, found: 440.0735. Consistent with reported literature values.[8]

***tert*-Butyl (*R*)-1-(4'-methoxy-2,3,4,5-tetrahydro-[1,1'-biphenyl]-2-yl)-1*H*-1,2,3-triazole-4-carboxylate (5.33)**



Chemical Formula: $C_{20}H_{25}N_3O_3$
Molecular Weight: 355.4380

Synthesised according to general procedure 2, using allylic azide **5.31** and *t*-butyl propiolate **5.32** as coupling partners. Purified by flash column chromatography (0 - 30%, EtOAc in hexane) to afford triazole **5.31** (46 mg, 0.13 mmol, 65%) as a white solid.

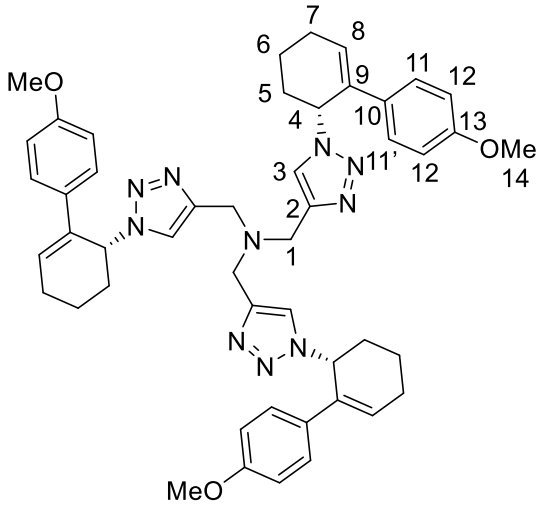
SFC analysis indicated an enantiomeric excess of 90% [Chiralpak® ID (3 μm, 150×3 mm); Flow rate: 1.5 ml/min; CO_2:MeOH with gradient of 99:1 to 70:30 in 0 to 5 min; gradient of 70:30 to 50:50 in 5 to 5.5 min; 50:50 isocratically from 5.5 to 7 min; 100:0

isocratically from 7 to 8 min; λ_{det} = 253.7 nm; t_R = 4.07 min (major), t_R = 4.35 min (minor)].

Alternatively, general procedure 2 was adapted using allylic azide **5.31** and *t*-butyl propiolate **5.32** as coupling partners with **5.34** as ligand in DCM. Purified by flash column chromatography (0 - 30%, EtOAc in hexane) to afford triazole **5.31** (52 mg, 0.15 mmol, 73%) as a white solid. SFC analysis indicated an enantiomeric excess of 20% [SFC conditions as above].

^{1}H NMR (400 MHz, $CDCl_3$) δ 7.84 (s, 1H, C$\underline{H}$-12), 7.21 – 7.13 (m, 2H, C$\underline{H}$-4;C$\underline{H}$-4'), 6.83 – 6.71 (m, 2H, C$\underline{H}$-3;C$\underline{H}$-3'), 6.55 – 6.45 (m, 1H, C$\underline{H}$-11), 5.89 – 5.79 (m, 1H, C$\underline{H}$-7), 3.73 (s, 3H, C$\underline{H}_3$-1), 2.48 – 2.36 (m, 1H, C$\underline{H}_a$H$_b$-10), 2.38 – 2.28 (m, 1H CH$_a\underline{H}_b$-10), 2.31 – 2.20 (m, 1H, C$\underline{H}_a$H$_b$-8), 2.21 – 2.08 (m, 1H, CH$_a\underline{H}_b$-8), 1.80 – 1.68 (m, 1H, C$\underline{H}_a$H$_b$-9), 1.55 (s, 9H, C$\underline{H}_3$-16;C$\underline{H}_3$-16';C$\underline{H}_3$-16''), 1.52 – 1.36 (m, 1H, CH$_a\underline{H}_b$-9); **^{13}C{^{1}H} NMR** (101 MHz, $CDCl_3$) δ 160.3, 159.4, 140.9, 132.0, 131.1, 130.6, 126.9, 126.4 (2C), 114.3 (2C), 82.3, 56.6, 55.3, 30.8, 28.3 (3C), 25.6, 16.8; **HRMS** (ESI) *m/z* calcd for $C_{20}H_{26}O_3N_3$ $[M+H]^+$: 356.1969, found: 356.1969. Consistent with reported literature values.[8]

Tris((1-((*R*)-4'-methoxy-2,3,4,5-tetrahydro-[1,1'-biphenyl]-2-yl)-1*H*-1,2,3-triazol-4-yl)methyl)amine (5.35)



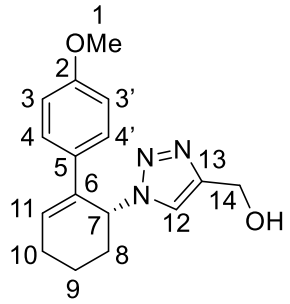
Chemical Formula: $C_{48}H_{54}N_{10}O_3$
Molecular Weight: 819.0270

Synthesised according to general procedure 1, using allylic azide **5.31** (0.25 mmol, 3.3 eq) and tripropargylamine **5.37** (0.075 mmol, 1.0 eq) as coupling partners. Purified by flash column chromatography (0 - 2%, MeCN in toluene) to afford a diastereomeric mixture of tristriazole **5.35** (29 mg, 0.035 mmol, 47%) as a transparent oil.

Data reported here is for a single diastereomer

^{1}H NMR (400 MHz, $CDCl_3$) δ 7.46 (s, 3H, 3 × C<u>H</u>-3), 7.18 – 7.10 (m, 6H, 3 × C<u>H</u>-11;C<u>H</u>-11'), 6.68 – 6.62 (m, 6H, 3 × C<u>H</u>-12;C<u>H</u>-12'), 6.43 – 6.36 (m, 3H, 3 × C<u>H</u>-8), 5.79 – 5.71 (m, 3H, 3 × C<u>H</u>-4), 3.62 (s, 9H, 3 × C<u>H</u>$_3$-14), 3.28 – 3.23 (m, 6H, 3 × C<u>H</u>$_2$-1), 2.50 – 2.37 (m, 3H, 3 × C<u>H</u>$_a$H$_b$-7), 2.37 – 2.25 (m, 3H, 3 × CH$_a$<u>H</u>$_b$-7), 2.25 – 2.11 (m, 6H, 3 × C<u>H</u>$_2$-5), 1.80 – 1.68 (m, 3H, 3 × C<u>H</u>$_a$H$_b$-6), 1.67 – 1.52 (m, 3H, 3 × CH$_a$<u>H</u>$_b$-6); **^{13}C{^{1}H} NMR** (101 MHz, $CDCl_3$, chemical shifts for triazole carbons were not observed) δ 159.0 (3C), 133.3 (3C), 131.4 (3C), 130.6 (3C), 126.8 (6C), 114.0 (6C), 56.8 (3C), 55.3 (3C), 46.9 (3C), 31.1 (3C), 25.6 (3C), 17.7 (3C); **HRMS** (ESI) *m/z* calcd for $C_{46}H_{56}O_3N_{10}$ $[M+H]^+$: 819.4453, found: 819.4445.

(*R*)-(1-(4'-methoxy-2,3,4,5-tetrahydro-[1,1'-biphenyl]-2-yl)-1*H*-1,2,3-triazol-4-yl)methanol (5.39)



Chemical Formula: $C_{16}H_{19}N_3O_2$
Molecular Weight: 285.3470

Synthesised according to general procedure 2, using allylic azide **5.31** and propargyl alcohol **5.38** as coupling partners with $[(MeCN)_4Cu]PF_6$ (1.9 mg, 0.0050 mmol, 0.025 eq) as copper source. Purified by flash column chromatography (20 - 80%, EtOAc in hexane) to afford triazole **5.39** (36 mg, 0.13 mmol, 63%) as a transparent oil.

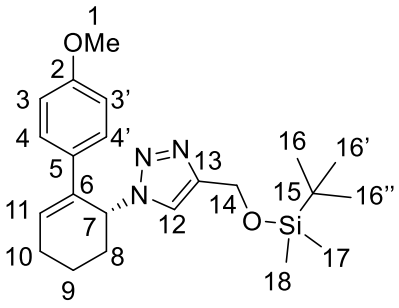
SFC analysis indicated an enantiomeric excess of 57% [Chiralpak® ID (3 μm, 150×3 mm); Flow rate: 1.5 ml/min; CO_2:MeOH with gradient of 99:1 to 55:45 in 0 to 9 min; 55:45 isocratically from 9 to 11 min; 100:0 isocratically from 11 to 12 min; λ_{det} = 252.2 nm; t_R = 4.79 min (major), t_R = 5.03 min (minor)].

Alternatively, TBAF (314 μL, 0.314 mmol, 1 M in THF) was added to a solution of **5.43** (114 mg, 0.285 mmol, 1.00 eq) in THF (5.0 mL) and stirred for 4 hours. The reaction mixture concentrated *in vacuo* and purified by flash column chromatography (20 - 80%, EtOAc in hexane) to afford triazole **5.39** (63 mg, 0.22 mmol, 77%) as a transparent oil. SFC analysis indicated an enantiomeric excess of 88% [SFC conditions as above].

^{1}H NMR (400 MHz, $CDCl_3$) δ 7.40 (s, 1H, C<u>H</u>-12), 7.23 – 7.13 (m, 2H, C<u>H</u>-4;C<u>H</u>-4'), 6.78 – 6.71 (m, 2H, C<u>H</u>-3;C<u>H</u>-3'), 6.49 – 6.42 (m, 1H, C<u>H</u>-11), 5.86 – 5.71 (m, 1H, C<u>H</u>-7), 4.74 – 4.55 (m, 2H, C<u>H</u>$_2$-14), 3.72 (s, 3H, C<u>H</u>$_3$-1), 2.95 (s, 1H, CH$_2$O<u>H</u>-14), 2.46 – 2.36 (m, 1H, C<u>H</u>$_a$H$_b$-10), 2.36 – 2.20 (m, 2H, CH$_a$<u>H</u>$_b$-10;C<u>H</u>$_a$H$_b$-8), 2.18 – 2.08 (m, 1H,

CH_aH_b-8), 1.78 – 1.68 (m, 1H, CH_aH_b-9), 1.56 – 1.42 (m, 1H, CH_aH_b-9); **$^{13}C\{^1H\}$ NMR** (101 MHz, $CDCl_3$) δ 159.2, 146.9, 132.5, 131.1, 130.7, 126.5 (2C), 121.4, 114.2 (2C), 56.6, 56.4, 55.3, 31.0, 25.7, 17.1; **HRMS** (ESI) *m/z* calcd for $C_{16}H_{20}O_2N_3$ $[M+H]^+$: 286.1550, found: 286.1551.

(*R*)-4-(((*tert*-butyldimethylsilyl)oxy)methyl)-1-(4'-methoxy-2,3,4,5-tetrahydro-[1,1'-biphenyl]-2-yl)-1*H*-1,2,3-triazole (5.43)



Chemical Formula: $C_{22}H_{33}N_3O_2Si$
Molecular Weight: 399.6100

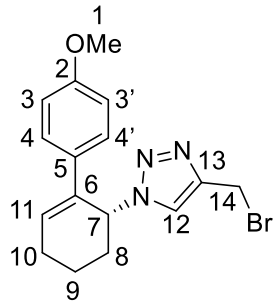
Synthesised according to general procedure 2, using allylic azide **5.31** and TBS-protected propargyl alcohol **5.42** as coupling partners. Purified by flash column chromatography (0 - 20%, EtOAc in hexane) to afford triazole **5.43** (60 mg, 0.15 mmol, 75%) as a transparent oil.

SFC analysis indicated an enantiomeric excess of 86% [Chiralpak® IE (3 μm, 150×3 mm); Flow rate: 1.5 ml/min; CO_2:MeCN with gradient of 99:1 to 90:10 in 0 to 22 min; gradient of 90:10 to 50:50 in 22 to 23 min; 50:50 isocratically from 23 to 24 min; 100:0 isocratically from 24 to 25 min; λ_{det} = 252.2 nm; t_R = 20.47 min (minor), t_R = 21.33 min (major)].

^1H NMR (400 MHz, $CDCl_3$) δ 7.31 (s, 1H, CH-12), 7.21 – 7.12 (m, 2H, CH-4;CH-4'), 6.82 – 6.71 (m, 2H, CH-3;CH-3'), 6.50 – 6.41 (m, 1H, CH-11), 5.81 – 6.74 (m, 1H, CH-7), 4.79 – 4.66 (m, 2H, CH_2-14), 3.73 (s, 3H, CH_3-1), 2.47 – 2.34 (m, 1H, CH_aH_b-10),

2.37 – 2.20 (m, 2H, $CH_a\underline{H}_b$-10;$C\underline{H}_aH_b$-8), 2.21 – 2.08 (m, 1H, $CH_a\underline{H}_b$-8), 1.80 – 1.68 (m, 1H, $C\underline{H}_aH_b$-9), 1.63 – 1.45 (m, 1H, $CH_a\underline{H}_b$-9), 0.82 (s, 9H, $C\underline{H}_3$-16;$C\underline{H}_3$-16';$C\underline{H}_3$-16''), -0.03 (s, 2H, $C\underline{H}_3$-17), -0.06 (s, 2H, $C\underline{H}_3$-18); **$^{13}C\{^1H\}$ NMR** (101 MHz, $CDCl_3$) δ 159.2, 147.8, 132.9, 131.3, 130.5, 126.6 (2C), 121.4, 114.1 (2C), 58.1, 56.3, 55.3, 31.1, 25.9 (3C), 25.7, 18.3, 17.3, -5.2 (2C); **HRMS** (ESI) *m/z* calcd for $C_{22}H_{34}O_2N_3{}^{28}Si$ $[M+H]^+$: 400.2415, found: 400.2409. Consistent with reported literature values.[8]

(*R*)-4-(bromomethyl)-1-(4'-methoxy-2,3,4,5-tetrahydro-[1,1'-biphenyl]-2-yl)-1H-1,2,3-triazole (5.44)



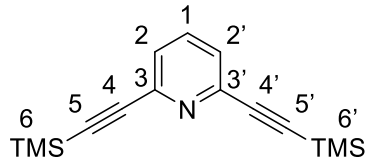
Chemical Formula: $C_{16}H_{18}BrN_3O$
Molecular Weight: 348.2440

Synthesised according to method adapted from Kim *et al*.[29] A flame-dried flask sealed under argon was charged with racemic triazole **5.39** (25 mg, 0.088 mmol, eq 1.0) followed by addition of anhydrous DCM (1 mL) and the resulting solution was cooled to 0 °C in an ice bath. After addition of CBr_4 (40 mg, 0.12 mmol, 1.4 eq) and PPh_3 (32 mg, 0.12 mmol, 1.4 eq), the reaction was stirred for 1 h. Upon full consumption of **5.39** (according to TLC, 10% EtOAc in hexane), the reaction mixture was concentrated *in vacuo* and purified by flash column chromatography (0 - 10%, EtOAc in hexane) to afford bromide **5.31** (16 mg, 0.046 mmol, 52%) as a transparent oil.

^1H NMR (400 MHz, $CDCl_3$) δ 7.43 (s, 1H, C$\underline{H}$-12), 7.21 – 7.12 (m, 2H, C$\underline{H}$-4;C$\underline{H}$-4'), 6.81 – 6.73 (m, 2H, C$\underline{H}$-3;C$\underline{H}$-3'), 6.52 – 6.44 (m, 1H, C$\underline{H}$-11), 5.83 – 5.74 (m, 1H, C$\underline{H}$-7), 4.49 (d, J = 11.5 Hz, 1H, $C\underline{H}_aH_b$-14), 4.43 (d, J = 11.3 Hz, 1H, $CH_a\underline{H}_b$-14), 3.75 (s,

3H, C<u>H</u>$_3$-1), 2.49 – 2.22 (m, 3H CH_2-10;C<u>H</u>$_a$H$_b$-8), 2.20 – 2.09 (m, 1H, CH_a<u>H</u>$_b$-8), 1.82 – 1.71 (m, 1H C<u>H</u>$_a$H$_b$-9), 1.56 – 1.39 (m, 1H, CH_a<u>H</u>$_b$-9).

2,6-bis((trimethylsilyl)ethynyl)pyridine (5.45)

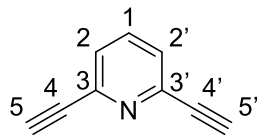


Chemical Formula: $C_{15}H_{21}NSi_2$
Molecular Weight: 271.5100

Synthesised according to the method adapted from Yang *et al*.[30] A flask (50 mL) was charged with 2,6-dibromopyridine **5.44** (2.00 g, 8.40 mmol, 1.00 eq), CuI (32 mg, 0.17 mmol, 0.02 eq) and $Pd(PPh_3)_4$ (195 mg, 0.168 mmol, 0.02 eq). After bringing the flask under argon atmosphere, THF (15 mL) and DIPA (15 mL) were added and the resulting reaction mixture was degassed by bubbling argon through the solution. After 15 minutes, TMS-acetylene (2.92 mL, 21.1 mmol, 2.50 eq) was added and the reaction was stirred at 50 °C for 6 h. After consumption of 2,6-dibromopyridine as indicated by TLC monitoring (50% CH_2Cl_2 in hexane) the mixture was cooled to room temperature, concentrated *in vacuo*, purified by flash column chromatography (50% CH_2Cl_2 in hexane) to afford 2,6-bis(trimethylsilylethynyl)pyridine **5.45** (2.26 g, 8.32 mmol, 99% yield) as white powder.

^{1}H NMR (400 MHz, $CDCl_3$) δ 7.62 – 7.55 (m, 1H, C<u>H</u>-1), 7.40 – 7.34 (m, 2H, C<u>H</u>-2;C<u>H</u>-2'), 0.25 (s, 18H, 3 × C<u>H</u>$_3$-6;3 × C<u>H</u>$_3$-6'); **^{13}C{^{1}H} NMR** (101 MHz, $CDCl_3$) δ 143.5 (2C), 136.3, 126.8 (2C), 103.3 (2C), 95.6 (2C), -0.2 (6C); **HRMS** (ESI) *m/z* calcd for $C_{15}H_{22}NSi_2$ $[M+H]^+$: 272.1285, found: 272.1285. Consistent with reported literature values.[30]

2,6-bis((trimethylsilyl)ethynyl)pyridine (5.46)

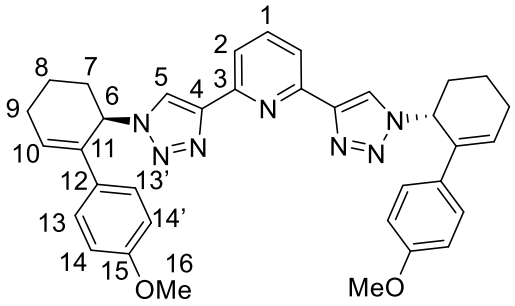


Chemical Formula: C_9H_5N
Molecular Weight: 127.15

Synthesised according to the method adapted from Yang *et al.*[30] K_2CO_3 (5.80 g, 42.2 mmol, 5 eq) was added to a solution of **5.45** (2.26 g, 8.32 mmol, 1.00 eq) in methanol (50 mL) and the reaction was stirred at room temperature for 4 h. The solution was diluted with H_2O (30 mL) and extracted with Et_2O (3 × 50 ml). The combined organic phases were dried (Na_2SO_4), concentrated *in vacuo* and purified by flash column chromatography (40% CH_2Cl_2 in hexane) to afford 2,6-bis(ethynyl)pyridine **5.46** (788 mg, 6.20 mmol, 75% yield).

^{1}H NMR (400 MHz, $CDCl_3$) δ 7.67 – 7.61 (m, 1H, C<u>H</u>-1), 7.47 – 7.40 (m, 2H, C<u>H</u>-2;C<u>H</u>-2'), 3.15 (s, 2H, C<u>H</u>-5;C<u>H</u>-5'); **^{13}C{^{1}H} NMR** (101 MHz, $CDCl_3$) δ 142.9 (2C), 136.7, 127.2 (2C), 82.2 (2C), 77.9 (2C); **HRMS** (ESI) *m/z* calcd for C_9H_6N $[M+H]^+$: 128.0495, found: 128.0494. Consistent with reported literature values.[30]

2,6-bis(1-((*R*)-4'-methoxy-2,3,4,5-tetrahydro-[1,1'-biphenyl]-2-yl)-1*H*-1,2,3-triazol-4-yl)pyridine (5.36)



Chemical Formula: $C_{35}H_{35}N_7O_2$
Molecular Weight: 585.7120

Synthesised according to general procedure 2, using allylic azide **5.31** (47 µL, 0.24 mmol, 2.4 eq) and bisalkyne **5.46** (12.7 mg, 0.100 mmol, 1.00 eq) as coupling partners. The reaction mixture was washed with an aqueous solution of NH_3 (17% w/w) in 0.1 M sodium-ethylenediaminetetraacetate, dried (Na_2SO_4), filtered, concentrated *in vacuo* and purified by flash column chromatography (0 - 20%, MeCN in toluene) to afford bistriazole **5.36** (57 mg, 0.097 mmol, 97%) as a white solid divided over fraction one (15 mg, 0.026 mmol, 26%), fraction two (23 mg, 0.039 mmol, 39%) and fraction three (7 mg, 0.012 mmol, 12%) (See Figure 5.15)**.**

SFC analysis indicated enrichment of minor isomer [Chiralpak® IB (3 µm, 150×3 mm); Flow rate: 1.5 ml/min; CO_2:MeOH with gradient of 99:1 to 86:14 in 0 to 1 min; gradient of 86:14 to 76:24 in 1 to 28 min; 55:45 isocratically from 28 to 29 min; 100:0 isocratically from 29 to 30 min; λ_{det} = 240.7 nm; t_R = 19.07 min (major), t_R = 21.11 min (medium), t_R = 22.36 min (minor)].

^{1}H NMR (500 MHz, Toluene-d_8) δ 8.35 – 8.27 (m, 2H, 2 × C<u>H</u>-2), 7.45 – 7.38 (m, 1H, C<u>H</u>-1), 6.98 (s, 2H, 2 × C<u>H</u>-5), 6.77 – 6.59 (m, 4H , 2 × C<u>H</u>-14; 2 × C<u>H</u>-14'), 6.49 – 6.38 (m, 4H, 2 × C<u>H</u>-13; 2 × C<u>H</u>-13'), 5.68 – 5.56 (m, 2H, 2 × C<u>H</u>-10), 5.49 – 5.30 (m, 2H, 2 × C<u>H</u>-6), 3.42 (s, 6H, 2 × C<u>H</u>$_3$-16), 1.80 – 1.53 (m, 4H, 2 × C<u>H</u>$_2$-9), 1.53 – 1.18 (m, 4H, 2 × C<u>H</u>$_2$-7), 1.03 – 0.78 (m, 2H, 2 × C<u>H</u>$_a$H$_b$-8), 0.67 – 0.36 (m, 2H, 2 × CH$_a$<u>H</u>$_b$-8); **^{13}C{^{1}H} NMR** (101 MHz, $CDCl_3$) δ 158.9 (2C), 150.9 (2C), 146.9 (2C), 137.8, 131.0 (4C), 126.0 (4C), 122.2 (2C), 119.3 (2C), 113.75 (2C), 113.66 (4C), 56.8 (2C), 55.3 (2C), 31.0 (2C), 29.8 (2C), 25.4 (2C); **HRMS** (ESI) *m/z* calcd for $C_{35}H_{36}O_2N_7$ $[M+H]^+$: 586.2925, found: 586.2922; **[α]**$^{25}_D$ = + 30.7 (c = 0.30, $CHCl_3$).

5.10 References

1 D. G. Blackmond, The Origin of Biological Homochirality, *Cold Spring Harb. Perspect. Biol.*, 2010, **2**, a002147–a002147.

2 B. L. Feringa and R. A. van Delden, Absolute Asymmetric Synthesis: The Origin, Control, and Amplification of Chirality, *Angew. Chemie Int. Ed.*, 1999, **38**, 3418–3438.

3 K. Soai, T. Shibata, H. Morioka and K. Choji, Asymmetric autocatalysis and amplification of enantiomeric excess of a chiral molecule, *Nature*, 1995, **378**, 767–768.

4 F. C. Frank, On spontaneous asymmetric synthesis, *Biochim. Biophys. Acta*, 1953, **11**, 459–463.

5 P. I. Dalko, *Enantioselective Organocatalysis: Reactions and Experimental Procedures*, Wiley-VCH, 2007.

6 D. G. Blackmond, Autocatalytic Models for the Origin of Biological Homochirality, *Chem. Rev.*, 2020, **120**, 4831–4847.

7 W. D. G. Brittain, B. R. Buckley and J. S. Fossey, Asymmetric Copper-Catalyzed Azide–Alkyne Cycloadditions, *ACS Catal.*, 2016, **6**, 3629–3636.

8 E.-C. Liu and J. J. Topczewski, Enantioselective Copper Catalyzed Alkyne-Azide Cycloaddition by Dynamic Kinetic Resolution, *J. Am. Chem. Soc.*, 2019, jacs.9b01091.

9 E. Vedejs and M. Jure, Efficiency in Nonenzymatic Kinetic Resolution, *Angew. Chemie Int. Ed.*, 2005, **44**, 3974–4001.

10 J. Meng, V. V. Fokin and M. G. Finn, Kinetic resolution by copper-catalyzed azide–alkyne cycloaddition, *Tetrahedron Lett.*, 2005, **46**, 4543–4546.

11 T. R. Chan, R. Hilgraf, K. B. Sharpless and V. V Fokin, Polytriazoles as Copper(I)-Stabilizing Ligands in Catalysis, *Org. Lett.*, 2004, **6**, 2853–2855.

12 J. R. Alexander, A. A. Ott, E.-C. Liu and J. J. Topczewski, Kinetic Resolution of Cyclic Secondary Azides, Using an Enantioselective Copper-Catalyzed Azide–Alkyne Cycloaddition, *Org. Lett.*, 2019, **21**, 4355–4358.

13 W. D. G. Brittain, B. R. Buckley and J. S. Fossey, Kinetic resolution of alkyne-substituted quaternary oxindoles via copper catalysed azide-alkyne cycloadditions, *Chem. Commun.*, 2015, **51**, 17217–17220.

14 F. Zhou, C. Tan, J. Tang, Y.-Y. Zhang, W.-M. Gao, H.-H. Wu, Y.-H. Yu and J. Zhou, Asymmetric Copper(I)-Catalyzed Azide–Alkyne Cycloaddition to Quaternary Oxindoles, *J. Am. Chem. Soc.*, 2013, **135**, 10994–10997.

15 T. Osako and Y. Uozumi, Enantioposition-selective copper-catalyzed azide-alkyne cycloaddition for construction of chiral biaryl derivatives, *Org. Lett.*, 2014, **16**, 5866–5869.

16 T. Song, L. Li, W. Zhou, Z.-J. Zheng, Y. Deng, Z. Xu and L.-W. Xu, Enantioselective Copper-Catalyzed Azide-Alkyne Click Cycloaddition to

Desymmetrization of Maleimide-Based Bis(alkynes), *Chem. - A Eur. J.*, 2015, **21**, 554–558.

17 P. S. Donnelly, S. D. Zanatta, S. C. Zammit, J. M. White and S. J. Williams, 'Click' cycloaddition catalysts: copper(i) and copper(ii) tris(triazolylmethyl)amine complexes, *Chem. Commun.*, 2008, **233**, 2459–2461.

18 S. N. Semenov, L. Belding, B. J. Cafferty, M. P. S. Mousavi, A. M. Finogenova, R. S. Cruz, E. V. Skorb and G. M. Whitesides, Autocatalytic Cycles in a Copper-Catalyzed Azide–Alkyne Cycloaddition Reaction, *J. Am. Chem. Soc.*, 2018, **140**, 10221–10232.

19 S. V. Athavale, A. Simon, K. N. Houk and S. E. Denmark, Demystifying the asymmetry-amplifying, autocatalytic behaviour of the Soai reaction through structural, mechanistic and computational studies, *Nat. Chem.*, 2020, **12**, 412–423.

20 W. G. Lewis, F. G. Magallon, V. V. Fokin and M. G. Finn, Discovery and Characterization of Catalysts for Azide−Alkyne Cycloaddition by Fluorescence Quenching, *J. Am. Chem. Soc.*, 2004, **126**, 9152–9153.

21 V. O. Rodionov, S. I. Presolski, D. Díaz Díaz, V. V. Fokin and M. G. Finn, Ligand-Accelerated Cu-Catalyzed Azide−Alkyne Cycloaddition: A Mechanistic Report, *J. Am. Chem. Soc.*, 2007, **129**, 12705–12712.

22 K. Kawasaki and T. Katsuki, Enantioselective allylic oxidation of cycloalkenes by using Cu(II)-tris(oxazoline) complex as a catalyst, *Tetrahedron*, 1997, **53**, 6337–6350.

23 R. Jacques, R. D. C. Pullin and S. P. Fletcher, Desymmetrization of meso-bisphosphates using copper catalysis and alkylzirconocene nucleophiles, *Nat. Commun.*, 2019, **10**, 21.

24 A. V. Brethomé, R. S. Paton and S. P. Fletcher, Retooling Asymmetric Conjugate Additions for Sterically Demanding Substrates with an Iterative Data-Driven Approach, *ACS Catal.*, 2019, **9**, 7179–7187.

25 H. You, E. Rideau, M. Sidera and S. P. Fletcher, Non-stabilized nucleophiles in Cu-catalysed dynamic kinetic asymmetric allylic alkylation, *Nature*, 2015, **517**, 351–355.

26 S. Karabiyikoglu, A. V. Brethomé, T. Palacin, R. S. Paton and S. P. Fletcher, Enantiomerically enriched tetrahydropyridine allyl chlorides, *Chem. Sci.*, 2020, **11**, 4125–4130.

27 R. B. Lauffer, Paramagnetic Metal Complexes as Water Proton Relaxation Agents for NMR Imaging: Theory and Design, *Chem. Rev.*, 1987, **87**, 901–927.

28 X. Wu, Y. Lu, H. Hirao and J. S. Zhou, Achieving Vinylic Selectivity in Mizoroki-Heck Reaction of Cyclic Olefins, *Chem. - A Eur. J.*, 2013, **19**, 6014–6020.

29 I. Kim, K. C. Ko, W. R. Lee, J. Cho, J. H. Moon, D. Moon, A. Sharma, J. Y. Lee, J. S. Kim and S. Kim, Calix[n]triazoles and Related Conformational Studies, *Org. Lett.*, 2017, **19**, 5509–5512.

30 B. Yang, H. Zhang, H. Peng, Y. Xu, B. Wu, W. Weng and L. Li, Self-healing metallo-supramolecular polymers from a ligand macromolecule synthesized via

copper-catalyzed azide–alkyne cycloaddition and thiol–ene double “click” reactions, *Polym. Chem.*, 2014, **5**, 1945–1953.

Chapter 6 Conclusions and Future Work

6.1 Physical autocatalysis driven by a copper catalyst

The aim of the work within this thesis was to develop and study self-reproducing systems, created from simple chemical building blocks, that exhibit emergent, life-like properties. Several different autocatalytic systems that are driven by copper-catalysed azide-alkyne cycloaddition reactions were described. Linking physical autocatalysis to a secondary catalyst afforded robust autocatalytic systems that were both resilient to environmental changes and compatible with orthogonal types of chemistry.

6.1.1 Self-reproducing micelles coupled to a secondary catalyst

In Chapter 2, a new autocatalytic reaction was developed based on surfactant formation from phase-separated components driven by CuAAC. We investigated the unique properties of this system where physical autocatalysis was driven by a copper catalyst. Hydrophilic maltose-derived azide was coupled to hydrophobic terminal alkynes to give triazole surfactant products that aggregated into micelles. The micelles aid phase-transfer of the alkynes into the aqueous phase, thereby accelerating their own formation and closing the autocatalytic cycle.

Seeding experiments at varying concentrations showed that product-induced rate acceleration was strongly concentration dependent and only occurred above the CMC. When surfactant analogues were investigated, alkynes with shorter hydrophobic tails reacted at faster rates in biphasic reactions, likely due to their increased solubility in the aqueous phase. However, shorter tailed surfactants benefited less from product-induced rate accelerations and experienced product inhibition at high concentrations of product seed. This inhibition was attributed to strong coordination of the triazole moiety to copper at higher concentrations in an aqueous environment.

Measurements of diffusion rates of the reaction components confirmed that physical autocatalysis proceeded through a mechanism where micelles encapsulate hydrophobic substrates, which are subsequently transferred to the aqueous phase. Overall, physical autocatalysis was successfully linked to a secondary CuAAC catalytic cycle opening up new opportunities to control the kinetics and phase behaviour of the overall system.

6.1.2 Controlling the Kinetics of Self-Reproducing Micelles

We expanded on the system of autocatalysis driven by CuAAC in Chapter 3 by exploiting the link between the secondary catalyst and the autocatalytic cycle to drive new reaction outcomes. The hydrophilicity of the copper complex in the system was altered by employing a hydrophobic or hydrophilic tris-triazole ligand. This control of the active catalyst solubility properties provided a handle to tune the kinetics of the system by virtue of phase behaviour. The hydrophilicity of the ligand controlled the physical location of the active catalyst complex in the biphasic system and provided a way to switch the rate limiting step of the reaction.

Furthermore, CuAAC-based physical autocatalysis tolerated an inversion of the polarity of the coupling partners and the use of a phosphocholine polar headgroup, showcasing the generality and robustness of the reaction. Various coupling partner and ligand combinations were studied and resulted in widely varying kinetic behaviour and autocatalytic efficiency for the biphasic CuAAC reaction. These variations were not caused by differences in substrate reactivity, but rather resulted from altered phase behaviour of the coupling partners and the catalyst complex.

A mechanistic study into diffusion and deuterium exchange rates of the CuAAC reaction components produced a model that considered how phase separation and mass transport influenced the relative rates of each step involved. Additionally, it was evaluated to which

the degree each step in the mechanism benefits from product-induced rate accelerations, and thus the model rationalised which set of reaction conditions afforded the most pronounced autocatalytic effect. Overall, a deeper mechanistic understanding of the link between physical autocatalysis and the secondary catalyst was obtained.

6.1.3 Out-of-Equilibrium Self-Reproducing Protocells

The work in Chapter 4 reported on the design of a self-reproducing protocell system driven by generation of phospholipids *via* CuAAC. This system modelled biological cells more faithfully, and enabled the study of dynamic kinetic and supramolecular behaviour of lipid aggregates. Transient formation of protocells was achieved by introducing hydrolysing conditions to the autocatalytic system, thus enabling degradation of the surfactant product. An out-of-equilibrium state of the system was maintained by performing the reaction in a CSTR setup, mimicking natural self-assembly processes.

Competition experiments between vesicular and micellar replicators for a common feedstock were investigated, to study selection processes among autocatalysts. The basicity of the reaction mixture acted as a selection pressure and controlled which autocatalytic species predominated. At neutral conditions micelle formation was favoured through a unique selection mechanism: micellar aggregates inhibit the synthesis of vesicle-forming surfactants by phase-separating substrates from the catalyst complex. Under basic conditions vesicular surfactants predominated as inhibitory micelles were quickly degraded, enabling formation of persistent vesicles resistant to hydrolysis.

To imitate metabolic processes in nature, orthogonal downstream chemical reactivity was incorporated into the protocell system through a network of linked reactions. Protocell vesicles facilitated *in situ* formation of an amphiphilic organocatalyst that subsequently

imbedded within the vesicle bilayer. The resulting nanoreactor catalysed formation of enantioenriched secondary metabolites.

Overall, a dynamic protocell system that exhibited multiple, emergent properties was developed. We have shown that through a bottom-up synthetic approach a simple molecular system can generate complex, life-like behaviour.

6.1.4 Future work

The reported work has established a robust autocatalytic system by linking physical autocatalysis to a secondary catalyst *via* CuAAC which has proven to be resilient to environmental changes and compatible with orthogonal chemical reactivity. This system design could be used as the foundation upon which to build a synthetic cell capable of a core-and-shell reproduction.

The incorporation of an *in situ*-generated organocatalyst in Chapter 4 showcased how vesicle self-reproduction can facilitate chemical processes within its "core". However, the secondary metabolites that were generated by the organocatalyst did not affect "shell" reproduction and therefore did not establish a core-and-shell reproduction cycle.

A next generation system could involve a secondary reaction in the core, to generate substrates that participate in the autocatalytic cycle giving metabolic closure (Figure 6.1). An *in situ*-generated catalyst (catalyst 3) could facilitate the deprotection of an apolar precursor to form a polar headgroup substrate, e.g. catalyst 3 could facilitate deprotection of a hydrophobic maltose precursor to give hydrophilic maltose-azide (Chapter 2 and 3).

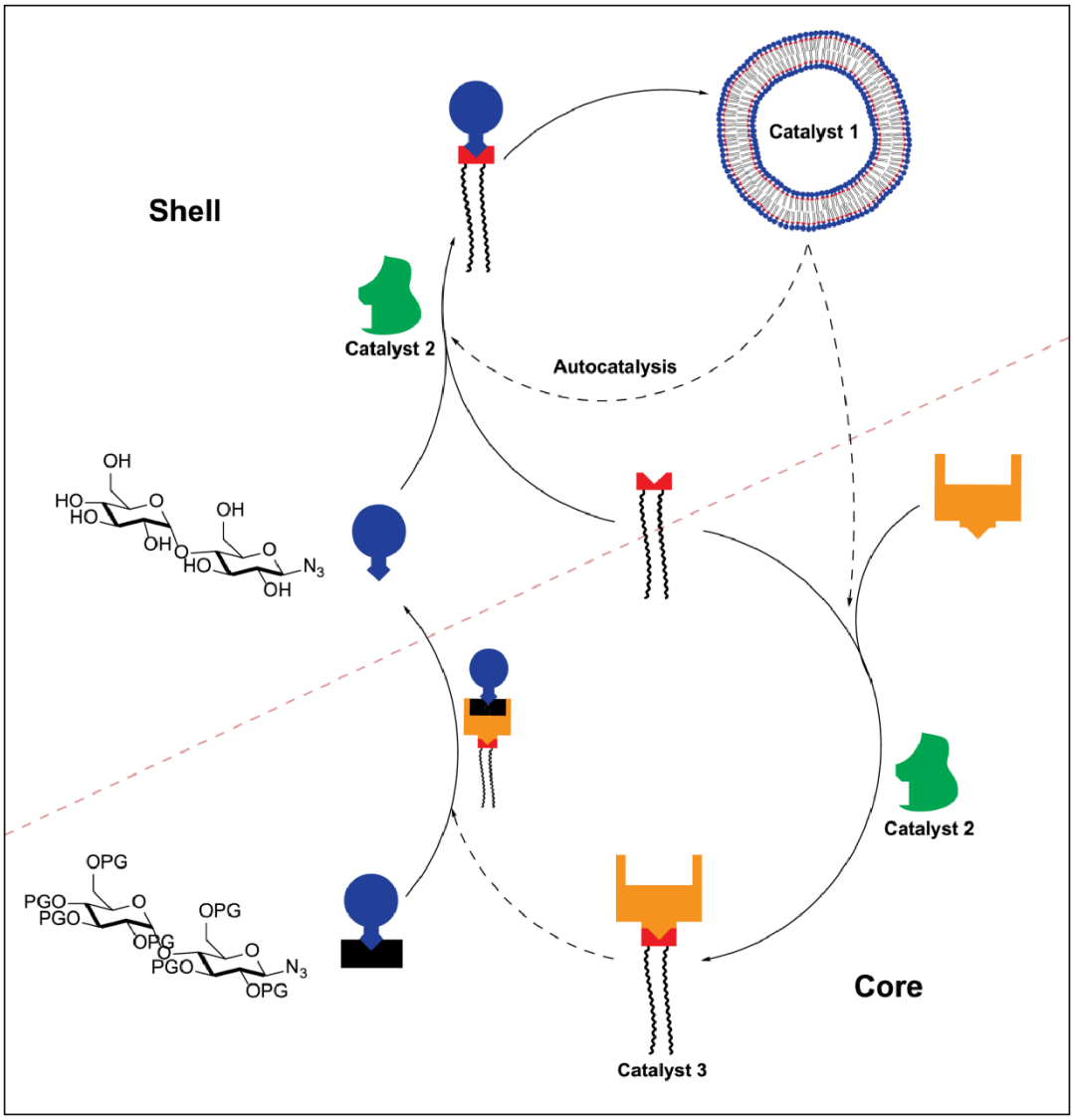


Figure 6.1 Proposed system of interlinked core-and-shell reproduction. A secondary catalyst (Catalyst **2**) drives the formation of a self-reproducing aggregate (Catalyst **1**) and the *in situ* generation of a tertiary catalyst (Catalyst **3**). Catalyst **1** accelerates its own formation but additionally facilitates formation of Catalyst **3**. Finally, Catalyst **3** enables synthesis a hydrophilic polar headgroup through deprotection of hydrophobic precursor. Dashed arrows represent catalytic interactions, whereas whole arrows represent reactions.

In such a system aggregate formation would be required to generate the tertiary catalyst, which in turn would need to deprotect the headgroup precursor before additional surfactant can form. This system would establish a core-and-shell reproduction cycle where all components in both the core and shell are continuously regenerated and most importantly the two subsystems are interlinked through a feedback mechanism.

A second issue that must be addressed in future bottom-up chemical systems, to better mimic biological cells, is the osmotic problem. As the internal complexity of a protocell

increases with the incorporation of an elaborate metabolic system, concentration gradients will develop between the inside and the outside of the cellular compartment.[1] Osmotic pressure will cause an influx of water through the semipermeable membrane of the protocell followed by swelling and ultimately bursting of the vesicles. Nature has developed transmembrane channels and pumps to combat this problem and maintain homeostasis. However, no self-reproducing system developed to date by scientists has addressed this issue.

Furthermore, concentration gradients are vital to life. ATP synthase is a highly conserved enzyme present throughout all kingdoms of life and harnesses proton gradients to store chemical energy in form of adenosine triphosphate (ATP).[2] Sodium-potassium gradients generate membrane potentials and are utilised to quickly send signals across neurons.[3] Novel systems that aim to develop higher chemical complexity in the vesicle interior relative to the aqueous environment must establish mechanisms to regulate the flow of materials across the membrane. This would enable new pathways to harness external energy from the environment to maintain out-of-equilibrium self-reproduction within the protocell system.

6.2 Asymmetric autocatalytic CuAAC

New asymmetric autocatalytic reactions must be developed to further our understanding of biological homochirality and to facilitate synthesis of chiral compounds in self-reproducing systems. Chapter 5 described the progress towards development of an asymmetric autocatalytic copper-catalysed alkyne-azide cycloaddition *via* dynamic kinetic resolution of allylic azides to obtain enantioenriched polytriazole ligands. This new class of ligand might be used in asymmetric CuAAC and an asymmetric autocatalytic

cycle might be established if the ligands are able to generate enantioenriched copies of themselves.

Synthetic routes towards two structurally different enantioenriched polytriazole ligands were explored: tris-triazole **5.35** with a central tertiary amine (analogous in structure to commonly used tris-triazole ligands, see Chapter 3 and 4) and bis-triazole **5.36** with a central pyridine ring inspired by the PYBOX class of ligands.

Standard conditions for asymmetric CuAAC *via* DKR did not afford enantioenriched tris-triazole ligand **5.35** due to complications during purification and determination of enantiomeric excess (Section 5.6). An alternative route towards **5.35** and other polytriazole ligands was explored *via* an enantioenriched allylic triazole precursor. The synthesis reached a stage one step away from the final compound, obtaining bromide-appended triazole **5.44** that might be converted to polytriazole compounds through nucleophilic attack by an amine-bearing substrate.

A route towards enantioenriched bis-triazole **5.36** was developed and undesired diastereomeric sideproducts were removed by column chromatography. The enantiomeric excess of **5.36** could not be determined with confidence as rotamer formation complicated SFC identification of all isomers in the racemate. Promisingly, a preliminary test showed that enantioenriched **5.36** acts as a chiral ligand during asymmetric CuAAC *via* DKR, as allylic triazole **5.33** was obtained in 20% ee.

Overall, a chiral polytriazole ligand was synthesised and it was verified that this class of ligands binds to copper and induces chirality in asymmetric CuAAC reactions.

6.2.1 Future work in asymmetric autocatalytic CuAAC

The results reported in Chapter 5 have shown that an asymmetric autocatalytic CuAAC reaction might be developed by generating chiral polytriazole ligands from allylic azides. As enantioenriched bis-triazole **5.36** facilitated asymmetric synthesis of **5.33**, it could potentially catalyse its own enantioselective formation and establish an asymmetric autocatalytic cycle.

There are several prerequisites that must be met before this asymmetric autocatalytic reaction can be studied. Firstly, suitable conditions must be found to identify all possible isomers of **5.36** in the racemate and allow for the unequivocal determination of the enantiomeric excess. This could be achieved by performing SFC measurements at higher column temperatures, as VT ^{1}H NMR analysis had shown that the energetic barrier to rotation by the atropisomers can be overcome at sufficiently high temperatures. This would remove atropisomerism in the sample and significantly simplify any further analysis. Alternatively, reversed-phase UPLC analysis with a suitable chiral column could afford better separation of all isomers of **5.36**.

Additionally, a large-scale synthesis of enantioenriched **5.36** would be required possibly under reoptimised conditions if enantiomeric excess obtained *via* current reaction conditions is deemed insufficient. Iterative crystallisations of this larger enantioenriched batch could remove any trace amounts of undesired enantio- and diastereomer to afford enantiopure **5.36**.

When optimised reaction conditions for asymmetric autocatalytic CuAAC have been established, mechanistic studies should be performed. Non-linear effects should be investigated as these are required for amplification of chirality. The formation and consumption of the intermediate mono-adduct should be analysed to confirm if other

asymmetric processes are occurring. The use of one equivalent of allylic azide would enable study of the enantioselectivity and rate of mono-triazole formation (Figure 6.2a).

Additionally, the reaction of racemic mono-adduct to from bis-triazole **5.36** could be investigated and the enantiomeric composition of the substrate could be followed (Figure 6.2b). Any non-zero value for the enantiomeric excess of unreacted mono-triazole would indicate preferential reaction by one of the enantiomers and thus involve a kinetic resolution of this intermediate. Osako and Uozumi observed a similar process where desymmetrisation of bis-alkyne **5.20** was followed by kinetic resolution of atropisomer product **5.21** (Section 5.2.2).[4]

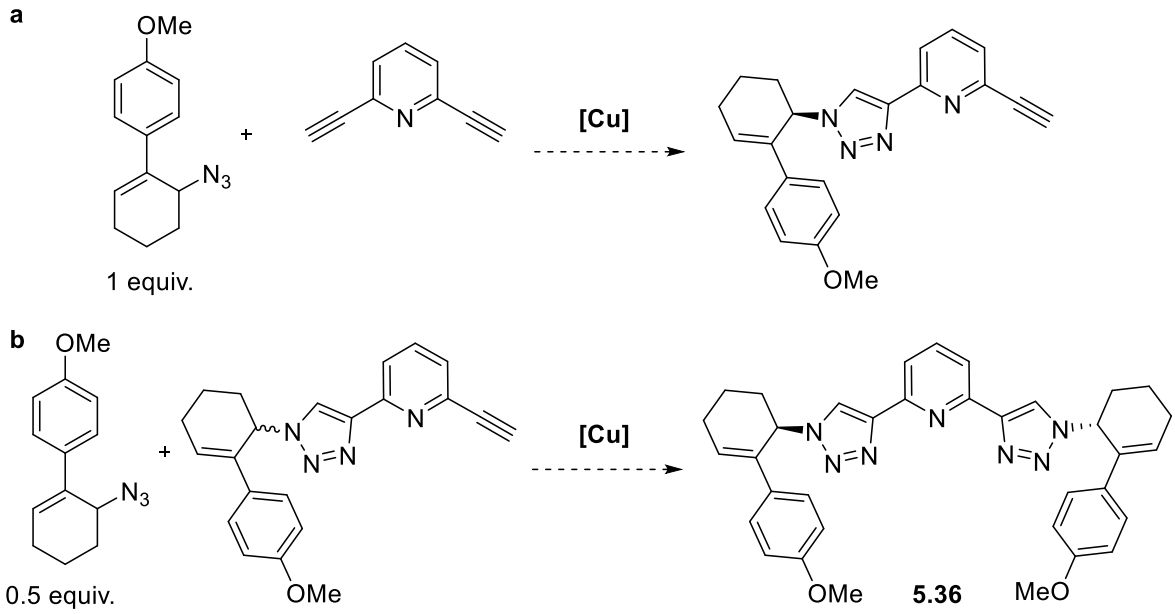


Figure 6.2 Methods to study the formation and consumption of the monotriazole intermediate.

6.2.2 Other ligand structures

There is no guarantee that ligand **5.36** will perform well in an asymmetric autocatalytic reaction after optimisation of the reaction conditions. Structural variations to **5.36** might be required that alter the steric or electronics properties of the ligand (Figure 6.3). The aromatic ring on the allylic azide could be varied in composition or substitution, the

cyclohexene ring could be expanded or contracted, and the central pyridine ring might be substituted.

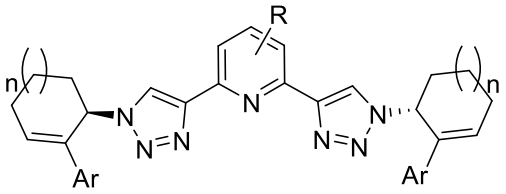


Figure 6.3 Potential sites for variation in the structure of bis-triazole ligands.

The polynuclear catalyst complexes required for amplification of chirality through non-linear effects are expected to be highly sensitive to the structure of the ligand. Prior models of the Soai reaction experienced asymmetric autocatalysis but the substrate went through multiple iterations[5–7] before the ideal product structure was found that facilitated amplification of chirality.[8] Only pyrimidyl aldehydes could form the tetrameric product-catalyst complex required for inhibition of the minor enantiomer through the formation of catalytically inactive heterochiral tetramers.[9]

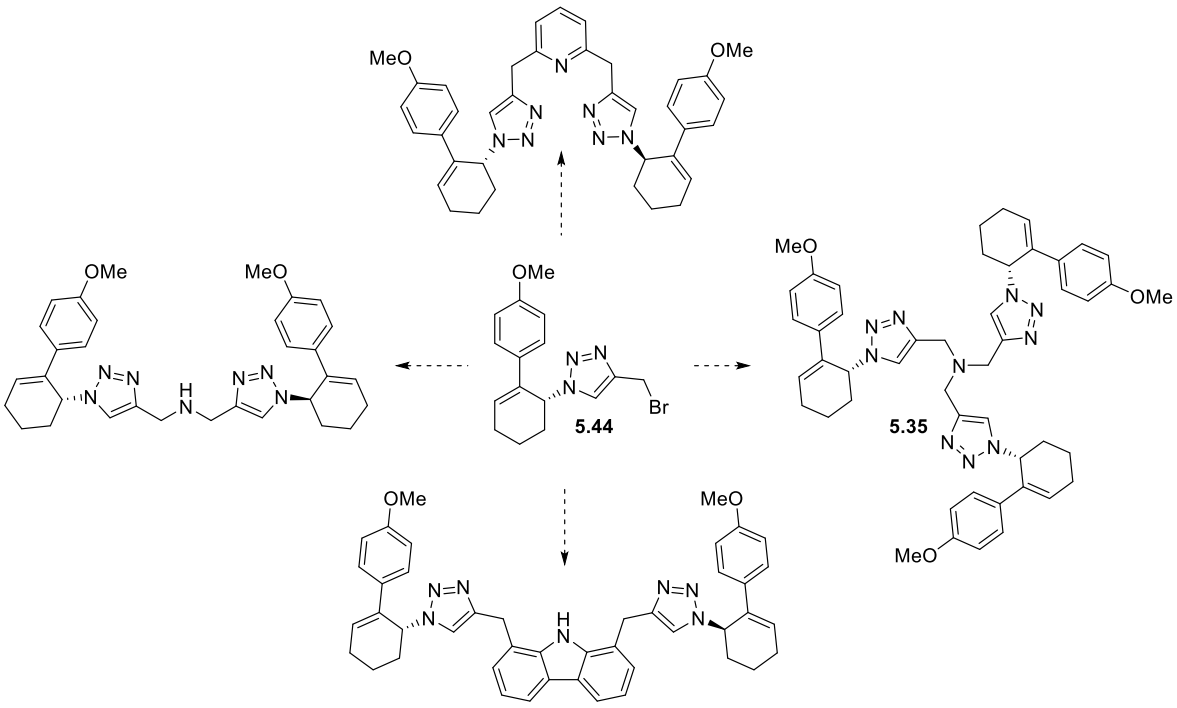


Figure 6.4 Alternative chiral polytriazole ligand structures for study in asymmetric autocatalytic CuAAC.

Similarly, ligand **5.36** and its derivatives might not capable of amplification of chirality through asymmetric autocatalytic CuAAC. Alternative polytriazole ligand structures could be synthesised from bromide **5.44** including tris-triazole **5.35** (Figure 6.4). These structurally different ligands could be screened for efficacy in asymmetric autocatalytic CuAAC and ultimately for their ability to amplify chirality.

The Soai reaction still remains the only experimental realisation of absolute asymmetric autocatalysis to date[8–10] and is a testament to the complexity and improbability of discovering a new reaction of this class. The system reported here might not exhibit perfect absolute asymmetric amplification if mutual antagonism is absent between the enantiomers, causing enantiomeric excess to slowly erode over time.

However, if this system were to exhibit any form of asymmetric amplification it could be used in other areas of chemistry contrary to the Soai reaction. Since the product is a copper ligand, the chirality generated during the reaction could be harnessed to catalyse other asymmetric reactions promoted by copper. We have already shown that chiral bis-triazole **5.36** can be used in asymmetric CuAAC *via* DKR to form a different allylic triazole enantioselectively, but it might also be employed as a chiral ligand in other types of asymmetric copper chemistry, allowing chirality to propagate across multiple different substrate classes. Furthermore, the reaction could potentially be integrated into a self-reproducing system to form chiral protocells capable of asymmetric reactions.

6.3 Concluding remarks

Study of rudimentary bottom-up chemical models of living systems help to further our understanding of the rules that govern and the forces that drive the creation of life. A synthetic chemical system might be defined as living when metabolism, hereditary

information, and compartmentalisation are unified into a functioning, dynamic whole that reproduces in an out-of-equilibrium state through continuous consumption of energy.

This thesis outlined a pathway towards such as system by starting out with the development of self-reproducing compartments. Several different autocatalytic systems were developed driven by copper-catalysed azide-alkyne cycloaddition reactions between phase separated surfactant precursors. Linking a secondary catalytic cycle to physical autocatalysis generated resilient systems tolerant to changes in their environment and to orthogonal chemical reactions. Furthermore, the kinetics of the reaction could be controlled through rational variations in the hydrophilicity of the copper ligand, and an in-depth mechanistic understanding of this system was obtained.

The platform of self-reproducing surfactants driven by CuAAC has shown to be amenable to out-of-equilibrium conditions, competition with other replicators and metabolic downstream reactivity. Metabolic closure might be achieved by incorporating an interlinked core-and-shell reproduction cycle.

Looking to future studies, CuAAC *via* dynamic kinetic resolution of allylic azides to form enantioenriched polytriazole ligands may prove suitable to develop a new autocatalytic system capable of asymmetric amplification but is currently still at a highly exploratory stage. This work aims to show that absolute asymmetric autocatalysis is not limited to the Soai reaction and can be found in other areas of chemistry, and that ultimately a prebiotic variant might have occurred on early Earth to afford the biological homochirality observed in nature.

6.4 References

1 K. Ruiz-Mirazo and A. Moreno, Basic Autonomy as a Fundamental Step in the Synthesis of Life, *Artif. Life*, 2004, **10**, 235–259.

2 H. Lodish, A. Berk, P. Matsudaira, C. A. Kaiser, M. Krieger, M. P. Scott, L. Zipursky and J. Darnell, *Molecular Cell Biology*, W. H. Freeman, New York, 2000.

3 Daniel Johnston and Samuel Miao-Sin Wu, *Foundations of Cellular Neurophysiology*, The MIT Press, Cambridge, 1994.

4 T. Osako and Y. Uozumi, Enantioposition-selective copper-catalyzed azide-alkyne cycloaddition for construction of chiral biaryl derivatives, *Org. Lett.*, 2014, **16**, 5866–5869.

5 K. Soai, S. Niwa and H. Hori, Asymmetric self-catalytic reaction. Self-production of chiral 1-(3-pyridyl)alkanols as chiral self-catalysts in the enantioselective addition of dialkylzinc reagents to pyridine-3-carbaldehyde, *J. Chem. Soc. Chem. Commun.*, 1990, 982.

6 K. Soai, T. Hayase and K. Takai, Catalytic chirally self-replicating molecule. Asymmetric autocatalytic reaction of a zinc alkoxide of chiral 1-ferrocenyl-2-methylpropan-1-ol, *Tetrahedron: Asymmetry*, 1995, **6**, 637–638.

7 K. Soai, T. Hayase, C. Shimada and K. Isobe, Catalytic asymmetric synthesis of chiral diol, bis[2-(1-hydroxyalkyl)-phenyl]ether, an asymmetric autocatalytic reaction, *Tetrahedron: Asymmetry*, 1994, **5**, 789–792.

8 K. Soai, T. Shibata, H. Morioka and K. Choji, Asymmetric autocatalysis and amplification of enantiomeric excess of a chiral molecule, *Nature*, 1995, **378**, 767–768.

9 S. V. Athavale, A. Simon, K. N. Houk and S. E. Denmark, Demystifying the asymmetry-amplifying, autocatalytic behaviour of the Soai reaction through structural, mechanistic and computational studies, *Nat. Chem.*, 2020, **12**, 412–423.

10 D. G. Blackmond, Autocatalytic Models for the Origin of Biological Homochirality, *Chem. Rev.*, 2020, **120**, 4831–4847.